Discovery and characterisation of transiting extra-solar planets with the Wide Angle Search for Planets (WASP) survey

Oliver David Turner

Doctor of Philosophy

Department of Physics, University of Keele.

June 2017

Abstract

In July of 2012 the WASP-South instrument was modified to allow it to collect data on brighter stars. This change was motivated by the dearth of planets known to orbit bright hosts in the southern hemisphere and the depth of study possible for HD 209458 b and HD 189733 b. These two planets orbit very bright stars in the northern hemisphere and have lead to a wealth of discoveries thanks to the relative ease with which they can be studied.

My initial work with the Wide Angle Search for Planets (WASP) project was to contribute to updating the existing automated data reduction pipeline. I investigated the effects of, and helped to implement, various changes made to the pipeline in order to optimise its performance for brighter stars. During these investigations I also contributed fixes for several pipeline bugs. As a result of these changes the pipeline provides a level of precision with the new data as the previous version did with data from the unmodified instrument.

The modified instrument was initially intended to collect data for 3 years. I performed an investigation in order to see if there was value to be gained in extending this period. I injected simplified transit signals into data gathered with the modified instrument that showed no known or candidate signals. These transit signals had a variety of different periods and depths, ranging from those we would expect to detect to those we would expect to be below our detection limits. My results showed that we can expect to recover between 42% and 72% of hot-Jupiters with transit depths between 0.5% and 2% and periods shorter than 10 days. This is comparable to a similar study of WASP-South before the modifications.

I have also contributed to the follow-up of several newly discovered and previously known planets. I have presented the tools used by WASP to discover and characterise exoplanetary systems and have applied them to the investigation of these systems. With new data, I update and refine parameters for 7 previously known WASP planets. I resolve discrepancies in previous studies of WASP-31, show that WASP-42 may be an

important probe of planet migration theory and show that seemingly "typical" systems may warrant re-observing. I present three newly discovered systems: WASP-120 b, a system with a star showing variable activity and a possibly eccentric planet orbit, WASP-122 b, which offers a good opportunity for atmospheric study, and WASP-123 b, which orbits an old star, ~ 7 Gyr.

Acknowledgements

I would first like to thank my supervisor, Dr. Pierre Maxted; for taking me on what seems like a long time ago, for his patience, advice, encouragement and insight. My thanks go also to my second supervisor, Dr. Coel Hellier for his straightforwardness and particularly his experience when it came to nursing my paper through to submission. Of course, this section would not be complete without a thanks to my adoptive supervisor Dr. David Anderson, who helped get me on my feet in my first months here, saw me (mostly safely) around the globe on various adventures "chasing the wind" and for many a master class in proposal writing, data reduction and Naming. Likewise, my co-conspirator Ben, thanks for some finer points of parallelisation without which the code for chapter 7 would still be running. You're welcome for all of the simpler solutions I've suggested. A special mention goes to Gabi as well for his advice with the final touches of LaTeX formatting.

To my old friends from the North East and my even older friends from Home, thank you for your continued friendship and interest though I am now far away. Here's to our future meet-ups wherever life takes us next. To my new friends from Keele, thank you for making life here fun and interesting. To those of the one and only karate club, thank you for actively encouraging me to hit things regularly, especially Jim, with whom I was destined to live in first year. Handy, that. Cathy, we got through a lot of shows and had adventures of our own, fantastic!

Finally, Mum, thank you for having prepared me so well for life, for always supporting me even when it worried you or you thought what I was doing was crazy, thanks for your trust. Thank you too for your thoughts and prayers as well as those of the people of Kay St. Baptist in Rawtenstall and St. Georges of Newcastle.

Contents

List of Figures

List of Tables

1 The diverse study of transiting exoplanets

1.1 Introduction

Theories on the existence of planets orbiting stars other than our Sun are not new. There are records of astronomers entertaining the notion as far back as the 1800's. While quickly dismissed as a possible explanation for the variability of some stars, the idea did not go away. In the 1930's the radial velocity detection of a Jupiter-like planet orbiting another star was ruled unfeasible with the equipment of the day. However, it was thought possible to detect the 1% dip in brightness a host star would experience during a transit by using a photoelectric cell.

Contrary to this expectation, 51 Peg b, the first known extrasolar planet orbiting a main sequence star was discovered via the radial velocity technique (Mayor & Queloz 1995). This discovery was possible because 51 Peg b has an orbital period of a few days rather than a few years, as expected based on the orbital periods of gas giants in the solar system. This set the trend for planet discovery from radial velocity measurements that would last until the detection of a periodic 1% drop in the brightness of the star HD 209458 (Henry et al. 2000; Charbonneau et al. 2000) a star already known to possess a planet detected via radial velocity. Since then there have been many searches dedicated to finding planets that transit their host stars of which the Wide Angle Search for Planets (WASP; Pollacco et al. 2006) is the most prolific ground-based example. Transiting planets open up a wide range of follow-up opportunities that are not possible for planets detected by radial velocity alone. Wide-field surveys also benefit from the tremendous number of stars that can be monitored at once.

What follows is the next chapter of WASP's already successful career, aimed at finding transiting planets around bright stars in the southern hemisphere. This shift has been motivated by the current dearth of such planets, illustrated in Fig. 1.1. The two northern examples of HD 209458 b and HD 189733 b (Bouchy et al. 2005) boast

the most robust and stunning discoveries in the field of transiting hot-Jupiters. These include the detection of atmospheric chemical constituents (Charbonneau et al. 2002; Swain et al. 2009; Vidal-Madjar et al. 2013), strong signatures of Rayleigh and Raman scattering (Berdyugina et al. 2011) and even detection of the planetary radial velocity (Snellen et al. 2010). Such discoveries are made easier by the larger signal-to-noise ratio achievable with bright stars. More bright targets will allow us to investigate more deeply the diversity and similarities between planetary systems.

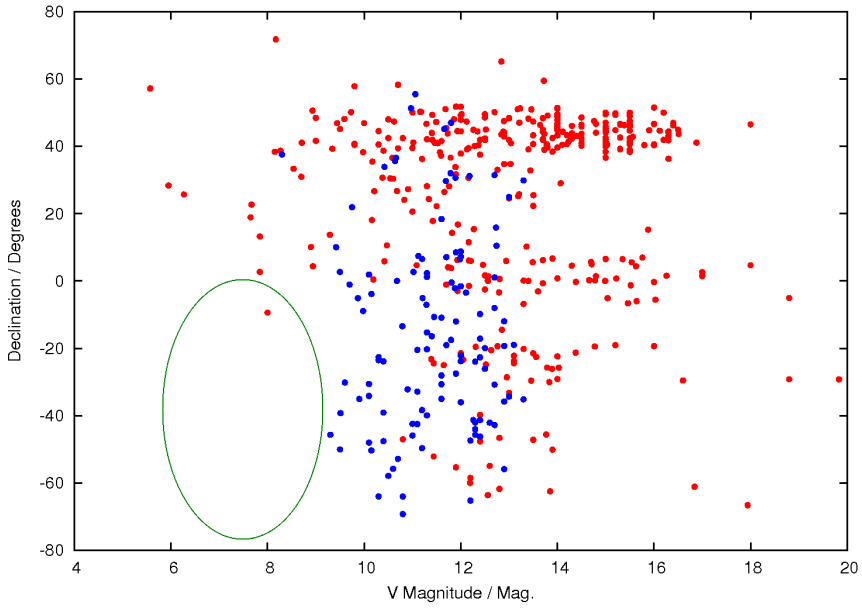

Figure 1.1: Plot of the visual magnitude of transiting planet host stars against their declinations. In blue are plotted systems discovered by SuperWASP, red are other surveys. The green ellipse highlights the lack of planets discovered brighter than 9$^{\text{th}}$ magnitude in the southern hemisphere. Data acquired from exoplanets.eu 07/2016.

1.2 Transit Surveys

1.2.1 Anatomy of a Transit

A transit occurs when a planet (or other object) passes through the line of sight between the observer and a star, blocking a portion of stellar light and causing a dip in the observed brightness of that star. In the case of an orbiting planet the period between these dips, P, tell us how long it takes to complete an orbit. Assuming a Keplerian orbit[1], the semi-major axis of the system, a, can be calculated as follows:

$$\frac{a^3}{P^2} = \frac{G(M_* + M_p)}{4\pi^2} \tag{1.1}$$

Here, M_*, is the mass of the star and M_p that of the planet. G is the gravitational constant. A simple geometric argument shows that for the transit of a planet of radius R_p that crosses the centre of its star of radius R_*, the maximum fractional change in flux ΔF can be expressed as:

$$\Delta F \equiv \frac{F_{\text{out of transit}} - F_{\text{in transit}}}{F_*} = \frac{\text{Planet Disk Area}}{\text{Stellar Disk Area}} = \left(\frac{R_p}{R_*}\right)^2 \tag{1.2}$$

This assumes the whole disk of the planet is on the face of an unblended star and neglects limb darkening. Thus, the depth of a transit reveals the planet-to-star radius ratio. These assumptions hold for much of the processing of transit photometry. This said, limb-darkening and the effects of a transit that does not cross the centre of the star are routinely taken into account. That there is a transit at all leads to the conclusion that the inclination of the system to our line of sight is $i \simeq 90°$. Fig. 1.2 shows the relationship between R_p, R_*, a and $i_{\min}$.

$$\cos i_{\min} \leq \frac{d_{max}}{a} = \frac{R_p + R_*}{a} \approx \frac{R_*}{a} \tag{1.3}$$

[1] i.e. considering only the gravitational attraction between the star and planet in question and assuming no other significant factors such as another gravitationally significant body or a non-spherical central body.

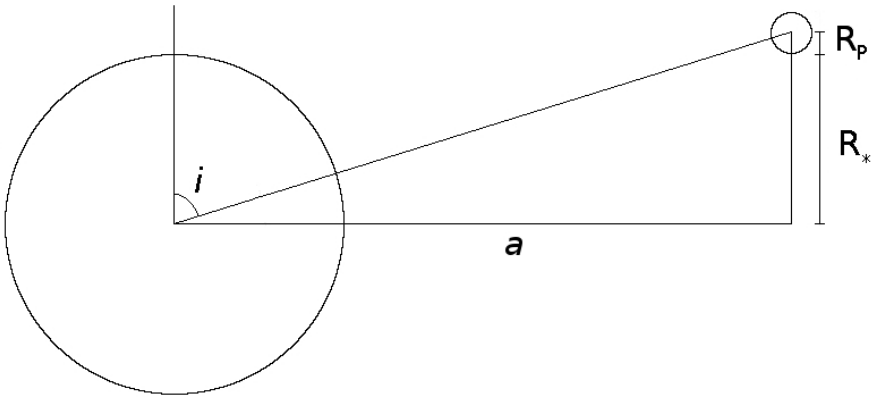

Figure 1.2: Minimum inclination, i, at which a transit is possible for a system with semi-major axis, a, stellar radius, R_*, and planet radius, R_p.

From a few simple measurements it is possible to build up a picture of broadly what an extrasolar system is like. Seager & Mallén-Ornelas (2003) showed that the bulk density of the host star can be calculated from a good quality lightcurve alone. Qualitatively, this is because the duration of a transit holds information about the mass of the material within the planet's orbit and the depth holds information about the stellar radius. Quantitatively this can be expressed as:

$$\rho_* = \frac{4\pi^2}{P^2 G}\left(\frac{(1-\sqrt{\Delta F}) - b^2[1-\sin^2(t_T\pi/P)]}{\sin^2(t_T\pi/P)}\right)^{3/2} \tag{1.4}$$

Here t_T is the total transit duration and b is the planet's impact parameter. The impact parameter is the distance between the path a transiting planet takes across its host star and a central crossing transit as a fraction of the stellar radius, $b = a/R_* \cos i$. One of the key assumptions in equation 1.4 is that the magnitude of the planet's orbital velocity is constant. This assumption is only true for circular orbits, but the same argument can be applied to eccentric orbits if the eccentricity and the orientation of the orbit as known, e.g., from the radial velocity curve. It also assumes that the planet is much less massive than the star, $M_p/M_* << 1$.

1.2.2 Discovering Transiting Planets

The methodology behind discovering planets using the transit method is remarkably simple: monitor how a star's brightness changes over time and look for periodic drops in brightness that have a particular shape as a function of time. Practically speaking, this is more challenging than it sounds. How do you select which stars to monitor? What about periodic gaps in the data due to the diurnal cycle or clouds? Once you have the data how do you search for transits?

Large scale transit surveys rely on automation wherever possible. This allows for large volumes of data to be collected over long periods of time. The data for each star in large patch of sky are then phase folded on different periods and fit to a simple transit model. If a period is found that results in a significant reduction in the χ^2 of this fit then a potential planet candidate has been found. An example of the results of this process are shown in Fig. 1.3. Further observations are required to confirm the candidate as a planet and constrain its characteristics. I will cover this process in more detail in chapter 2.

1.2.3 Mimic Rejection

Various astrophysical objects can mimic the signal we expect from a transiting planet, the most common being eclipsing binary stars. Typically, the signal produced when one star eclipses another is much larger than that of a planet. However, if the eclipse is grazing, diluted by the light of another nearby star or caused by a stellar remnant of similar size to a planet, then the signal can look remarkably similar to a planetary transit especially to the automated χ^2 fit.

It is possible to eliminate grazing eclipses and some blends by-eye as they produce a lightcurve with a v-like shape, where as a transit normally has a more u-like shape. These can also be eliminated if a second, smaller, event is evident in the phase folded lightcurve due to the secondary eclipse in a binary system. While it is possible to detect the reduction in brightness of a system as a planet passes behind its host star, this is

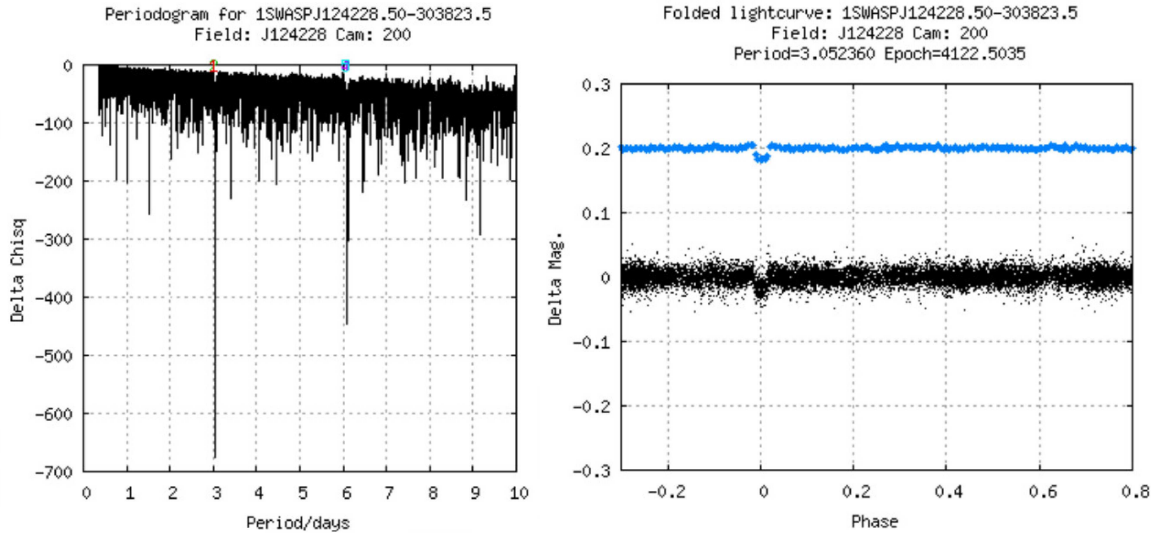

Figure 1.3: Graphs produced when WASP photometry are searched for transits. Left: A periodogram showing the variation of the fit's χ^2 when the WASP photometry is folded on various periods and fit by a simple transit model. The troughs correspond to when the fit to a transit is improved. There are several strong troughs which occur on multiples of the best fitting frequency as these also produce a transit like signature. Right: WASP photometry folded on the best fitting period found with the periodogram. Black points are un-binned photometry while blue points have been binned and offset for clarity. The depth, shape and lack of a second dip in brightness at phase ≈ 0.5 are the indicators sought in planet candidates.

beyond the capabilities of the WASP-South instrument. Thus a detectable secondary eclipse implies the candidate is a binary star. A smooth variation in brightness with phase due to the tidal distortion of a star by a massive companion (ellipsoidal effect) can also be used to identify and reject binary systems. Spurious transit-like features in the light curve can often be rejected because they are too narrow or too wide to yield a realistic density for the host star for any reasonable assumption about the orbital eccentricity.

If no blending or secondary eclipses are evident it is still possible the candidate could be a mimic. As eclipse depth is dependent the radius-ratio of two bodies causing a transit-like event, a small star orbiting a much larger or evolved star can also produce

a mimic.

If this is not ruled out by the presence of a secondary eclipse the reduced proper motion (RPM) of the primary star can be considered. This considers the star's colour and proper motion across the sky with respect to other stars. If the proper motion is small and the star is bright or relatively red in colour it is more likely to be a large main sequence or an evolved star. If the star has none of these characteristics then there is a better chance the candidate is a planet (Gould & Morgan 2003).

1.2.4 Initial Follow-up

From the WASP photometry alone we know relatively little about the planet or host star. Depending on the baseline of observations, from the phase folding procedure we can find the period to a good degree of accuracy. Using equation 1.2 we can estimate the ratio of the star and planet radii, though the precision on the photometry is low. More importantly, without knowing either the planet or star radius uniquely we cannot find the other. Using published photometric colours, e.g., 2MASS JHK photometry (Skrutskie et al. 2006) it is possible to estimate the star's effective temperature and, assuming it is a main-sequence star, make a crude estimate of its mass and radius. From these estimates a similarly crude, initial value of the planet radius can be derived. The resulting density can be compared to the stellar density from the transit lightcurve as an initial check against the assumption the star is on the main sequence.

Radial velocity follow-up is particularly powerful when the planet in question transits its star. Planets detected by radial velocity methods alone can only have a minimum value for their mass assigned. Having a measure of the inclination from transit detection allows ambiguity here to be reduced.

$$K_1 = \left(\frac{2\pi G}{P(M_* + M_p)^2}\right)^{1/3} \frac{M_p \sin i}{(1-e^2)^{1/2}} \tag{1.5}$$

The radial velocity semi-amplitude, K_1, and eccentricity, e, determined from the amplitude and shape of the radial velocity curve fit (see Fig. 1.4) can be used along

with the transit depth, ΔF, and period, P, to determine the surface gravity of the orbiting exoplanet (Southworth 2009).

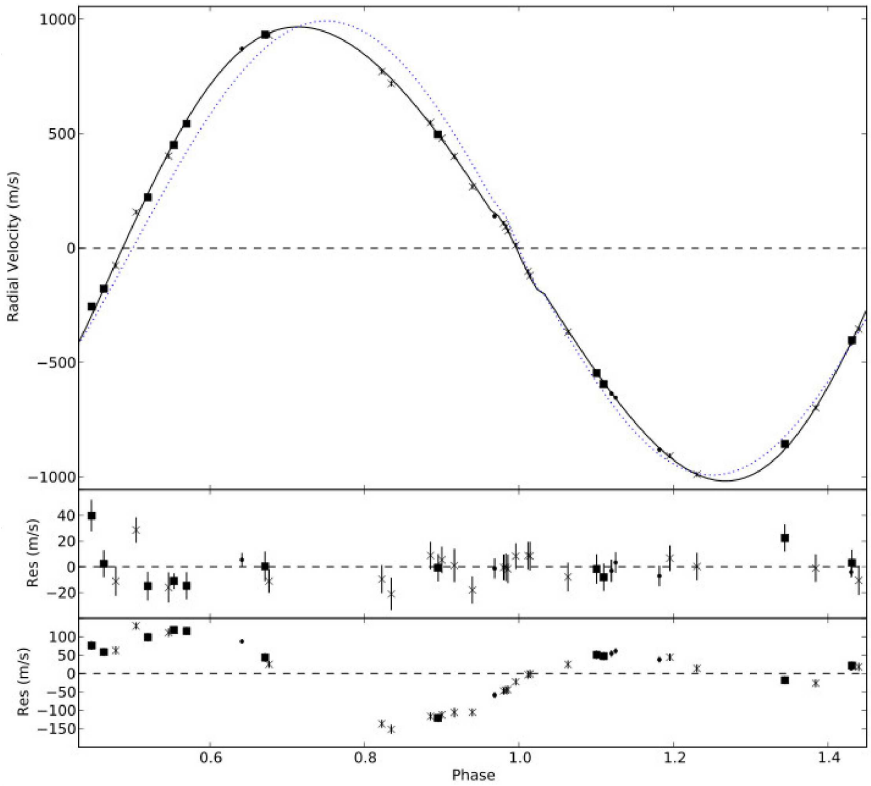

Figure 1.4: Radial velocity data for WASP-14. Top: The solid line shows the best fitting solution with $e = 0.088$. The dotted line shows a solution with $e = 0$, i.e. a circular orbit. Middle: Residuals for the eccentric solution. Bottom: Residuals for the circular solution. Figure taken from Husnoo et al. (2011).

Calculating more accurate values for stellar and planetary mass, M_* and M_p, precise radii, R_* and R_p, and planetary density, ρ_p, require the use of stellar models based on other observables such as stellar effective temperature, surface gravity and metal abundance (Southworth 2009). These observables are compared to stellar models to obtain a mass for the star in question which is then used, with Kepler's Law (equation 1.1), to derive an orbital semi-major axis, a. With this it is possible to get individual values for the properties M_*, M_p, R_*, R_p and ρ_p. When obtained, these can give an idea

of possible planetary compositions, both gaseous (Fortney, Baraffe & Militzer 2011) and terrestrial-like (Wu & Lithwick 2013) though an average density is not enough to uniquely constrain the composition of a planet (Adams, Seager & Elkins-Tanton 2008).

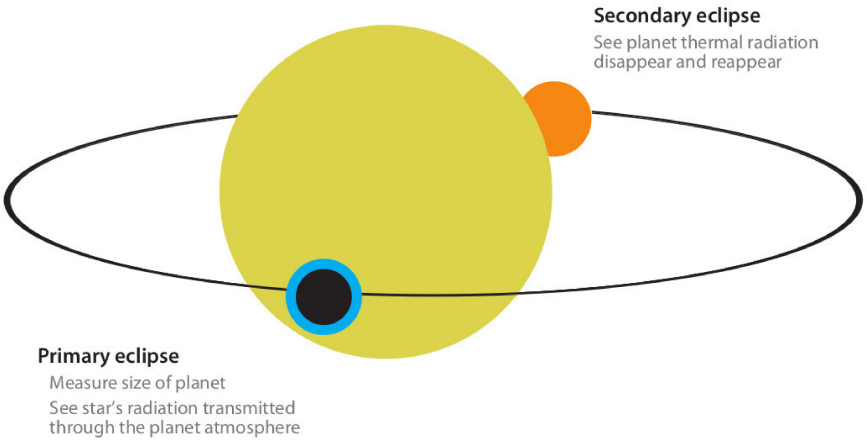

Figure 1.5: Cartoon of a planet transit (primary eclipse) and occultation (secondary eclipse). During both events the apparent brightness of the star drops. In transit this is due to blocked light and in occultation this is due to the loss of light reflected from the planet and its own thermal emission. Figure taken from Seager & Deming (2010).

1.3 Probing Planets

The follow up mentioned so far mostly focuses on constraining the orbit of an exoplanet, with some broad implications for its make-up (i.e its mass and density). With other techniques it is possible to gain more detailed information on a planet's orbit, giving clues as to its formation history, or to begin to characterise exoplanet atmospheres. In general this is easier to do for brighter targets and large planets around small stars as the signals produced in these cases are larger.

1.3.1 Rossiter-M^{c}Laughlin Effect

The Rossiter-M^{c}Laughlin (RM) effect is an observation of an apparent change in radial velocity of a star caused as a transiting planet blocks red- or blue-shifted light from a rotating star, an effect originally detected for binary stars (McLaughlin 1924; Rossiter 1924). The circumstances of the effect are illustrated in Fig. 1.6. The exact shape of the anomaly in the radial velocity profile allows the orientation of the planet's orbit to the stellar rotational axis (spin-orbit alignment) and projected stellar spin velocity to be measured (Ohta, Taruya & Suto 2005). An example of RM observations is shown in Fig. 1.7.

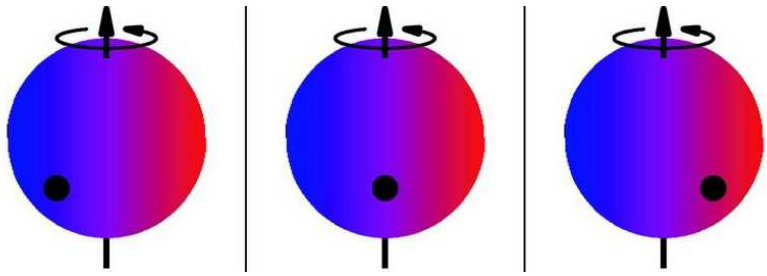

Figure 1.6: Planet transit of a rotating star. For a rotating star, light emitted from its surface will be red- or blue-shifted according to if that part of the star is rotating towards or away from the Earth. As a transiting planet passes across the stellar disk it blocks light from different areas of the star as seen in the illustration. If the planet disk blocks light from the blue-shifted portion of the stellar disk the star will appear to be more red-shifted as the blocked blue-shifted light normally cancels the effect due to the rotating stellar surface. If a red-shifted portion is blocked the opposite occurs. Figure modified from Gaudi & Winn (2007).

There is still much debate about the implications of Rossiter-M^{c}Laughlin observations, summarised well in Brown et al. (2012b). It is thought that the spin-orbit alignment may give clues as to the formation history of an extra-solar system. If there is close alignment it can be suggestive of a 'quiet' formation history consistent with the core accretion model. Large misalignments or even retrograde orbital motion are indicative of a rather more chaotic sequence of events involving planet-planet scattering,

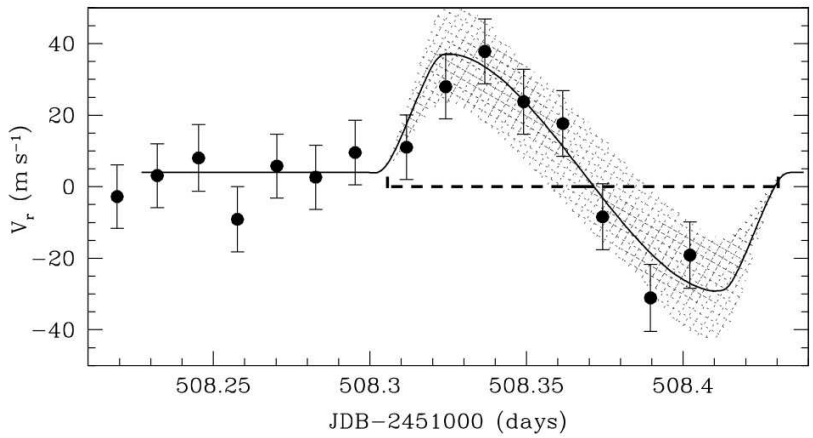

Figure 1.7: High precision radial velocity measurements of HD209458 (V = 7.65; Queloz et al. 2000) observed during a transit taken with the 1.93m telescope at Observatoire de Haute Provence using the ELODIE spectrograph. This shows the shape of the residuals after subtracting the effect due to the stars's orbital motion. The best-fit sky-projected spin-orbit angle is $\lambda = 3.9^{+18}_{-21}{}^{\circ}$. Figure from Queloz et al. (2000).

a close fly-by of another star after the disk phase or other such mechanism.

Spin-orbit alignment has been observed to correlate with stellar effective temperature, $T_{\rm eff}$, and system age. Older systems and systems with cooler host stars tend to show smaller misalignments. From these correlations it is suggested that large misalignments are not seen in systems with cool stars as the star has a large convective envelope which can realign due to strong dissipation of tidal forces (Winn et al. 2010b). Winn et al. (2010b) highlight the HAT-P-11, WASP-8 and HD80606 systems as apparent outliers to this trend. However, these systems have longer periods and/or smaller planet masses so tidal effects causing realignment are expected to be weaker. Weaker tidal forces would explain the preservation of their misalignments.

Older systems have had more time for tidal forces to erase any misalignment. Triaud (2011) finds that for systems of $M_* \geq 1.2 M_\odot$ and older than 2.5 Gyr there is generally good alignment between stellar spin and planet orbit. Brown et al. (2012b) put forward the idea that strong misalignments could be leading to the disruption of those planets on these time-scales but points out that Triaud (2011) does not find

evidence for this.

1.3.2 Transmission Spectroscopy

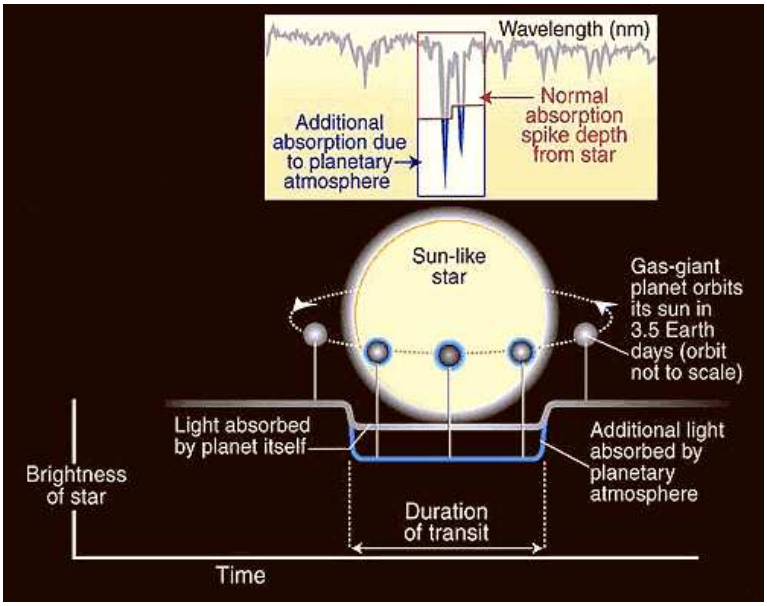

Figure 1.8: Cartoon of the effect of a planetary atmosphere on transit depth, exaggerated for clarity. The inset shows the difference in absorption due to sodium in and out of transit. Credit: A.Feild, Space Telescope Science Institute

Observations of a transit at different wavelengths can give information on the existence and properties of the planet's atmosphere. Transmission spectra can give an idea as to what elements are present. Observations are taken both in and out of transit and the relative depths of absorption features are compared, similar to Fig. 1.8. The depth of the absorption features increases with the abundance of the absorbing material so excess absorption measured during transit implies an atmosphere containing the corresponding substance.

So far features due to hydrogen, silicon, carbon, alkali metals and molecules such as carbon monoxide have been detected (Charbonneau et al. 2002; Linsky et al.

Star	Spectral Resolution (R)	Instrument	Detection Goal	Excess Detected $\times 10^{-5}$ (ΔF)	References
HD 189733	60000	9.2m Hobby-Eberly telescope	NaI	67.2 ± 20.7	Redfield et al. (2008)
XO-2	$4\times \sim 1000$	OSIRIS, Gran Telescopio Canarias (GTC)	KI	(See note)	Sing et al. (2011)
XO-2	~ 500	OSIRIS, GTC	Full Spectrum	N/A	Sing et al. (2012)
XO-2	~ 500	OSIRIS, GTC	NaI	47 ± 9	Sing et al. (2012)
WASP-17	~ 12500	GIRAFFE, Very Large Telescope (VLT)	Na 'D'	550 ± 130	Wood et al. (2011)

Table 1.1: Ground-based detections of exoplanet atmospheres. The high spectral resolution measurement of sodium absorption in HD 189733 was conducted by examining the residuals from an in transit spectrum after subtraction of an out of transit spectrum. A similar approach was used in the attempt to take a full spectrum of XO-2b this time using a reference star. Slit losses hampered the attempt. Note: This was achieved by differential spectrophotometry; essentially examining the differences in transit depth at different wavelengths. Further information in Fig. 1.9.

2010). Sodium and potassium have been detected from the ground by various methods summarised in Table 1.1 and Figs. 1.8 and 1.9.

These studies are useful to show that there are multiple viable techniques to detect features in planetary atmospheres. However it is currently only strong features that are reliably detectable due to practical challenges involved in achieving high enough signal-to-noise ratios. The atmosphere essentially presents an annulus around the planet a small fraction of the planet's own radius. As can be seen from transit lightcurves, the effect of the planet transiting is small, consequently the effect of the atmosphere is tiny. For example, WASP-17 b has a greatly inflated radius and so should show a strong atmospheric signal. The signal caused by the atmosphere of WASP-17 b in the Na D lines of $0.55 \pm 13\%$ which is roughly a third of the transit depth (Wood et al. 2011; Southworth et al. 2012). Other examples in Table 1.1 show signals an order of magnitude smaller.

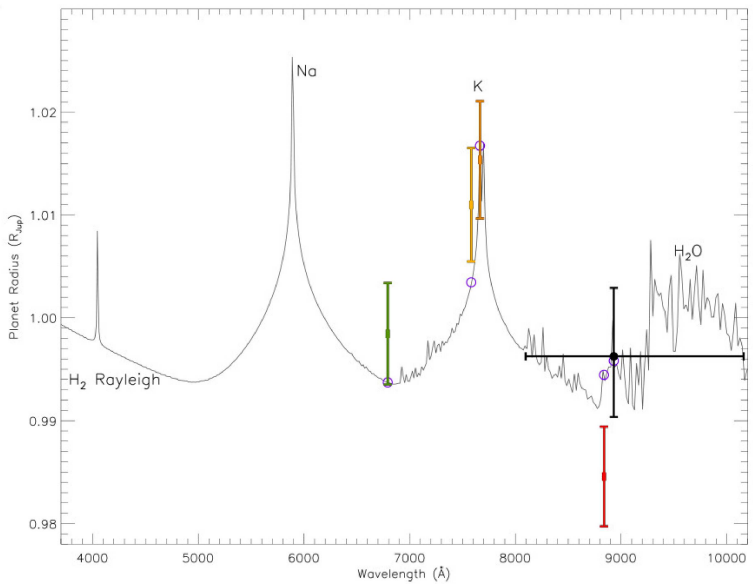

Figure 1.9: Broadband spectrophotometry of XO-2. Plot shows the transit depths observed in 4 wavelength bands each with a width of 12 Å, taken from Sing et al. (2011). From left to right these bands are centred on 6792.0 Å (green), 7582.0 Å (yellow), 7664.9 Å (orange), 8839.0 Å (red). The 5^{th}, black, point comes from the z-band radius observed by Fernandez et al. (2009). Overplotted is a model spectrum binned to a spectral resolution of 500. The depth change matches well the predicted K feature.

1.3.3 Secondary Eclipse

A secondary eclipse is caused by an exoplanet passing behind its host star. The planet's contributions to the observed luminosity via reflection and the planet's own thermal emission are blocked. The hotter a host star, the greater the difference between the wavelength at which planet's emission peaks and the wavelength at which the star's emission peaks. The greater the difference in the respective peaks of emission profiles the easier it becomes to detect features from the planet as observations can target the wavelength at which the planet will appear brightest relative to the star. A more detailed examination of the following can be found in Cowan, Agol & Charbonneau (2007). At infrared wavelengths the depth of a secondary eclipse essentially gives the

ratio of stellar flux, F_*, to planetary day side flux, F_{day} because the contribution of reflected light is negligible. The flux ratio is then,

$$\frac{F_{\rm day}}{F_*} = \frac{B_\lambda(T_{\rm day})}{B_\lambda(T_{\rm bright})} \left(\frac{R_p}{R_*}\right)^2 \tag{1.6}$$

where $B_\lambda(T)$ is the specific intensity radiated by a black body with temperature T at wavelength λ. Planets and stars do not radiate exactly as black bodies so the brightness temperatures, $T_{\rm day}$ and $T_{\rm bright}$ are wavelength-dependent quantities in this equation.

As the planet orbits it will appear to go through phases similar to the Moon or inferior planets in our solar system. The peak to trough amplitude of these phase variations for an extrasolar planet with $i \approx 90^\circ$can be described by equation 1.7.

$$\frac{F_{\rm day} - F_{\rm night}}{F_*} = \frac{B_\lambda(T_{\rm day}) - B_\lambda(T_{\rm night})}{B_\lambda(T_{\rm bright})} \left(\frac{R_p}{R_*}\right)^2 \tag{1.7}$$

The amplitude of this variation ("thermal phase curve") as a function of orbital phase, ϕ, is given by equation 1.8, below.

$$\frac{\Delta F(\phi)}{\langle F_* \rangle} = \sin i \cos\phi \frac{F_{\rm day} - F_{\rm night}}{2F_*} \tag{1.8}$$

Observations of the thermal phase curve provides information on day and night side temperatures, planetary albedo and the efficiency of energy redistribution from the planet day side. Even with a small sample size this has revealed differences between the characteristics of hot Jupiters (Cowan, Agol & Charbonneau 2007) which suggest different compositions and conditions. There is even the possibility of indirectly mapping planetary surface/upper cloud deck temperature distribution (Williams et al. 2006; Knutson et al. 2007).

The presence of a secondary eclipse also adds constraints to the eccentricity of an exoplanet orbit and its argument of periastron. Orbital velocity varies throughout an eccentric orbit which leads to deviations of transit and secondary eclipse timings and durations from those expected for a circular orbit (Charbonneau 2003, see also Fig. 1.10).

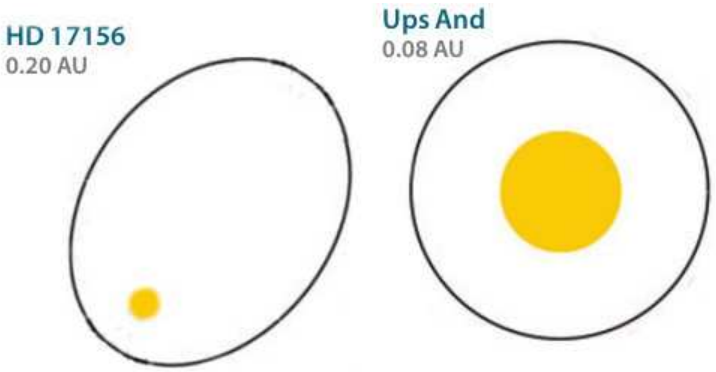

Figure 1.10: Cartoons showing eccentric (left) and circular (right) orbits. If both are occulted by their stars the planet in the circular orbit will do so half a period after its transit. The planet in an eccentric orbit will be occulted earlier or later than half an orbital period depending on the direction of the orbit. Adapted from Seager & Deming (2010).

The first detection of thermal emission from an extrasolar planet was made using Spitzer Space Telescope observations of TrES-1 centred around a time half a period after the time of a transit event. Observations were taken in two of Spitzer's passbands centred on 4.5μm and 8.0μm; the respective secondary eclipse depths were found to be 0.00225 ± 0.00036 and 0.00066 ± 0.00013 (Charbonneau et al. 2005). They were also able to demonstrate the improvements timings of secondary eclipse observations can make to the accuracy of the values of eccentricity and argument of periastron.

Since then there have been successful detections of occultations at both visible (though far into the red) and infra-red wavelengths from the ground. Such detections remain technically challenging. An investigation of WASP-19b has measured an occultation depth of 0.0004 ± 0.0001 in the z'-band using TRAPPIST and Eulercam and an occultation depth of 0.0017 ± 0.0008 at 1.19μm with HAWK-I's NB1190 filter (Lendl et al. 2013). This z'-band measurement disagrees with earlier work by Burton et al. (2012), who found a z'-band occultation depth of 0.0009 ± 0.0002 using ULTRACAM on NTT.

Observations of secondary eclipses combined with atmospheric models can give

clues about the pressure-temperature profile of an exoplanet. Different wavelengths of light are absorbed or emitted with varying intensity which change with depth in the atmosphere and atmospheric composition. However, the models used suffer from significant degeneracies as the few data points we are able to gather can be fit equally well by multiple models. This is further frustrated by the lack of instruments capable of very high precision photometry at mid-infrared wavelengths, particularly since the loss of cryogenic cooling on the *Spitzer* satellite meaning fewer wavelengths can be observed during occultation. Madhusudhan & Seager (2010) suggest a thorough exploration of temperature profiles and atmospheric compositions is required before conclusions are drawn with confidence. This thorough examination requires finding common features between well fitting models leading to more solid conclusions.

1.3.4 High Dispersion Spectroscopy

Observations with spectrographs capable of very high spectral resolutions at near infrared wavelengths have been used to look for the signatures of molecules in planetary atmospheres directly. This was, of course, first performed on HD 209458 b (Snellen et al. 2010). A more detailed description of the technique can be found in Brogi et al. (2016) detailing its use to investigate HD 189733 b − a broad summary is as follows. High resolution spectra of the host star are taken as the planet transits, as in transmission spectroscopy or observation of the Rossiter-M^{c}Laughlin effect. A model stellar spectrum is fit to the data and subtracted, as are telluric lines. A model spectrum of the planet atmosphere is then cross-correlated with this residual spectrum. An example of the results of this procedure can be found in Fig. 1.11 (Snellen et al. 2010).

Removing the Doppler shift caused by the planetary motion allows the remaining planet spectra to be combined. This technique is particularly useful for finding chemical species that are expected not to be in the spectrum of the host star. Snellen et al. (2010) detected CO in this way while Brogi et al. (2016) detected CO and H_2O. Hoeijmakers et al. (2015) attempted to use the technique with archival data from Subaru to find the signature of TiO. Hoeijmakers et al. (2015) report that their attempt was hindered by

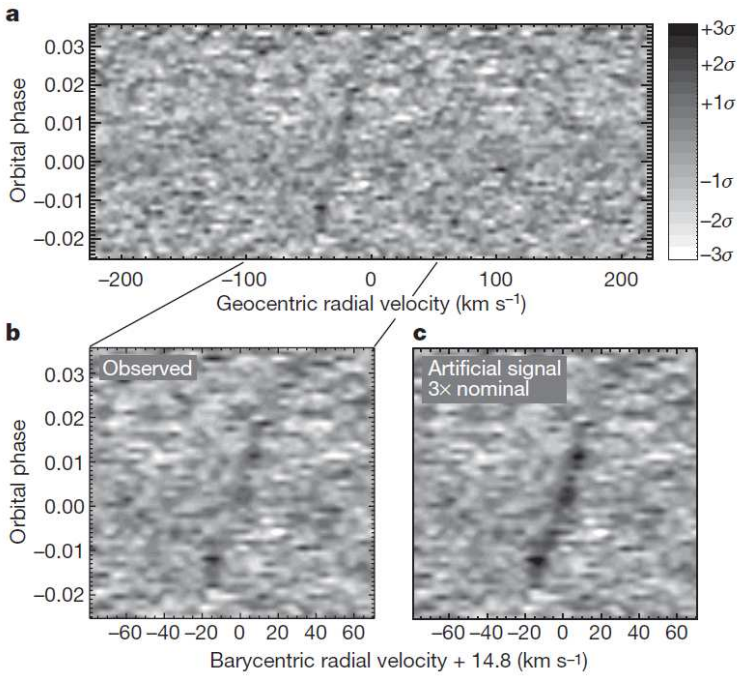

Figure 1.11: Cross-correlations of high dispersion spectra of HD 209458 taken during a transit. Panel a shows the strength of the cross correlation of a template CO spectrum with the spectra. Panel b highlights the area of high correlation and panel c shows this with the model spectrum added at 3 times the magnitude of the detected signal for illustration purposes. Figure 1 from Snellen et al. (2010).

inaccuracies in the line database. Snellen et al. (2013) propose that biomarkers could be revealed using this method. In addition to measuring atmospheric constituents, Snellen et al. (2010) made measurements of the star and planet masses (using the spectra from both like a double lined binary) and the planetary wind speed. Brogi et al. (2016) went on to make measurements of the planetary wind speeds and rotational velocity. These detailed measurements require very high signal-to-noise, i.e., large telescopes with efficient spectrographs observing bright targets with deep transits.

1.3.5 Atmospheric Observation Implications

Probing exoplanet atmospheres in these ways has the potential to reveal the origins of thermal inversions, tell us much about how hot Jupiters absorb and redistribute energy from their host stars, and inform our ideas about exoplanet atmospheric chemistry.

A thermal inversion is an effect where a substance in an atmosphere traps heat so that the atmospheric temperature does not simply decrease with increasing altitude. In the Earth's atmosphere, this occurs in the stratosphere due to absorption of sunlight by ozone. In hot Jupiter atmospheres, the absorbing substance is expected to be a gaseous molecular species, with likely candidates being titanium oxide (TiO) or vanadium oxide (VO) (Fortney et al. 2008), though this is not yet unambiguously confirmed (Désert et al. 2008; Sing et al. 2008; Hoeijmakers et al. 2015). Knutson, Howard & Isaacson (2010) point out this is unlikely to be the whole story though as there are certain planets that, while thought capable of hosting gaseous TiO, do not display thermal inversions, and vice versa. They also propose a link between stellar activity and the presence of inversions suggesting the higher UV flux experienced by these planets breaks down the substance responsible for the inversion.

Planetary albedo (a measure of how much light the planet reflects) and heat redistribution can be assessed in a similar way to atmospheric composition and pressure temperature profiles. A range of models are constructed and used to fit measurements; Burrows, Budaj & Hubeny (2008) and Budaj (2011) demonstrate two different methods to do so, the latter adapting code initially designed to study binary stars. Such models are often informed by using elemental abundances similar to those of the Sun or our solar system's giant planets. Cowan & Agol (2011) find that for a sample of transiting giant exoplanets they all have low albedos. For cases with directly observed secondary eclipse depths, for which "unambiguous" albedo determinations can be made, they find extremely low albedos, $< 10\%$. The low observed albedo of exoplanets implies an absence of the substances that give the solar system giants their relatively high reflectivities. This fits with the idea that hot-Jupiter planets are too warm for clouds of such materials to condense. There are of course drawbacks to the assumptions these

models are based on. Not all stars have elemental abundances like the Sun's so it is reasonable that not all exoplanets will have similar abundances to either the Sun or solar system planets. This is supported by instances of direct imaging of extrasolar giant planets sufficiently far from their host stars to gather spectra from them alone. For example, Lee, Heng & Irwin (2013) find that the best fitting models to directly observed spectra of HR 8799 b require super-solar metallicities and C/O ratios. Madhusudhan (2012) suggests the C/O ratio of exoplanets can be used to infer the abundances of other chemical species. For example, carbon abundant atmospheres would be expected to be enhanced in carbon containing species such as CH_4, HCN, etc. while these would be less abundant in an oxygen dominated atmosphere.

1.4 Contemporary Ground-based Transit Surveys

In principle, the transit method is a very simple way to detect planets. Ground-based searches are biased towards finding short-period, giant planets (see Fig. 1.12) but can be run much more cheaply than their space-based counterparts. After the discovery of very short period planets by radial velocity surveys many groups initiated ground-based transit surveys. Horne (2003) lists 23 surveys as of 2002 though little came of many of these. Each survey detailed here monitors the sky with an array of cameras but the hardware and strategies vary. A summary of the vital statistics of each of WASP's contemporaries is shown in Table 1.2.

1.4.1 Wide Angle Search for Planets

The Wide Angle Search for Planets (WASP; Pollacco et al. 2006) operates two instruments to observe both hemispheres of the sky. Super-WASP is the northern hemisphere instrument located at the Roque de los Muchachos Observatory on the island of La Palma. WASP-South, the southern hemisphere instrument, is located at the South African Astronomical Observatory (SAAO) in Sutherland, South Africa. Both instru-

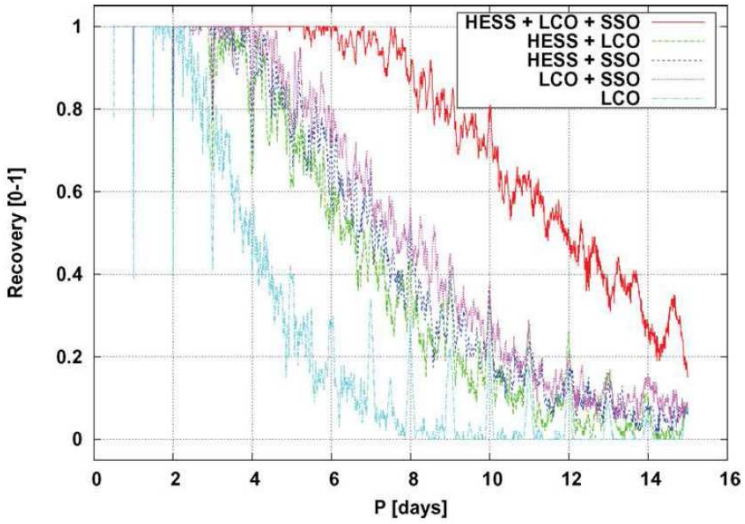

Figure 1.12: Transit detection probability of ground-based surveys using multiple sites. The results are from a simulation to investigate the recovery rate of planets with periods ranging up to 15 days when observed for 2 months carried out by Bakos et al. (2009) for HAT-South. The red curve shows the recovery rate using data from all 3 sites. The light-blue curve shows the recovery rate when using only one site. The purple, green and dark-blue curves are various combinations that use two sites. Recovery of long period planets is much improved by combining data from multiple sites. Figure 2 from Bakos et al. (2009).

ments use an array of 8 cameras with overlapping fields of view and, prior to this project, were almost identical.

1.4.2 Qatar Exoplanet Survey

The Qatar Exoplanet Survey (QES; Alsubai et al. 2013) operates a single instrument in New Mexico. The instrument consists of one camera with a 200-mm lens and 4 with 400-mm lenses. All the cameras occupy a single mount and the field of view of the 200-mm lens completely overlaps with the four 400-mm lens fields which have no overlap with each other. With its 200-mm lens, QES targets stars with V magnitudes between 8 and 12 while the 400-mm lens targets stars with V magnitudes between 11

Survey	Lens	Field of View (°)	Plate scale arcseconds / pixel	V Mag. Range	Planets
WASP	200-mm	64	13.7	9 - 13	132**
QES	200-mm	121	9.26	8 - 12	2
–	4 × 400-mm	27.45	4.64	11 -15	–
HAT-Net	7 × 200-mm	67.24	14.76	8.7 - 14	58
HAT-South	3 × 2 × 4 × 180-mm*	17.47	3.76	11.9 - 14.8	35
KELT	80-mm	676	23	8 - 11.9	13
KELT (North, Alt. lens)	200-mm	116.64	9.5	–	–

Table 1.2: Comparison of various parameters of WASP's contemporary transit surveys. References: Qatar Exoplanet survey (QES; Alsubai et al. 2013), Hungarian-made Automated Telescope Network (HAT-Net; Bakos et al. 2004), HAT-South (Bakos et al. 2013), Kilo-degree Extremely Little Telescope (KELT; Pepper et al. 2007; Pepper et al. 2012). Where possible, the stated magnitude ranges denote the range over which each survey has discovered planets. *HAT-South does not use lenses but optical tube assemblies, this is their aperture. **These are the number of confirmed systems that have been made public.

and 15.

1.4.3 HAT-Net

The Hungarian-made Automated Telescope Network (HAT-Net; Bakos et al. 2004) operates 7 independent cameras, each uses a 200-mm lens. The Fred L. Whipple Observatory (FLWO) in Arizona hosts 5 of the instruments and the other two are based on Mauna Kea, Hawaii. As of July 2016 the HAT-Net survey has discovered 58 planets with visual magnitudes between 8.7 and 14.

1.4.4 HAT-South

HAT-South (Bakos et al. 2013) is the southern counterpart of the Hungarian-made Automated Telescope Network. HAT-South operates from 3 sites; Las Campanas Observatory in Chile, the High Energy Spectroscopic Survey (HESS) site in Namibia and Siding Spring Observatory in Australia. Each site hosts two instruments comprised of 4 optical tube assemblies with 180-mm apertures. As the observing sites are distributed

around the southern hemisphere, HAT-South can monitor fields with less interruption from the day-night cycle. The project aims to combine data from the three sites in order to detect longer period planets. As of July 2016 HAT-South has discovered 35 planets with V magnitudes between 11.9 and 14.8. Of the planets discovered by HAT-South, HATS-17 b has the longest orbital period at over 16-days (Brahm et al. 2016).

1.4.5 Kilo-degree Extremely Little Telescope

Like WASP, the Kilo-degree Extremely Little Telescope (KELT; Pepper et al. 2007; Pepper et al. 2012), operates with one instrument in the northern hemisphere and a second in the south. Each telescope uses a single 80-mm lens, though the northern installation can use a 200-mm lens to provide a "narrow-angle campaign mode". KELT is targeting stars with V magnitudes between 8 and 10. In practice it has discovered 13 planets with host stars as faint as V = 11.9 (Oberst et al. 2016). KELT currently boasts the discovery of the brightest known planet host in the southern hemisphere, KELT-11 (V=8; Pepper et al. 2016).

1.5 Bright Host Stars from WASP-South

In July of 2012 the WASP-South instrument and observing strategy were modified to target brighter stars without saturating the detector. The changes are summarised in Table 1.5. The 200-mm lenses were replaced with smaller aperture 85-mm lenses (see Fig. 1.13), the broadband filter was replaced with a less broad SDSS r' filter and the observing strategy was changed from a set of 2, 30-s exposures at each pointing to 3, 20-s exposures. The lens change also increased the field of view reducing the number of pointings needed to cover the sky in a night thus increasing the number of images taken of each field. The changes in FoV and a typical observing night are illustrated in Fig. 1.14.

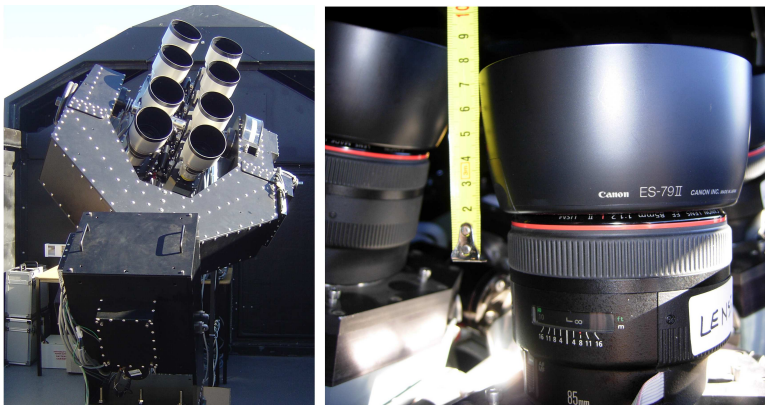

Figure 1.13: Left: Photo of the WASP-South instrument prior to the hardware change. Image credit David Anderson. Right:Photo of a lens used after the hardware change. Image credit: Pierre Maxted.

Figure 1.14: Left: Illustrative projection of the footprints of the combined field of view (FoV) of the WASP-South array for pointings on a typical night observing before the hardware changes. Right: Projection of footprints of the WASP-South FoV for pointings of a typical night after the hardware upgrade. Image credit: David Anderson

In this thesis I describe how I adapted the software used by the WASP survey for use with the new hardware of WASP-South and demonstrate if it is up to the task of detecting planets orbiting bright host stars in the southern sky.

Lens	200-mm	85-mm
Field of View (degrees^2)	64	353
Plate scale (arcsec/pixel)	13.7	33
Target V Mag. Range	9 - 13	< 9
Filter	Broadband $400 - 700$-nm	SDSS r'
Exposures	2×30-s	3×20-s

Table 1.3: Comparison of various parameters of a single WASP-South camera using the 200-mm lenses and the new 85-mm lenses.

2 Discovery and follow-up methods

2.1 Historical Photometry

People have been measuring the brightness of stars for thousands of years. One of the earliest photometric catalogues is that of Hipparchus. By eye, he assigned stars to one of 6 groups based on how long into evening twilight they became visible (Sterken & Manfroid 1992, Ch. 1). This was the beginning of the magnitude system used today as a result of the logarithmic nature of human perception (Hecht 1924). This system was modified and adapted over time, continuing to compare the brightness of stars by eye until the invention of photographic plates and, later, photoelectric photometers. At this point, precision photometry became two disciplines; *imaging photometry* (or 2-D photometry) which used the relative sizes of stars on photographic plates to measure brightness (Hall & Genet 1988, Ch.1.2) and *aperture photometry* which gave much more precise measurements of brightness for individual stars (see Hall & Genet 1988 more broadly).

Imaging photometry used film or glass plates coated with a photographic emulsion that would undergo a chemical reaction when exposed to light. When developed, the size of a stellar image on the plate would be used to measure its brightness. *Aperture photometry* used a photoelectric device to measure the brightness of a single target. This had the advantages that it was much more accurate (essentially being a photon counting method) and that the response of the device could be made to respond linearly to the intensity of light to which it was exposed. While more complicated than in modern photometry, it was also possible to use photoelectric photometers to measure the background brightness of the sky close to a star of interest and even preform a kind of differential photometry by moving back and forth between a target and comparison star.

Modern photometry using charge-coupled devices (CCDs) combines the strengths of these two techniques. The WASP instruments are a particularly good example of this

as they are capable of precision photometry over a vast area of sky. What follows in this chapter is a description of how we discover, confirm and follow up planets discovered using WASP. The main focus will be on photometry in its various applications through the WASP survey with a short explanation of planet confirmation using spectroscopic methods.

2.2 Modern Photometry

2.2.1 The Ideal Detector

The characteristics of an ideal light detector are as follows (c.f Sterken & Manfroid 1992, Sec. 1.4.1):

- Every incident photon would produce a signal, with absolutely no signal produced if there is no light.
- The whole area of the detector is sensitive to light and has an infinite spatial resolution.
- There is no limit to the signal that can be recorded (it never saturates).
- The time resolution is perfect; every incident photon can be identified regardless of arrival time.
- The spectral resolution is perfect; the wavelength of every incident photon can be identified.

2.2.2 The CCD

A CCD is made up of semi-conductor elements from which electrons are readily displaced. When the CCD is exposed to light each photon can cause electrons to be displaced from the semi-conductor into a 'well' where they are stored for the duration

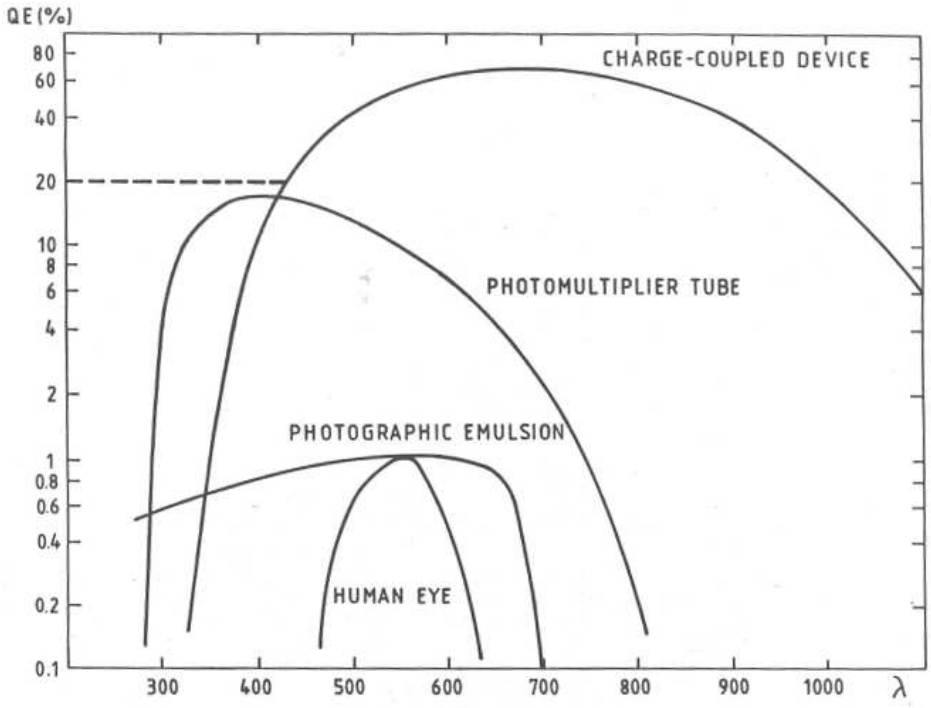

Figure 2.1: Wavelength dependence of the quantum efficiency (QE) for various detectors. Originally figure 13.4 of Sterken & Manfroid (1992).

of the exposure. When the exposure is complete the charge stored in each well, which is proportional to the intensity of the incident light, is read and a numerical value is assigned to pixels in an image that correspond to the pixels that make up the CCD. In this way both the position and brightness of each 'cell' of sky, as seen by the CCD, is recorded. The following will consider the criteria describing an ideal detector and assess how well CCDs fulfil them.

The efficiency with which a CCD responds to incident photons, its *quantum efficiency* (Q.E.), is very high; modern CCDs can exceed Q.Es of 90%. For example, the WASP CCDs achieve a Q.E of 90% or more for wavelengths between around $500 - 700$ nm (Pollacco et al. 2006). For comparison, this is very much higher than photographic emulsion (Q.E $< 1\%$; Kristian & Blouke 1982) and several times that of photoelectric photometers (Q.E. $\lesssim 30\%$; Gianni, Mazzitelli & Natali 1975). This means that, while

not ideal, nearly every photon received can be measured. The caveat to this is that the Q.E. of CCDs (like other detectors) varies across the electromagnetic spectrum, see Fig. 2.1. Thus, the wavelength range of interest is important when choosing or making a detector.

The area of a CCD that is sensitive to light is somewhat variable, it depends on the CCD architecture. Some detectors have requisite electronics behind the light gathering pixels, some crop the light sensitive area to place the electronics to the side of each pixel leading to dead zones. In this respect, photographic plates could give better spatial resolution as their light sensitive elements, granules of photo-sensitive coating, are very small[1]. The angle on the sky covered by a distance on the detector (the plate scale, p_s) depends on the optics of the telescope in use:

$$p_s = \frac{206265\text{arcsec/mm}}{Dn} \tag{2.1}$$

where D is the diameter of the telescope aperture and n is the f-ratio of the lens or mirror. The resolution, therefore, also depends on the physical size of the imaging element, thus smaller pixels give better resolution. While a CCD must fall short of an ideal detector in this area, the right instrument and observation techniques (such as the use of adaptive optics) can lead to very good spatial resolution.

CCDs are not read out as and when photons arrive, in this they depart from the ideal detector described. However, depending on the brightness of the target the time resolution allowed by CCDs can be very good. Some modern astronomical CCDs are designed to be read out very quickly, like the RISE frame-transfer CCD on the Liverpool Telescope (Steele et al. 2008). Frame-transfer CCDs have an area of pixels, the same size as the detector, to which charge can be transferred very quickly. While charge is being read from the extra storage area, the main detector can be exposed again reducing the dead time. Other detectors allow the user to select a portion, or "window", that will be read properly while the rest of the CCD is ignored e.g. DFOSC on the Danish

[1]The resolution of photographic emulsions could reach 200 lines/mm (Sterken & Manfroid 1992, Sec. 14.2) which is roughly equal to a resolution element of 2.5-μm.

1.54-m telescope (Andersen et al. 1995). Given that perfect time resolution is not achievable, the aim in time-series photometry is the maximisation of the 'duty cycle'. The duty cycle is the fraction of the observation time spent exposing the CCD and gathering useful signal. In cases of bright targets and unavoidably high readout times the telescope is often defocused for transit photometry. Defocusing spreads the light collected out over a larger number of pixels and allows for a longer exposure without saturating the detector. The fact the detector can saturate is another departure from an ideal detector. Saturation tends not to be a large problem to time series photometry as long as observations are planned in such a way to avoid it.

CCDs record ensembles of photons rather than each individual event so a perfect spectral resolution is not possible. There are ways to mitigate this using filters to isolate portions of the spectrum or dichroics to send different wavelengths to multiple detectors. Indeed, there are detectors specifically designed with simultaneous, multi-band photometry in mind but they still work over a spectral range rather than isolated photon detections, for example BUSCA on the CAHA 2.2-m telescope (Reif et al. 1999) or GROND on the ESO 2.2-m telescope (Greiner et al. 2008). To do better than this true spectroscopy is required.

2.2.2.1 Read Noise

Read noise is introduced to the counts of each pixel when transferring and measuring the charge collected. Modern CCDs typically have little readout noise, tens of electrons at most. This noise cannot be corrected for like the other sources mentioned and thus must be accounted for in the overall uncertainty of any photometry performed. Its contribution can be minimised by use of a low readout noise CCD and by keeping the number of pixels used in a photometric aperture small. Reducing the number of reads would also reduce the contribution but is less practical to time series photometry used in studying exoplanet transits and only adds to each data point once.

2.2.2.2 Bias

The bias is a kind of background reading inherent to the pixels of the CCD when no photons have been counted. It is the result of a voltage deliberately added so that a positive value is always recorded when the CCD is read out. In effect it is the reading that would be made by observing nothing with a zero exposure time and introduces an additive offset to science frames. The overscan region of a CCD image ("bias strips") are virtual pixels added to the image corresponding to the signal from the read-out electronics when they are disconnected from the physical CCD pixels. When read, the counts in each row of a bias strip/overscan region, can be averaged to give a measure of the counts caused by the bias voltage.

2.2.2.3 Dark Current

Each pixel is essentially a light sensitive diode which can produce a current due to thermal effects without needing illumination. This dark current can be modelled by the diode law (Widenhorn et al. 2002):

$$I = I_0 \exp\left(\Delta E / k_B T\right) \tag{2.2}$$

where I is the dark current, ΔE is the activation energy, k_B is Boltzman's constant and T is the temperature of the device. This is made slightly more complicated as, while quite uniform, this response is individual to each pixel. Clearly, this effect can be reduced by cooling the CCD though this can change the wavelength dependent quantum efficiency of the CCD. The dark current introduces a time-dependent additive offset to science frames and contributes to Poisson counting noise.

2.2.2.4 Non-uniform Exposure

A non-uniform exposure can be the result of various factors such as the finite travel time of the camera shutter (particularly for shorter exposures) or opaque material somewhere

in the optical path e.g. dust on a telescope lens or mirror. If the objects to be measured are observed at different parts of the detector then inaccurate correction for this non-uniform illumination will result in systematic errors in the measured brightness.

2.3 Performing Aperture Photometry

2.3.1 Preparing a Frame

2.3.1.1 Bias Frames

Bias frames can be acquired by taking exposures with zero duration. The un-exposed CCD is read out leaving us with a measure of the inherent bias. While this process is short, it is possible for random factors like cosmic ray strikes to create spurious readings. To mitigate this we generally take multiple bias frames and average them in some way. A good option for this is the median value for each pixel from our multiple frames. This is not affected by any spuriously large values like the mean would be. This master bias frame can then be subtracted from all other calibration and science frames as the bias should not change from exposure to exposure. Alternatively, the reading from the bias strips can be used.

2.3.1.2 Dark Frames

The effects of thermal noise can be taken into account by taking exposures without illuminating the CCD. We do this by taking long exposures to maximise the signal from the dark current in each pixel. These long exposures are more susceptible to cosmic rays striking the detector during the exposure and producing anomalously high readings. As with the bias, a median averaging of several dark frames effectively removes these. The signal produced by the dark current is linear in time so, once these frames are bias subtracted and appropriately averaged, they can then be scaled to the duration of the exposure of the science and flat-field images and subtracted.

2.3.1.3 Flat-Fields

Flat-fields are images of a source expected to be of uniform brightness used to flatten the variable sensitivity of the CCD from multiple sources. Differential exposure levels can also be accounted for by dividing out a scaled exposure map of the detector[2]. There are three methodologies for taking flat-fields:

- Take exposures of a uniformly illuminated area inside the telescope enclosure.
- Take exposures of the twilight sky while varying the duration to ensure uniform exposure[3].
- Take long exposures of an area of the night sky that contains few stars.

The last two methods require moving the telescope such that starlight does not consistently illuminate the same pixels. The uniformly illuminated images can then be bias and dark subtracted, averaged and normalised to divide out of the science images. The choice of flat-field source can itself cause problems for broad-band observations like those of WASP due to the wavelength dependence of pixel sensitivity. The spectrum of the flat-field source can be very different from that of the objects under observation and so introduce trends as what is "flat" when observed with blue light may not flatten properly for a object with a spectral peak at longer wavelengths. For example, the twilight sky is brighter towards the blue end of the spectrum while flat field lamps are more similar to black bodies with T $\approx$ 1000K, and both are different from stellar spectra.

2.3.2 Photometry of an object

The last calibration to be made is the subtraction of the sky background counts from the pixels containing light from the target star. This is normally determined from the

[2]The WASP pipeline does this. It will be discussed in section 2.4

[3]WASP photometry uses twilight flats for calibration. Over the WASP field of view the sky is not uniform. This will be discussed in section 2.4.

pixels inside an annulus around an aperture containing the star. The inner radius of this annulus is sufficiently large that the light contributed by the target is negligible compared to the sky background. The sky background counts can be determined in one of several ways, we will specify this when describing the individual reduction pipelines we use.

After all of the image correction, aperture photometry is a case of summing counts from each pixel that contains light from the star the brightness of which is to be measured. This is made more complicated as the stellar point spread function (PSF) extends to great distances, albeit to a vanishingly small degree far from the star. With aperture photometry we only capture a fraction of this. However, so long as the fraction measured is consistent between our target and suitable comparison star(s), we can derive very accurate magnitudes from the measured brightness ratios. This is particularly powerful in the case of transit photometry as we are only concerned with the brightness *variation* of the target relative to nearby, non-variable, comparison stars (c.f. the conclusions of Howell 1989 in the case of measuring the total flux from a star).

Fig. 2.2 helps with the following explanation. When performing aperture photometry we choose an aperture radius that is a compromise between the flux measured from the target star, the contribution of the sky background noise and contamination of the aperture by other stars. The sky background contributes both random noise from all the pixels included in the aperture plus a systematic error from the uncertainty in the value of this background level. The cartoon aperture and PSF (Fig. 2.2; left) shows this choice. Pixels marked 1 are clearly dominated by the PSF, those marked 2 are arguably so, while pixels marked 3 are similar to the "sky-dominated" unmarked pixels.

Naylor (1998) shows that the ideal aperture size can be calculated as a simple fraction of the PSF's full-width half-maximum (FWHM) but points out that this requires that the PSF is well sampled. The cut-through of a simulated stellar PSF (Fig. 2.2; right) illustrates that this "fine-pixelation" assumption can invalid for a well focused image on a real CCD. If the assumption of fine-pixelation is not valid it becomes important exactly which pixels are summed and which excluded as the sum depends

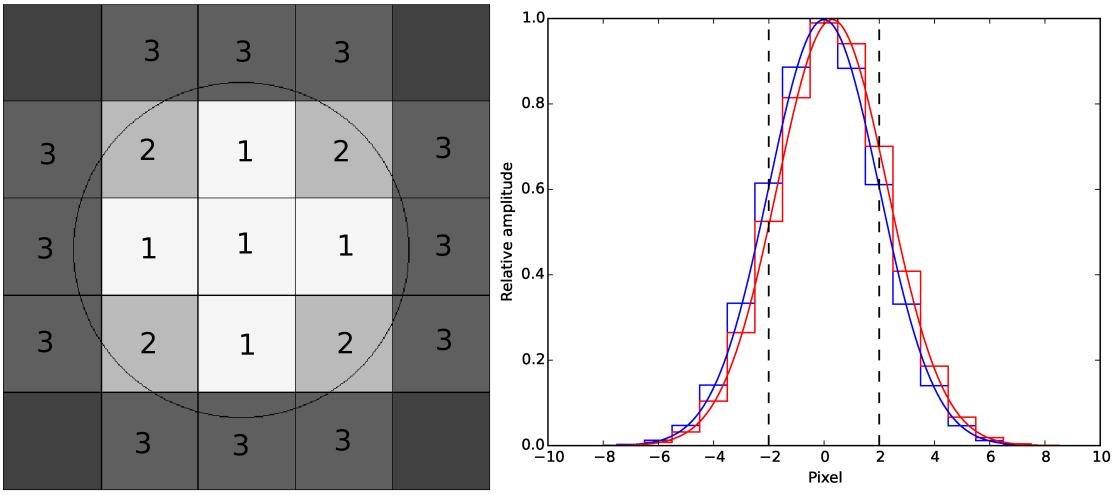

Figure 2.2: Left: Cartoon of an aperture projected onto the pixels of a CCD containing a stellar PSF. The numbered pixels are to aid the explanation of pixel weighting. Typically, all counts from pixels numbered 1 will be used while none will be counted from un-numbered pixels. Counts from pixels numbered 2 and 3 will be weighted between the two extremes with '2' pixels carrying a greater weight than '3' pixels. Right: Two identical PSFs offset by ± 0.3 pixels from the centre (dotted lines) with a comparison to the PSFs re-sampled by CCD pixels (solid lines). The differing levels in the pixels offset from 0 manifests as "pixel noise".

on where the PSF is centred on the pixels. This can be seen for the 3 whole pixels between the dashed lines in the cut through PSF of Fig. 2.2. If just these three pixels are summed the total of the red, offset PSF (once pixelated) is slightly smaller than that of the blue, well-centred, PSF. This variability leads to "aperture noise" (Shahbaz, Naylor & Charles 1994; Naylor 1998).

The effects of aperture noise are most pronounced for 'hard-edged' apertures where pixels are either completely included or completely excluded based on whether their centres are inside or outside of the photometry aperture. For example, in this regime pixels marked 1 and 2 in Fig. 2.2 would be given equal weight while those marked 3 would be ignored entirely. Meanwhile, with a small shift in the centring of the aperture, some pixels marked 2 would become excluded entirely while some marked 3 would become included. To mitigate this effect some weighting function is generally employed to take account of these partial pixels. As with measuring the sky background there are various regimes available for this weighting function which I will describe in the relevant pipeline section.

2.4 WASP pipeline

Data collected using the WASP-South instrument is shipped to the UK from SAAO in Sutherland on hard drives. When received in Keele the data are copied onto the section of the computing cluster reserved for raw data. We then check that all the data we expected has arrived on the hard drive and that the data has not become corrupt in transit. We can then replace small volumes of missing or corrupt data from a copy temporarily held at WASP-South. From here, the raw data are backed up in a second location before being distributed to the reduction cluster.

Data reduction has been heavily automated by David Anderson (DRA, Anderson 2013) for use with the data from the 200-mm lenses. The pipeline procedure I describe here is largely the same as the one already developed, but modified to optimise it for the 85-mm lens data. The pipeline modifications are covered in a subsequent chapter.

Once the data has been distributed to the reduction machines, a script puts a LAUNCHER3 script in each directory. This contains all of the information needed to run a full reduction, i.e. the paths to directories containing reduction scripts and other software, raw data and calibration images, designated output directories, stellar catalogue directories, and which reduction options to use. The reduction options allow the user to choose which of the following actions to perform; classify frames, make master calibration frames and reduce the data. The latter options are only possible if the preceding actions have taken place or have been selected to be performed as well. Typically frame classification and calibration frame creation are done together first in order to allow the master calibrations to be quality checked. If the calibrations are deemed to be of a sufficient standard the full reduction is performed.

LAUNCHER3 first runs ID_FRAMES3. This script checks that required directories can be read from and written to and checks how many of each kind of frame ("Object[4]", Bias, Dark and Flat) there are. The reduction procedure stops here if the run is "classify only", otherwise the calibration files are prepared. If the night under consideration does not have enough bias frames to make a master bias it searches for a usable master bias from a previous night. This process is repeated for the dark frames. After this other scripts are called that handle the creation of appropriately corrected master bias, dark and flat frames. As the area of sky imaged by each WASP camera is large, the usual assumption that the sky will produce a uniform flat-field is not strictly valid. The finite shutter travel time also affects the uniformity of the exposure of the shortest duration flats. When making the flat fields, the pipeline corrects for the shutter travel time by dividing each flat-field by a scaled sensitivity map. To mitigate the non-uniformity of the sky each flat is rotated 180°about the centre of its vignetting pattern, subtracted from the original flat and has a plane fit to the residuals (Pollacco et al. 2006). This gradient is then also divided out. Log keeping and quality checks are performed and the process continues to a full reduction if this has been requested and there are object frames to reduce.

[4]Object frames are the images containing observations upon which photometry is performed.

In the case of a full reduction, ID_FRAMES3 runs DO_ASTROM_3 on each object frame. This opens the object frame to be reduced, finds any saturated pixels and performs the bias correction, dark subtraction and flat field division using the master calibration frames. The mean, standard deviation and median of the counts in the corrected frame are recorded and an auto-cross-correlation[5] is performed using the central area of the frame to work out the full-width at half-maximum (FWHM) of typical stellar images in the frame.

A routine, EXTRACTOR, detects and measures the positions of objects in the frame and the file header information is used to select a star catalogue to use to identify the stars in the image. If an appropriate catalogue does not exist then one is extracted. This is done for both an astrometric catalogue based on the bright stars found in Tycho-2 (Høg et al. 2000) and a photometric catalogue based on the United States Naval Observatory catalogue (USNO-B; Monet et al. 2003). The astrometric catalogue uses a brighter magnitude limit than the photometric catalogue and is used by WASP_CAT2FOCPLN3 to calibrate the transformation between CCD pixel position and RA-Dec sky position. The brightest objects in the object catalogue extracted from the frame are matched to the brightest objects in the astrometric catalogue and the distances and angles between them are calculated. These "similar triangles" are cross identified to map the image. The coordinate transform is refined over multiple iterations of this cross-matching. If this step fails the reason for the failure is recorded to a log, otherwise header information is updated.

Bad or saturated pixels are flagged and the corrected object frame is passed to WASP_MODSKY3 which fits a 2D polynomial to the sky pixels. The bad and saturated pixels are excluded and a magnitude dependent area around each star is masked so it does not affect the fit. This step is also used to eliminate frames heavily affected by clouds if too many pixels are masked or the fit is poor. Rejected frames have ".badsky" appended to their file name and are not used further.

From there, DO_ASTROM3 calls WASP_3APERTURE_PHOT3 to perform the aper-

[5]Cross-correlation of the frame with itself.

ture photometry proper. WASP_3APERTURE_PHOT3 opens the image, the sky fit, the astrometry catalogue, the EXTRACTOR catalogue, puts the information into a form it can use and loads the sky mask used by WASP_MODSKY3 to blank out other stars. Weightings, $\omega(i - x_0, j - y_0)$, are then calculated for each pixel based on its position, (i,j), relative to the centre of the aperture (x_0,y_0) and the aperture radius, R, in three reduction apertures like so:

$$\omega(i - x_0, j - y_0) = \begin{cases} 1, & \\ & \text{if } (i - x_0)^2 + (j - y_0)^2 < (R - 0.5)^2 \\ 1/(1 + \alpha((i - x_0)^2 + (j - y_0)^2)^\beta), & \\ & \text{if } (R - 0.5)^2 < (i - x_0)^2 + (j - y_0)^2 < (R + 0.5)^2 \\ 0, & \\ & \text{if } (i - x_0)^2 + (j - y_0)^2 > (R + 0.5)^2 \end{cases} \tag{2.3}$$

The values of α and β are calibrated so that the weight of a Fermi-Dirac like weighting function varies smoothly from 1 to 0 in the range between $R - 0.5$ and $R + 0.5$. Then for each object in the EXTRACTOR catalogue WASP_APER3 is run to calculate the flux in apertures with three different pre-determined radii. For the 85-mm data these radii are 3, 4 and 5 pixels. The sky subtraction is carried out in two steps. First, the sky value given by the sky model is subtracted from each pixel in the object and sky apertures, then the mean difference between the sky model and the value recorded in the sky aperture is subtracted. If a star is too near the edge of the frame or if the largest reduction aperture contains a bad pixel, the star's flux is set to a nonsense value and ignored.

WASP_BLENDS uses the fluxes from the three apertures to calculate the degree of blending, if any, present for each star. Each star is given an index that depends on if it is blended, its colour and, in the case of blended stars, its aperture flux ratios relative to unblended stars; these range from 0 to 5. A blend index of 7 indicates a blending regime cannot be identified[6]. A blend index of 8 indicates the star has a

[6]There is no regime indexed as 6.

negative flux in one of its apertures. A blend index of 9 indicates the star is either saturated or has a bad pixel in an aperture. Only stars with an index of 0 are used in subsequent calibration steps. The results for each star are written to a FITS file and header information is recorded.

Once these steps are complete IDFRAMES3 takes over again. It identifies the different fields observed for the night and makes logs for each individual field in order to make tracking nightly trends easier. These log files (known as "trendlogs") record, for each frame; the file's name, observation date and time, count statistics, exposure time, coefficients of the coordinate transform, fit uncertainties and FWHM. The trendlog headers also contain reduction software version information. After this, various parameters used by the post-processing calibration program, PPWASP, are initialised and a master parameter file is linked if one exists for the field. The master parameter file contains catalogue identifier, RA and declination positions and magnitudes from both USNO-B and Tycho, average instrumental and pipeline calibrated magnitudes as well as the uncertainties on these magnitudes for a number of standard reference stars from the Tycho catalogue. PPWASP uses static memory allocation, so an optimal version is selected based on the number of lines in the USNO-B photometry catalogue associated with the field and an estimate of the number of orphans[7] in the field.

The aim of PPWASP is to detrend and calibrate a night's photometry, then to normalise it against a previous night with good conditions. This ensures the data for a given field are consistent across an observing season allowing them to be combined to search for planet signals. To do this, PPWASP loads the processed fluxes of all objects from all good images of the field in question as magnitudes. From here it identifies bad data; points with a blend index of ≥ 7 or a negative magnitude. If an individual star has too many points marked as bad it is flagged as not usable in calibration. Likewise, if a frame has too many points marked as bad it is flagged as unusable. For each remaining star with enough data a model magnitude is initialised to the mean instrumental magnitude. A sample of calibration stars are chosen and

[7]Orphans are objects found by EXTRACTOR that do not appear in the USNO-B catalogue.

used to model the flux variation of objects in the field. In addition to not being flagged by the preceding step these stars must:

- have valid Tycho B and V magnitudes.
- have sufficient valid WASP measurements.
- be marked as unblended.

First the model residuals are calculated. The residuals are then detrended with respect to airmass. The airmass detrending can be set to fit either a single extinction term based on airmass alone or it can fit two terms, one for airmass and the other is a function of airmass and colour. The colour term uses the B−V colour of an approximately solar type star as a reference. After this, the residuals are detrended against detector position. The model is updated and the procedure repeated until either the model parameter changes are smaller than a given threshold or a set limit of iterations have passed. This model is applied to all objects to minimise the effects of non-stellar brightness variations. This is repeated for each field and night specified to be reduced. Afterwards there are quality checks to make sure all the steps have completed successfully. Any step that has failed is investigated and that date re-run from the point of failure.

2.4.1 Candidate Identification

The processed data are transferred to the WASP data archive at Warwick University where each object is searched for periodic signals following the method of Collier Cameron et al. (2006), a short summary of which follows. First, all stars in a field have their weighted mean magnitude calculated. The weights use the formal variance calculated by the reduction pipeline with an extra component that is frame dependent to account for extra transient phenomena which degrade the photometry such as cloud or Sahara dust events. A zero-point correction is then applied to each frame. This time each star in the frame is weighted accounting for the formal errors and inherent

variability of the star. After this the data are further decorrelated using a version of the SysRem algorithm of Tamuz, Mazeh & Zucker (2005) in which correlated residuals common to all the stars in the frame are removed using principal component analysis.

The decorrelated lightcurves are searched using an adaptation of the boxed-least-squares (BLS) algorithm of Kovács, Zucker & Mazeh (2002). A grid of trial periods and epochs is compiled, the difference between the periods and epochs used are equivalent to the expected transit duration at the longest period. The expected transit duration is calculated using Kepler's 3$^{\rm rd}$ law assuming a stellar mass of $0.9M_{\odot}$.

At each trial period and epoch the transit depth and "goodness-of-fit" statistic (which has units of χ^2) are calculated for a simple box shaped transit model. The best fitting model at each trial period is selected and the transit depth, change in χ^2 from a fit to a flat lightcurve ($\Delta\chi^2$) and the goodness-of-fit of the out-of-transit section (χ^2_h) are recorded. Any fits with $\chi^2/N > 3.5$, where N is the number of data points, are rejected. Any fits that contain fewer than 2 transits or have gaps larger than 2.5 times that of the transit duration after phase folding are also rejected. Further cuts are made based on the "signal-to-red-noise" ratio, $S_{\rm red}$ and the "anti-transit ratio", $\Delta\chi^2/\Delta\chi^2_-$. $S_{\rm red}$ is a measure of the strength of the signal to correlated noise instead of regular white-noise. $\Delta\chi^2/\Delta\chi^2_-$ is the ratio of the strongest peak in $\Delta\chi^2$ relating to a dimming with that of the strongest peak relating to a brightening. Burke et al. (2006) suggest that this is a good way to eliminate false positives if there is no reason for systematic noise to produce periodic dimmings more strongly than periodic brightenings. Thus a low ratio would suggest the dimmings and brightenings are of a similar magnitude while a higher ratio suggests the dimmings are of a greater magnitude than the brightening events. The remaining candidates are subjected to another BLS search where the spacing between trial periods and epochs is reduced from the expected transit duration to half the expected transit duration. Other refinements are made on this run, including the use of a "softened box-like" function to more closely approximate the transit shape.

From here, lightcurves are checked for large amplitude ellipsoidal variations which could indicate the transiting object is massive enough to distort the host star's shape, therefore being more massive than a planet. Finally, the estimated system parameters

are checked for consistency against the hypothesis that a Jupiter-sized object is orbiting a main-sequence star. Stellar mass and radius are estimated using WASP instrumental and K-band magnitudes from the Two Micron All Sky Survey (2MASS; Skrutskie et al. 2006). The stellar radius is used to estimate the planet radius and stellar mass is used to check the transit duration is consistent with a Jupiter-mass object. The reduced proper motion is also calculated as a way to identify objects that are likely to be distant red giant stars, rather than nearby dwarf stars (Gould & Morgan 2003). In addition to these requirements, a candidate lightcurve must not show an obvious secondary eclipse and preferably not have a star less than 5 magnitudes fainter within the main reduction aperture.

2.5 Planet confirmation and follow-up

WASP photometry is good enough to identify stars with periodic drops in brightness of 1% or less, but not good enough to characterise the shape and depth of these dips accurately. The depth of a transit can be affected by systematic errors due to blending with nearby stars or the detrending process, and the photometric precision is not good enough to measure the contact points of the eclipse. This makes distinguishing between a planet transit and a shallow binary star eclipse difficult from the discovery photometry alone. The discovery photometry will normally be comprised of several transit-like events from different nights, each of which covers only part of the total transit. When these incomplete transit observations are phase folded without a lightcurve of a full event, the overlap region between them can cause uncertainty in the event duration. The spatial resolution of WASP is low compared with that of telescopes normally used for optical astronomy which, aside from questions about the true depth of the transit, can lead to uncertainty about which star a signal is coming from. Follow-up observations of likely candidates allow us to clear up these uncertainties and find out more about the systems. These observations come from two sources, spectroscopic observations of candidate systems and high-precision photometry.

2.5.1 Spectroscopy

Spectroscopy involves spreading out the light from the target star into its constituent wavelengths and making measurements of the shape and position of lines imposed by elemental (and molecular) species in the stellar atmosphere. The spectrographs used by WASP for initial follow up are all fibre-fed. This means that an optical fibre is centred on the stellar PSF and used to relay the light to the main spectrograph assembly. The spectrum is then imaged using a CCD. These spectral images are bias, dark and flat-field corrected in the same way as photometric observations. From here the treatment differs depending on what information will be extracted from the spectra.

2.5.1.1 Planet Confirmation

Measurements of the radial velocity (RV) variations caused by a companion object are a good way to separate planet mimics from real planets. From the radial velocity semi-amplitude and an estimate of the primary star's mass, the mass of the companion object can be determined. To do this, model spectra are cross-correlated with observed spectra and the red- (or blue-) shift of the spectral lines from their rest wavelengths is used to calculate the RV. The measured radial velocity changes over time as the star orbits the planet-star barycentre. The amplitude and shape of the RV curve provides information about the companion object's mass and the orbital eccentricity. If a signal is detected that is associated with the target star and results in a mass in the range of a planet ($M \lesssim 13 M_{\rm Jup}$)[8] then this is a good sign, but, alone it does not confirm the companion is a planet or even real.

The stellar spectral lines are asymmetric. Shifts in this asymmetry can mimic the lines moving very slightly. The asymmetry arises due to granulation of the stellar surface caused by hotter material rising and cooler material sinking. The rising material is blue-shifted while the sinking material is red shifted, see Fig. 2.3. There is no difference in the composition of these two cases so the spectra of both will be the same

[8]This boundary is poorly defined.

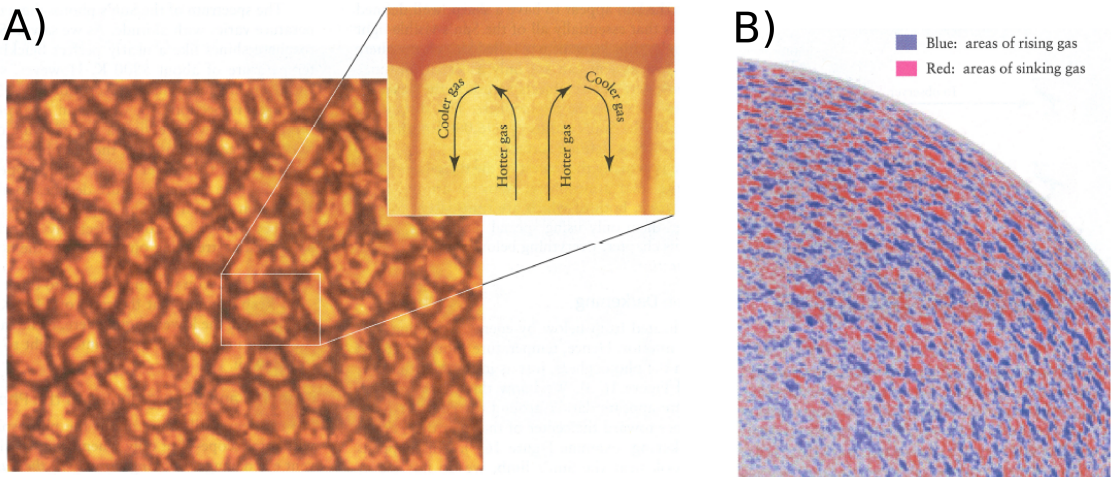

Figure 2.3: Diagrams showing the flow of stellar material leading to granulation. Figures 16.9 and 16.10 from Universe (Freedman, Geller & Kaufmann 2011).

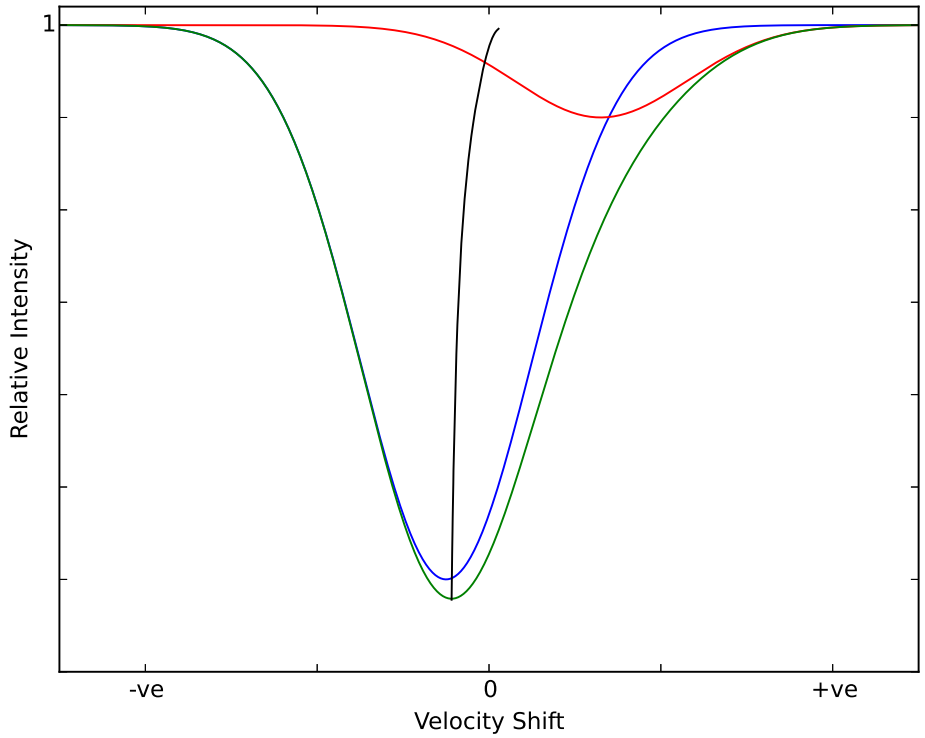

Figure 2.4: Cartoon of the effect of stellar convection on a spectral line. The blue line corresponds to rising material, the red line corresponds to sinking material and the green line is the overall line profile neglecting a detailed treatment of other complicating effects. The black line is the bisector of the green, overall line.

so we can consider any individual spectral line for ease. Fig. 2.4 illustrates the effect this has on the spectral line. The measured spectral line is a combination of the bright, blue-shifted line of the rising material and the dimmer, red-shifted line of the sinking material. The offset is very small, so the result is a single line with a maximum depth around that of the blue-shifted material and a tail on one side caused by the red-shifted material. Thus the line is not symmetric about the RV induced offset. We can see this by plotting the "line-bisector", they have a c-shape, seen in Figs. 2.4 and 2.5.

Variation in the asymmetry of the spectral lines can lead to spurious RV signals. These can be caused by stellar activity as in the case of HD 166435 (Queloz et al. 2001). Variable star-spot coverage lead to a shift in the relative contributions of red- and blue-shifted light as the star rotates causing the asymmetry of the line bisector to change resulting in an apparent RV variation. Bisector shape variation can also be the result of blended stars. For example, Santos et al. (2002) showed for the case of a planet-like signal detected in HD 41004 that the bisector variation of the primary K0 star is due to an asymmetry caused by a second set of spectral lines from a close M-dwarf companion blending with that of the primary, rather than a more subtle change in the pattern of granulation. In either case there were clear correlations between the RV shift and the bisector shape. This correlation strongly implies the RV signal is not the result of orbital motion and so casts doubt on the interpretation that it is caused by a planet. Figs 2.6 and 2.7 illustrate the case of strong and weak correlation between bisector spans.

Santos et al. (2002) also found that the RV semi-amplitude they measured varied depending on the set of spectral lines they used. This can be explained if the lines are blended to differing degrees, causing the measured RV variation due to the changing line shape to vary. An RV signal caused by an orbiting companion would induce the same shift in the spectral lines irrespective of which lines are used to measure it. This is another possible avenue to explore if there is doubt as to the origin of an RV signal.

In addition to confirming the planetary nature of a candidate, RV measurements can also reveal the presence of extra objects in the system. If long-term drifts in the systemic velocity are seen this can point to a massive object on a longer period orbit.

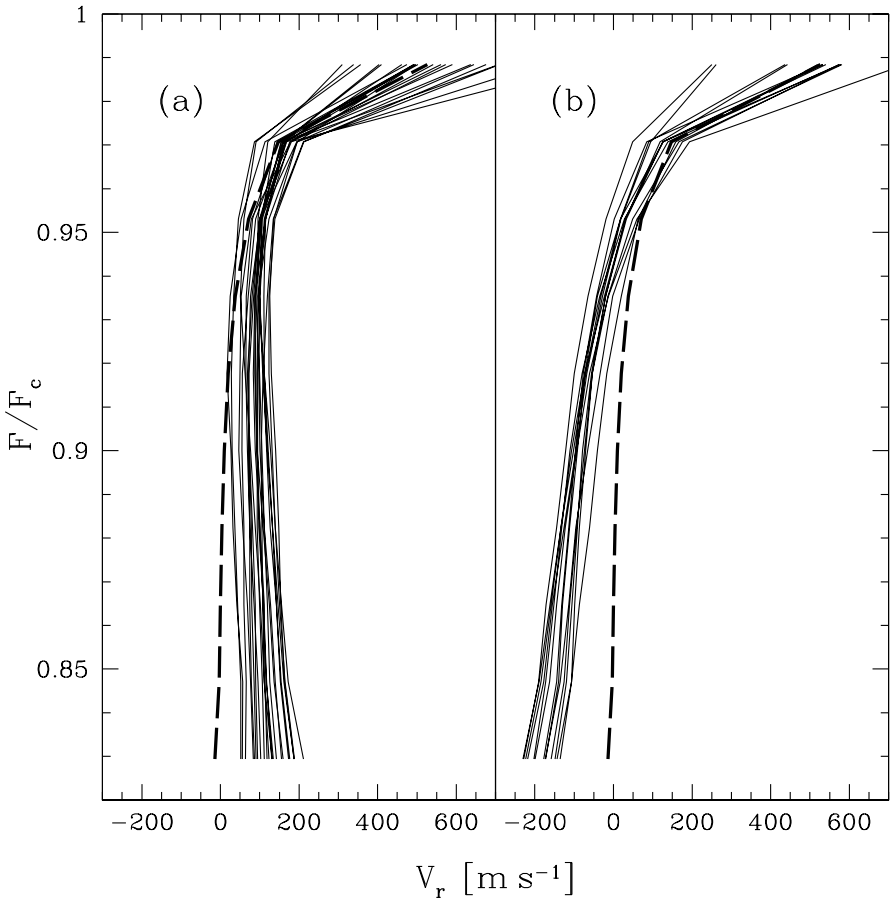

Figure 2.5: Individual bisectors for two sets of spectra chosen from opposite phases of a radial velocity cycle observed in the star HD 166435. The phase at 'a' is 0.0 ± 0.1 while the phase at 'b' is 0.5 ± 0.1. The dashed line is the overall mean. The shift mimicked the kind of RV signal that could be induced by a planetary companion which was ruled out by this investigation. Figure 6 from Queloz et al. (2001).

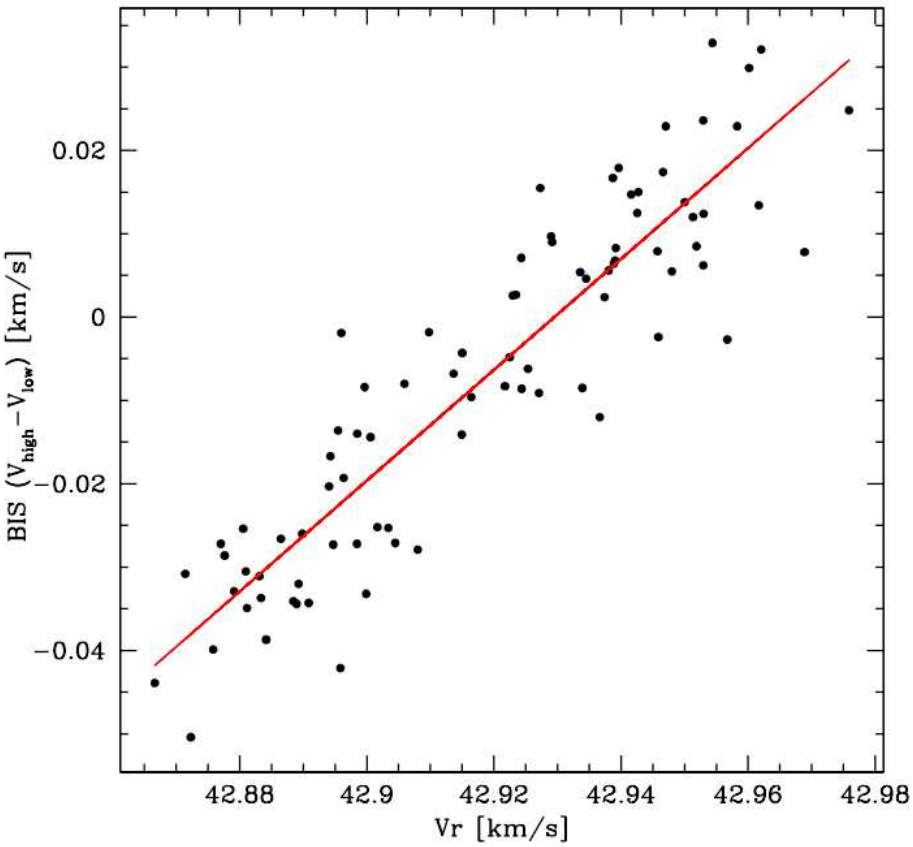

Figure 2.6: Graph showing the strong correlation between bisector span and radial velocity for HD41004 observed by Santos et al. (2002). The slope of the best fit line here is 0.67.

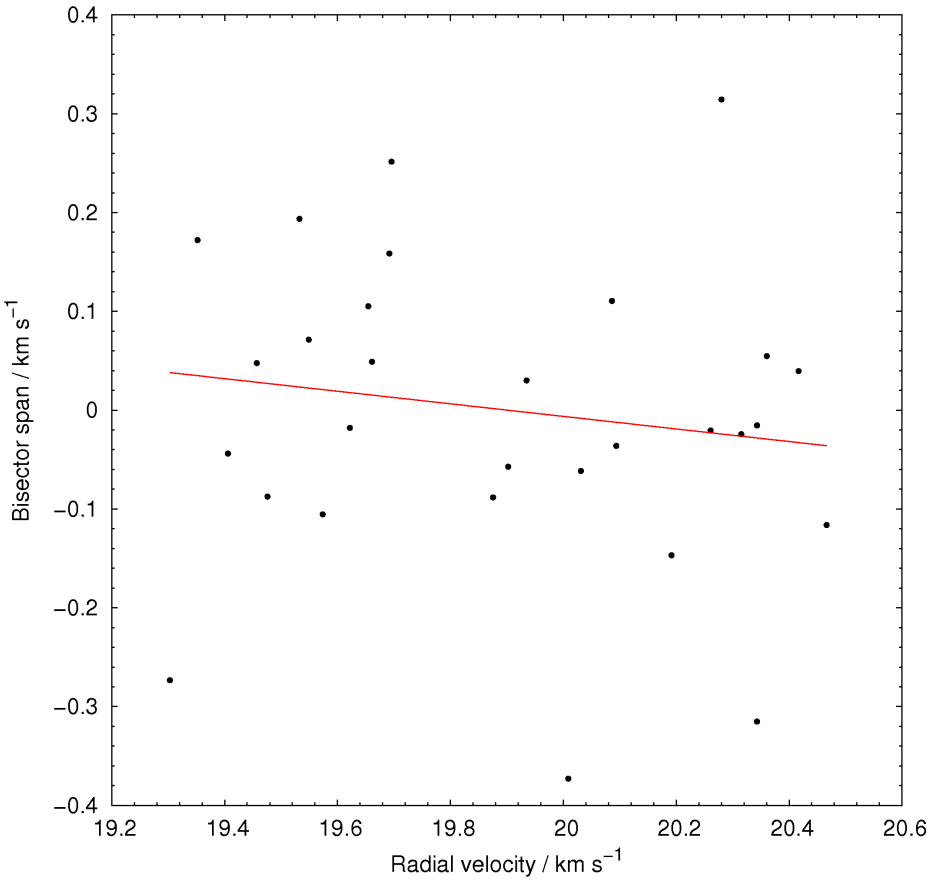

Figure 2.7: Graph showing no obvious correlation between bisector span and radial velocity for the planet host star WASP-120. Graph has been adapted from data in Turner et al. (2016c) to look more similar to that of Figure 2.6. Here the best fit slope is -0.06 ± 0.07.

2.5.1.2 Stellar Parameters

Spectroscopy is also vital for characterising planet host stars. The planetary properties we determine from photometry and RVs are highly dependent on the assumed stellar properties. The planet radius and mass can be determined from the transit depth, ΔF, and radial velocity semi-amplitude, K_1, as shown below:

$$\Delta F = \left(\frac{R_p}{R_*}\right)^2 \tag{2.4}$$

$$K_1 = \left(\frac{2\pi G}{P}\right)^{1/3} \frac{M_p}{(M_* + M_p)^{2/3}} \frac{\sin i}{\sqrt{1-e^2}} \tag{2.5}$$

The key thing to note in these equations is the star-planet parameter ratios R_p/R_* and $M_p/(M_* + M_p)^{2/3}$. Without knowledge of the stellar mass and radius any attempt to determine the planetary parameters is impossible. Likewise, the accuracy of planetary parameters is heavily dependent on the accuracy with which they can be determined for the host star.

To place estimates on stellar mass and radius we typically use an empirical calibration that uses quantities that can be derived from stellar spectra. Early WASP discoveries used the calibration of Torres, Andersen & Giménez (2010) which uses stellar effective temperature, $T_{\rm eff}$, surface gravity, $\log g$, and metallicity, [Fe/H]. This calibration is based on precise mass and radius measurements for eclipsing binary star systems. For exoplanet host stars, stellar density is used in place of $\log g$ as it can be determined to high precision from transit observations. Calibrations based on density have been published by Enoch et al. (2010) and Southworth (2011a). For typical WASP stars we use the Hα line to measure the effective temperature, Na D and Mg b lines to measure the surface gravity and several unblended Fe I lines to measure the metallicity (Gillon et al. 2009; Doyle et al. 2013). We can determine other properties like projected stellar rotational velocity by fitting the profiles of the Fe I lines after convolving with the instrumental resolution, micro- and macro-turbulence (Doyle et al. 2013; Doyle et al. 2014).

Recently we have used the method of Maxted, Serenelli & Southworth (2015), BAGEMASS, to place constraints on stellar mass and radius. This also uses the stellar density derived from transit lightcurves with other stellar parameters ($T_{\rm eff}$, [Fe/H] and luminosity) to perform a Markov chain Monte Carlo (MCMC) analysis to fit them to different stellar models. The quantitative nature of this analysis is particularly useful. For example, if there are degenerate solutions a preference can be given based on the relative fraction of the Markov chain. It also gives us an estimate of the age of the star without needing to use an empirical relation like that of gyrochronology or lithium abundance.

2.5.2 Photometric False Positive Rejection

Using spectroscopy to confirm the presence of a suspected planet around a blended star can be an expensive waste of time if it does turn out to be a blended eclipsing binary system. An easier, less resource intensive way of checking the source of a potentially blended signal is higher resolution photometry. This kind of observation is referred to as an "on-off". The idea is that a candidate with multiple stars in the WASP reduction aperture is observed around the time of a predicted transit event with a telescope with a finer plate scale. This way each star in the WASP aperture can be analysed individually. Then, the object that is displaying photometric variability can either be confirmed as a potential planet transit and followed up with spectroscopy or rejected as a blended eclipsing binary. An example of the results of an observation like this are shown in Fig 2.8.

2.5.3 Photometry

2.5.3.1 Observations

The pipeline in the following section has been used regularly by myself and DRA to reduce follow-up observations of WASP candidates. DRA was responsible for the initial

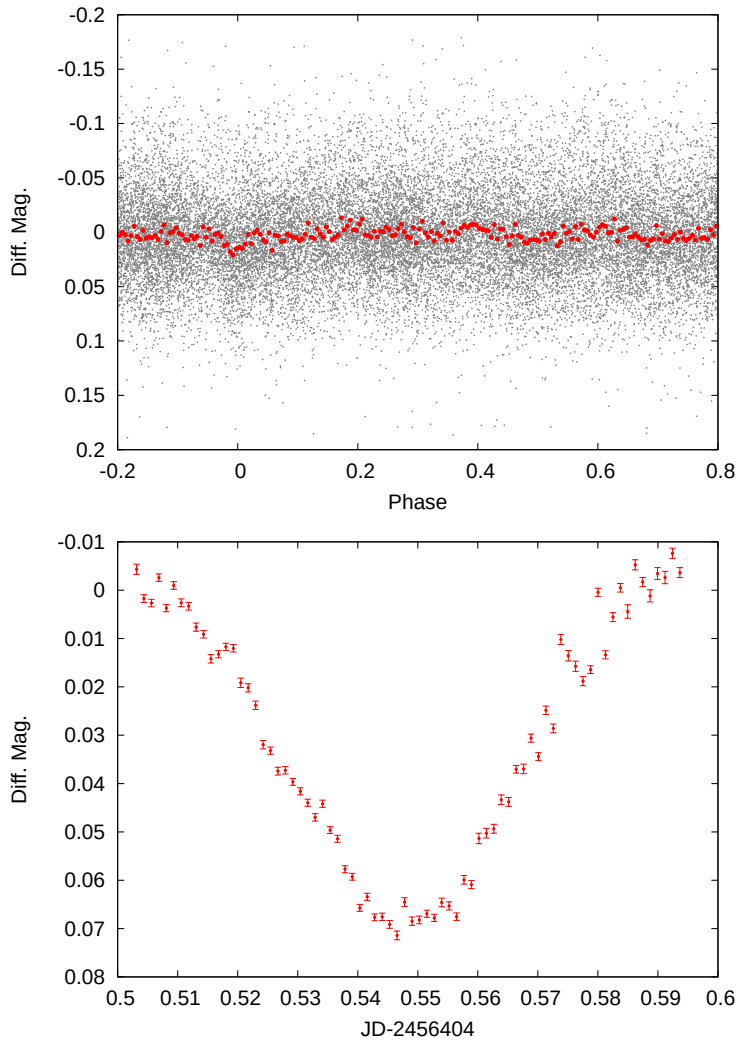

Figure 2.8: Comparison of WASP discovery data and "on-off" follow-up data for a blended eclipsing binary system. WASP discovery data for object 1SWASP J064315.84-400437.5 (top): after the transit search algorithm this object was found to have a signal with a period of 1.25-days and a transit depth of $\approx 1\%$. It was flagged as requiring an "on-off" as there are stars blended in its reduction aperture. The results of observations taken with the Danish 1.54-m telescope (bottom) show it to be a blended eclipsing binary with a depth of $\approx 6\%$.

development of the pipeline based on steps taken by the automated WASP pipeline. During use I have streamlined it, skipping steps that are made unnecessary due to the greater degree of human interaction, e.g. automated source location is replaced with by-eye identification. We have used it with data collected with the DFOSC instrument on the Danish 1.54-m telescope (Andersen et al. 1995) as well as IO:O and RISE on the 2-m Liverpool telescope (Steele et al. 2008).

In the case of data collected with the DFOSC instrument it was necessary to take calibration frames which I applied to the science images as described in Section 2.3.1. We acquired flat-fields using the twilight sky method described and combined our calibration frames using the median rather than the mean. Data acquired using RISE and IO:I is automatically corrected before being made available to the telescope users.

When making photometric follow-up observations of planet transits we defocus the telescope. Defocusing has several advantages for time series photometry. It helps to reduce the contribution of flat-fielding inaccuracies as they are averaged over a larger number of pixels and allows a greater duty cycle as exposures can be longer, even on bright targets, without saturating the detector pixels.

2.5.3.2 Photometry Pipeline

In preparation for aperture photometry using the *iraf* '*phot*' routine, the user first gathers some information on the behaviour of the background counts throughout the observation run. An area with no stars visible in an image is selected and the '*imstatistics*' routine is run in order to find the midpoint and standard deviation of the background for each image. These are used these to determine a "minimum good value" for the sky background. Various keywords are set to extract information from the FITS header; the Julian date (JD) of the observation is necessary while others, such as the airmass are useful, though not always recorded. From a visual inspection the approximate centres of the target and comparison stars to be measured are found and record in a co-ordinates file to supply to *iraf*. The approximate FWHM of the

target star is determined and used to set limits on the bounding box of the centroiding algorithm used. A range of reduction aperture sizes are chosen guided by the method of Naylor (1998). The *phot* routine is then used to determine the number of counts in each aperture for each star. It uses a softened aperture where the weighting of the counts in each pixel is determined by:

$$\omega(i-x_0, j-y_0) = \begin{cases} 1, & \\ & \text{if } (i-x_0)^2 + (j-y_0)^2 < (R-0.5)^2 \\ 0.5 - R + \sqrt{(i-x_0)^2 + (j-y_0)^2}, & \\ & \text{if } (R-0.5)^2 < (i-x_0)^2 + (j-y_0)^2 < (R+0.5)^2 \\ 0, & \\ & \text{if } (i-x_0)^2 + (j-y_0)^2 > (R+0.5)^2 \end{cases} \tag{2.6}$$

Where x_0 and y_0 are the co-ordinates of the centre of the reduction aperture, $\omega(i-x_0, j-y_0)$ is the weighting of a pixel centred at (i, j) with an aperture centre of (x_0, y_0) and radius R. After this, the lightcurves are visually inspected for any anomalous points. If there appear to be any, the corresponding images are inspected to determine the likely cause and, if appropriate, the data-point is removed from each star's lightcurve.

Each potential comparison star lightcurve is visually inspected for trends or anomalies by dividing it against another comparison star, normally the brightest. Any that show significant trends or trends more complex than quadratic in time are rejected. A master comparison lightcurve is made with the remaining comparison stars which are given equal weighting. The target's lightcurve is then divided by the master comparison. When I am performing the reduction, I cycle through different aperture choices to find the one with the least scatter. I made an attempt to increase the automation of this part of the pipeline by writing a post-photometry pipeline, referred to hence as *pphot*. The idea behind *pphot* was to automatically strip anomalous points from the lightcurves of the target and comparison stars via sigma clipping. Then, using data collected before ingress and after egress, *pphot* was to determine which combination of aperture size and comparison stars gave the lowest scatter. This method did

not work reliably. Trends in the data rendered this less simple than initially believed and other factors, such as the airmass variation during an observation run, meant that the aperture giving the lowest scatter at the beginning and end of the observations was not necessarily the best overall. However, *pphot* is useful once an aperture size and set of comparison stars has been decided on and can be useful in this determination if observing conditions have been favourable. It does reliably exclude spurious points from lightcurves, normalises the resulting lightcurve, calculates the uncertainties on each point (factoring in photon noise, sky background and read noise), converts the lightcurve from flux to magnitude and applies the barycentric and exposure time corrections if they are supplied.

Once reduced, I compile extra information; the co-ordinates of the centre of the target in each image, the FWHM of the target in each image, the airmass of each image, the sky background of the target and the exposure time. These can be useful in determining the sources of errors, differences in scatter and for detrending. For example, my reduction of WASP-59 showed a strange v-shaped drop in brightness after egress, see Fig. 2.9. Using this extra information we linked it with the target passing very close to the zenith. The Liverpool Telescope is an alt-az design so we expect the cause is the poorer field tracking and rapid field rotation experienced for observations near zenith.

2.6 Expected Instrumental Sensitivity

It is known that changing the WASP-South Canon 200-mm, f/1.8 lenses to Canon 85-mm, f/1.2 lenses will alter the range of stars it is possible to gather data from. We can estimate how this range will change based of the new equipment and the photometric theory outlines with some simplifying assumptions.

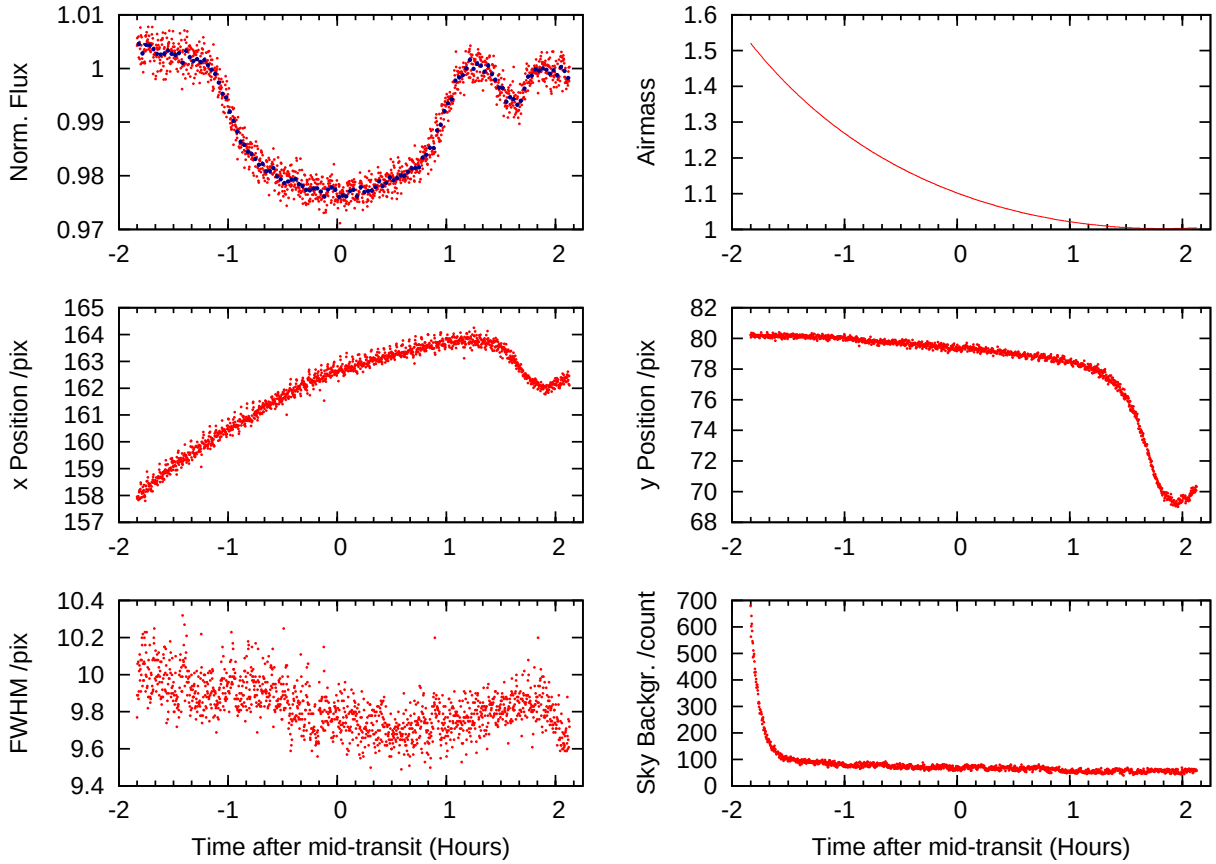

Figure 2.9: Graphs of fully reduced transit observations of WASP-59 with plots of detrending information. The v-shaped dip correlates well with an airmass of 1 and a large change in the x and y positions of the target star on the detector.

2.6.1 Photon Counting

The number of photons the detector can receive from a star depends on the flux from that star and the aperture of the instrument. Equation 2.7 demonstrates how the flux takes account of the star's inherent brightness in a bandpass centred on wavelength, λ_c, and the distance to that star.

$$F_{\lambda_c} = \frac{L_{\lambda_c}}{4\pi d^2} \tag{2.7}$$

This flux, F_{λ_c}, gives the energy passing through a square meter area at distance, d, from a star with luminosity, L_{λ_c}, in the band centred on λ_c, per second. To calculate the total energy received by a detector from this star F_{λ_c} must be multiplied by the collecting area of the detector (equivalent to a circular aperture of diameter D) and the exposure time, t, used:

$$E_\nu = F_{\lambda_c} \times \pi \frac{D^2}{4} \times t \tag{2.8}$$

This can then be divided by the average energy of a photon in that band, $\bar{E_\gamma}$. Here we approximate this to the energy of a photon with wavelength λ_c to calculate the number of photons:

$$N_{\gamma,\nu} = \frac{E_\nu}{\bar{E_\gamma}} \tag{2.9}$$

This can further be simplified by converting the zero magnitude fluxes in Janskys[9] from Bessell (1979) into photon fluxes per unit time and area.

$$m_{\lambda_c} - m_{\mathrm{ref},\lambda_c} = -2.5 \log \left(\frac{F_{\lambda_c}}{F_{\mathrm{ref},\lambda_c}} \right) \tag{2.10}$$

The relationship between the flux and magnitude of a zero magnitude reference star and a target is shown in equation 2.10, which can be rearranged as follows in equation 2.11. Here C_ν denotes flux in Janskys and F the flux in $\mathrm{Js^{-1}m^{-2}}$.

[9] 1 Jansky (Jy) = $10^{-26}\mathrm{Js^{-1}m^{-2}Hz^{-1}}$.

$$\begin{aligned} F_{\lambda_c} &= F_{ref,\lambda_c} 10^{m_{-\lambda_c}/2.5} \\ &= C_\nu 10^{-26} \Delta\nu 10^{-m_{\lambda_c}/2.5} \end{aligned} \tag{2.11}$$

Above, ν is the frequency corresponding to the central wavelength λ_c and $\Delta\nu$ the width of the passband in Hz.

The energy of a single photon is given by $E_\gamma = h\nu$ (h being Plank's constant), which leads to the number of photons received by the detector below, assuming the width of the passband is sufficiently small:

$$\begin{aligned} N_\gamma &= \frac{C_\nu 10^{-26} \Delta\nu 10^{-m_{\lambda_c}/2.5} \times \pi \frac{D^2}{4} t}{h\nu} \\ &= \frac{C_\nu 10^{-(26+m_{\lambda_c}/2.5)}}{h} \frac{\Delta\lambda}{\lambda} \times \pi \frac{D^2}{4} t \end{aligned} \tag{2.12}$$

2.6.2 Comparison

It is possible to integrate equation 2.12 factoring in a stellar spectral energy distribution (SED), filter throughput and CCD response to calculate the number of photons detected during an exposure. I performed this calculation in order to estimate the ratio of the number photons collected with the 85-mm lenses, N_{85}, to the number collected using the 200-mm lenses, N_{200}. I used the spectral energy distribution (SED) of the Sun[10], along with the CCD and filter responses, integrated over the filters' passbands illustrated in Fig. 2.10. For the new WASP filter I used a standard r' band response curve. The response of the previous filter, approximated by a V+R filter, was reported in Wilson (2007). As the factor of interest is the ratio of starlight collected and the stars being considered can be placed at the same distance from the Earth, distance effects can be neglected. This gives the ratio of photons collected, $N_{85}/N_{200} = 0.155$. Therefore, the same sun-like star appears 15.5% as bright with the new equipment. This shifts the magnitude range anticipated by (Pollacco et al. 2006) by -2.0, resulting

[10]Sourced from DIPSO V3.6-3. (Howarth et al. 2004)

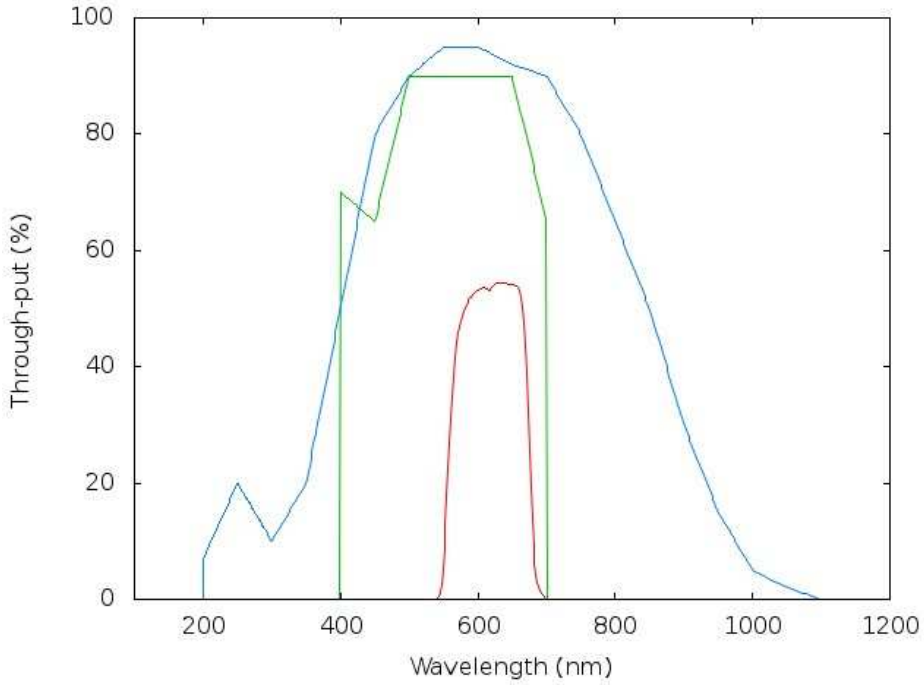

Figure 2.10: Old WASP V+R (green), new WASP r' (red) and CCD response (blue) curves showing through-put with respect to wavelength. The 'blocky' nature of the curves comes from the simple linear interpolation used to map them to the same resolution as the solar spectral energy distribution used.

in a range shift to V = 5 to 9.5 for 1% photometric accuracy. Further improvements to this estimate could be made by increasing the wavelength resolution on the WASP V+R filter response curve and by adding effects due to the opacity of the Earth's atmosphere.

Looking at those planets detected by the previously identical SuperWASP and WASP-South instruments and statistics gathered during reduction, a more realistic range of operations for planet detection is $8 < M_v \leq 13$[11]. A similar assertion of $9 < M_v \leq 12$ is made in Smalley (2014). Figures 2.11 and 2.12 also suggest this is a more realistic range. These figures show log(rms) for each stars' brightness for a night's observations of a particular field against the stellar magnitude from the Tycho-2 catalogue. The bright tail of the distribution flattens below around V = 10 in the plot of 200-mm data and below around V = 8.5 in the 85-mm data (see Figs. 2.11 and 2.12). The flattening of the rms distributions for brighter stars is caused by "red-", or time-correlated noise. This is noise that has some structure in time the cause of which is not well understood. Time-correlated noise affects all time series photometry and contributes more strongly for brighter stars. This lessens the benefit of the greater number of photons that would drive down the scatter in purely white noise limited observations. Meanwhile, the two distributions of outliers intersect around 14.2 in the 200-mm data and 13 in the 85-mm data. The bright limit of the distributions is determined by the point at which stars saturate. When pixels saturate the reduction pipeline ignores them. Another contributing factor for the 85-mm lens data is the increasing rarity of stars at brighter magnitudes.

2.7 Conclusion

In this chapter I have looked at the theory behind CCD photometry. I have considered the principles behind image correction and considered how they are practically applied.

[11] exoplanet.eu

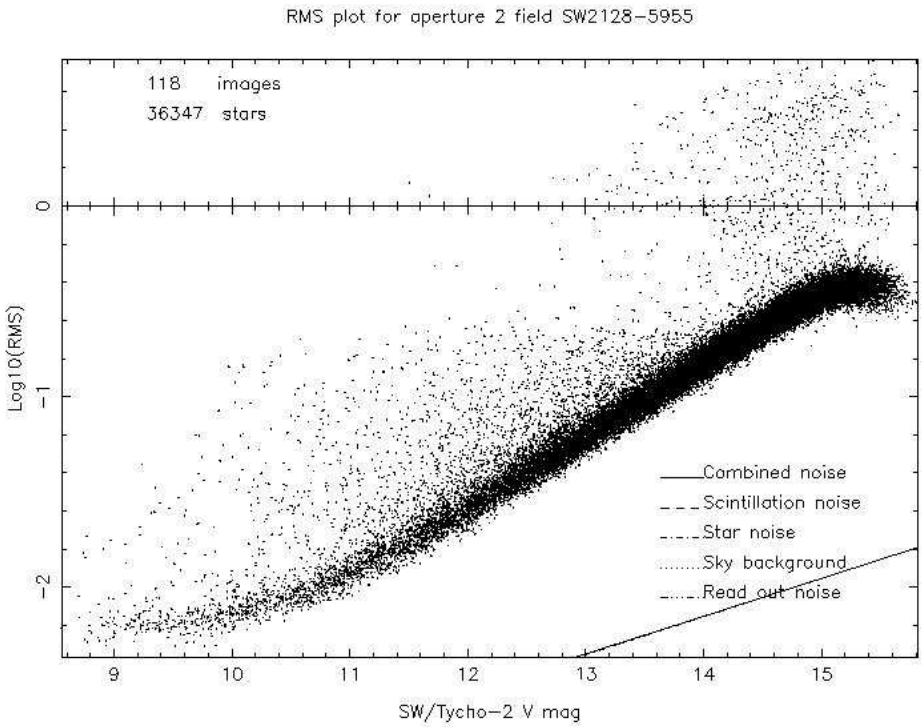

Figure 2.11: Photometric scatter, log(RMS), as a function of stellar magnitude for a field observed by WASP-South from the night of 2012-05-08 using 200-mm lenses. The positive slope shows the increase of RMS for dimmer stars. The distribution flattens below around V = 10 and above around V = 15. The brightest stars with usable data are just brighter than V = 9. The outliers seem to form two populations which intersect at around V = 14.2, this feature is highlighted simply as another point of reference for the magnitude shift.

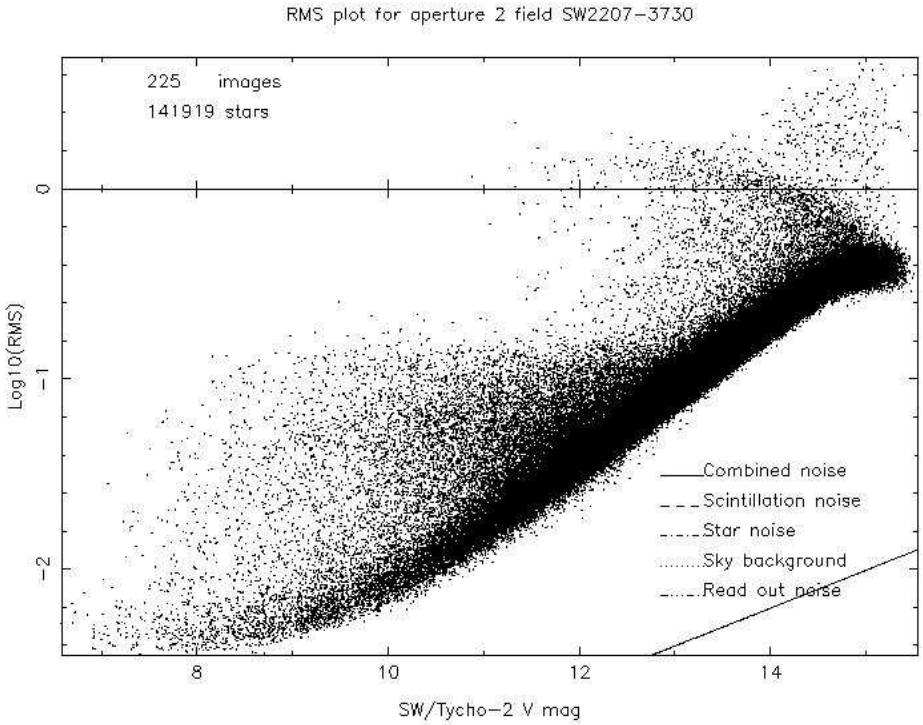

Figure 2.12: Photometric scatter, log(RMS), as a function of stellar magnitude for a field observed by WASP-South from the night of 2012-09-08 using 85-mm lenses. The distribution flattens below about V = 8.5 and above around V = 14.7 with the populations of outliers intersecting around V = 13. The brightest stars with usable data just brighter than V = 7. This shows a shift, at the bright end, of around 2 magnitudes.

I have outlined two photometric pipelines; the automated one used to process WASP data and a more flexible pipeline applicable to a wide range of telescopes used to follow-up candidate planets. While the complexity of the pipelines differs due to the volume of data they are intended to cope with the photon counting methods used to perform photometry are very similar. I have gone on to use the idea of counting photons to estimate the new effective magnitude range of WASP-South using the new 85-mm lenses. I have also looked at the methods used to eliminate false positives and confirm the planetary nature of WASP candidates. These will be used in a later chapter concerning the discovery of 3 planets found using 200-mm WASP-South data.

3 WASP data reduction pipeline update

This chapter will serve as an overview of the updates required by the WASP reduction pipeline to process data collected using the new equipment. The main considerations during this process were; the effect of having a larger plate scale and optimisation to gather data on bright stars. The main changes were modifications of various acceptance limits and the size of the reduction apertures. These changes were mainly carried out by David Anderson (DRA) and myself while DRA was helping to familiarise me with the pipeline. We would consider what changes we thought were needed. I would then investigate the current performance of the pipeline using test reductions done on initial data sets gathered with the modified WASP-South instrument. Finally, we would look at the results of my investigations and make the most appropriate changes. While performing these updates we also found and fixed some bugs in the pipeline. Aside from the limit modifications and bug fixes, the reduction procedure is unchanged from that detailed in the previous chapter.

Changes to the pipeline were made over a period of a few months and several iterations. Often investigations into the effect of a change lead to the discovery of other changes that were needed. As such, I will not document a diary of the changes here but only the end result of the change and reasoning behind it.

3.1 Magnitude Limit

The need to change the pipeline magnitude limit was driven by practical observational reasons and considerations of the computational power required to preform data reduction. The purpose of the change in equipment was to observe brighter stars, thus the quality of data for dimmer stars became poorer. The plate scale of each camera increased leading to a greatly increased number of stars at fainter magnitudes. If the faint magnitude limit of the pipeline had remained unchanged much of the reduction would be dominated by poor quality data of dim stars.

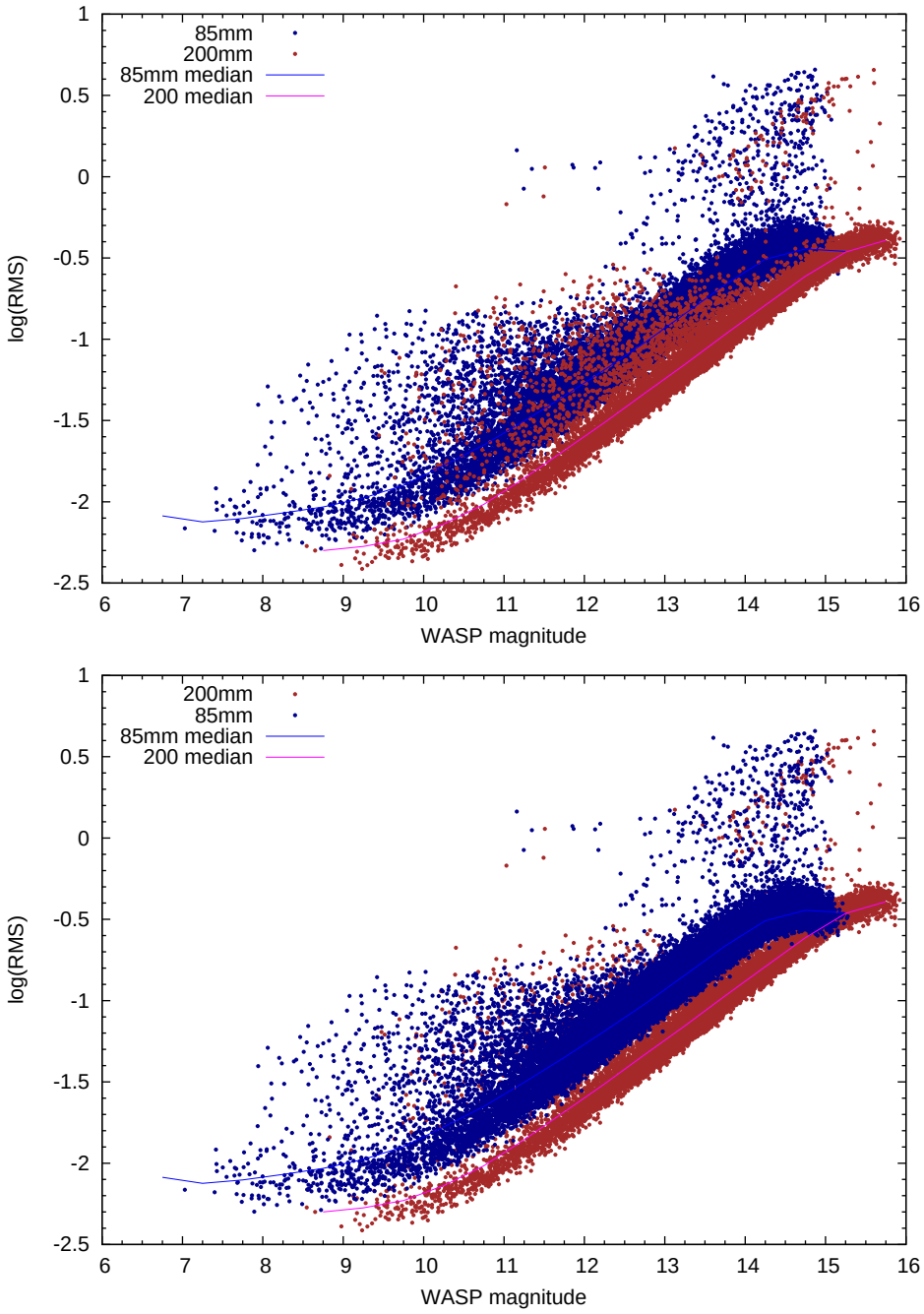

Figure 3.1: Graph of log(RMS) against WASP instrumental magnitude for two fields on two typical nights. Red points are from WASP-South using the old 200-mm lenses, blue points are from using the new 85-mm lenses. Each data point represents the variability of a single star in the field during a night of observation. Overplotted are median lines from bins 0.5 magnitudes wide; blue for 85-mm data, pink for 200-mm data. This graph includes all stars down to a USNO-B R2 magnitude of 15.

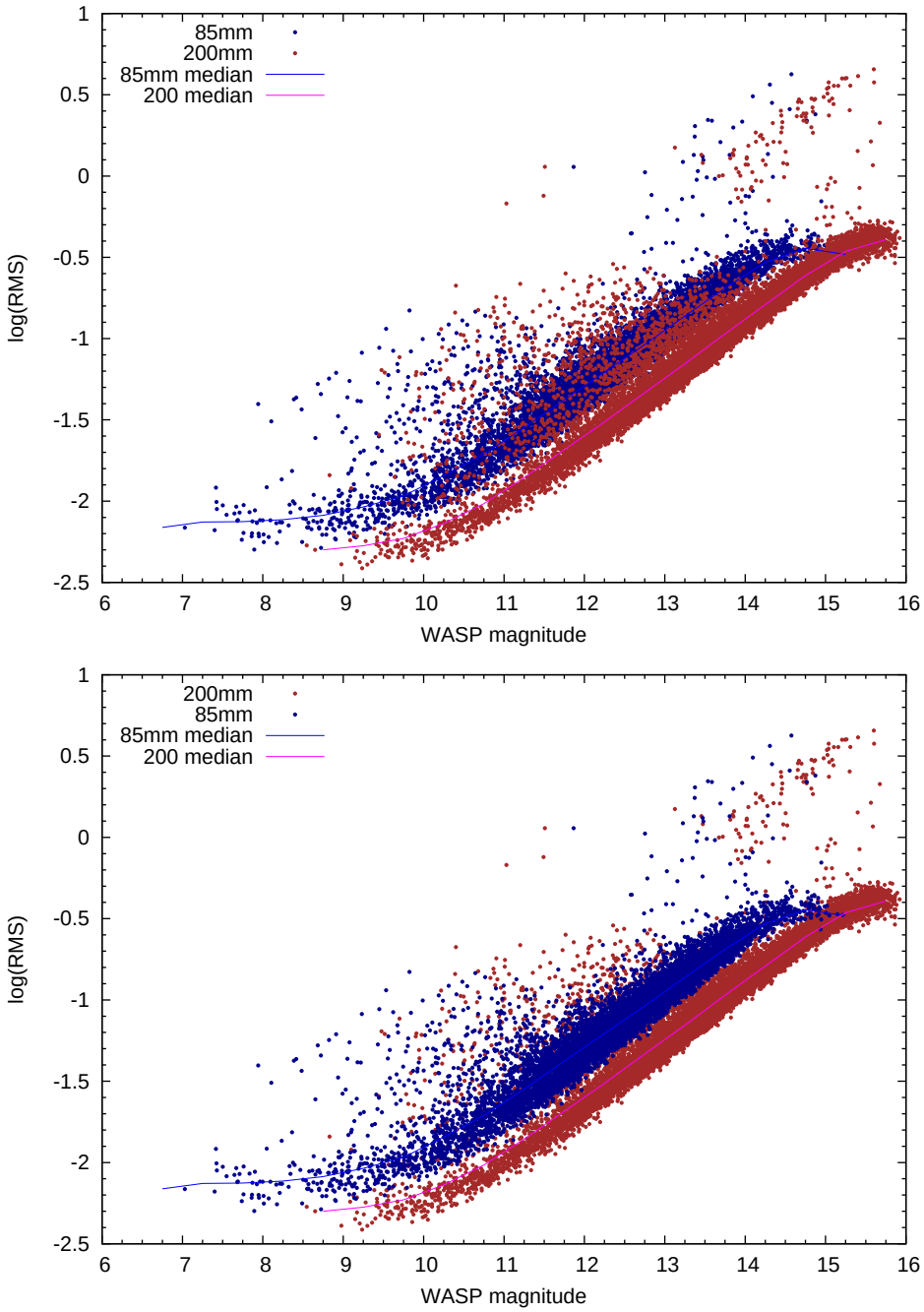

Figure 3.2: log(RMS) as a function of instrumental magnitude for same nights and fields as Fig. 3.1. Here a cut off of USNO-B R2 magnitude of 13 is used. There is a drop in median og(RMS) below WASP instrumental magnitude 12.

Figs. 3.1 and 3.2 are adapted from figures already output by the data reduction pipeline. They show how a night's photometric precision behaves as a function of magnitude. Both have been selected from a similar field with good quality data from a clear night that has been reduced using the unmodified version of the pipeline. Therefore, any differences should be due to the effects of the plate scale, filter and exposure time changes.

While the graphs have a similar shape the data from the new setup feature a plateau around magnitude 14. It is unlikely that the precision obtained on photometry of a magnitude 15 star is comparable to that of a magnitude 13 star, over a factor of 6 brighter. Therefore this plateau represents the limit at which the measurement of precision given by this graph becomes unreliable. Fig. 3.3 are the same results plotted in Figs. 3.1 and 3.2 with the magnitude converted from the WASP-South instrumental magnitude to the recorded USNO-B R2 catalogue magnitude. It shows a spread of rms for dimmer stars suggesting that this precision comes not from the expected star but a nearby, brighter, blended star. Cutting at a magnitude of 13 removes just over 75% of the stars in the example field. This reduces the number of stars for which no useful photometry can be obtained and the reduction in the number of stars per frame also reduces the time taken to process the data. This decision is also backed by my calculations from the previous chapter, where I show that we can expect precision limits to move brighter by about 2 magnitudes. The typical number of stars with cuts on various parameters can be found in Table 3.1

3.2 Aperture Choice

Photometry quality is dependent on the size of aperture used; the brighter a star is, the more easily the stellar point spread function (PSF) can be distinguished from the background level. For a brighter star the counts recorded in a larger aperture will be more dominated by the star than the background; the optimal aperture is larger. For dimmer stars the background dominates more easily and so a smaller

Table 3.1: Comparison of the number of stars per field observed with WASP-South before and after the lens change. The values given are the median and median square deviations for 108 fields observed with 200-mm lenses and 28 fields observed with the 85-mm lenses. Values have been rounded to the first significant figure of the median square deviation.

Stars in field	200-mm lens fields	85-mm lens fields
Total	53000 ± 20000	30000 ± 5000
WASP magnitude < 13	11000 ± 5000	22000 ± 5000
WASP magnitude < 9	80 ± 40	800 ± 200
Precision $< 1\%$	2000 ± 700	1000 ± 200

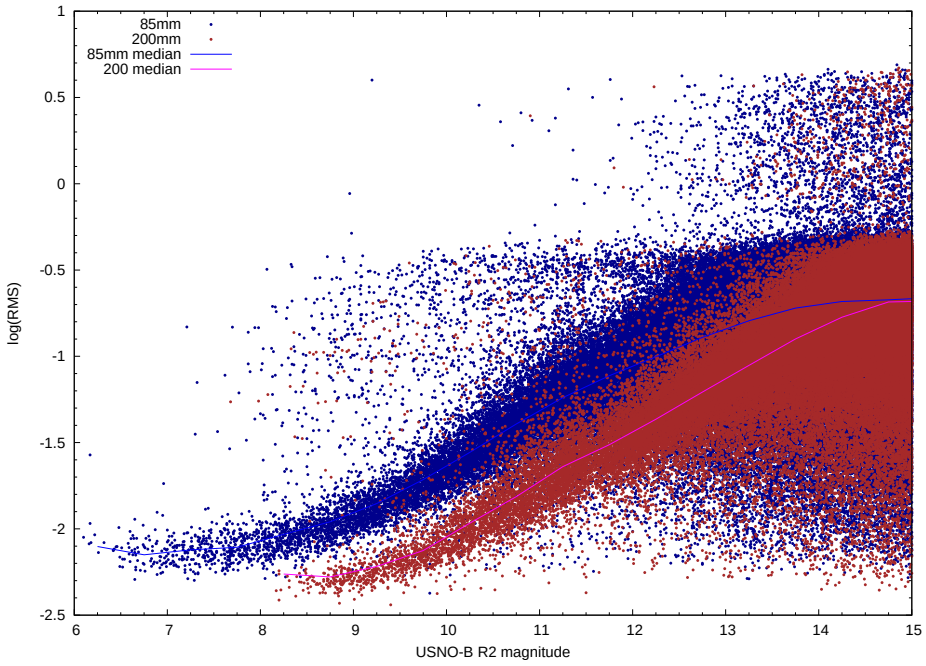

Figure 3.3: Log(RMS) vs USNO-B R2 catalogue magnitude for same nights and fields as Fig. 3.1.

aperture excludes the background variation more effectively; the optimal aperture is smaller (Naylor 1998). While it would arguably produce better photometry, the WASP pipeline has never used a variable aperture radius based on the brightness of the star to be measured. With our focus shifted to brighter targets I investigated what change to the reduction aperture size, if any, would be most effective.

The pipeline optimised for 200-mm lens data used a reduction aperture with a radius of 3.5 pixels with two apertures with radii of 2.5 and 4.5 pixels to assess blending. I investigated apertures of 2.5, 3, 3.5, 4, 4.5 and 5 pixels by reducing data using the old 3.5 $\pm$ 1 pixel apertures and a new set of 4 $\pm$ 1 pixel apertures. The behaviour of precision as a function of magnitude is shown in Fig. 3.4 for each aperture considered. The apertures behave as expected; larger apertures perform better than smaller ones for brighter magnitudes and vice versa. The medians are calculated for bins half a magnitude wide. An offset in zero-point magnitude calibration between different apertures can cause a shift along the x axis. This would result in an apparent change in precision, log(RMS), which could lead to an interpretation that an aperture is performing better or worse than it is in reality. The offset value is recorded in the pipeline logs for each field. To ensure comparability, I removed the offset applied to each individual reduction and applied the mean of the offsets all the results.

Fig. 3.4 shows that aperture radii of 4 pixels, 4.5 pixels and 5 pixels all perform similarly well at WASP instrumental magnitudes brighter than 9. However, the performance of the apertures with radii of 4.5 pixels and 5 pixels falls off more rapidly than the aperture with a radius of 4 pixels. While the performance of the aperture with a radius of 3.5 pixels falls off less rapidly than the one with a radius of 4 pixels, the improvement is minimal at instrumental magnitudes brighter than 10. The project's main focus is detecting planets orbiting bright stars, so we require better performance for brighter stars more than we need an aperture that performs optimally at all magnitudes. As a result, we decided to use a main reduction aperture radius of 4 pixels. The secondary apertures were kept at one pixel larger and smaller, i.e. radii of 3 pixels and 5 pixels.

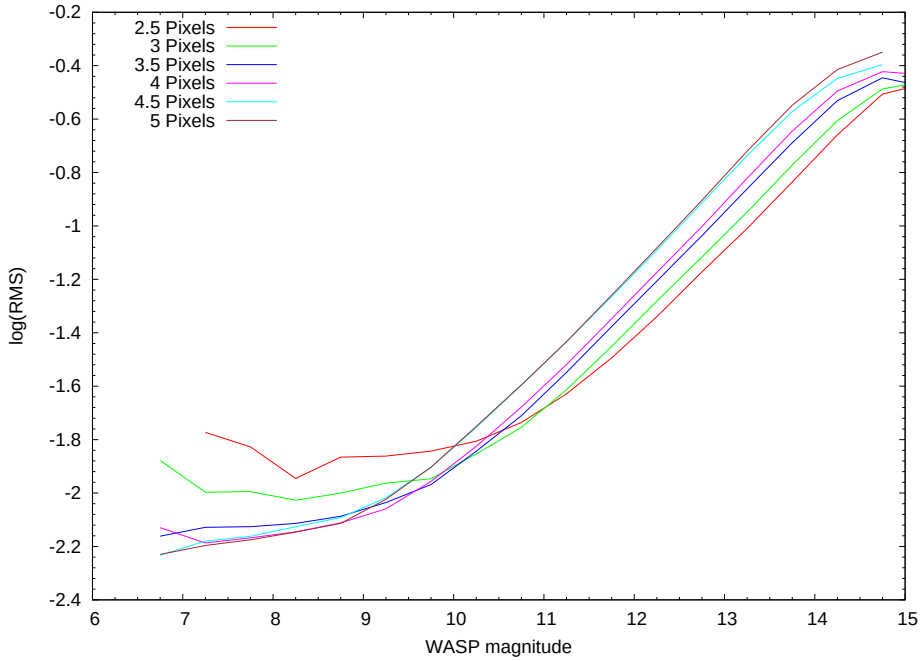

Figure 3.4: Graph showing RMS as a function of WASP instrumental magnitude after the switch to 85-mm lenses. Median lines computed from one good night for a field reduced using 6 candidate apertures. These results demonstrate the expected behaviour; larger apertures result in lower RMS scatter for brighter stars.

3.3 'Badsky' Rejection Limit

Before aperture photometry is performed the pipeline creates a model of the sky background flux. To assess only the background it places circular masks on the images at the positions of all the stars in the input catalogue. The mask radii are scaled proportional to the star's brightness. Solar system planets are also masked from the fields. If the χ^2 of the fit is high or a large proportion of the pixels are masked the frame is labelled with '.badsky' and not processed further. The purpose of this is to reject crowded frames or frames with cloud present that could affect the photometry. Fig. 3.5 shows the relationship between χ^2 and the ratio of unmasked-to-masked pixels for a field from a good night and a cloudy night. The new and old rejection limits are also shown. The data from the good night follows a coherent trend while the data from cloudy conditions does not. The old limits rejected data from the good night that appears consistent with the trend followed by the rest of the data from the good night. The previous rejection limits were a ratio of unmasked-to-masked pixels of 2 and a sky fit reduced χ^2 of 5. The shift in the limits now accepts this coherent data without accepting more cloudy data than before the change. The new limits are a ratio of 1 and a sky fit reduced χ^2 of 4. For comparison, using the old rejection limits, the poor quality night used in Fig. 3.5 would have had 1868 of its 6849 frames rejected. Using the new rejection limits 2111 of the 6849 frames from the poor quality night would be rejected. The new rejection limits are at least as stringent as the previous limits.

3.4 Bug Fixes

3.4.1 Catalogue Extraction

The catalogue extraction performed by wasp_extract_tycho2 and wasp_extract_usnob utilise a program called *SCAT* which is part of the WCSTools package (Mink 1997). The scripts construct queries which are then given as inputs to *SCAT* which performs

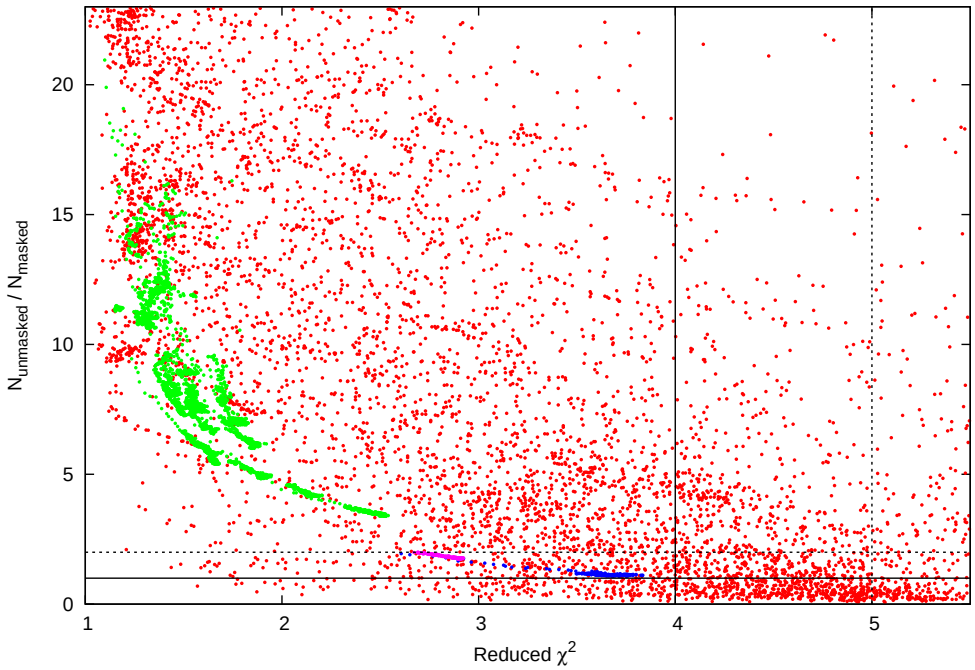

Figure 3.5: Sky background flux fit rejection limits used by original and modified versions of the WASP-South pipeline. Original limits (dashed lines) are a ratio of 2:1 (unmasked : masked pixels) and a reduced χ^2 of 5. New limits (solid lines) are a ratio of 1:1 and a reduced χ^2 of 4. Similar numbers of cloudy frames (red) are excluded using both limits. The new limits keep all data from a typical good night for all cameras (Green, purple and blue points). Formerly points from cameras 5 (purple) and 6 (blue) were rejected as too many pixels were masked in the sky fit.

the actual extraction. As an initial re-optimisation this was set to extract a square catalogue with sides 20° long in both RA and declination to account for the larger field of view of the 85-mm lenses compared to the 200-mm lenses. During tests a bug in the *SCAT* extraction was discovered that affected fields close to the poles. Instead of extracting a square, it would extract an annulus around the pole between two declinations. This would then trip a built in limit to the pipeline that flagged the field as too densely packed with stars to process. As a result all images from the field would not be processed. If not corrected for, this would have significantly affected the volume of data processed and available to search for transits. I attempted several solutions; writing a new extraction routine using python and the *Vizier* database and tiling multiple fields extracted by *SCAT*. Ultimately I found that extracting a single, oversized circular field with *SCAT* was simple and sufficient. The pipeline required some further adaptation to use circular catalogues but this caused little trouble.

3.4.2 Photometric Catalogue Read-in

I found a bug in the routine responsible for reading in the extracted USNO-B catalogue for use by the pipeline, 'wasp_getsbase'. The read-in routine was lacking a variable to read a star-galaxy separator flag used in the catalogue. As a result the flag values were read as stellar proper motion in RA while the proper motion in RA values were read as declination proper motion. The declination proper motions were never read.

Fortunately, the scale of this problem was very small and would have been even less pronounced with the new equipment. For example, given the plate scale of the new equipment the position of Barnard's Star[1] (Barnard 1916) would be offset by just over 4 pixels. Using a sample of $\sim$ 93500 stars from previously extracted catalogues, only 8 would have shifted by more than 1 pixel. Only one would have shifted by more than 2. From the same sample with the old equipment the problem may have been more marked but still minor; 177 stars would be offset by more than a pixel, 21 by

[1]Barnard's Star has the highest observed proper motion

more than 2 pixels and 3 by more than 3 pixels. As the star-galaxy separator was not used at any point in the pipeline to solve this I added a dummy variable to the code so that the proper motions were loaded correctly.

3.5 Conclusion

In this chapter I have detailed the changes made to the automated reduction pipeline for use with data collected using the modified WASP-South instrument. From the point of view of data analysis, the only required change was to the size of photometric reduction aperture. This change will help to maximise the pipeline's photometric precision for our primary targets, bright stars. The main advantage to the modification of the catalogue brightness limit is the reduction in computing time required to process new data and subsequently to search it for transits. The 'badsky' rejection limit changes and bug fixes are important modifications as they will limit the erroneous rejection of useful data, thus maximising the volume of useful data collected.

4 Determination of system parameters

4.1 Introduction

Transiting planets are valuable targets for exoplanet studies because we can accurately measure R_p/R_* from the transit light curve. When combined with the planet mass from radial velocities (RVs) we can calculate the planet's bulk-density (or average density) which leads to an initial constraint on the planet composition. A bulk-density can tell us if we expect a planet to becomprised mostly of gas or mostly of rock e.g. Fig 4.1. Of course, this constraint is only as good as the measurement with the least precision. The less precise a radius or mass measurement is, the poorer the constraint the bulk density can provide. While radii tend to be more easy to determine to high precision they contribute to the density as R^{-3} thus contributing more to the uncertainty. Large planets, discovered by ground-based surveys like WASP, can be followed up relatively easily from the ground with more specialised equipment as described in chapter 2. The smallest planets have so far been discovered by space-based surveys like the *Kepler* or CoRoT satellites. Space-based surveys inherently have much better precision than ground based surveys which is passed on to the derived planet radii. Due to their higher precision, space-based surveys can find smaller planets orbiting dimmer stars which can make their masses difficult to measure. Using the data available at exoplanet.eu[1] for transiting planets; 9% of the entries have a mass determined to 10% precision or better. This falls to 5% for a precision of 5% or better. Most of these have masses greater than $0.8M_{Jup}$. For comparison, 39% of planets have radii determined to 10% or better which drops to 16% for precisions of 5% or better. These are more evenly distributed across the range of known planet radii. This is illustrated in Fig. 4.2

A precise measurement of R_p/R_* is imperative to other areas of investigation as well. Transmission spectroscopy boils down to measuring the wavelength dependency

[1]Retrieved May 2016

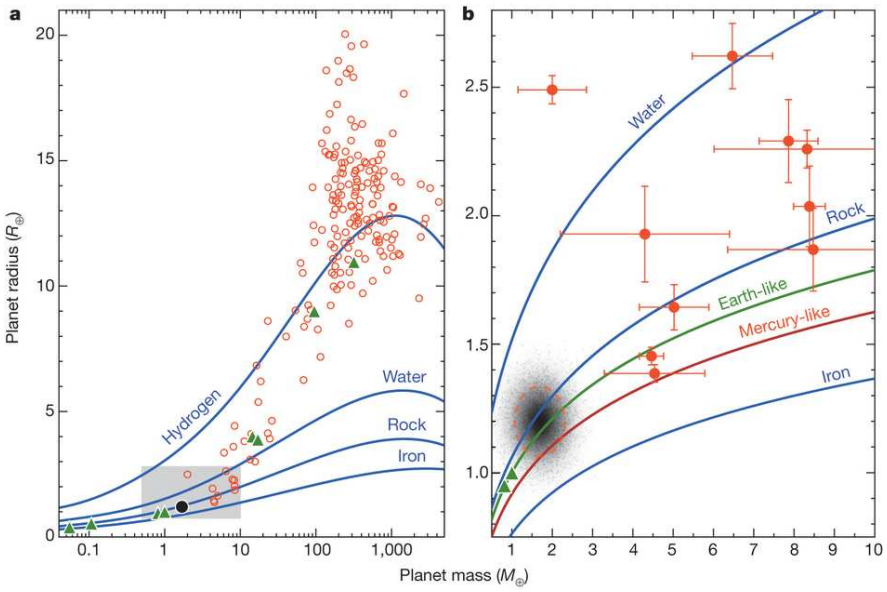

Figure 4.1: Masses and radii of exoplanets (orange circles), solar system planets (green triangles) and Kepler-78 b (left: black circle, right: black distribution). Solid lines show the theoretical relations for different compositions. The right hand figure corresponds to the grey shaded area in the left. Figure 2 from Howard et al. (2013).

of R_p/R_*. This holds regardless of the resolution, be it very low (spectrophotometry) or high (true spectroscopy performed during a transit). Spectrophotometry is best searching for broad features. An interesting application of this is observing a planet's Rayleigh scattering slope. This can be used to put a constraint on a planet's atmospheric composition by measuring its mean molecular mass. Alternatively, in the case where a planet's mean molecular mass can be inferred from other observations or assumed (e.g. hydrogen dominated gas-giants), the method could be used to measure the planet mass in cases where RVs are ineffective e.g. WASP-33 (de Wit & Seager 2013). Transmission spectroscopy looks for elemental and molecular species by comparing spectra taken in transit to those taken out of transit. Signatures of sodium (Redfield et al. 2008), magnesium (Vidal-Madjar et al. 2013) water, methane and carbon dioxide (Swain et al. 2009) have been detected in this way.

Analysis of planetary occultations needs R_p/R_* to calculate the planetary day-

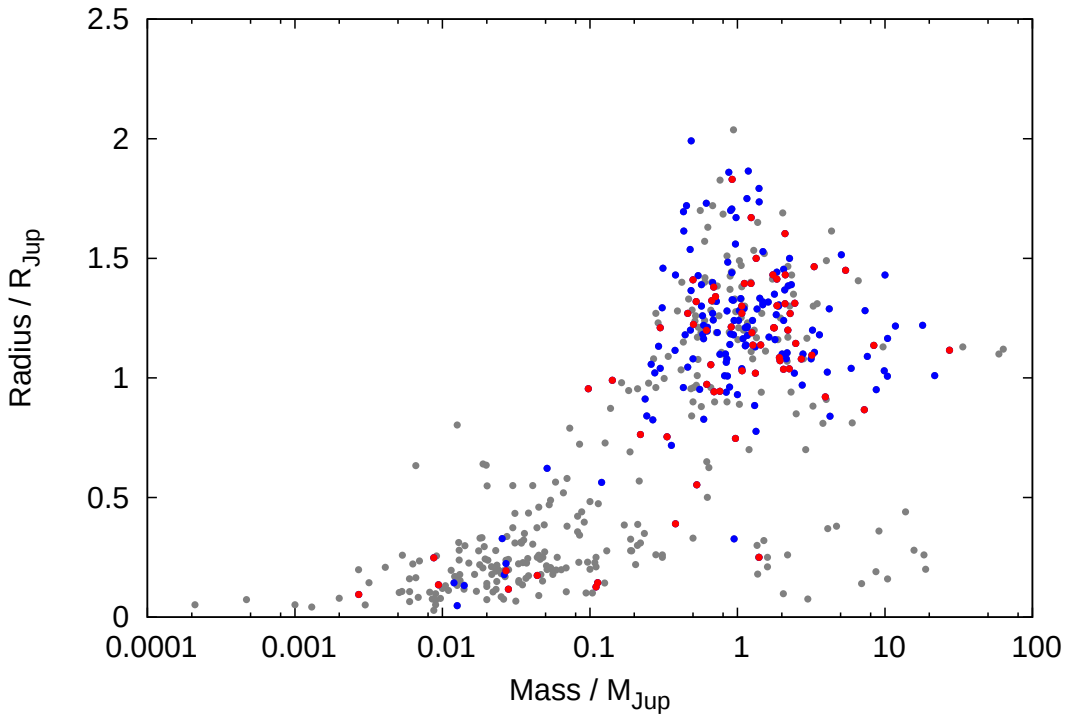

Figure 4.2: Mass-radius distribution of transiting planets. All planets recovered from the exoplanet.eu database are grey. Planets with masses and radii with uncertainties of 10% or less are blue while those with uncertainties of 5% or less are red. Data retrieved May 2016.

side temperature:

$$\frac{F_{\rm day}}{F_*} \approx \frac{B_\lambda(T_{\rm day})}{B_\lambda(T_*)} \left(\frac{R_p}{R_*}\right)^2 \tag{4.1}$$

These measurements then feed into atmospheric models which can suggest planetary pressure-temperature profiles and compositions. Extreme precision is needed for occultation depths to distinguish between degenerate models, thus lower radius uncertainties are beneficial. An accurate estimate of the planet-star radius ratio is also needed for the analysis of the RM effect.

In order to determine R_p/R_*, and other system parameters, we fit models to our observations. A very effective way to do this is via χ^2 minimisation. This statistic is a measure of how well a model fits observations and can be calculated taking into account the associated uncertainties. This means, the lower an observation's uncertainty the more weight it is given when considering if the model fits and vice versa. I have already mentioned how this is used to find periodic signals in the chapter 2. In that case the search program constructs a grid of possible models and finds the best fit; the one with the lowest χ^2. However, methods like this run into issues when models have a "high-dimensionality" (Tegmark et al. 2004), i.e. lots of parameters to fit. Large numbers of parameters make compiling grids very computer time intensive. While it would find the best fitting model, it typically takes too long to do so. What is desirable is a way to use the strength of χ^2 minimisation that is faster than compiling a grid. This can be done by throwing a little chaos into the mix. The Markov Chain Monte Carlo (MCMC) technique is how we choose to do this. An MCMC could be summarised as a (somewhat guided) random walk around the parameter space constrained by the data and the model(s) we fit to it.

4.2 The Bayesian background of MCMC

This section will reasonably closely follow the framework of Ford (2005, 2006) to explain the idea behind why Markov Chain Monte Carlo analysis is effective. Bayesian

inference, used as part of MCMC, is a powerful tool for exploring unknown quantities using observable quantities. For instance, consider two events x and y that we can treat in a statistical way such that $p(x)$ is the probability of event x and $p(y)$ is the probability of event y. So long as the two events are not completely independent we can work out how the probability of one event occurring is modified if we know the other occurs like so:

$$p(x|y) = \frac{p(x \cap y)}{p(y)} = \frac{p(x,y)}{p(y)} \tag{4.2}$$

Thus, the probability of event x *given that* event y has occurred, $p(x|y)$, is the ratio of the probability that both events occur, $p(x \cap y)$, and the probability of event y irrespective of x. This *joint probability distribution* of two events, scalars or even vectors of variables can also be written as $p(x,y)$. If we have only the joint probability, $p(x,y)$, we can find the *marginalised probability distribution* of one set of variables by integrating $p(x,y)$ with respect to the other $p(y) = \int p(x,y)dx$. Thus, because $p(x,y) = p(x|y)p(y) = p(y|x)p(x)$ can write the conditional probability from above as:

$$p(x|y) = \frac{p(x,y)}{\int p(x,y)dx} = \frac{p(y|x)p(x)}{\int p(y|x)p(x)dx} \tag{4.3}$$

The utility of this becomes more obvious if we identify y with a set of parameters we can measure from observational data, $\mathbf{d}$, and x with a set of unobservable model parameters, $\mathbf{m}$.

$$p(\mathbf{m}|\mathbf{d}) = \frac{p(\mathbf{m},\mathbf{d})}{\int p(\mathbf{m},\mathbf{d})d\mathbf{m}} = \frac{p(\mathbf{d}|\mathbf{m})p(\mathbf{m})}{\int p(\mathbf{d}|\mathbf{m})p(\mathbf{m})d\mathbf{m}} \tag{4.4}$$

This lets evaluate the likelihood of our model given our observations, $p(\mathbf{m}|\mathbf{d})$, if we can evaluate the likelihood of making our observations given our model, $p(\mathbf{d}|\mathbf{m})$, and know the marginalised probability distribution of our model, $p(\mathbf{m})$.

The difficulty here lies in performing the integration as the number of observable and model parameters can quickly become very large. Instead of performing a full integration we use MCMC to generate a stochastic chain of parameter values, $\mathbf{m}_i$ sampled from the probability distribution we want to know about which, for now we

will call $f(\mathbf{m})$. We can construct this chain by specifying a starting point in the form of an initial set of values, $\mathbf{m}_0$ and a *transition probability*, $p(\mathbf{m}_{n+1}|\mathbf{m}_n)$. In order for this to be a valid method of exploring $f(\mathbf{m})$, the transition probability must result in a chain which is:

- not periodic.
- able to reach any (possible) set of parameters from any other starting set (irreducible).
- able to return from any end set of parameters to the previous set (reversible).

Reversibility is ensured by using the Metropolis-Hastings algorithm which governs the generation of each new $\mathbf{m}$:

$$p(\mathbf{m}'|\mathbf{m}_n) = q(\mathbf{m}'|\mathbf{m}_n)\alpha(\mathbf{m}'|\mathbf{m}_n) \tag{4.5}$$

We construct the transition probability function by using a *candidate transition probability function*, $q(\mathbf{m}'|\mathbf{m}_n)$, and an *acceptance probability*, $\alpha(\mathbf{m}'|\mathbf{m}_n)$, that is based on how well the candidate parameters, **m'** fit the data. If they are a better fit $\mathbf{m}_{n+1}$ is set to $\mathbf{m}'$, otherwise $\mathbf{m}_{n+1}$ is set to $\mathbf{m}'$ with the probability reached by $\alpha(\mathbf{m}'|\mathbf{m}_n)$. If $\mathbf{m}'$ is not accepted, $\mathbf{m}_{n+1}$ is set to $\mathbf{m}_n$ and a new $\mathbf{m}'$ generated.

As the acceptance is dependent on the fit of the model to the data, what we're really exploring with $f(\mathbf{m})$ is the probability of making the observations given various model parameters,$p(\mathbf{d}|\mathbf{m})$ using a known $p(\mathbf{m})$. Thus, using $f(\mathbf{m})$ we arrive at:

$$f(\mathbf{m}) = p(\mathbf{d}|\mathbf{m}) = p(\mathbf{m})p(\mathbf{m}|\mathbf{d}) \tag{4.6}$$

4.2.1 Procedural Application

When applying MCMC to specific problems we have some choices to make. These involve the functions $p(\mathbf{m})$, $q(\mathbf{m}'|\mathbf{m}_n)$ and $\alpha(\mathbf{m}'|\mathbf{m}_n)$. Good choices for these can greatly increase the efficiency of the MCMC and poor choices can lead to a procedure

that looks like it works but has hidden biases. An obvious, simplifying choice given equation 4.6 is to chose model parameters that have a flat prior probability distribution, $p(\mathbf{m}) = 1$. It is for this reason that eccentricity, e, the argument of periastron, ω, line of sight stellar spin velocity, $V \sin i_*$, and spin-orbit angle, λ are determined via $\sqrt{e}\sin\omega$, $\sqrt{e}\cos\omega$, $V_{sur}\sin\lambda$ and $V_{sur}\cos\lambda$ where, $V_{sur} = \sqrt{V \sin i_*}$. It also helps to use parameters that are directly related to observed features in the observed data, e.g., transit width, since this tends to reduce correlations between the parameters. Errors associated with observations are assumed to follow a Gaussian distribution. If the data are described by the proposed model parameters, then the probability of generating those observations for given model parameters, $p(\mathbf{d}|\mathbf{m})$, should be proportional to $e^{-\chi^2/2}$, where χ^2 is used as the measure of how well the model fits. The acceptance probability function, $\alpha(\mathbf{m}'|\mathbf{m}_n)$, considers the ratio of the probability of the proposed model parameters with that of the previous set. So;

$$\alpha(\mathbf{m}'|\mathbf{m}_n) = \min\left\{\exp\left(\frac{\chi^2_{\mathbf{m}} - \chi^2_{\mathbf{m}'}}{2}\right), 1\right\} = \min\left\{\exp\left(\frac{\Delta\chi^2}{2}\right), 1\right\} \tag{4.7}$$

Our candidate transition probability function, $q(\mathbf{m}'|\mathbf{m}_n)$, generates a new value, m_i', for each parameter in our model, m_i, using the uncertainty on the model parameter, σ_i, the scale factor, β, and a number drawn from the unit normal distribution $N(0,1)$, as below:

$$m_i' = m_i + \sigma_{m_i}\beta N(0,1) \tag{4.8}$$

The uncertainty on each σ_i is derived in one of two ways. The uncertainty of an observational constraint can be used such as the formal uncertainty on values obtained from stellar spectra for example $T_{\rm eff}$ or metallicity. Alternatively, if there is no good estimate for a parameter known a priori, it is calculated during an initial MCMC chain referred to as "burn-in". During burn-in a rough approximation of the uncertainty is given initially. Every 10 steps the acceptance rate is calculated. If too many proposals are accepted or rejected during each interval the mean and variance of accepted values

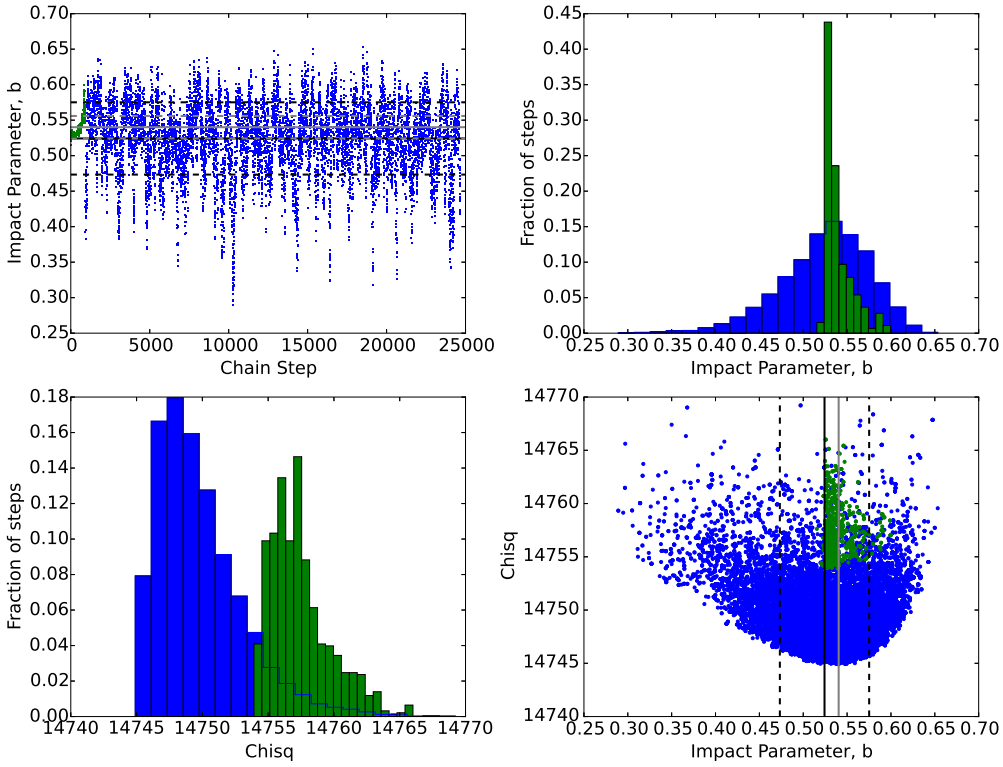

Figure 4.3: Graphs showing distributions of the impact parameter and the fit χ^2 for an MCMC analysis. Data relating to the burn-in chain is green, data relating to the main chain is blue. Top-left: Accepted value of the impact parameter for each step of an MCMC. Black/grey solid lines show the median value of the main/burn-in chain. Corresponding dotted lines are one standard deviation of the distribution. Top-right: Histogram of the values from the MCMC chains. Bottom-left: Histogram of the fit χ^2 values from the MCMC. Bottom-right: Plot of step impact parameter value against χ^2 value. The solid/dotted black lines show the median/one standard deviation of the impact parameter values. The grey line is the impact parameter value corresponding to the step with the smallest χ^2.

for each parameter is calculated. The standard deviation is then used as the new uncertainty. This is repeated until a set number of burn-in steps have been accepted or until a consistent acceptance rate of ~ 0.25 (Gelman et al. 2003) is reached. For each parameter, the mean and standard deviation of the distribution of accepted values is used to initialise a second, main, MCMC chain. The mean is used as the new initial value while the standard deviation is used as σ_i for that chain unless an uncertainty from an observational constraint is used. Derived parameters are calculated from the jump parameters at every step and recorded within the program. The final value for each derived parameter is the mean of its distribution of values generated in the second chain. Its upper and lower uncertainties are calculated from the values at the 15.85% and 84.15% percentile limits of its posterior distribution. The same procedure is used for the jump parameters.

The final values output by the MCMC are therefore not "best fitting" parameters but well-fitting parameters with an estimate of their uncertainties. Figure 4.3 illustrates this process with one jump parameter from the analysis of the WASP-123 system presented in chapter 6. This parameter is one without an initial uncertainty estimate so the burn-in chain is used to estimate the value which is then used in the main chain. The histogram then illustrates how the final value is obtained. The χ^2 vs value plot shows that the final value is not the same as the value for which the χ^2 is smallest. The histogram of the χ^2 distributions also illustrates this. The "best-fit" value according to the χ^2 can be unclear where there is numerical noise and/or a wide range of solutions with very similar χ^2 close to the minimum. The mean of the distribution is more robust, but does have the disadvantage that the model corresponding to the quoted parameters might not be a good fit.

Figure 4.4 is a corner plot and can be used to see how the posterior distributions correlate with one another. Most of the distributions appear as circles when both axes have the same scale relative to the parameter standard deviations, showing that the parameters are independant. There is a strong correlation between the systemic radial velocity and the radial velocity semi-amplitude. Weaker correlations can also be seen: transit duration with transit epoch, depth and impact parameter; impact parameter

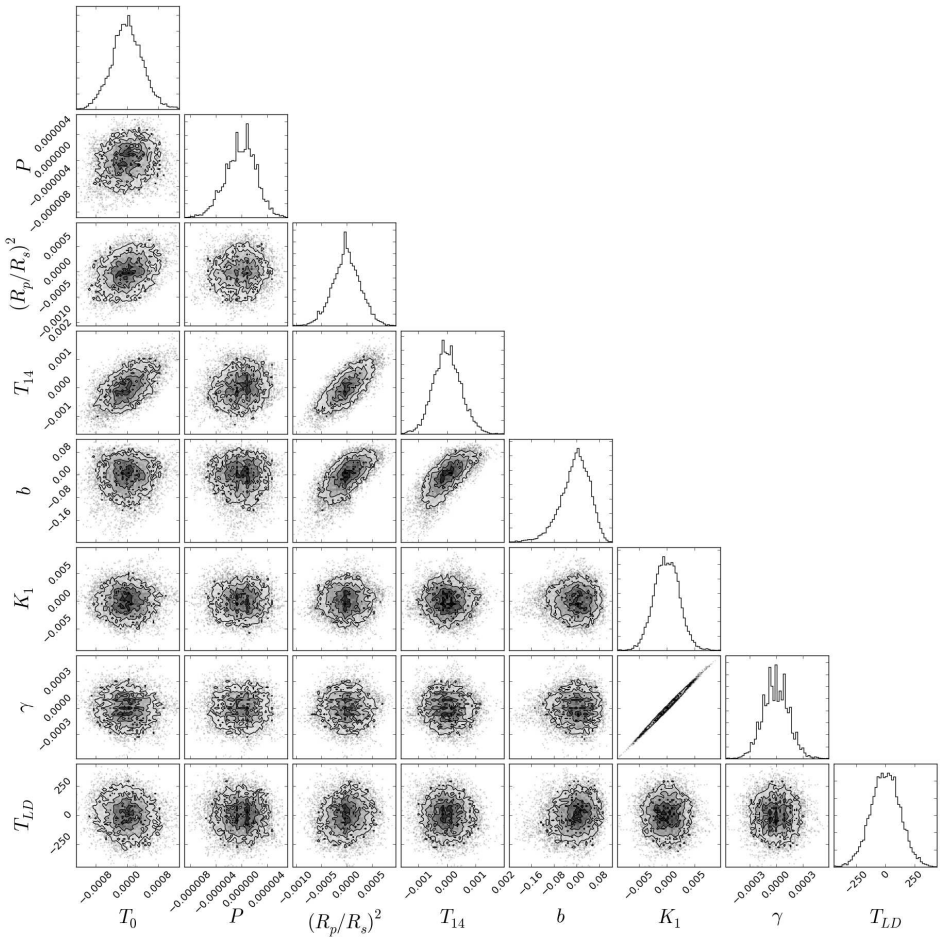

Figure 4.4: Plots showing the relationships of various jump parameters T_0, P, $(R_P/R_*)^2$, T_{14}, b, K_1, γ, [Fe/H], $T_{\rm LD}$, from the analysis of WASP-123 presented in chapter 6. The distributions have had the mean value of the analysis subtracted. Plots were prepared with a modified version of triangle.py by Foreman-Mackey et al. (2014)

Jump Parameter	Definition
T_0	A reference epoch of mid transit.
P	Orbital period
T_{14}	Transit duration
ΔF	Transit depth
b	Impact parameter
$T_{\rm eff}$	Stellar effective temperature. (Sometimes called $T_{\rm L-D}$)
[Fe/H]	Stellar surface metallicity.
K	Radial velocity semi-amplitude.
$\sqrt{e}\cos\omega$	e - eccentricity
$\sqrt{e}\sin\omega$	ω - argument of periastron
γ	Systemic velocity
$\dot{\gamma}$	Drift in systemic velocity
$V_{sur}\sin\lambda$	V_{sur} - $\sqrt{V\sin i_*}$ where $V\sin i_*$ is the line of sight stellar spin velocity.
$V_{sur}\cos\lambda$	λ - Spin-Orbit obliquity
M_*	Stellar mass

Table 4.1: List of the jump parameters that make up **m** and are perturbed at each step of the MCMC. M_* is either computed from $T_{\rm eff}$, [Fe/H] and ρ_* from an empirical calibration or randomly sampled from a Gaussian prior with specified mean and standard deviation from an independent estimate.

also shows a correaltion with transit depth.

4.3 Parameters

The parameters which comprise **m** and have new values proposed at each step according to equation 4.8 are called jump parameters. The jump parameters are summarised in Table 4.1. We use these to calculate the derived parameters. Some are less complex to derive physical parameters from than others.

Seager & Mallén-Ornelas (2003) showed that the scaled stellar radius, R_*/a, impact parameter, b, and stellar density, ρ_*, can be derived directly from the shape of a transit lightcurve. Other parameters and their definitions are illustrated in Figs. 4.5

and 4.6. Our MCMC calculates various parameters using the simplified equations they detail in their section 3.3. The main assumption behind these is that the semi-major axis is much larger than the stellar radius, $R_* \ll a$. As a key parameter in these equations is the radius ratio, R_p/R_* we must calculate this ratio from the proposed parameters. For complete transits the portion of light blocked is governed by the ratio of the area of the planetary and stellar disks. Thus, we can use the transit depth, ΔF:

$$\frac{R_p}{R_*} = \sqrt{\Delta F} \tag{4.9}$$

This does not hold for the case of grazing transits; transits where the planet disk is never completely on the stellar disk. In these cases we use instead the following expression in which the limb of the star crossed by the planet is approximated using a straight line:

$$\frac{R_p}{R_*} = \frac{b - 1 + \sqrt{(1-b)^2 + 8\Delta F}}{2} \tag{4.10}$$

In order to take into account eccentricities we modify the relations set out in Seager & Mallén-Ornelas (2003). The geometry in that paper assumes a circular orbit, thus the planet-star separation at transit is a. We will use a_t to denote the planet-star separation at transit for an orbit that accounts for eccentricity. Thus to calculate R_*/a_t we require P, T_{14}, b, e and ω:

$$\frac{R_*}{a_t} = \frac{\pi T_{14}}{P\sqrt{(1 + R_p/R_*)^2 - b^2}} \frac{1 + e\sin w}{\sqrt{1 - e^2}} \tag{4.11}$$

where:

$$\frac{a}{a_t} = \frac{1 + e\sin w}{\sqrt{1 - e^2}} \tag{4.12}$$

If we use values in terms of astronomical units (AU), solar masses ($M_\odot$) and radii ($R_\odot$), and the stellar mass is much larger than the planetary mass we can use Kepler's 3rd law to calculate the stellar density in terms of the density of the Sun:

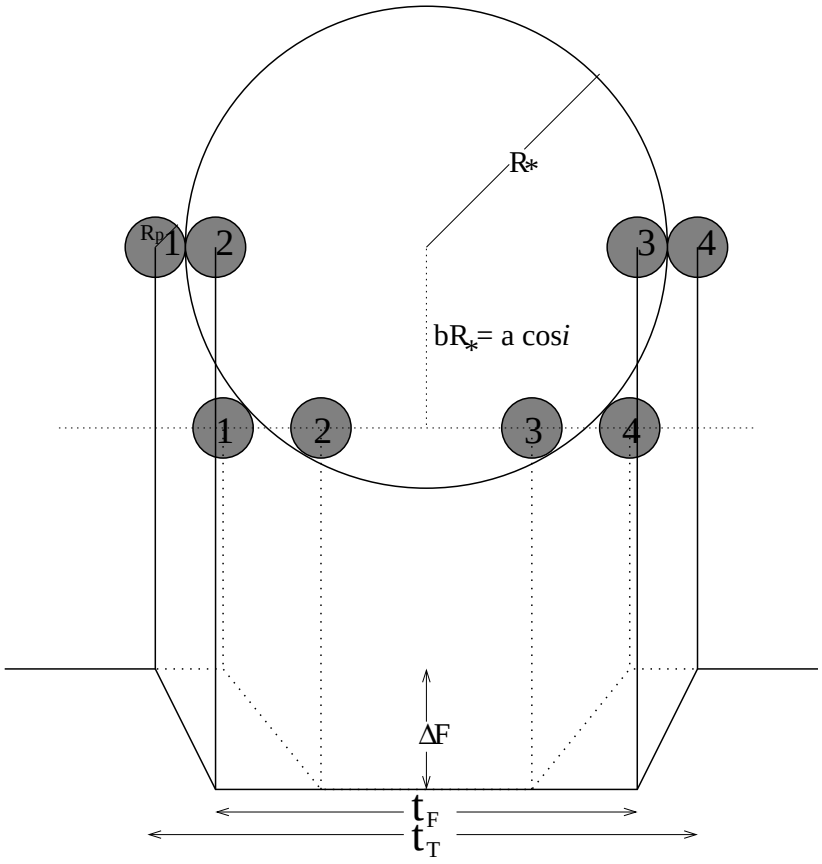

Figure 4.5: Diagram showing definitions of various parameters dictating the shape of the transit lightcurve. R_*, R_p, ΔF, b, a, and i have the same meaning as in the main text. t_T corresponds to T_{14} while t_F is the duration of totality, T_{23}. T_{23} is not a parameter used by our MCMC but is calculated from the final output. Two lightcurves are illustrated corresponding to two impact parameters, $b = 0$ and $0 < b < 1$. Figure 1 from Seager & Mallén-Ornelas (2003).

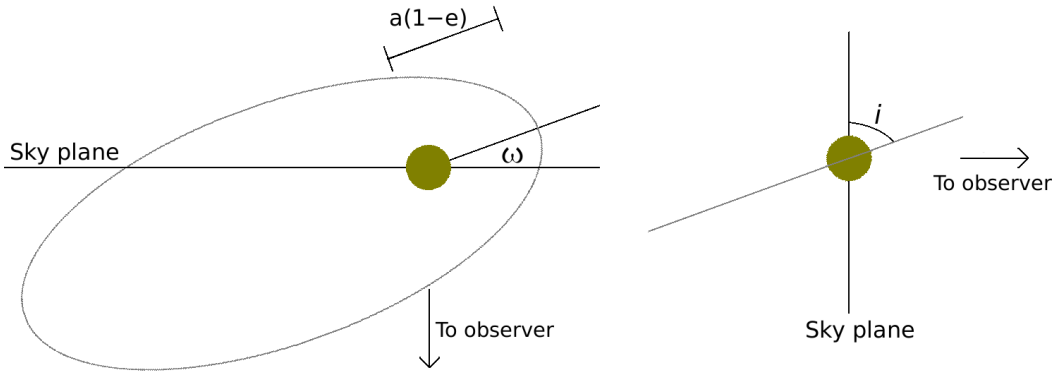

Figure 4.6: View from above and from the side of an eccentric orbit, inclined to the observer. The diagram shows the definitions of the argument of periastron, ω, star-planet distance at perihelion in terms of semi-major axis, a and eccentricity, e, and the orbital inclination, i.

$$\rho_* = \left(\left(\frac{R_*}{a_t}\right)^3 P^2\right)^{-1} = \left(\left(\frac{R_*}{a_t}\right)^3 \left(\frac{a^3}{M_*}\right)\right)^{-1} \approx \frac{M_*}{R_*^3} \tag{4.13}$$

If we have chosen to use an empirical mass calibration we then use ρ_*, with the effective temperature, $T_{\rm eff}$, and metallicity, [Fe/H], to generate the host star mass. If we have a mass estimate from another source then a mass will have been drawn like the other jump parameters. With this we calculate the mass dependent parameters a and R_* and as a result the planet radius, R_p:

$$a(\mathrm{AU}) = \sqrt[3]{P(\mathrm{yr})^2 M_*(M_\odot)} \tag{4.14}$$

$$R_*(R_\odot) = \frac{R_*}{a_t} a(\mathrm{AU}) \times 215.09... \tag{4.15}$$

$$R_p(R_{\rm Jup}) = R_*(R_\odot) \frac{R_p \times 9.73...}{R_*} \tag{4.16}$$

Here, the radius of the planet is given in units of the equatorial radius of Jupiter ($R_{\rm Jup}$). Equations 4.13 and 4.15 are acceptable so long as the eccentricity is small. To

determine the system inclination to the observer's line of sight, i, we calculate $\cos i$ using b, R_*/a_t and a_t/a determined from the planet's eccentric anomaly in transit:

$$\cos i = \frac{bR_*}{a_t} \tag{4.17}$$

Finally, with i, a and P the mean velocity of the planet, V_p, is calculated and used with the proposed semi-amplitude, K, and M_* to determine the mass of the planet, M_p:

$$M_p = \frac{K}{V_p - K} M_* \tag{4.18}$$

Orbital eccentricity, e, argument of periastron, ω, stellar surface velocity, V_{sur} and the inclination of the planet orbit to the stellar spin axis, λ are determined from their jump parameters ($\sqrt{e}\sin\omega$, $\sqrt{e}\cos\omega$, $V_{sur}\sin\lambda$ and $V_{sur}\cos\lambda$). The initial value of V_{sur} is calculated from the $V\sin i_*$ derived from spectra as described in section 2.5.1.2. A summary of the derived parameters can be found in Table 4.2. It is these parameters, along with the timing parameters T_0 and P, that are used in the calculation of the models fit to the data.

Some parameters that can be derived from the jump parameters are also calculated, including planetary density, ρ_p, planetary surface gravity, $\log(g_p)$ and planetary equlibrium temperature, T_{eq}. Both ρ_p and $\log(g_p)$ come from the derived mass and radius while T_{eq} is calculated using:

$$T_{eq} = T_{eff}\sqrt{\frac{R_*}{2a}} \tag{4.19}$$

4.4 Models

4.4.1 Radial Velocities

Detailed derivations of the model we use to fit radial velocity observations to data can be found in various sources e.g. section 1.3 of Beauge, Ferraz-Mello & Michtchenko

Derived Parameter	Definition
M_*	Stellar mass.
R_*	Stellar radius.
M_p	Planet mass.
R_p	Planet Radius.
i	System inclination to observer's line of sight.
e	Eccentricity.
ω	Argument of periastron.
V_{sur}	Projected stellar surface velocity.
λ	Inclination angle of planetary orbit to stellar spin.
T_{eq}	Equlibrium temperature of the planet asuming zero albedo.

Table 4.2: List of the derived parameters that are used in the models fit to the available data.

(2008). We make the assumption that the system we observe contains a primary object, the host star, and a secondary object, the planet, in a Keplerian orbit that is not subject to significant forces from further unseen objects. For our model of $V(t)$, the radial velocity as a function of time, we need; γ, the systemic velocity, K, the radial velocity semi-amplitude, e, the orbital eccentricity and ω the argument of periastron. These are related as:

$$V(t) = \gamma + K(e\cos\omega + \cos(\nu(t) + \omega)) \tag{4.20}$$

The true anomaly, $\nu(t)$, is the angle formed by the star and planet between some reference time, T_0, and the observation time. We convert from times to ν by:

$$M(t) = \frac{2\pi}{P}(t - T_0) \tag{4.21}$$

$$E(M) = M + e\sin(E) \tag{4.22}$$

$$\nu(E) = \arctan\left(\frac{\sqrt{1+e}}{\sqrt{1-e}}\tan\frac{E}{2}\right) \tag{4.23}$$

The RV is calculated using the model for each observation and the χ^2 of the fit is calculated. During the analysis we can choose to perform a linear regression on the residuals of this fit to the data to look for a long term RV trend, $\dot{\gamma}$. We can use this to place a lower limit on the mass, M_2, semi-major axis, a_2, and inclination, i_2, of unseen companions (Montet et al. 2014):

$$\dot{\gamma} \leq (6.57\mathrm{m\,s^{-1}\,yr^{-1}}) \left(\frac{M_2}{M_{\mathrm{Jup}}}\right) \left(\frac{a_2}{5\mathrm{AU}}\right)^{-2} \sin i_2 \tag{4.24}$$

At present our MCMC code is not designed to deal with the case of systems hosting multiple planets detectable by RV observations. Assuming the planets are sufficiently non-interacting, such that our initial assumption holds, this can be modelled as the sum of multiple $V(t)$ functions as described above. We could then subtract the model of the other planets to fit separately with our MCMC.

4.4.2 Planetary Transit

Our MCMC code uses the non-linear limb darkening law of Claret (2000, 2004) with the models of Mandel & Agol (2002). As the WASP project is primarily concerned with Jupiter-like planets orbiting F-, G- and K-stars we use the small-planet approximation found in Mandel & Agol (2002) section 5. The full treatment can be found in their paper.

Transit lightcurves are calculated by considering the change in area covered by an opaque disk as it transits a limb-darkened star. Much like the radial velocities, for each data point in a transit lightcurve the model is used to compute an expected flux, F, normalised to the out of transit level:

$$F = 1 - \frac{I^*(z)}{4\Omega}\left[p^2 \cos^{-1}\left(\frac{z-1}{p}\right) - (z-1)\sqrt{p^2-(z-1)^2}\right] \tag{4.25}$$

Here, z is the radial distance from the centre of the stellar disk normalised to the stellar radius and p is the planet-to-star radius ratio, R_p/R_*. Both of these are illustrated in Fig. 4.7. $\Omega = \sum_{n=0}^{4} c_n(n+4)^{-1}$, where n indicates the index of the

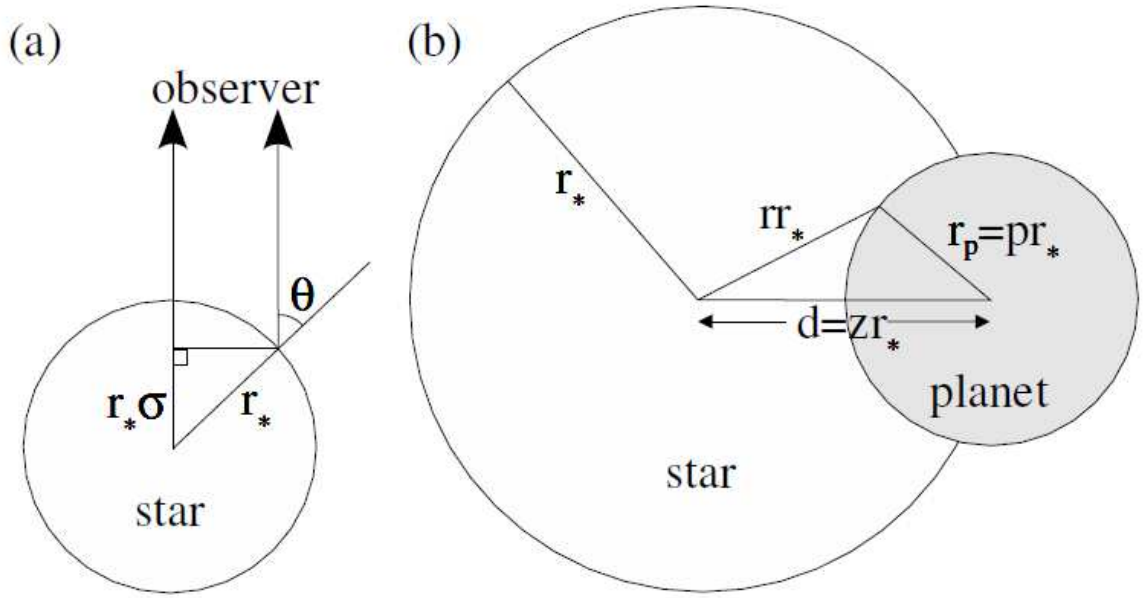

Figure 4.7: a) Star as seen from above showing how θ is defined for the purposes of limb-darkening. θ is the angle between the normal of the stellar surface and the observer. b) Transit geometry face on. Figure 1 taken from Mandel & Agol (2002)

associated non-linear limb darkening coefficient and $c_0 = 1 - c_1 - c_2 - c_3 - c_4$. $I^*(z)$ is the intensity of a point at z on the star. In equation 4.25, $I^*(z)$ is calculated via:

$$I^*(z) = (1 - (z-p)^2)^{-1} \int_{z-p}^{1} \left[1 - \sum_{n=1}^{4} c_n (1 - \mu^{n/2}) \right] 2r dr \tag{4.26}$$

The parameter $\mu = \cos\theta$ where θ is the angle between the observer and the normal to the stellar surface, illustrated in Fig. 4.7. Equation 4.25 assumes that the planet is small in comparison to the star, $p \lesssim 0.1$, and that the surface brightness under the planet is constant. Using the timing information, T_0 and P, and the physical orbital parameters a, i, e and ω, we can calculate z for each epoch for which we have data. When used with the limb darkening parameters and equation 4.25, we can compute the model flux and calculate the χ^2 of the fit to the photometry.

4.4.2.1 Limb-darkening

The limb-darkening parameters themselves we explore using the $T_{\rm eff}$. For each set of photometric data that we supply to the MCMC we also supply a table of limb-darkening parameters extracted from the tables of Claret (2000, 2004). These are specific to the photometric band of the observations, the stellar metallicity and stellar micro-turbulent velocity derived from spectra. The limb-darkening coefficients are interpolated according to $T_{\rm eff}$ for each proposed set of parameters and contribute to the χ^2 of the transit lightcurve.

4.4.3 Rossiter-M$^{\rm c}$Laughlin Effect

There are multiple models and methods available in the MCMC we use to fit the Rossiter-M$^{\rm c}$Laughlin effect. A full explanation of all of these is beyond the scope of this chapter. I will look at the model of Hirano et al. (2011) as I use this model in a later chapter.

In the Hirano et al. (2011) model the shape of a stellar spectral line as a function of its velocity shift, v, relative to the centre of the absorption line, $\mathcal{F}_*(v)$, is calculated as:

$$\mathcal{F}_*(v) = -S(v) * B(v) \tag{4.27}$$

Where $S(v)$ is the intrinsic stellar line shape neglecting stellar rotation, macro-turbulence and convective blue-shift. $B(v)$ is the broadening kernel that includes rotation and macro-turbulence. $B(v)$ is calculated by integrating the Doppler-shift component of the stellar surface caused by both rotation and macro-turbulence, $\Theta(v)$ over the limb-darkened stellar disk:

$$B(v) = \iint_{\rm stellardisk} \frac{1 - u_1(1-\cos\theta) - u_2(1-\cos\theta)^2}{\pi(1 - u_1/3 - u_2/6)} \times \Theta(v - x\Omega\sin i)\frac{dxdy}{R_*^2} \tag{4.28}$$

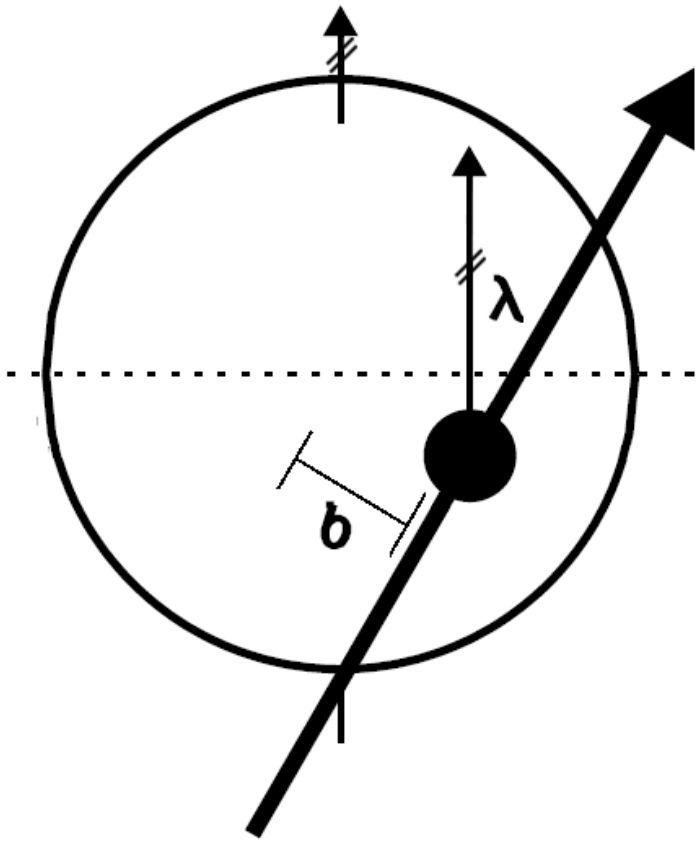

Figure 4.8: Diagram showing how λ and b define the path a planet takes across the stellar disk. Heavily modified from Gaudi & Winn (2007) figure 2 showing a spin-orbit angle of 60°and b of 0.5.

where u_1 and u_2 are quadratic limb-darkening parameters and Ω is the stellar angular spin velocity.

Then the line shape during a transit is calculated by considering the portion of the spectrum that is blocked, $F_p(v)$:

$$F_p(v) = -S(v) * B'(v) = -FS(v) * \Theta(v - v_p) \tag{4.29}$$

where $v_p \equiv X\Omega \sin i$, and is the velocity of the element on the stellar surface blocked by the planet[2] calculated using the planetary position X on the stellar disk. X is calculated for each in transit RV datum using the proposed λ, impact parameter and orbital ephemeris. Thus the in-transit line shape is:

$$F_{\text{transit}}(v) = F_*(v) - F_p(v) \tag{4.30}$$

which can be used to calculate the expected velocity offset. A full treatment of this can be found in Hirano et al. (2011).

4.4.4 Planetary Occultations

The model used for secondary eclipses (planetary occultations) is conceptually very simple. The planet is taken to be a uniformly bright disk. Kepler's laws are used with the proposed model parameters to calculate the orientation of the planet and star in the observer's line of sight at the epoch of each secondary eclipse datum. The fraction of the planet visible is calculated from this. The drop in brightness expected is the fraction of the disk that is occulted multiplied by the proposed eclipse depth.

The full procedure is more complicated if data from the *Spitzer* space telescope is used due to its intra-pixel sensitivity variations, documented by Knutson et al. (2008) and references there-in. These are modelled as set out in Charbonneau et al. (2008) (and others), but are not discussed further here.

[2]The sub-planet velocity.

4.4.5 Other Constraints

We place Bayesian priors on other parameters for which we have observational constraints. Both the stellar effective temperature, $T_{\rm eff}$, and surface metallicity, [Fe/H], can be measured via spectroscopy and added to the total value of the χ^2 as:

$$\chi^2_i = \frac{(m'_i - m_0)^2}{\sigma_i^2} \tag{4.31}$$

The observed [Fe/H] is used as a prior like this if we choose to use the MCMC's empirical mass calibration (Southworth 2011b) as our stellar mass constraint. If instead we constrain the mass by another method such as BAGEMASS (Maxted, Serenelli & Southworth 2015), we give that, with its variance as a prior in the same way. We can also choose to penalise models that deviate from a main-sequence mass-radius relationship for the star by calculating the expected radius for the proposed mass ($R_* = M_*^{0.8}$; Kippenhahn, Weigert & Weiss 2012 Ch. 22) and propagating the uncertainty on the stellar mass to find σ_{R_*}.

4.5 Other analysis methods

While the range of effects that can be fit using our MCMC is broad, it is not exhaustive in its scope. Our MCMC takes all the available data and uses it as a whole to reach conclusions on a system's parameters. Some effects, like searching for wavelength dependence in the planet radius, require lightcurves to be analysed individually. In these cases we reach a global solution using all the available data and then model transits individually or in ensembles that suit our purposes; e.g. grouping lightcurves by observation band.

4.5.1 Timing Variations

Timing variations fall into three categories: transit timing variations (TTVs), transit duration variations (TDVs) and period change. To study these effects the parameters

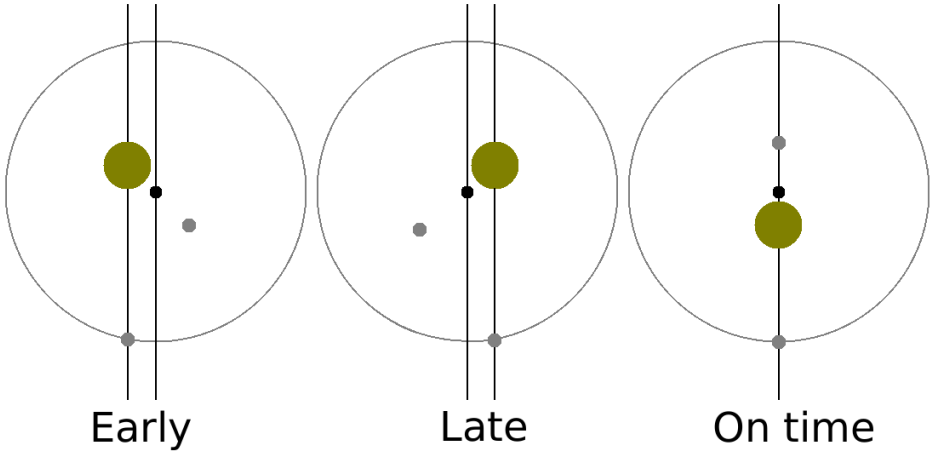

Figure 4.9: Diagram showing transit time changes due to a planet on an orbit interior to that of a transiting planet. Recreated following Figure 1 from Agol et al. (2005). The yellow circle is the host star, the grey circles are planets and the black circle indicates the barycentre of the star and inner planet.

of interest from the analysis of each individual lightcurve are the time of mid-transit and the transit duration.

With TTVs the times of mid-transit differ periodically from those predicted by the ephemeris produced by our global analysis. They occur if the planet and star positions relative to each other are subtly different from transit to transit, see Fig 4.9. This can indicate the presence of extra objects in the system as they orbit a common barycentre with the star and known planet. As they orbit the barycentre they cause an offset in the relative positions of the star and transiting planet at transit. Moons can also cause this effect as the transiting planet orbits the planet-moon barycentre. At some phases of this orbit it will lead the moon causing transits to happen earlier, sometimes it will lag delaying transits.

With TDVs the duration of transits is observed to differ from one to the next. This is another indicator of the presence of moons. If the moon is moving opposite to the planet-moon system's motion around the star during transit then the planet will transit more quickly. If the moon is moving with the system's orbital motion the planet

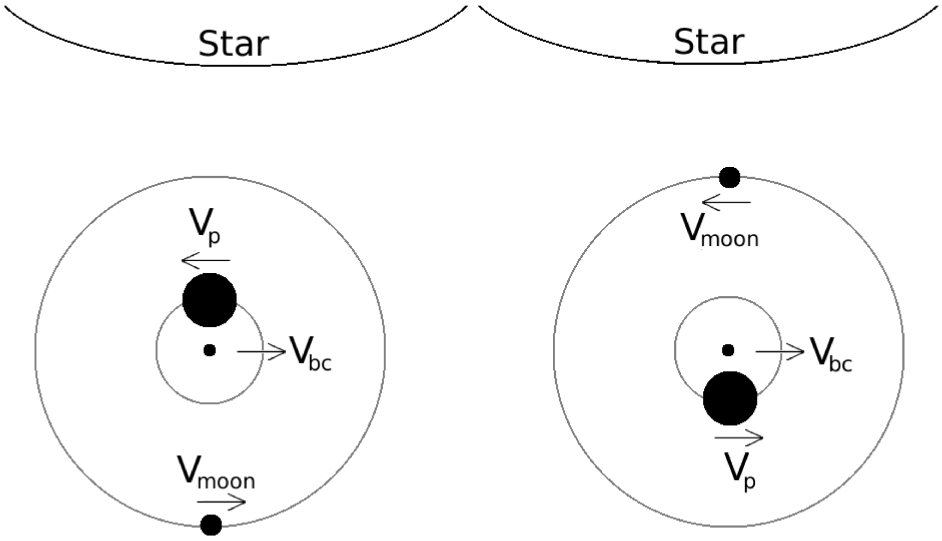

Figure 4.10: Diagram showing a planet-moon system resulting in transit duration variations. The planet-moon barycentre moves with some velocity, V_{bc}. At different points in the orbit the planet velocity, V_p, around the barycentre will add to V_{bc}, resulting in a shorter transit. At other times it will subtract from V_{bc} resulting in a longer transit.

will transit more slowly (cf Fig 4.10). See Kipping et al. (2012) for more information on how these effects are analysed.

The most obvious form of period change is orbital decay, where the time between the transits shortens with each successive orbit. This is the most straight forward to model and interpret. A simple χ^2 regression using equation 4.32 is all that is needed (cf Murgas et al. 2014; Chen et al. 2014).

$$T_{mid}(n) = T_0 + nP + n(n-1)\dot{P} \tag{4.32}$$

The time of mid-transit of the nth transit, T_{mid}, after a reference epoch, T_0, can be calculated using the period, P, and the decay rate, $\dot{P}$.

4.5.2 Depth Dependence On Wavelength

To study the dependence of the transit depth on wavelength we can group the lightcurves available to us by observation band and analyse the ensemble. There are two ways we can do this. As transits are grouped by their observation band, they can use the same limb darkening coefficients and should arrive at the same transit depth. Thus they can be analysed together in the MCMC allowing us to use all the data at once to inform the model parameters. However, the transit depth of each lightcurve is sensitive to the presence of star-spots. Variable coverage of the star by unocculted star-spots would cause variation in the depths between each lightcurve. An alternate method, therefore, is to model the transits individually and find weighted mean of the depths from each band afterwards. This allows us to mitigate the effect of transit-to-transit depth variations. The interpretation of these results, like that of occultation depths, requires the use of atmospheric models.

4.6 Useful Additions

As the previous section shows, the MCMC we use does not completely cover all the avenues of investigation that are open to us using transit observations. Adding individual jump parameters for each lightcurve to allow for depth, transit duration and mid-time variation would make it easier to routinely check for atmospheric signatures or the presence of timing variations. However, this would be offset by the need to account for the added complexity to the models.

4.6.1 RV Jitter

A less involved addition is that of the "jitter" term to the RV modelling as a jump parameter. Currently we add jitter manually to account for excess scatter in the RVs. This involves adding jitter in quadrature with the uncertainty on each measurement

such that the reduced χ^2 of the fit to the model is unity. This does not allow us to explore or optimise the parameter with the same robustness as other parameters so we cannot be as confident about its uncertainty or variation. In order to do this we would need to modify the calculation of χ^2 during the MCMC to penalise over-large jitter values. Without this modification the χ^2 of the spectroscopic orbit would be artificially reduced as the uncertainties are over estimated. In their paper on improving the efficiency of MCMCs for exoplanet analysis Ford (2006) describe an MCMC that uses:

$$q(m_i'|m_i) = \frac{1}{\sqrt{2\pi\beta_i^2}} \exp\left(-\frac{(m_i' - m_i)^2}{2\beta_i^2}\right) \tag{4.33}$$

as a candidate transition probability function. Thus, $p(\mathbf{d}|\mathbf{m})$ for an RV model becomes:

$$p(\mathbf{d}|\mathbf{m}) = \prod_k \frac{1}{\sqrt{2\pi}\sigma_k} \exp\left(-\frac{(d_{k,m}' - d_k)^2}{2\sigma_k^2}\right) \tag{4.34}$$

where d_k is an observed velocity at a given time using a given spectrograph, $d_{k,m}$ is the predicted velocity according to the model parameters $\mathbf{m}$, and σ_k is the associated uncertainty. The acceptance probability function, $\alpha(\mathbf{m}'|\mathbf{m}_n)$, is still the ratio between the proposed and previously accepted $p(\mathbf{d}|\mathbf{m})$. In the case where σ_k is just the observational uncertainty $\sigma_{k,obs}$, the acceptance probability is unchanged as the factor outside the exponent cancels. If an aditional source of uncertainty, σ_+, is introduced, i.e. the unknown jitter, then the uncertanty becomes $\sigma_k^2 = \sigma_{k,obs}^2 + \sigma_+^2$ and the ratio is modified:

$$\frac{p(\mathbf{d}|\mathbf{m}')}{p(\mathbf{d}|\mathbf{m})} = \prod_k \frac{\sqrt{\sigma_{k,obs}^2 + \sigma_+^2}}{\sqrt{\sigma_{k,obs}^2 + \sigma_+'^2}} \exp\left(-\frac{1}{2}\left[\frac{(d_{k,m}' - d_k)^2}{2\sigma_k'^2} - \frac{(d_{k,m} - d_k)^2}{2\sigma_k^2}\right]\right) \tag{4.35}$$

The part inside the exponent becomes the familiar $\Delta\chi^2$, so models that have a larger value of χ^2 are penalised. Meanwhile the pre-factor penalises models with a larger value of σ_+. This avoids the additional, unknown uncertainty artificially increasing

the acceptance of poorly fitting models. This has not yet been implemented as it would require changing how all of the jump parameters are generated and acceptance probabilities are handled rather than just the parameter for the RV fit. Ford (2006) note that the inclusion of an unknown uncertainty like this can improve the speed at which an MCMC explores a given parameter space by "smoothing out" local minima.

4.6.2 Small Planet Approximation

Some current and near-future transit survey missions are specifically targeting smaller stars. The idea is that, for a given photometric precision, the same transit depth associated with a smaller host star results in a smaller planet. M-dwarfs in particular are being targeted as part of the K2 mission using the *Kepler* satellite and the Next Generation Transit Survey (NGTS). While the goal is small planets, hot-Jupiter type planets are likely to be detected too. These would pose a problem for our MCMC in its current form as the small planet approximation assumes $p \lesssim 0.1$. For instance, an inflated Jupiter ($R_p = 1.5R_{Jup}$) orbiting a $0.5R_\odot$ star would have $p \approx 0.3$. Fig. 4.11 illustrates the deviation between the small planet approximation and the full treatment of Mandel & Agol (2002) in three scenarios. The scenarios are approximated by a $1.5R_{Jup}$ planet orbiting a G0, K3 and M0 star. The magnitude of the deviations are most pronounced at ingress and egress. The maximum difference is $\approx 0.03\%$ for the G0-host, $\approx 0.2\%$ for the K3-host and $\approx 0.7\%$ for the M0-host. This deviation is not detectable from the ground for larger stars. However, the deviations shown for the K3-host are marginally detectable while those of the M0-host are well within the realms of detectability for follow-up lightcurves.

4.7 Conclusion

We have looked at the theory of MCMC and the models we use to characterise exoplanet systems. We have considered the application and some of the limitations of this method.

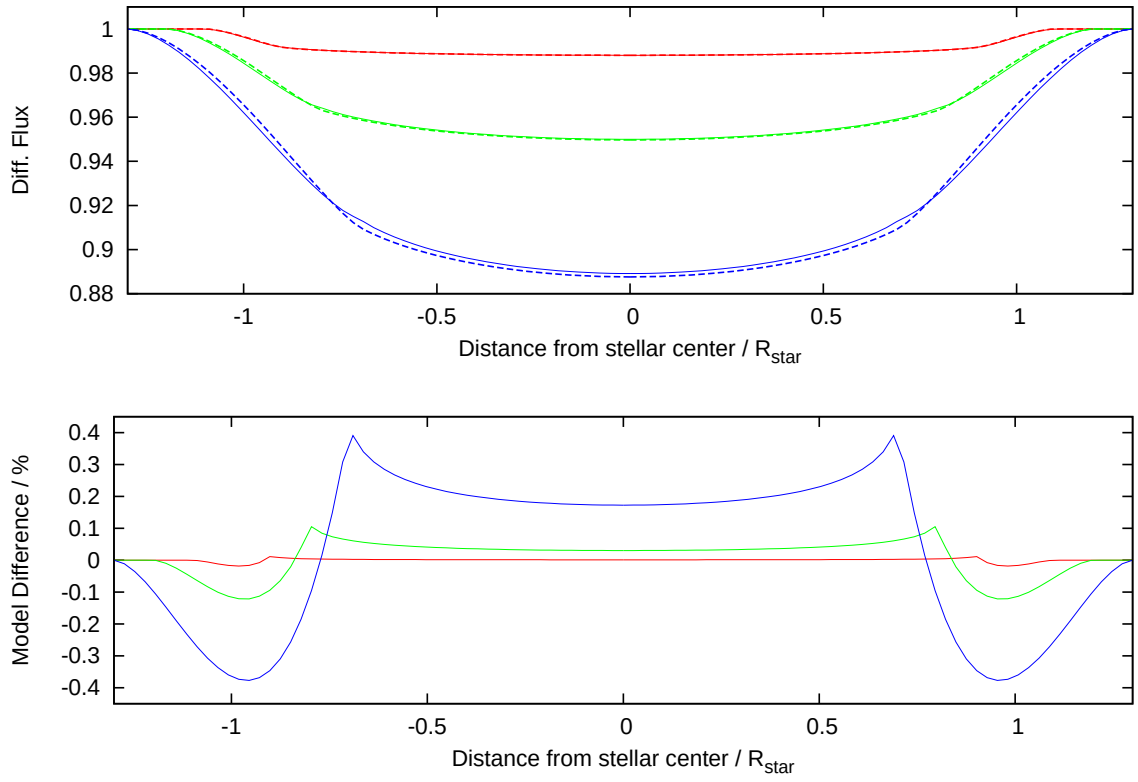

Figure 4.11: Top: Limb-darkened transit models using the equations from Mandel & Agol (2002). Solid lines correspond to the full treatment while dotted lines use the small planet approximation. Bottom: Difference between the models computed using the full treatment and small planet approximation. Both: The red models uses $p = 0.1$ with limb-darkening parameters of a G0-star. The green models uses $p = 0.2$ with limb-darkening parameters of a K3-star. The blue models use $p = 0.3$ with limb-darkening parameters of an M0-star. Discrepancies between the models are most apparent at ingress and egress and with larger p.

In the next two chapters we will apply the techniques to the confirmation and further characterisation of new and known systems.

5 New data and Updated parameters of 7 WASP planets.

5.1 Introduction

The diversity of hot-Jupiter systems naturally leads some to be repeatedly and closely investigated while others remain largely ignored. Various factors can contribute to the preference for some systems: inherent brightness of the host star is a strong factor (e.g. HD209458; Charbonneau et al. 2000); something that makes the planet particularly odd like the short periods of WASP-43 and WASP-103 (Hellier et al. 2011; Gillon et al. 2014); a scarcity of other examples at the time of the planet's discovery (e.g. GJ3470 b; Bonfils et al. 2012, GJ1412 b; Charbonneau et al. 2009). This discrimination can be unfortunate as apparently un-interesting systems can harbour further discoveries. For example, WASP-47 b was initially pronounced entirely typical for a hot-Jupiter (Hellier et al. 2012). While this may remain true for the planet itself, the system has been shown to be quite atypical for one hosting a hot-Jupiter. Two more close-in planets have recently been serendipitously discovered with photometry from the *Kepler* satellite (Becker et al. 2015) and a further, massive planet in a distant orbit has been found from dedicated radial velocity monitoring of the system (Neveu-VanMalle et al. 2016). These discoveries show that there can be reward for further investigation of apparently unremarkable systems.

A lack of intermediary study can frustrate further follow up of "uninteresting" systems e.g. WASP-57 which was recently found to be transiting around 30 minutes earlier than the published ephemeris predicted (Southworth et al. 2015). If the initial discovery data and early follow-up are taken close together, the resulting short baseline can introduce inaccuracies to further study for which transit timings are important.

Rossiter-McLaughlin (RM) observations benefit from accurate contact point timings and an accurate ephemeris is essential to observing the effect. The initial discovery of WASP-42 (Lendl et al. 2012) missed such an observation because of an inaccurate

ephemeris. Recent interpretations of the distribution of spin-orbit alignments in hot-Jupiter systems suggest that tidal realignment plays a role in systems with cooler host stars (Winn et al. 2010a). WASP-42 occupies an as-yet unexplored area of parameter space and as such a measurement of the spin-orbit alignment of the system could have proved highly informative (see our discussion of WASP-42). The exoplanet transit database and contributions of amateur astronomers can be a useful resource in cases where timings are desired but unknown. However, even supplemented by these, coverage can prove patchy and some lightcurves lack sufficient accuracy.

In this chapter we perform a global analysis using archival spectroscopy, photometry and new photometry of 7 WASP planets. These 7 planets were chosen primarily for their observability during the time available at the Danish Telescope. We make general improvements to ephemerides and take another look at some systems that have had no investigation since their original publication. *Transits of several other stars were observed during the run that have been used in other studies (WASP-87, WASP-108, WASP-109; Anderson et al. 2014, WASP-41; Neveu-VanMalle et al. 2016). David Anderson and I planned and performed the observations made with the Danish Telescope. I performed the image correction and data reduction of the data from the Danish Telescope for the systems in this chapter and the papers cited. The TRAPPIST data in this chapter were planned, observed and reduced by Michael Gillon and Laetitia Delrez. The data analysis and interpretation in this chapter were done by myself while that of the cited papers were performed by their respective authors.*

5.2 Observations

Details of all new observations presented here are given in Table 5.1. We made observations with the Danish 1.54-m telescope in La Silla, Chile using the DFOSC instrument. This provided us with a field of view of $13.3' \times 13.3'$ and a pixel scale of 0.39 arcsec/pixel. All our observations with the Danish Telescope used an R-band filter. Some exposures suffered from a known issue where the shutter sticks preventing it from

opening properly. We discarded the affected images prior to analysis. In addition to these observations we obtained five dark frames 200 seconds in length, 20 bias frames and 18 twilight flat fields. We took flats on the night beginning 2013-04-19.

We also used TRAPPIST, a remotely operated 0.6-m telescope also located at La Silla, Chile. The telescope has a $22' \times 22'$ field of view and a pixel scale of 0.64 arcsec/pixel (Gillon et al. 2011b). The observation of WASP-24 on the night of 2013-05-21 used an R filter and all observations of WASP-46 used blue-blocking filter ("BB") except for the night of 2011-05-07. The remainder of the observations used an I+z filter.

As standard procedure, when scheduling and weather permitted, we included time before and after each transit to establish a baseline brightness. To maximise the duty cycle we defocused the telescope and, in the case of the Danish Telescope, operated in windowed mode. The windowing mode allowed us to selectively read out an area of the CCD and so reduce our overall dead time.

Table 5.2 summarises the sources of the archival lightcurves used in the analysis. The new lightcurves will be made available via CDS.

5.2.1 Reduction

We created master calibration frames from the median combined and appropriately corrected calibration images as detailed in a previous chapter. We cut sections of these to match the windows used in observations of targets. We made our master calibration frames, corrections and final reductions using standard *iraf* routines.

We created master comparison lightcurves using different ensembles of comparison stars of similar brightness to the target and different aperture sizes. We divided the raw target lightcurve by these comparison star lightcurves and selected the combinations that appeared to have the lowest scatter for use in our analysis. In the case of data from the Danish Telescope we removed the sporadic points caused by the shutter issue before use in the analysis. The TRAPPIST data reduction procedure is similar (Gillon et al. 2011a; Gillon et al. 2012) without the need to screen sporadic points.

Table 5.1: Observations taken of systems presented.

Date	Source	N.Obs. / Filter	Exp. Time (sec)
WASP-24			
2011-06-14	TRAPPIST	I+z	10
2013-04-18	Danish	R	80
2013-05-21	TRAPPIST	R	10
WASP-31			
2011-01-08	TRAPPIST	I+z	30
2011-05-04	TRAPPIST	I+z	30
2012-02-07	TRAPPIST	I+z	25
2012-02-14	TRAPPIST	I+z	25
2012-05-16	TRAPPIST	I+z	25
2013-04-25	Danish	R	60
2014-04-21	TRAPPIST	I+z	20
WASP-36			
2013-04-18	Danish	R	150
WASP-37			
2011-03-03	TRAPPIST	I+z	40
2011-03-28	TRAPPIST	I+z	40
2012-05-09	TRAPPIST	I+z	25
2013-03-09	TRAPPIST	I+z	25
2013-04-21	Danish	R	100
WASP-42			
2013-04-19	Danish	R	100
WASP-43			
2012-01-07	TRAPPIST	I+z	10
2012-02-11	TRAPPIST	I+z	15
2012-05-05	TRAPPIST	I+z	15
2012-06-05	TRAPPIST	I+z	10
2013-04-19	Danish	R	100
WASP-46			
2011-05-07	TRAPPIST	I+z	54
2011-09-13	TRAPPIST	BB	20
2011-09-23	TRAPPIST	BB	20
2011-10-23	TRAPPIST	BB	20
2011-11-02	TRAPPIST	BB	20
2012-05-20	TRAPPIST	BB	20
2012-07-05	TRAPPIST	BB	20
2013-04-24	Danish	R	100

Table 5.2: Sources of archival lightcurves used in analysis.

System	Paper	Source
WASP-24	Southworth et al. (2014)	Available via CDS.
	Smith et al. (2012b)	WASP archive.
	Sada et al. (2012)	Provided by author.
	Simpson et al. (2011b)	RVs tabulated in paper.
	Street et al. (2010)	WASP archive. RVs tabulated in paper.
WASP-31	Brown et al. (2012a)	Available via CDS.
	Albrecht et al. (2012)	Online journal additional material.
	Dragomir et al. (2011)	Provided by author.
	Anderson et al. (2011)	WASP archive.
WASP-36	Turner et al. (2016b)	Provided by author.
	Mancini et al. (2016)	Provided by author. Available via CDS.
	Maciejewski et al. (2016)	Online: www.home.umk.pl/∼gmac/TTV/doku.php?id=download
	Smith et al. (2012a)	WASP archive
WASP-37	Simpson et al. (2011a)	WASP archive. (Previously available via http://nsted.ipac.caltech.edu)
WASP-42	Southworth et al. (2016)	http://www.astro.keele.ac.uk/jkt/data-teps.html
	Lendl et al. (2012)	Available via CDS.
WASP-43	Jiang et al. (2016)	Online journal additional material.
	Ricci et al. (2015)	Available via CDS.
	Murgas et al. (2014)	Available via CDS.
	Chen et al. (2014)	Available via CDS.
	Stevenson et al. (2014)	Provided by author.
	Gillon et al. (2012)	Available via CDS.
	Hellier et al. (2011)	WASP archive
WASP-46	Ciceri et al. (2016)	Provided by author
	Anderson et al. (2012)	Online journal additional material.

5.3 Analysis

5.3.1 System Parameters

For our global analysis we first ran our Markov Chain Monte Carlo (MCMC) code using all existing spectroscopic and photometric transit data to derive an initial set of parameters. These were then used with the newer lightcurves (Danish, TRAPPIST and those of more recent publications) in further MCMCs to derive parameters from the complete, available ensemble of data. We then looked at the models and residuals to eliminate poorly fitting or lower quality data. We also looked at the parameters derived by fitting the individual lightcruves to see if this would help identify outliers. After some trials with this method, a visual inspection of the lightcurves and fits gave better results. Particulars of individual analysis decisions are included in the corresponding results section. The code itself determines system parameters using both WASP and follow-up photometry along with with radial velocity (RV) measurements.The method is described in detail by Collier Cameron et al. (2007) and Anderson et al. (2015a) a summary of which follows.

We modelled our transit lightcurves using the formulation of Mandel & Agol (2002) and accounted for limb-darkening using the four-parameter non-linear law of Claret (2000, Claret (2004). We determined the mean stellar density, ρ_*, from the transit lightcurves and used the empirical mass calibration by Southworth (2011b) as a constraint on the stellar mass and radius allowing us to derive the corresponding mass and radius of the planet.

The free parameters in our MCMC analysis were, T_0, P, $(R_p/R_*)^2$, T_{14}, b, K_1, γ, $T_{\rm eff}$ and [Fe/H]. Here, T_0 is the epoch of mid-transit, P, is the orbital period, $(R_p/R_*)^2$ is the planet-to-star area ratio, T_{14} is the total transit duration, b is the impact parameter of the planet's path across the stellar disc, K_1 is the reflex velocity semi-amplitude, γ is the systemic velocity, $T_{\rm L-D}$, the limb-darkening temperature is the stellar temperature for which the limb darkening parameters were extracted and [Fe/H] is the stellar metallicity. At each step these values are perturbed by a small

random value, the χ^2 of the model with the resulting parameters is calculated and is accepted if $\Delta\chi^2 < 0$, otherwise the step is accepted with a probability proportional to $\exp(-\Delta\chi^2/2)$. We placed priors on both $T_{\rm L-D}$ and [Fe/H] using the values derived from previous papers. For the systems WASP 24 and WASP 31 we used the most recent values of $T_{\rm eff}$, $V \sin i_*$, $V_{\rm mac}$ and $V_{\rm mic}$ from Doyle et al. (2014). We used the most recent values of [Fe/H] from Mortier et al. (2013) for WASP 24, WASP 31, WASP 36 and WASP 42. For WASP 36 and WASP 42 we used the updated value of $T_{\rm eff}$ from Mortier et al. (2013). There is no evidence for significant eccentricity in most of our target systems so we adopt circular orbits in these cases. In the case of WASP-42 we allowed the MCMC to explore eccentric solutions. However, as there is no strong evidence for a non-zero eccentricity we ultimately settled on setting $e = 0$.

5.3.2 Transit Timings

We used a modified version of our MCMC code to find the mid-transit times of our individual lightcurves. We fixed the period to that found during the global analysis allowing the other parameters to vary as described. We rescaled the photometric error bars to account for red-noise (Gillon et al. 2010; Gillon et al. 2012). We then modelled the mid-transit times using a linear ephemeris (equation 1) and one allowing for period change (equation 2) following previous studies (Murgas et al. 2014; Chen et al. 2014):

$$T_{\rm mid} = T_0 + nP \tag{5.1}$$

$$T_{\rm mid} = T_0 + nP + n(n-1)\dot{P} \tag{5.2}$$

Here, $T_{\rm mid}$ is the time of mid transit, n, is the number of transits since the reference epoch, T_0, P is the period and $\dot{P}$ is the orbital decay rate.

Table 5.3: System parameters of WASP-24

Parameter (Unit)	This Work	Southworth et al. (2014)	Smith et al. (2012b)	Sada et al. (2012)	Simpson et al. (2011b)	Street et al. (2010)
Period (d)	$\mathbf{2.34122163^{+0.00000039}_{-0.00000030}}$	$2.34122170 \pm 0.00000008$	2.3412132 ± 0.0000018	2.3412162 ± 0.0000014	2.341213 ± 0.000002	2.341212 ± 0.000002
Transit Epoch, T_0	$\mathbf{5968.702495 \pm 0.000086}$	–	5149.27535 ± 0.00015	5081.3803 ± 0.0001	5081.37941 ± 0.00017	5081.37941 ± 0.00016
Transit Duration, T_{14} (d)	$\mathbf{0.11400 \pm 0.00047}$	–	0.11364 ± 0.00069	0.1060 ± 0.0014	–	0.1118 ± 0.0007
Scaled Semi-major Axis, a/R_*	$\mathbf{5.766 \pm 0.072}$	5.94 ± 0.13	5.75 ± 0.11	$7.08^{+0.66}_{-1.12}$	5.98 ± 0.15	–
Transit Depth, $(R_p/R_*)^2$	$\mathbf{0.010857 \pm 0.000077}$	0.01036 ± 0.00014	0.01102 ± 0.00013	0.0112 ± 0.0031	0.01008 ± 0.00012	0.01008 ± 0.00012
Impact Parameter, b	$\mathbf{0.664 \pm 0.011}$	–	0.669 ± 0.016	–	–	0.653 ± 0.018
Orbital Inclination, i ($^\circ$)	$\mathbf{83.39 \pm 0.19}$	83.87 ± 0.38	83.3 ± 0.3	86.4 ± 2.6	83.64 ± 0.29	83.64 ± 0.31
Semi-amplitude, K_1(ms^{-1})	$\mathbf{153.1^{+1.7}_{-2.1}}$	152.1 ± 3.2	150.6 ± 2.5	–	148.2 ± 2.5	145.2 ± 4.5
Semi-major Axis, a (au)	$\mathbf{0.03666 \pm 0.00091}$	0.0364 ± 0.0059	0.03619 ± 0.00027	–	–	0.03651 ± 0.00028
Stellar Mass, M_* ($M_\odot$)	$\mathbf{1.200 \pm 0.089}$	1.168 ± 0.057	1.154 ± 0.025	–	–	1.184 ± 0.027
Stellar Radius, R_* ($R_\odot$)	$\mathbf{1.367 \pm 0.042}$	1.317 ± 0.036	1.354 ± 0.032	–	–	1.331 ± 0.032
Stellar Density, ρ_* ($\rho_\odot$)	$\mathbf{0.469^{+0.020}_{-0.016}}$	0.512 ± 0.034	0.465 ± 0.028	–	–	0.50 ± 0.03
Stellar Surface Gravity, $\log(g_*)$ (cgs)	$\mathbf{4.245 \pm 0.015}$	4.267 ± 0.021	4.236 ± 0.017	–	–	4.263 ± 0.017
Stellar Effective Temperature, $T_{\rm eff}$ (K)	$\mathbf{6103 \pm 85}$	6107 ± 77	6038 ± 95	–	6075 ± 100	6075 ± 100
Stellar Metallicity, [Fe/H]	$\mathbf{-0.06 \pm 0.12}$	-0.0 ± 0.1	0.099 ± 0.071	–	–	–
Planet Mass, M_p ($M_{\rm Jup}$)	$\mathbf{1.137 \pm 0.058}$	1.109 ± 0.043	1.091 ± 0.025	–	–	1.071 ± 0.037
Planet Radius, R_p ($R_{\rm Jup}$)	$\mathbf{1.385 \pm 0.044}$	1.303 ± 0.043	1.383 ± 0.039	–	–	1.300 ± 0.038
Planet Density, ρ_p ($\rho_{\rm Jup}$)	$\mathbf{0.428 \pm 0.025}$	0.469 ± 0.042	0.412 ± 0.032	–	–	0.487 ± 0.041
Planet Surface Gravity, $\log(g_p)$ (cgs)	$\mathbf{3.132 \pm 0.014}$	3.209 ± 0.027	3.115 ± 0.022	–	–	3.160 ± 0.026
Planet Equilibrium Temperature, T_{eq}(K)	$\mathbf{1797 \pm 28}$	1772 ± 29	1781 ± 34	–	–	1801 ± 36
Stellar Rotational Velocity, $V \sin i$ (km s^{-1})	$\mathbf{5.23 \pm 0.45}$	–	–	–	7.0 ± 0.9	–
Spin-Orbit Angle, λ($^\circ$)	$\mathbf{-6.5 \pm 4.3}$	–	–	–	-5 ± 4	–

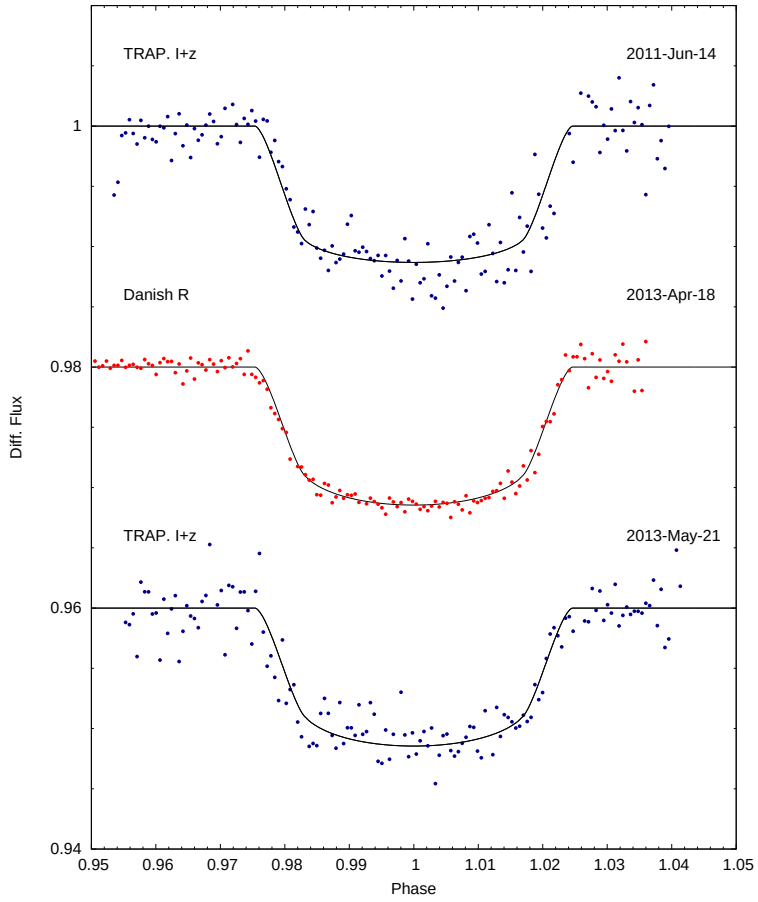

Figure 5.1: New data for WASP-24 b. Lightcurves are plotted in date order as detailed in Table 5.1. All lightcurves have been binned in two minute intervals. The new TRAPPIST data sets are blue and our Danish Telescope data are red.

5.4 Results and Discussion of Systems

5.4.1 WASP-24

Our reanalysis supports the new period put forward by Southworth et al. (2014, hereafter S14), disagreeing with the others by $> 3\sigma$. Our transit duration agrees with the updated value from Smith et al. (2012b) and disagrees with the durations of Street et al. (2010) by $\approx 2.5\sigma$ and Sada et al. (2012) by $> 5\sigma$. This is a result of our use

of several lightcurves which are of superior quality allowing for a tighter constraint on the ingress and egress timings. Our scaled semi-major axis is consistent with those of S14 (1.2σ), Sada et al. (2012) (1.2σ) and Simpson et al. (2011b) (1.3σ).

The transit depth we find agrees with that of Smith et al. (2012b) but is different from Street et al. (2010) by $> 5\sigma$ and S14 by 3σ, which is carried through to the planet radius though less significantly ($\lesssim 1.5\sigma$). In the case of the discovery paper we benefit from a number of higher quality lightcurves, S14 required further investigation. If we used just the ensemble of photometry used by S14 then we found a depth that is slightly larger than, but consistent to 1σ with their findings. The depth we found this way was inconsistent with the one found using all our available photometery by $\approx 2.3\sigma$. If we analysed all the available photometry excluding the lightcurve from RISE in the discovery paper and the Kitt Peak National Observatory (KPNO; Sada et al. 2012) lightcurve, we found a depth in agreement with our analysis of the ensemble used by S14 and weakly inconsistent ($\approx 1.5\sigma$) with both the depth presented by S14 and the depth we found using all available photometry. Therefore we concluded, in the case of S14, the difference is due in part to our use of MCMC rather than the weighted mean of individually modelled lightcurves and part to our inclusion of the RISE and KPNO photometry. This is illustrated in Fig. 5.2 Our inconsistencies lead to the inconsistency of $\log(g_p)$ between our results and those of S14 to just under 2σ. Parameters other than those mentioned agree to $\simeq 1\sigma$.

The results of our transit timing investigation can be found in Fig. 5.3. There is no evidence for orbital period change. The period of our non-linear ephemeris differs from the linear one by $4.8 \pm 4.4 \times 10^{-5}$ days and has $\dot{P} = 3.3 \pm 2.7 \times 10^{-3}$ seconds per year.

5.4.2 WASP-31

We chose to exclude the photometry from Dragomir et al. (2011) (taken 2011-Jan-25) and a lightcurve obtained with TRAPPIST on 2011-Mar-07 as they are deeper than other transits. A comparison of the transit models we arrive at by fitting only

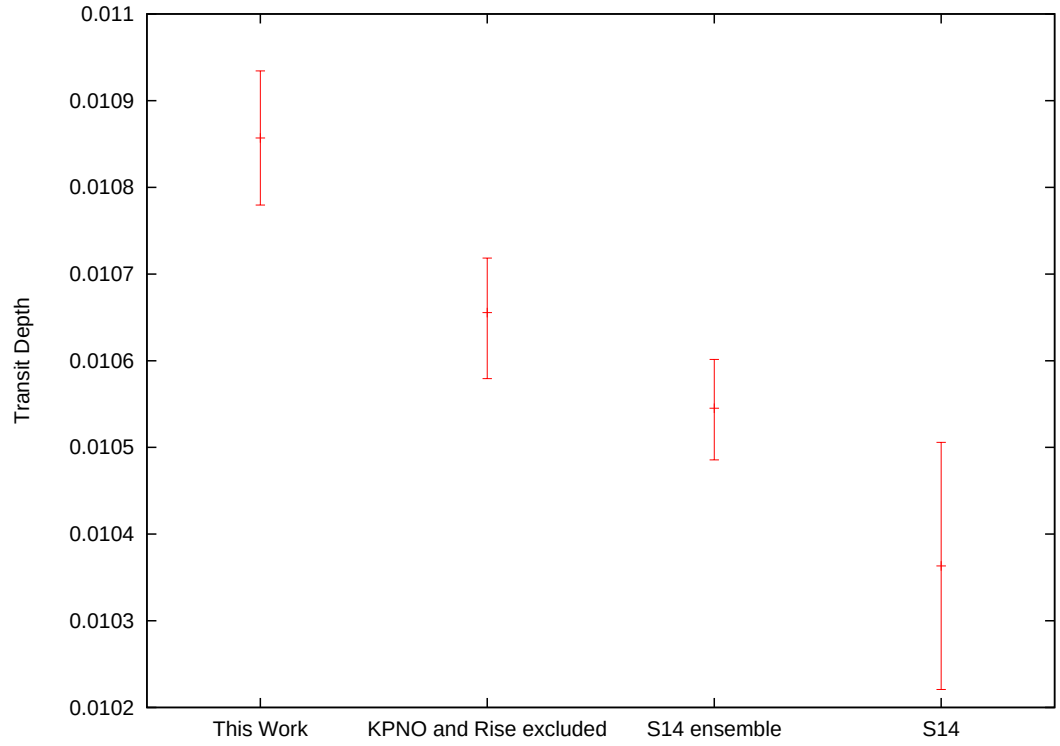

Figure 5.2: Comparison of the transit depths of WASP-24 found using different ensembles of photometry and by different methods. This work refers to our solution using all available photometry. The next is our solution with the RISE and KPNO lightcurve excluded. The S14 ensemble is the result of our MCMC using just the photometry used in S14. The final point is the result of S14 itself.

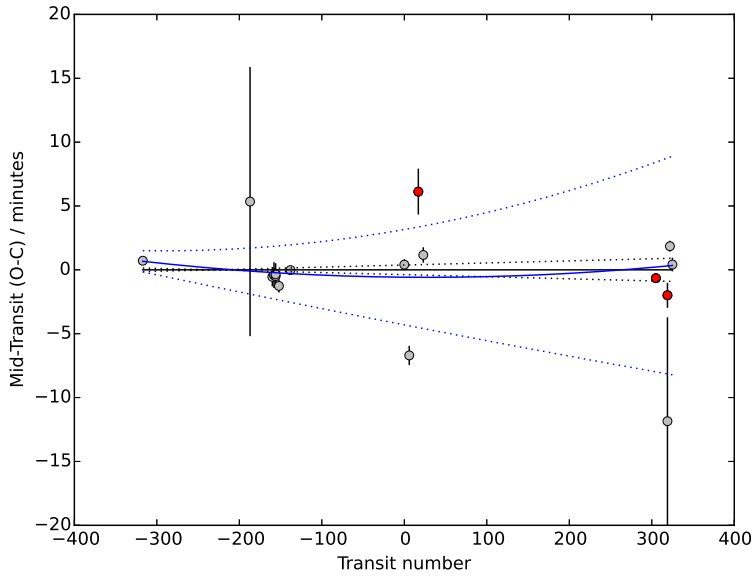

Figure 5.3: Transit times for all lightcurves of WASP-24. Grey circles are archival data while red circles are our new data. The solid lines show the linear (black) and quadratic (blue) ephemeris. The dotted lines show the 1σ uncertainties on their respective ephemeris.

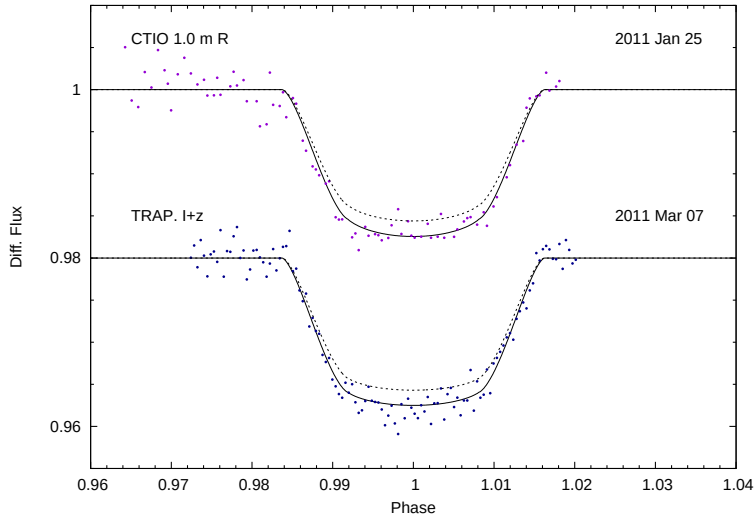

Figure 5.4: Data for WASP-31 b excluded from analysis. Caption as for Fig. 5.1 with the addition that data from Dragomir et al. (2011) are purple. The solid line is the model we find when fitting just these lightcurves. The dotted line is the model of the solution we find when excluding them. The depth difference is 0.00168.

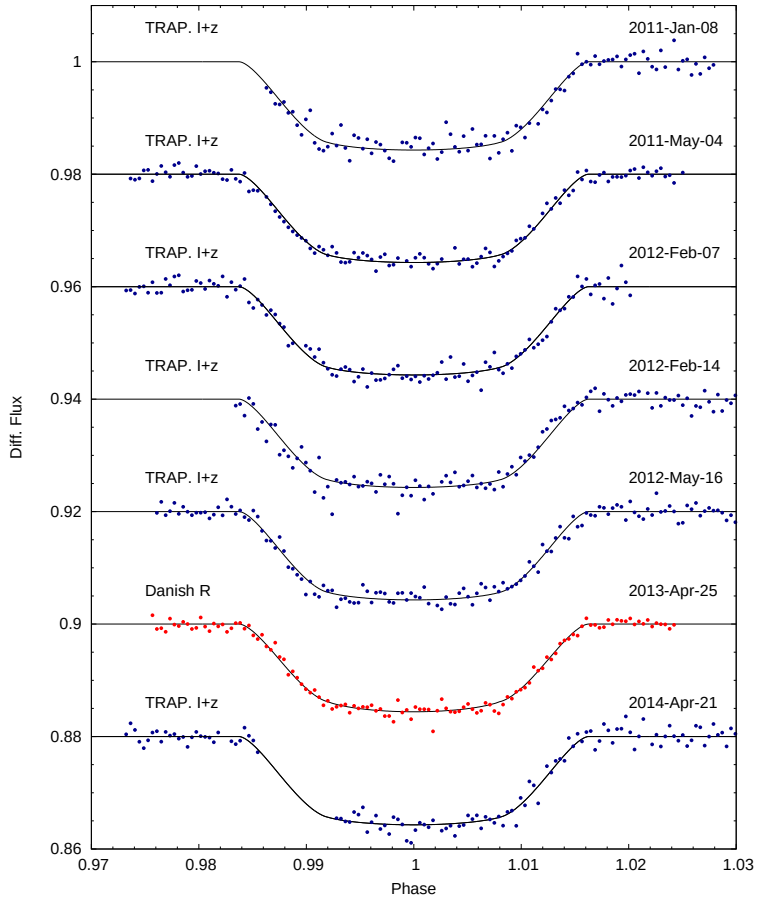

Figure 5.5: New data for WASP-31 b. Caption as for Fig. 5.1.

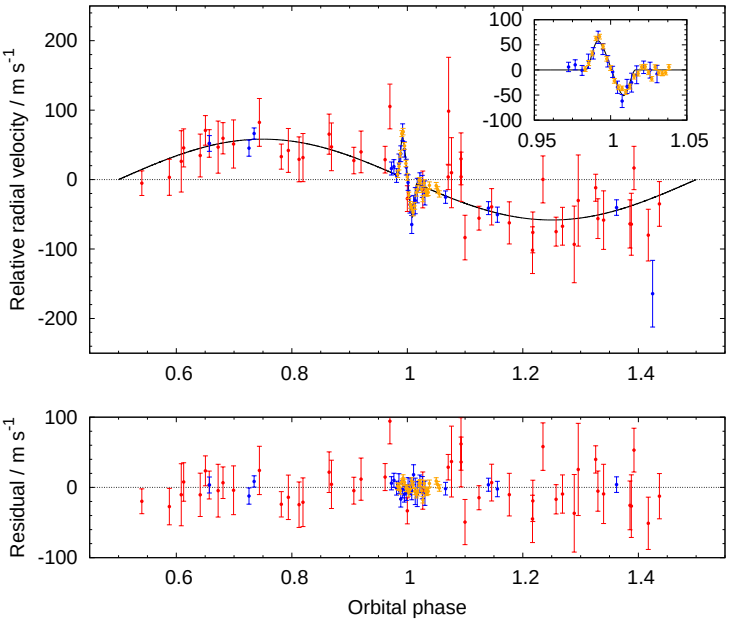

Figure 5.6: Archival radial velocity data for WASP-31 with our best fit orbital solution. Below: residuals. Inset:Our best fit Rossiter-McLaughlin solution with the slope due to orbital motion subtracted. CORALIE (red) data are from Anderson et al. (2011). HARPS RM data from Brown et al. (2012a) is in blue while that of Albrecht et al. (2012) is orange.

these lightcurves with the models found by excluding them from the global analysis are shown in Fig. 5.4; the depth difference is 0.00168. While the star has not been noted as being active, the depth discrepancy could be explained by a short-lived, unocculted group of star spots as no evidence of this effect is seen in the TRAPPIST lightcurves of 2011-Jan-08 and 2011-May-04. As part of their study Sing et al. (2015) monitored WASP-31 for photometric variability that could be caused by stellar activity. WASP-31 was found to have little photometric variability, its peak-to-peak amplitude over a period of 3 years was just 0.0031 ± 0.0006 mag. Unfortunately the monitoring of Sing et al. (2015) ran from 2011-Oct to 2014-Jan and so misses the period covered by our observations that may be affected by spot activity. They see no later period of activity suggesting, if our observations were affected by spots, such events are rare. The Hubble Space Telescope (HST) data from Sing et al. (2015) were not available for our analysis.

Our analysis finds parameters largely in agreement with previous studies. We find a different period to the original discovery paper (Anderson et al. 2011) but consistent with the lower value found by Dragomir et al. (2011) at a higher precision due to our longer baseline. This is supported by Sing et al. (2015), though our refined periods disagree by $\sim 3\sigma$.

Two groups have previously investigated the spin-orbit alignment of WASP-31 b with its host star. Brown et al. (2012a) observed a transit using the HARPS spectrograph while Albrecht et al. (2012) used HIRES. Both groups found a small orbital obliquity, λ, leading them to conclude that the planet's orbit is well aligned with the stellar spin axis. However, Albrecht et al. (2012) notes that the precise obliquity depended on the ephemeris used. When they used the updated ephemeris from Dragomir et al. (2011) they found an obliquity of $\lambda = -6^{\circ} \pm 3^{\circ}$, which is inconsistent with the results of Brown et al. (2012a); $\lambda = 2\overset{\circ}{.}8 \pm 3\overset{\circ}{.}1$. When they used the ephemeris from the discovery paper (Anderson et al. 2011) they found $\lambda = 2^{\circ} \pm 3^{\circ}$which agrees with Brown et al. (2012a). Brown et al. (2012a) used an MCMC similar to ours to model the photometry presented in Anderson et al. (2011). So, while they do not present the ephemeris their analysis produced, it is reasonable to assume it is similar to the discovery paper i.e. consistent with the ephemeris Albrecht et al. (2012) used from

the discovery paper. As the results they obtained depended on the timing information used Albrecht et al. (2012) expressed doubt in the formal errors on the obliquities and chose to inflate their errors.

When we re-analysed the RVs from both groups, together with our 7 new lightcurves, we find $\lambda = -2\overset{\circ}{.}4 \pm 1\overset{\circ}{.}5$. This agrees with the results of Albrecht et al. (2012) even without the inflation of their error and is different from Brown et al. (2012a) at only the 1.5σ level. As we confirm the revised period presented in Dragomir et al. (2011) we suggest that Albrecht's use of the updated ephemeris lead to a more accurate determination of the spin-orbit angle than that of Brown et al. (2012a). We also re-analysed each set of RV data separately with our new lightcurves. The results of these analyses can be found in Table 5.4. Our obliquities using the Rossiter-McLaughlin datasets separately agree to within 1σ with our combined determination supporting this conclusion.

The results of our non-liner ephemeris fit can be found in Fig. 5.7. Including the mid times from Sing et al. (2015) we find a period of 3.4058807 ± 0.0000053 days, a difference of $9.1 \pm 5.3 \times 10^{-6}$ days from the linear fit with $\dot{P} = 0.44 \pm 0.23$ seconds per year. (Without their mid times we find a period of 3.405876 ± 0.0000059 days, a difference of $1.3 \pm 0.6 \times 10^{-5}$ days from the linear fit. We find $\dot{P} = 0.61 \pm 0.25$ seconds per year.) While the non-linear fit looks quite striking it is mostly due to the final point. This lightcurve is missing the ingress of the transit resulting in a large uncertainty on its mid time.

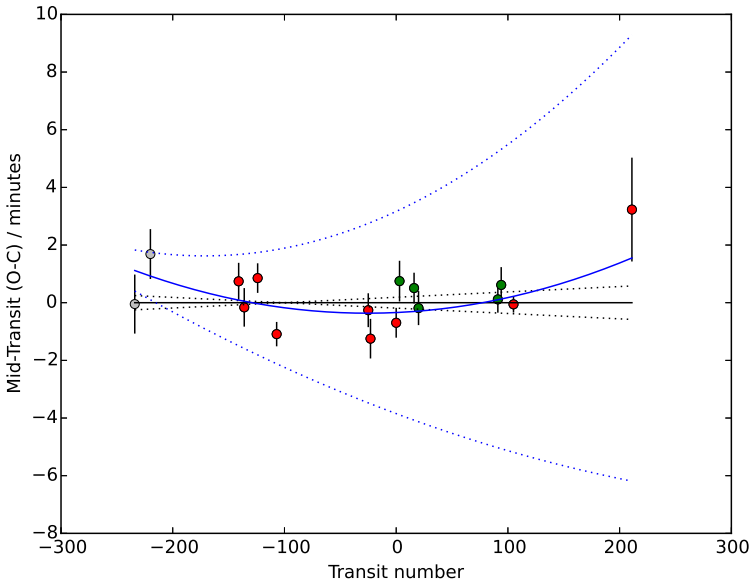

Figure 5.7: Transit times for all WASP-31 lightcurves. Caption as for Fig. 5.3. In addition, the green points use mid-transit time offsets of ETD lightcurves reported by Sing et al. (2015).

Table 5.4: Comparison of our final combined determination of Vsin(i) and λ for WASP-31 with the results of Albrecht, Brown and our reanalysis of their individual data sets.

Result	$V \sin(i)$ ($\mathrm{km\,s^{-1}}$) ($\mathrm{Km\,s^{-1}}$)	λ (°)
This work (All RVs)	8.16 ± 0.42	$-2.4^{+1.5}_{-1.6}$
Brown et al. (2012a)	7.5 ± 0.7	2.8 ± 3.1
This Work (Brown RVs)	$7.17^{+0.65}_{-0.64}$	$-0.7^{+2.4}_{-2.9}$
Albrecht et al. (2012)	6.8 ± 0.6	-6 ± 6
This Work (Albrecht RVs)	$8.48^{+0.40}_{-0.36}$	$-4.5^{+1.8}_{-1.7}$

Table 5.5: System parameters of WASP-31

Parameter (Unit)	This Work	Brown et al. (2012a)	Albrecht et al. (2012)	Dragomir et al. (2011)	Anderson et al. (2011)
Period (d)	$\mathbf{3.40588967 \pm 0.00000085}$	3.405909 ± 0.000005	–	3.405883 ± 0.000012	3.405910 ± 0.000005
Transit Epoch, T_0	$\mathbf{6255.32572 \pm 0.00015}$	–	–	5209.71890 ± 0.00029	5192.6887 ± 0.0003
Transit Duration, T_{14} (d)	$\mathbf{0.10992^{+0.00062}_{-0.00049}}$	–	–	$0.111^{+0.027}_{-0.022}$	0.1103 ± 0.0013
Scaled Semi-major Axis, a/R_*	$\mathbf{8.054^{+0.097}_{-0.075}}$	–	–	$8.52^{+1.04}_{-0.81}$	8.00 ± 0.19
Transit Depth, $(R_p/R_*)^2$	$\mathbf{0.01591^{+0.00014}_{-0.00011}}$	–	–	0.0171 ± 0.0016	0.01615 ± 0.00027
Impact Parameter, b	$\mathbf{0.776 \pm 0.006}$	–	–	–	0.780 ± 0.013
Orbital Inclination, i (°)	$\mathbf{84.50 \pm 0.10}$	84.54 ± 0.27	–	85 ± 1	84.41 ± 0.22
Semi-amplitude, $K_1(\mathrm{ms}^{-1})$	$\mathbf{58.2 \pm 3.2}$	–	–	58.2 ± 3.5	58.1 ± 3.4
Semi-major Axis, a (au)	$\mathbf{0.0461 \pm 0.0012}$	0.04657 ± 0.00034	–	0.04657 ± 0.00035	0.04659 ± 0.00035
Stellar Mass, M_* $(M_\odot)$	$\mathbf{1.129 \pm 0.087}$	1.161 ± 0.026	–	1.161 ± 0.026	1.163 ± 0.026
Stellar Radius, R_* $(R_\odot)$	$\mathbf{1.234 \pm 0.033}$	1.241 ± 0.039	–	$1.18^{+0.14}_{-0.11}$	1.252 ± 0.033
Stellar Density, ρ_* $(\rho_\odot)$	$\mathbf{0.604 \pm 0.019}$	–	–	$1.01^{+0.37}_{-0.29}$	0.592 ± 0.042
Stellar Surface Gravity, $\log(g_*)$ (cgs)	$\mathbf{4.309 \pm 0.014}$	–	–	$4.363^{+0.107}_{-0.083}$	4.31 ± 0.02
Stellar Effective Temperature, $T_{\rm eff}$ (K)	$\mathbf{6317 \pm 93}$	6300 ± 100	–	–	6302 ± 102
Stellar Metallicity, [Fe/H]	$\mathbf{-0.208 \pm 0.093}$	–	–	–	-0.20 ± 0.09
Planet Mass, M_p $(M_{\rm Jup})$	$\mathbf{0.470 \pm 0.036}$	0.48 ± 0.03	–	0.48 ± 0.03	0.478 ± 0.029
Planet Radius, R_p $(R_{\rm Jup})$	$\mathbf{1.514 \pm 0.041}$	1.54 ± 0.06	–	$1.53^{+0.20}_{-0.16}$	1.55 ± 0.05
Planet Density, ρ_p $(\rho_{\rm Jup})$	$\mathbf{0.1355 \pm 0.0097}$	–	–	$0.177^{+0.070}_{-0.057}$	0.129 ± 0.014
Planet Surface Gravity, $\log(g_p)$ (cgs)	$\mathbf{2.672 \pm 0.026}$	–	–	$2.724^{+0.117}_{-0.095}$	2.659 ± 0.036
Planet Equilibrium Temperature, T_{eq}(K)	$\mathbf{1574 \pm 25}$	–	–	–	1575 ± 32
Stellar Rotational Velocity, $V \sin i$ (km s^{-1})	$\mathbf{8.16 \pm 0.42}$	7.5 ± 0.7	6.8 ± 0.6	–	7.9 ± 0.6
Spin-Orbit Angle, $\lambda(^\circ)$	$\mathbf{-2.4 \pm 1.5}$	2.8 ± 3.1	-6 ± 6	–	–

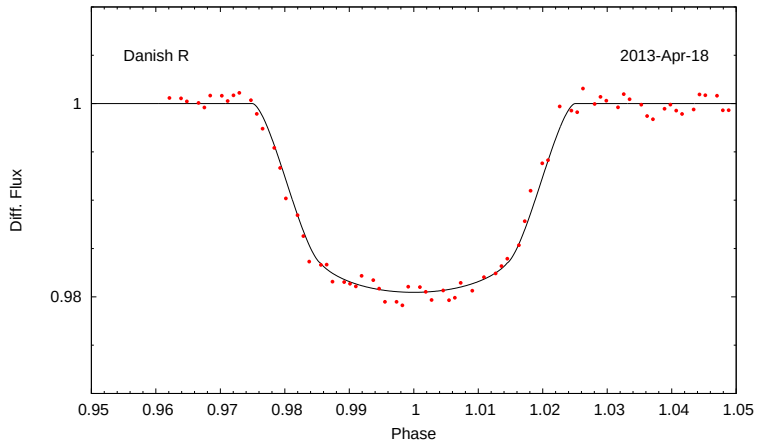

Figure 5.8: New data for WASP-36 b. Caption as for Fig. 5.1.

5.4.3 WASP-36

There have been several recent studies of the WASP-36 system. Using the additional data, we arrive at parameters that agree with those in the original discovery paper Smith et al. 2012a to within 1.5σ or better, but that are more accurate. The largest deviation is between the values of $\log(g_*)$ of 1.8σ. Of the more recent studies we match most closely with Mancini et al. (2016). Their revised period, scaled semi-major axis, orbital inclination and stellar density all agree with our values to within 1σ. The transit depth, semi-major axis, stellar mass, radius and planet mass all agree to 1.6σ or better. There are small discrepancies between planet radius, density and equilibrium temperature (at 1.8σ, 2.3σ and 1.9σ respectively). Similarly to the discovery paper, most of our values agree with Maciejewski et al. (2016) and Turner et al. (2016b) to within 1.5σ. The largest deviations are between their transit depths and the period derived by Turner et al. (2016b). In these cases, we have the benefit of using all the available data.

The results of our non-linear ephemeris fitting can be found in Fig. 5.9. We find a period of $1.53736710018 \pm 0.0000010$ days (a difference of $1.2 \pm 1.0 \times 10^{-6}$ days) and $\dot{P} = -0.048 \pm 0.039$ second per year. This ephemeris is just barely above a 1σ

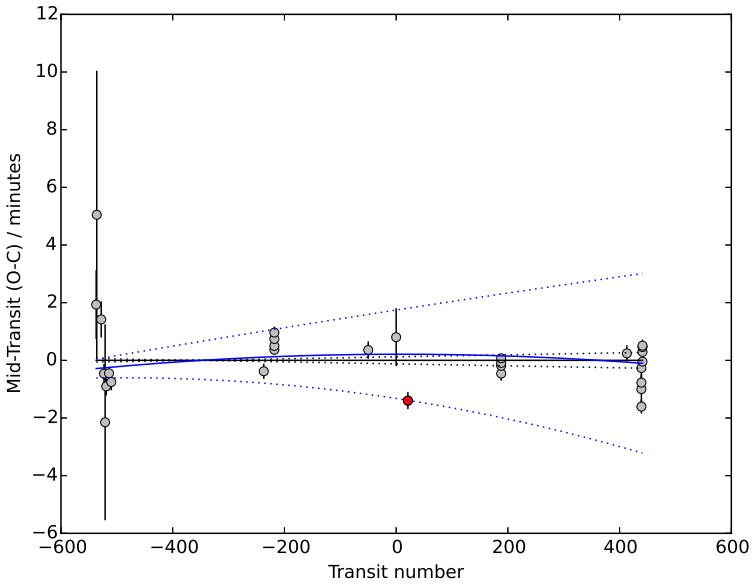

Figure 5.9: Transit times for all WASP-36 lightcurves. Caption as for Fig. 5.3.

significance, thus we conclude that there is no evidence for a period change.

Table 5.6: System parameters of WASP-36. Note, for Turner et al. (2016b), where they present wavelength dependent values we compare to their R band results.

Parameter (Unit)	This Work	Turner et al. (2016b)	Mancini et al. (2016)	Maciejewski et al. (2016)	Smith et al. (2012a)
Period (d)	$\mathbf{1.537365936 \pm 0.000000097}$	$1.53736423 \pm 0.00000057$	$1.53736596 \pm 0.00000024$	1.5373639 ± 0.0000014	1.5373653 ± 0.0000026
Transit Epoch, T_0	$\mathbf{6472.271302^{+0.000036}_{-0.000030}}$	5569.8382 ± 0.0001	5569.83771 ± 0.00046	5569.83802 ± 0.00013	5569.837310 ± 0.000095
Transit Duration, T_{14} (d)	$\mathbf{0.07603 \pm 0.00014}$	0.0760 ± 0.0005	–	–	0.07566 ± 0.00042
Scaled Semi-major Axis, a/R_*	$\mathbf{5.853 \pm 0.024}$	–	5.848 ± 0.055	5.91 ± 0.11	5.977 ± 0.082
Transit Depth, $(R_p/R_*)^2$	$\mathbf{0.018791 \pm 0.000059}$	0.019182 ± 0.000029	0.018706 ± 0.000021	0.019349 ± 0.000044	0.0192 ± 0.0002
Impact Parameter, b	$\mathbf{0.6828 \pm 0.0039}$	–	–	0.657 ± 0.031	0.665 ± 0.013
Orbital Inclination, i (°)	$\mathbf{83.302 \pm 0.066}$	83.61 ± 0.21	83.15 ± 0.13	83.62 ± 0.28	83.61 ± 0.21
Semi-amplitude, K_1(ms^{-1})	$\mathbf{392.2 \pm 8.4}$	–	–	391 ± 6	391.5 ± 8.3
Semi-major Axis, a (au)	$\mathbf{0.02571 \pm 0.00067}$	0.02643 ± 0.00026	0.02677 ± 0.00021	0.02641 ± 0.00026	0.02643 ± 0.00026
Stellar Mass, M_* ($M_\odot$)	$\mathbf{0.959 \pm 0.075}$	–	1.081 ± 0.025	–	1.040 ± 0.031
Stellar Radius, R_* ($R_\odot$)	$\mathbf{0.945 \pm 0.025}$	–	0.985 ± 0.012	0.960 ± 0.019	0.951 ± 0.018
Stellar Density, ρ_* ($\rho_\odot$)	$\mathbf{1.137 \pm 0.014}$	–	1.132 ± 0.032	1.176 ± 0.063	1.21 ± 0.05
Stellar Surface Gravity, $\log(g_*)$ (cgs)	$\mathbf{4.469 \pm 0.012}$	–	4.486 ± 0.009	4.490 ± 0.025	4.499 ± 0.012
Stellar Effective Temperature, $T_{\rm eff}$ (K)	$\mathbf{6163 \pm 101}$	–	–	–	5959 ± 134
Stellar Metallicity, [Fe/H]	$\mathbf{-0.29 \pm 0.12}$	–	–	–	-0.3 ± 0.1
Planet Mass, M_p ($M_{\rm Jup}$)	$\mathbf{2.18 \pm 0.12}$	2.286 ± 0.066	2.361 ± 0.062	2.295 ± 0.058	2.303 ± 0.068
Planet Radius, R_p ($R_{\rm Jup}$)	$\mathbf{1.261 \pm 0.033}$	1.281 ± 0.026	1.327 ± 0.019	1.330 ± 0.029	1.281 ± 0.029
Planet Density, ρ_p ($\rho_{\rm Jup}$)	$\mathbf{1.093 \pm 0.045}$	1.017 ± 0.068	0.945 ± 0.041	0.976 ± 0.069	1.096 ± 0.067
Planet Surface Gravity, $\log(g_p)$ (cgs)	$\mathbf{3.4990^{+0.0097}_{-0.0134}}$	3.538 ± 0.028	3.521 ± 0.014	3.528 ± 0.018	3.507 ± 0.018
Planet Equilibrium Temperature, T_{eq}(K)	$\mathbf{1801 \pm 30}$	1724 ± 39	1733 ± 19	–	1724 ± 43

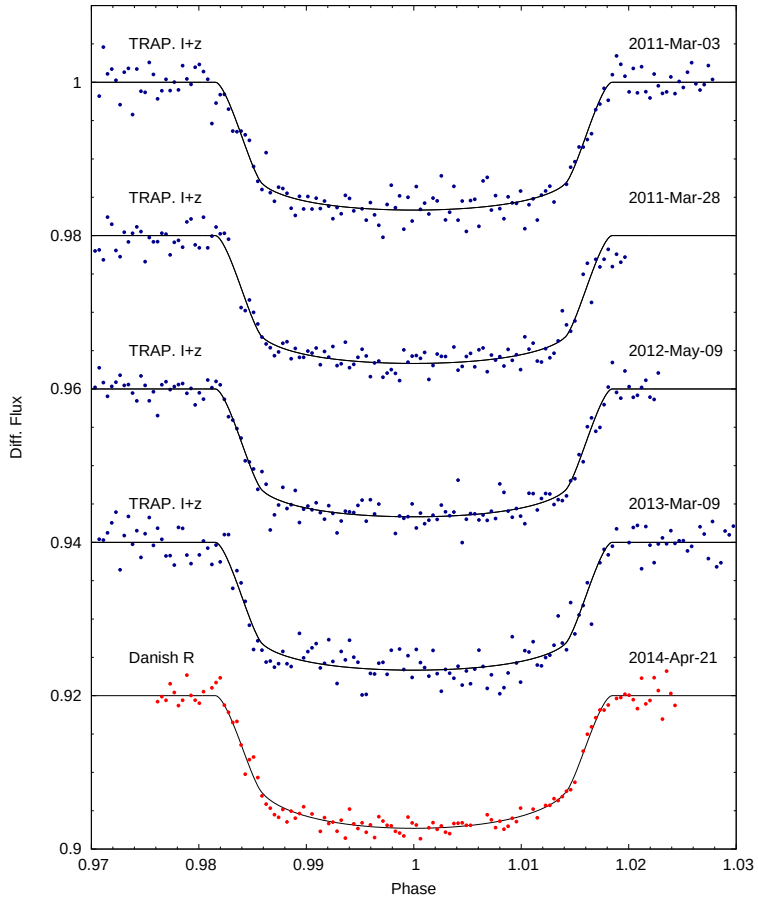

Figure 5.10: New data for WASP-37 b. Caption as for Fig. 5.1.

5.4.4 WASP-37

The addition of several complete transit lightcurves lead us to system parameters largely consistent with the discovery paper (Simpson et al. 2011a). Our period is slightly longer but consistent at a $\sim 1.3\sigma$ level, we attribute this difference to our longer baseline. We also find the a slightly larger, but consistent ($< 1.7\sigma$ different), transit depth. Our use of complete lightcurves prevents the erroneous subtraction of linear trends during analysis which could cause the apparent depth differences. Our use of an updated stellar mass calibration does not arrive at a different mass to the

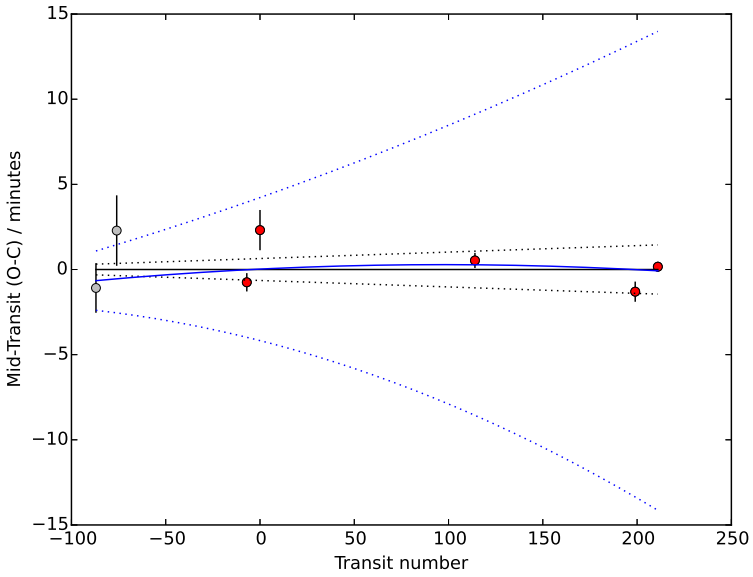

Figure 5.11: Transit times for all WASP-37 lightcurves. Caption as for Fig. 5.3.

mass presented in the discovery paper.

The discovery paper finds the age of the star to be highly uncertain but concludes that it is a member of an older population of stars. We use the stellar density from our analysis with the spectroscopic values of [Fe/H] and $T_{\rm eff}$ from the discovery paper with BAGEMASS (Maxted, Serenelli & Southworth 2015) to find an age of 8 ± 2 Gyr. This agrees with the determination of an advanced age and is consistent with that of Bonfanti et al. (2015); 6.2 ± 2.7 Gyr.

The results of our non-linear ephemeris fit can be found in Fig. 5.11. We find no evidence of orbital period change. Neither the difference between the linear and non-linear period, $(0.5 \pm 1.6) \times 10^{-5}$ days, nor $\dot{P}$, -0.3 ± 0.8 seconds per year, is significant.

Table 5.7: System parameters of WASP-37

Parameter (Unit)	This Work	Simpson et al. (2011a)
Period (d)	$\mathbf{3.5774833 \pm 0.0000014}$	3.577469 ± 0.000011
Transit Epoch, T_0	$\mathbf{6093.46837 \pm 0.00014}$	5338.6188 ± 0.0006
Transit Duration, T_{14} (d)	$\mathbf{0.13145 \pm 0.00079}$	0.1304 ± 0.0017
Scaled Semi-major Axis, a/R_*	$\mathbf{9.34 \pm 0.21}$	9.57 ± 0.65
Transit Depth, $(R_p/R_*)^2$	$\mathbf{0.01491 \pm 0.00022}$	$0.01427^{+0.00030}_{-0.00023}$
Impact Parameter, b	$\mathbf{0.310^{+0.060}_{-0.076}}$	0.20 ± 0.13
Orbital Inclination, i (°)	$\mathbf{88.10 \pm 0.46}$	88.82 ± 0.81
Semi-amplitude, K_1(ms^{-1})	$\mathbf{250.6 \pm 8.7}$	250.7 ± 8.4
Semi-major Axis, a (au)	$\mathbf{0.0446 \pm 0.0012}$	0.0446 ± 0.0019
Stellar Mass, M_* ($M_\odot$)	$\mathbf{0.926 \pm 0.076}$	0.93 ± 0.12
Stellar Radius, R_* ($R_\odot$)	$\mathbf{1.027 \pm 0.039}$	1.003 ± 0.053
Stellar Density, ρ_* ($\rho_\odot$)	$\mathbf{0.854 \pm 0.057}$	$0.931^{+0.064}_{-0.099}$
Stellar Surface Gravity, log(g_*) (cgs)	$\mathbf{4.381 \pm 0.021}$	4.25 ± 0.15
Stellar Effective Temperature, $T_{\rm eff}$ (K)	$\mathbf{5950 \pm 116}$	5800 ± 150
Stellar Metallicity, [Fe/H]	$\mathbf{-0.41 \pm 0.12}$	-0.40 ± 0.12
Planet Mass, M_p ($M_{\rm Jup}$)	$\mathbf{1.79 \pm 0.12}$	1.80 ± 0.17
Planet Radius, R_p ($R_{\rm Jup}$)	$\mathbf{1.220 \pm 0.052}$	1.160 ± 0.065
Planet Density, ρ_p ($\rho_{\rm Jup}$)	$\mathbf{0.991 \pm 0.096}$	1.15 ± 0.14
Planet Surface Gravity, log(g_p) (cgs)	$\mathbf{3.441 \pm 0.028}$	$3.48^{+0.03}_{-0.04}$
Planet Equilibrium Temperature, T_{eq}(K)	$\mathbf{1377 \pm 31}$	1323^{+25}_{-15}

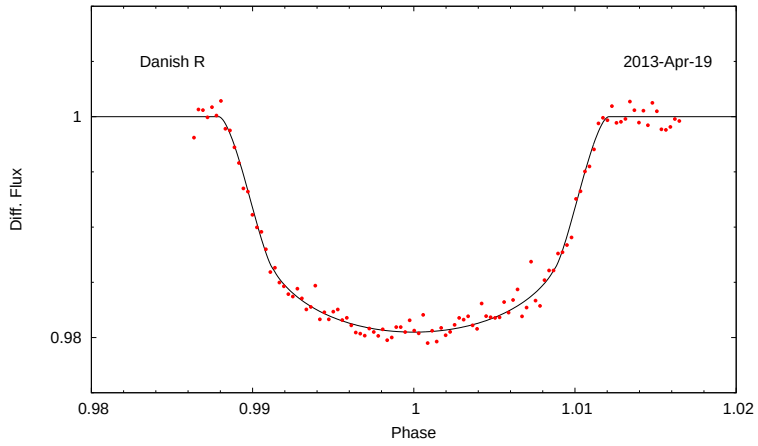

Figure 5.12: New data for WASP-42 b. Caption as for Fig. 5.1.

5.4.5 WASP-42

We find no significant deviation between our results and those published in the discovery paper for WASP-42b (Lendl et al. 2012). Our metallicity differs but this is due to our use of updated stellar parameters from Mortier et al. (2013). Our parameters agree with those found by Southworth et al. (2016). Our periods differ at a 4σ level, though this translates to a difference of only 0.5 seconds. For this analysis we excluded the lightcurve of Southworth et al. (2016) from 2013 May 24 as it is shallower than the rest, see Fig. 5.13.

The results of our non-linear ephemeris fit can be found in Fig. 5.14. We find no evidence of orbital period change. Neither the difference between the linear and non-linear period, $(0.8 \pm 3.9) \times 10^{-5}$ days, nor $\dot{P}$, -0.7 ± 3.0 seconds per year, is significant. WASP-42 has $a/R_* = 13.65 \pm 0.16$, this is smaller than the proposed cut off for good spin-orbit alignment of $a/R_* > 15$ (Anderson et al. 2015c) but in an area of parameter space with no measured spin-orbit angles. As such it could help determine boundary of proposed a/R_* alignment cut off. This may then inform tidal theory and allow for better calibration of the empirical alignment time-scale relation of Albrecht et al. (2012).

5.4.6 WASP-43

After our initial analysis using all the available photometry we chose to exclude the TRAPPIST lightcurves from 2011-Jan-23 and 2011-Dec-12 as they show features that may adversely affect further analysis, see Fig. 5.16. We excluded the observations of Ricci et al. (2015) from 2014 March 7 and the Gunn i' band observations from 2014 March 29 for the same reason. As the stellar mass calibration we used is unreliable for stars with effective temperatures below 5500K, for WASP-43 ($T_{\rm eff}$ = 4400K) we used the BAGEMASS code (Maxted, Serenelli & Southworth 2015) to place a prior on the stellar mass. This stellar mass agrees with the alternative solution of Hellier et al. (2011).

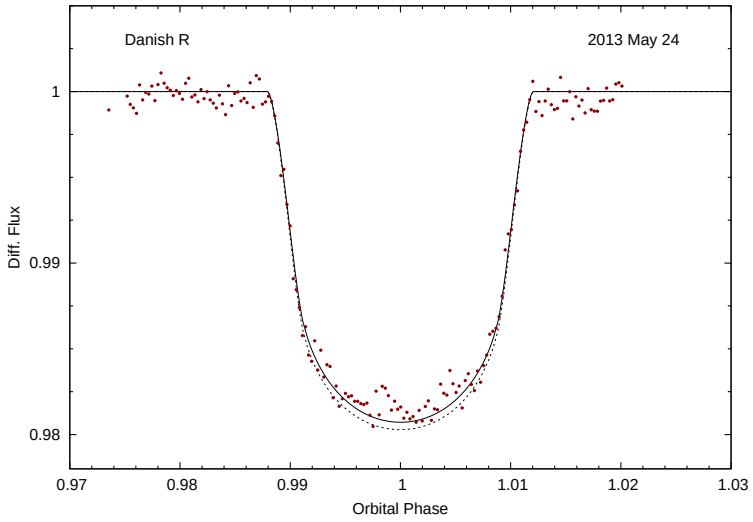

Figure 5.13: Danish R band transit of WASP-42 from 2013 May 24 from Southworth et al. (2016) excluded from the global analysis. The solid line is the best fit solution to this lightcurve alone. The dotted line is the final best fit solution.

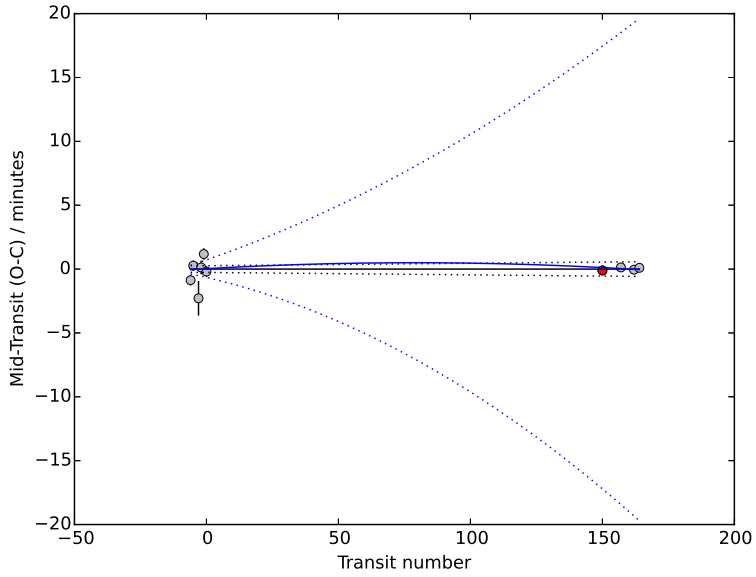

Figure 5.14: Transit times for all WASP-42 lightcurves. Caption as for Fig. 5.3.

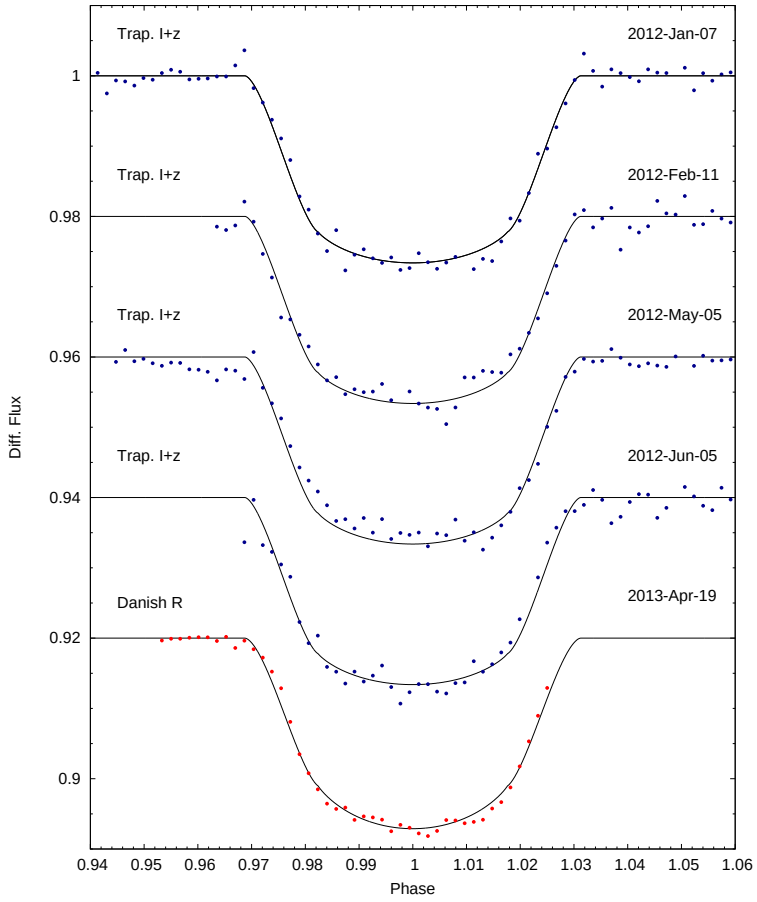

Figure 5.15: New data for WASP-43 b. Caption as for Fig. 5.1.

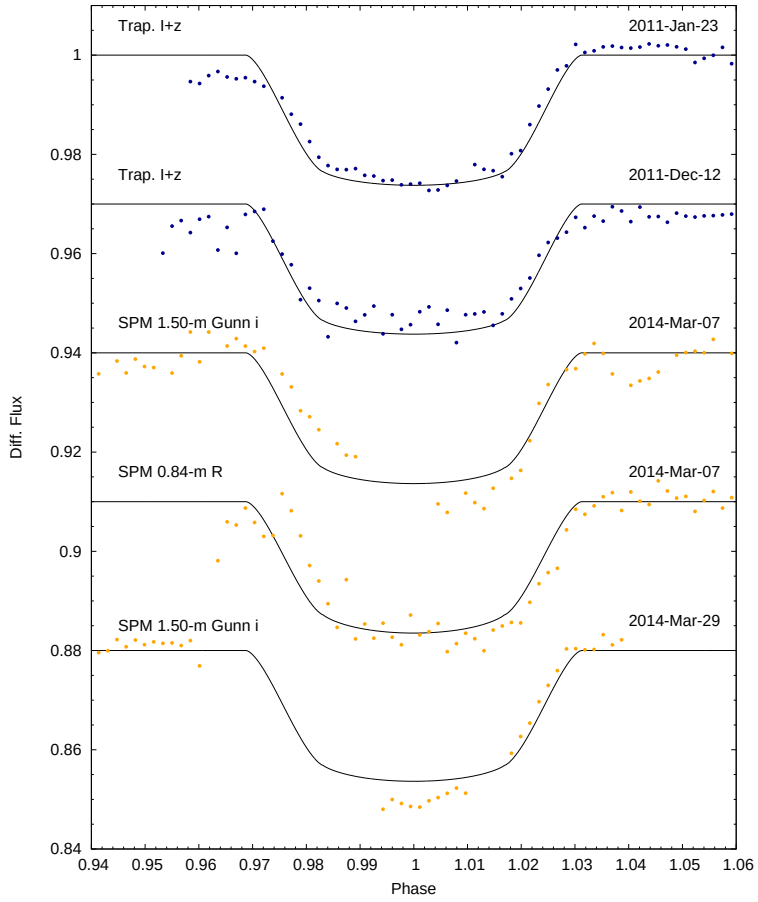

Figure 5.16: Data for WASP-43 b excluded from analysis. Caption as for Fig. 5.1.

Table 5.8: System parameters of WASP-42

Parameter (Unit)	This Work	Southworth et al. (2016)	Lendl et al. (2012)
Period (d)	$\mathbf{4.981689 \pm 0.000001}$	4.9816819 ± 0.0000011	4.9816877 ± 0.0000071
Transit Epoch, T_0	$\mathbf{6203.533626 \pm 0.000084}$	5650.56728 ± 0.00015	5650.56723 ± 0.00024
Transit Duration, T_{14} (d)	$\mathbf{0.12035 \pm 0.00043}$	–	0.12042 ± 0.00097
Scaled Semi-major Axis, a/R_*	$\mathbf{13.59 \pm 0.16}$	13.53 ± 0.31	13.84 ± 0.34
Transit Depth, $(R_p/R_*)^2$	$\mathbf{0.01679 \pm 0.00014}$	0.016718 ± 0.000027	0.01650 ± 0.00039
Impact Parameter, b	$\mathbf{0.46 \pm 0.02}$	–	0.41 ± 0.05
Orbital Inclination, i (°)	$\mathbf{88.05 \pm 0.11}$	88.70 ± 0.39	88.30 ± 0.24
Semi-amplitude, K_1(ms^{-1})	$\mathbf{64.5 \pm 1.5}$	64.8 ± 1.7	64.3 ± 1.7
Semi-major Axis, a (au)	$\mathbf{0.0575 \pm 0.0013}$	0.0561 ± 0.0007	0.0547 ± 0.0017
Stellar Mass, M_* ($M_\odot$)	$\mathbf{1.021 \pm 0.068}$	0.951 ± 0.037	0.881 ± 0.083
Stellar Radius, R_* ($R_\odot$)	$\mathbf{0.910 \pm 0.023}$	0.892 ± 0.021	0.850 ± 0.035
Stellar Density, ρ_* ($\rho_\odot$)	$\mathbf{1.355 \pm 0.047}$	1.338 ± 0.092	1.43 ± 0.11
Stellar Surface Gravity, $\log(g_*)$ (cgs)	$\mathbf{4.528 \pm 0.013}$	4.515 ± 0.022	4.5 ± 0.1
Stellar Effective Temperature, $T_{\rm eff}$ (K)	$\mathbf{5364 \pm 71}$	5315 ± 79	5200 ± 150
Stellar Metallicity, [Fe/H]	$\mathbf{0.287 \pm 0.051}$	0.29 ± 0.05	0.05 ± 0.13
Planet Mass, M_p ($M_{\rm Jup}$)	$\mathbf{0.549 \pm 0.027}$	0.53 ± 0.02	0.497 ± 0.035
Planet Radius, R_p ($R_{\rm Jup}$)	$\mathbf{1.147 \pm 0.032}$	1.122 ± 0.033	1.063 ± 0.051
Planet Density, ρ_p ($\rho_{\rm Jup}$)	$\mathbf{0.364 \pm 0.021}$	0.349 ± 0.029	0.412 ± 0.045
Planet Surface Gravity, $\log(g_p)$ (cgs)	$\mathbf{2.980 \pm 0.016}$	3.016 ± 0.025	–
Planet Equilibrium Temperature, T_{eq}(K)	$\mathbf{1028 \pm 15}$	1021 ± 19	988 ± 31

All our physical parameters agree well with the earlier studies of Hellier et al. (2011) and Gillon et al. (2012), though this is in part due to the lower precision that these studies were able to achieve. The more recent studies of Ricci et al. (2015), Jiang et al. (2016) and Hoyer et al. (2016) focus mainly on ephemerides and jump parameters a/R_*, R_p/R_* and i. We compare these in Fig. 5.17 by calculating the transit depth and impact parameter, $b = a/R_* \cos i$, using their results.

While our solution differs from the recent global analyses of Jiang et al. (2016) and Hoyer et al. (2016) we note that there is some correlation between the depth an impact parameter which are related to the transit shape. The shape is also affected by the limb darkening parameters which we explore via T_{L-D} using the stellar effective temperature as a prior. The Transit Analysis Package (TAP; Gazak et al. 2012) uses limb-darkening coefficients directly. By allowing T_{L-D} to vary more freely we can converge on a solution that is in better agreement with recent studies but this requires temperatures in excess of 6000K which are clearly unphysical for WASP-43.

The WASP-43 system has been intensely studied for signs of orbital period decay.

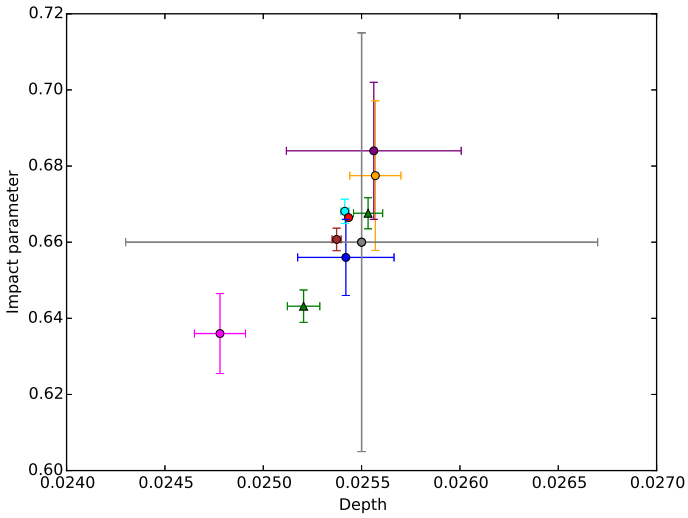

Figure 5.17: Comparison of transit depth and impact parameter values for previous studies of the WASP-43 system. Grey: Hellier et al. (2011), blue: Gillon et al. (2012) , pink: Chen et al. (2014) , purple: Murgas et al. (2014), red: Stevenson et al. (2014), yellow: Ricci et al. (2015), cyan: Hoyer et al. (2016), brown: Jiang et al. (2016), . The green points are our values. The larger transit depth and impact parameter value relates to the unphysical temperature range.

Indeed, of the previous studies most have focused on this rather than the system parameters. The most recent of these Hoyer et al. (2016) concluded there is no evidence for orbital decay counter to the claims of Ricci et al. (2015) (-0.03 ± 0.03 s yr^{-1}) and Jiang et al. (2016) (-0.029 ± 0.008 s yr^{-1}). While the data from Hoyer et al. (2016) were not available for our global analysis we did include their mid times. Doing so results in a period of $0.81347459 \pm 0.00000039$ days, a difference of $1.3 \pm 1.2 \times 10^{-7}$ days from that of our linear ephemeris. We also find a decay rate of -0.027 ± 0.017 s yr^{-1}. This is in agreement with the decay rates of Ricci et al. (2015) and Jiang et al. (2016) but has a low significance. However, it is still larger than the 1σ uncertainty from Hoyer et al. (2016). When we checked our transit mid times with those of Hoyer et al. (2016) for the lightcurves we had common access to we found that only one deviated significantly by more than 2 minutes; the Gunn i' band observation of 2014 March 29 from Ricci et al. (2015). We cannot conclusively rule out the result of Hoyer et al. (2016) but do suggest that orbital period decay is still an open question.

5.4.7 WASP-46

We excluded from our analysis two of the new TRAPPIST lightcurves likely affected by the activity reported in this star, Fig. 5.20. The first excluded lightcurve is missing the egress, has a likely spot-crossing event and a possible linear trend. The second excluded lightcurve shows an early ingress as compared to the model, which could be explained by a stellar plage, and a possible spot crossing shortly after.

When compared with the discovery paper (Anderson et al. 2012) we see broad agreement in system parameters. Overall, we see closer agreement with the updated values from Ciceri et al. (2016), with most parameters matching to within 1σ. However, in both cases we see differences between the periods and transit depths. In the case of the discovery paper we have access to many more lightcurves and a longer baseline of observations thus we expect to be able to refine these parameters. Like Ciceri et al. (2016), we improve on the precision of the transit depth and our revised value is smaller lying between Ciceri et al. (2016) and that of the discovery paper. As with WASP-24

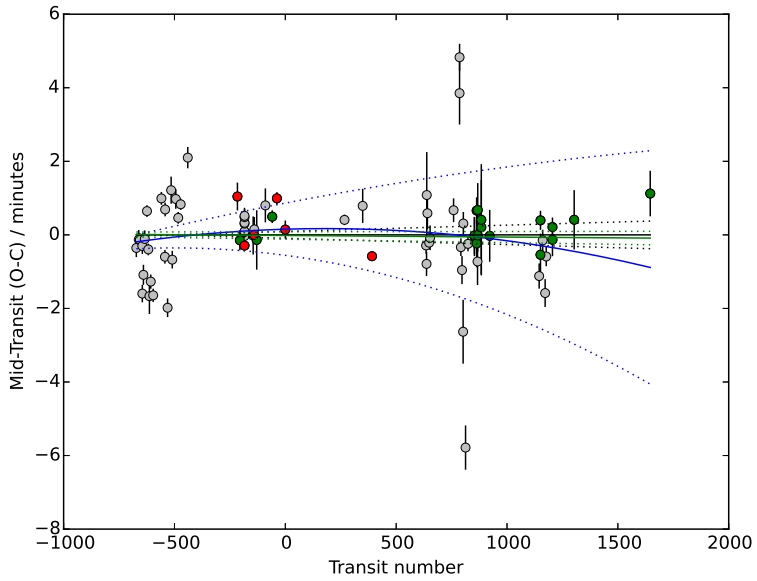

Figure 5.18: Transit times for all WASP-43 lightcurves. Caption as for Fig. 5.3. In addition, the green points use mid-transit time offsets for lightcurves observed by Murgas et al. (2014) and Hoyer et al. (2016) not used in the global analysis.

this is likely due to our different analysis methods and lightcurve ensembles. If we fit only the data used in Ciceri et al. (2016) our transit depth becomes shallower, differing from our presented solution at a 1.8σ level rather than the $\sim 7\sigma$ difference of the Ciceri et al. (2016) depth. This is also in part due to a larger depth uncertainty which reduces the significance of the depth difference. However, as we note, the rest of our physical parameters agree well.

The differences between the ephemerides is less easy to explain. As a check during our investigation of evidence for TTVs we fit a linear ephemeris by regression as Ciceri et al. (2016) do. This method finds a period in agreement with the one we find using our MCMC. This is the case if we include the mid-times from the Exoplanet Transit Database (ETD) presented by Ciceri et al. (2016) or not. In addition, we find no evidence of period variation with or without the EDT mid-times. We find a period difference of $(0.1 \pm 7.8) \times 10^{-7}$ days and $\dot{P} = (-0.5 \pm 2.0) \times 10^{-2}$ seconds per year

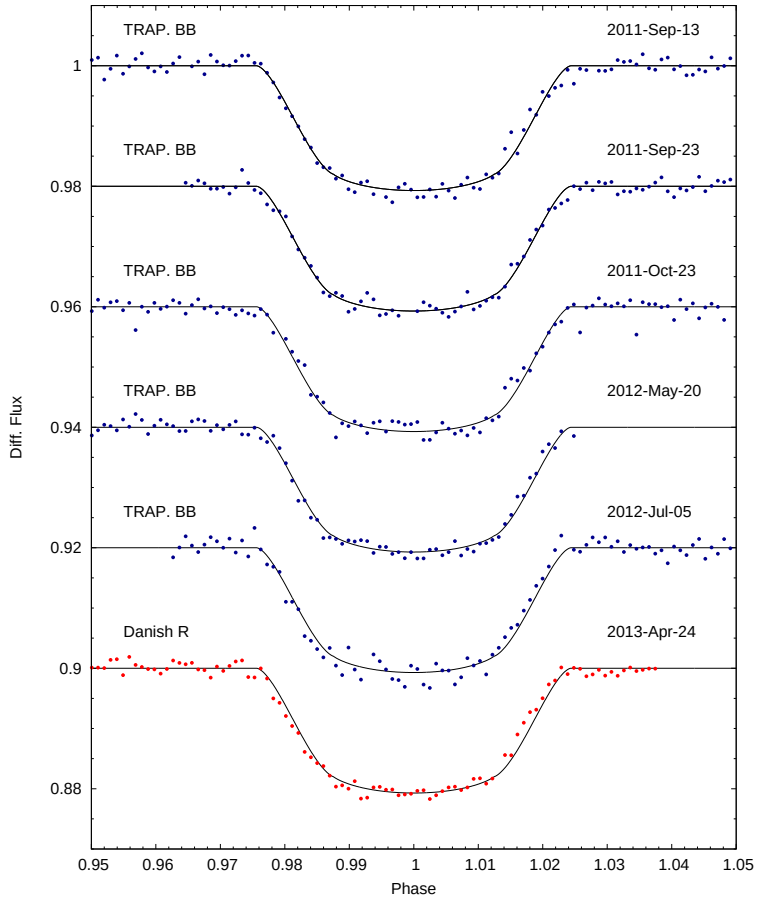

Figure 5.19: New data for WASP-46 b. Caption as for Fig. 5.1.

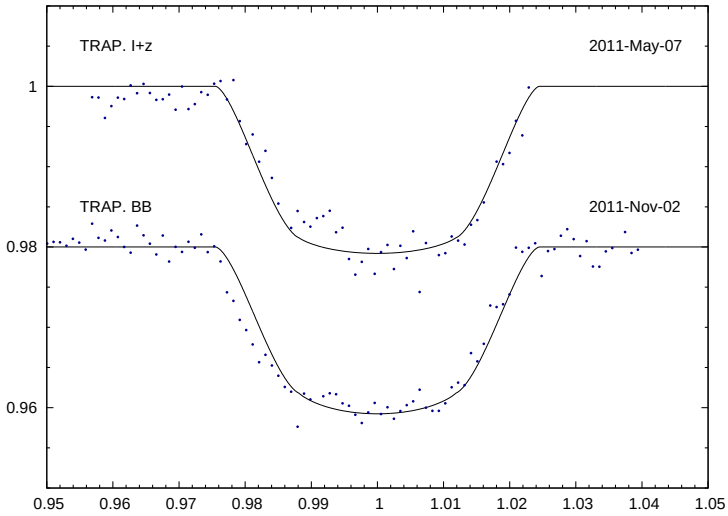

Figure 5.20: Data for WASP-46 b excluded from analysis. Caption as for Fig. 5.1.

when excluding the ETD mid times. While, using the ETD mid-times we find a period difference of $(0.56 \pm 9.99) \times 10^{-7}$ days and $\dot{P} = (0.7 \pm 4.3) \times 10^{-2}$ seconds per year, see Fig. 5.21.

5.5 Reliability of the Error Estimates

Some of the parameters we have determined show significant disagreement with the results of previous studies. There are several factors that can contribute to these discrepancies. This can be partly attributed to differences in analysis method, as shown with the WASP-24 system. In other cases, e.g. WASP-43, there are degeneracies in the fitting of parameters. Use and availability of different ensembles of data play a role, most prominently between updated results and the relevant discovery papers. In particular this is present in the parameters for WASP-24 and Sada et al. (2012). There are also model dependencies for derived parameters e.g. masses and radii which require constraints on these properties of the star which themselves are model dependent.

However, it is likely that the uncertainties on parameters derived directly from

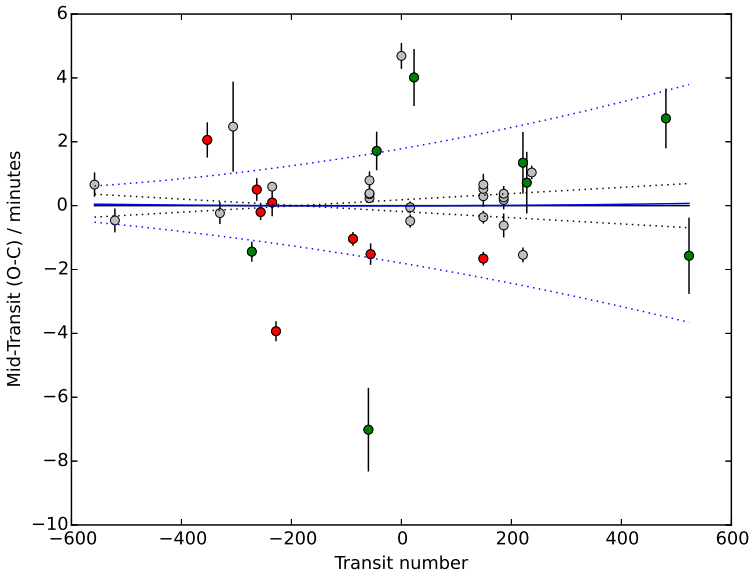

Figure 5.21: Transit times for all WASP-46 lightcurves. Caption as for Fig. 5.3. In addition, the green points use mid-transit time offsets of ETD lightcurves reported by Ciceri et al. (2016).

lightcurves are underestimates in general, here and in the literature more broadly. This is most evident for the TTV plots and is also illustrated in Fig.5.17 in which it is shown not to be confined to my results alone. The uncertainties in the system parameters presented here cover the same order of magnitude range as the other studies cited.

The underestimation of uncertainties is due to approximating the noise in the data as being well-modelled by a Gaussian distribution, i.e. white noise. The noise in transit observations is not purely white noise, time-correlated noise contributes as well. Applying models that assume purely white-noise is simpler but it can lead to underestimation of the uncertainties on derived parameters (Carter & Winn 2009). Observations made from the ground are particularly susceptible to underestimated errors due to the limited amount of time available to gather data out-of-transit to characterise the noise.

A possible solution is taking multiple observations and/or monitoring a system for a long time. This is expensive and time consuming. For example, in this chapter

WASP-43 has the most lightcurves available for analysis at 60. These have been gathered over a period of 7 years and have only been gathered in such volume due to this being a particularly interesting and short-period system. Even then, this large number of lightcurves comes from a variety of different instruments which will have a varying contribution and characteristic of time-correlated noise. By comparison, WASP-37 has the fewest available most of which have been provided by this work.

There are also methods being developed to include noise as a free parameter similar to the idea of including jitter in the radial velocity models mentioned in chapter 4. Carter & Winn (2009) detail a method using wavelets to model noise, including red noise. Alternatively, Gibson et al. (2012) use Gaussian processes to infer transit parameters in the presence of systematic noise. Their method "naturally allows for the correlated nature of the noise".

5.6 Conclusions

We have presented new data of seven known WASP exoplanets. We find parameters that are largely in agreement with previous studies with an increase in precision in many cases. We resolve the apparent discrepancy in the orbital inclination of WASP-31 b with our new photometry. We suggest that WASP-42 has the potential to be a strong probe of tidal interaction that hot-Jupiters are expected to undergo. We also suggest that orbital decay in the WASP-43 system is still an open question. We also make a case for the re-observation of planets with only one or two published lightcurves. If there are few lightcurves available that were were observed close together, the effects of temporary features like unocculted star spots may be missed. For example, if at publication a system only had lightcurves analogous to the anomalous data for WASP-31, the system would be found to have erroneous parameters. Erroneous parameters could then cause anomalies when ensembles of similar planets are studied.

Parameter (Unit)	**This Work**	Hoyer et al. (2016)	Jiang et al. (2016)	Ricci et al. (2015)	Murgas et al. (2014)
Period (d)	$\mathbf{0.813473919 \pm 0.000000037}$	$0.813473978 \pm 0.000000035$	$0.81347395 \pm 0.00000004$	$0.813473740 \pm 0.000000073$	$0.81347385 \pm 0.00000015$
Transit Epoch, T_0	$\mathbf{6563.60748 \pm 0.00003}$	5528.868634 ± 0.000046	5528.868605 ± 0.000036	5528.868483 ± 0.000037	5528.86861 ± 0.00011
Transit Duration, T_{14} (d)	$\mathbf{0.050032 \pm 0.000081}$	–	–	–	–
Scaled Semi-major Axis, a/R_*	$\mathbf{4.99 \pm 0.02}$	4.867 ± 0.023	4.837 ± 0.021	4.82 ± 0.11	4.752 ± 0.066
Transit Depth, $(R_p/R_*)^2$	$\mathbf{0.025205^{+0.000073}_{-0.000092}}$	0.025415 ± 0.000021	0.025373 ± 0.000023	0.02557 ± 0.00013	0.02556 ± 0.00044
Impact Parameter, b	$\mathbf{0.6432 \pm 0.0043}$	–	–	–	0.684 ± 0.018
Orbital Inclination, i (°)	$\mathbf{82.592 \pm 0.079}$	82.1 ± 0.1	82.149 ± 0.085	81.92 ± 0.54	81.72 ± 0.32

Parameter (Unit)	This Work	Chen et al. (2014)	Stevenson et al. (2014)	Gillon et al. (2012)	Hellier et al. (2011)	Hellier et al. (2011) (Alt.)
Period (d)	$\mathbf{0.813473919 \pm 0.000000037}$	$0.81347437 \pm 0.00000013$	–	$0.81347753 \pm 0.00000071$	0.813475 ± 0.000001	0.813475 ± 0.000001
Transit Epoch, T_0	$\mathbf{6563.60748 \pm 0.00003}$	5934.79224 ± 0.00004	–	5726.54336 ± 0.00012	5528.86774 ± 0.00014	5528.86774 ± 0.00014
Transit Duration, T_{14} (d)	$\mathbf{0.050032 \pm 0.000081}$	0.05115 ± 0.00022	–	0.05037 ± 0.00022	0.0483 ± 0.0011	0.0483 ± 0.0011
Scaled Semi-major Axis, a/R_*	$\mathbf{4.99 \pm 0.02}$	4.97 ± 0.05	4.855 ± 0.002	4.918 ± 0.052	–	–
Transit Depth, $(R_p/R_*)^2$	$\mathbf{0.025205^{+0.000073}_{-0.000092}}$	0.02478 ± 0.00013	0.0254339 ± 0.0000002	0.02542 ± 0.00024	0.0255 ± 0.0012	0.0255 ± 0.0012
Impact Parameter, b	$\mathbf{0.6432 \pm 0.0043}$	0.64 ± 0.01	–	0.66 ± 0.01	$0.66^{+0.04}_{-0.07}$	$0.66^{+0.04}_{-0.07}$
Orbital Inclination, i (°)	$\mathbf{82.592 \pm 0.079}$	82.64 ± 0.19	82.11 ± 0.01	82.3 ± 0.2	$82.6^{+1.3}_{-0.9}$	$82.6^{+1.3}_{-0.9}$
Semi-amplitude, K_1(ms^{-1})	$\mathbf{550.7 \pm 6.6}$	–	–	547.9 ± 5.5	550.3 ± 6.7	550.3 ± 6.7
Semi-major Axis, a (au)	$\mathbf{0.015012 \pm 0.000014}$	0.01524 ± 0.00025	–	0.01526 ± 0.00018	0.0142 ± 0.0004	0.0142 ± 0.0004
Stellar Mass, M_* ($M_\odot$)	$\mathbf{0.6820 \pm 0.0019}$	0.713 ± 0.019	–	0.717 ± 0.025	0.58 ± 0.05	0.71 ± 0.05
Stellar Radius, R_* ($R_\odot$)	$\mathbf{0.6473 \pm 0.0026}$	0.6600 ± 0.0085	–	0.67 ± 0.01	$0.60^{+0.03}_{-0.04}$	0.67 ± 0.04
Stellar Density, ρ_* ($\rho_\odot$)	$\mathbf{2.51 \pm 0.03}$	2.482 ± 0.075	–	2.410 ± 0.077	$2.70^{+0.61}_{-0.36}$	2.35 ± 0.35
Stellar Surface Gravity, log(g_*) (cgs)	$\mathbf{4.6493 \pm 0.0035}$	4.652 ± 0.006	–	4.64 ± 0.01	$4.65^{+0.06}_{-0.04}$	$4.65^{+0.06}_{-0.04}$
Stellar Effective Temperature, $T_{\rm eff}$ (K)	$\mathbf{4656 \pm 45}$	4536 ± 92	–	4520 ± 120	4400 ± 200	4400 ± 200
Stellar Metallicity, [Fe/H]	–	???±???	–	-0.01 ± 0.12	-0.05 ± 0.17	-0.05 ± 0.17
Planet Mass, M_p ($M_{\rm Jup}$)	$\mathbf{1.982 \pm 0.023}$	2.029 ± 0.038	–	2.034 ± 0.051	1.8 ± 0.1	2.0 ± 0.1
Planet Radius, R_p ($R_{\rm Jup}$)	$\mathbf{0.9997 \pm 0.0053}$	1.034 ± 0.014	–	1.036 ± 0.019	$0.93^{+0.07}_{-0.09}$	1.06 ± 0.05
Planet Density, ρ_p ($\rho_{\rm Jup}$)	$\mathbf{1.985 \pm 0.042}$	2.434 ± 0.066	–	1.826 ± 0.081	$2.21^{+0.73}_{-0.41}$	0 ± 0
Planet Surface Gravity, log(g_p) (cgs)	$\mathbf{3.6569 \pm 0.0074}$	3.692 ± 0.009	–	3.672 ± 0.013	$3.672^{+0.081}_{-0.059}$	$3.672^{+0.081}_{-0.059}$
Planet Equilibrium Temperature, T_{eq}(K)	$\mathbf{1474 \pm 15}$	–	–	1440 ± 40	1370 ± 70	1370 ± 70

Table 5.9: System parameters of WASP-46

Parameter (Unit)	This Work	Ciceri et al. (2016)	Anderson et al. (2012)
Period (d)	$\mathbf{1.43037307 \pm 0.00000018}$	$1.43036763 \pm 0.00000093$	1.4303700 ± 0.0000023
Transit Epoch, T_0	$\mathbf{6296.311353 \pm 0.000035}$	5392.31659 ± 0.00058	5392.3155 ± 0.0002
Transit Duration, T_{14} (d)	$\mathbf{0.06886 \pm 0.00014}$	–	0.0697 ± 0.0009
Scaled Semi-major Axis, a/R_*	$\mathbf{5.820 \pm 0.027}$	5.851 ± 0.038	5.74 ± 0.15
Transit Depth, $(R_p/R_*)^2$	$\mathbf{0.020461 \pm 0.000073}$	0.019811 ± 0.000014	0.02155 ± 0.00049
Impact Parameter, b	$\mathbf{0.7292 \pm 0.0038}$	–	0.737 ± 0.019
Orbital Inclination, i (°)	$\mathbf{82.803 \pm 0.071}$	82.80 ± 0.17	82.63 ± 0.38
Semi-amplitude, $K_1(\mathrm{ms}^{-1})$	$\mathbf{381.2^{+4.8}_{-6.5}}$	–	387 ± 10
Semi-major Axis, a (au)	$\mathbf{0.02378 \pm 0.00068}$	0.02335 ± 0.00063	0.02448 ± 0.00028
Stellar Mass, M_* ($M_\odot$)	$\mathbf{0.877 \pm 0.076}$	0.828 ± 0.067	0.956 ± 0.034
Stellar Radius, R_* ($R_\odot$)	$\mathbf{0.879 \pm 0.026}$	0.858 ± 0.024	0.917 ± 0.028
Stellar Density, ρ_* ($\rho_\odot$)	$\mathbf{1.291 \pm 0.018}$	1.310 ± 0.025	1.2 ± 0.1
Stellar Surface Gravity, $\log(g_*)$ (cgs)	$\mathbf{4.493 \pm 0.013}$	4.489 ± 0.013	4.493 ± 0.023
Stellar Effective Temperature, T_{eff} (K)	$\mathbf{5939 \pm 109}$	–	5620 ± 160
Stellar Metallicity, [Fe/H]	$\mathbf{-0.37 \pm 0.13}$	–	-0.37 ± 0.13
Planet Mass, M_p (M_{Jup})	$\mathbf{1.96 \pm 0.12}$	1.91 ± 0.11	2.101 ± 0.073
Planet Radius, R_p (R_{Jup})	$\mathbf{1.223 \pm 0.037}$	1.174 ± 0.033	1.310 ± 0.051
Planet Density, ρ_p (ρ_{Jup})	$\mathbf{1.067 \pm 0.042}$	1.10 ± 0.05	0.94 ± 0.11
Planet Surface Gravity, $\log(g_p)$ (cgs)	$\mathbf{3.4749^{+0.0094}_{-0.0075}}$	3.54 ± 0.14	3.447 ± 0.033
Planet Equilibrium Temperature, T_{eq}(K)	$\mathbf{1741 \pm 34}$	1636 ± 44	1654 ± 50

6 WASP-120 b, WASP-122 b and WASP-123 b: Three newly discovered planets from the WASP-South survey

6.1 Introduction

This chapter presents the discovery of three planets; WASP-120 b, WASP-122 b and WASP-123 b. Its contents are originally a paper published in the Publications of the Astronomical Society of the Pacific, Volume 128, Issue 964 with myself as the lead author. I performed the analysis, interpretation of the data and wrote the paper. Vetting of the WASP discovery data was performed by Coel Hellier. Radial velocity follow-up observations and reductions were made by Amaury Triaud. Photometric follow-up observations with the TRAPPIST Telescope and their data reduction was performed by Laetitia Delrez while those using EulerCam we performed by Monika Lendl. Pierre Maxted checked the WASP lightcurves for rotational modulation, Barry Smalley performed the spectroscopic analysis of the host stars and Daniel Evans performed the calculations to check the plausibility that WASP-120 is physically associated with a faint companion star.

The Wide Angle Search for Planets (WASP) survey is a prolific contributor to the field of exoplanet science having published the discovery of 104 planets to date. Our effective magnitude range of $9 < V < 13$ means that WASP systems are conducive to further study. Examples from the extremes of this range are the bright WASP-33 ($V = 8.3$; Collier Cameron et al. 2010) and WASP-18 ($V = 9.3$; Hellier et al. 2009) and the relatively dim WASP-112 ($V = 13.3$; Anderson et al. 2014, Sub.).

Here we present the discovery of: WASP-120 b, a system with a star showing variable activity and a possibly eccentric planet orbit, WASP-122 b, which offers a good opportunity for atmospheric study, and WASP-123 b, which orbits an old star, ~ 7 Gyr.

6.2 Observations

The transits of these planets were discovered in photometry gathered from the WASP-South installation hosted by the South African Astronomical Observatory. The WASP-South instrument is an array of 8 cameras using 200mm $f/1.8$ lenses to survey the sky at a cadence of $\sim$ 10 minutes. For more information on the WASP instrument, see Pollacco et al. (2006). The data were processed and searched for transits as described in Collier Cameron et al. (2006) with candidate selection following the procedure in Collier Cameron et al. (2007). A more detailed description of these procedures can also be found in Chapter 2. Details of observations for each star in this chapter can be found in Table 6.1. The phase-folded WASP data are displayed in the top panels of Figs. 6.1, 6.2 and 6.3. We used the method of Maxted et al. (2011) to search the WASP photometry for modulations caused by star spots. We detected no rotational modulation above 2 mmag which suggests that the hosts are inactive.

We obtained spectra of the three stars with the CORALIE spectrograph on the 1.2-m Swiss telescope as outlined in Table 6.1. We used these data to measure radial velocity (RV) variations and confirm the planetary nature of the candidates (Table 6.2; Bottom panel of Figs. 6.1, 6.2 and 6.3). We obtained 9 of the WASP-120 spectra after the spectrograph was upgraded in November 2014. The lack of correlation between the bisector spans and RVs (Fig. 6.4) indicate that the RV variations are not a result of blended eclipsing binaries. For example, Santos et al. (2002) found a brown dwarf mass companion that produces a correlation between the RVs and bisector spans with a gradient of 0.67. The largest gradient from amongst our planets is an order of magnitude smaller and not significant; 0.06 ± 0.07 for WASP-120. While we cannot strictly rule out the case of blended planet hosting stars we can eliminate brown dwarf blends and more massive objects.

We acquired the follow-up photometry needed to accurately determine the system parameters from the 0.6-m TRAPPIST telescope (Gillon et al. 2011b) and EulerCam (Lendl et al. 2012) on the Swiss telescope at La Silla, Chile. The TRAPPIST telescope's equatorial mount requires a meridian flip when the target culminates during an

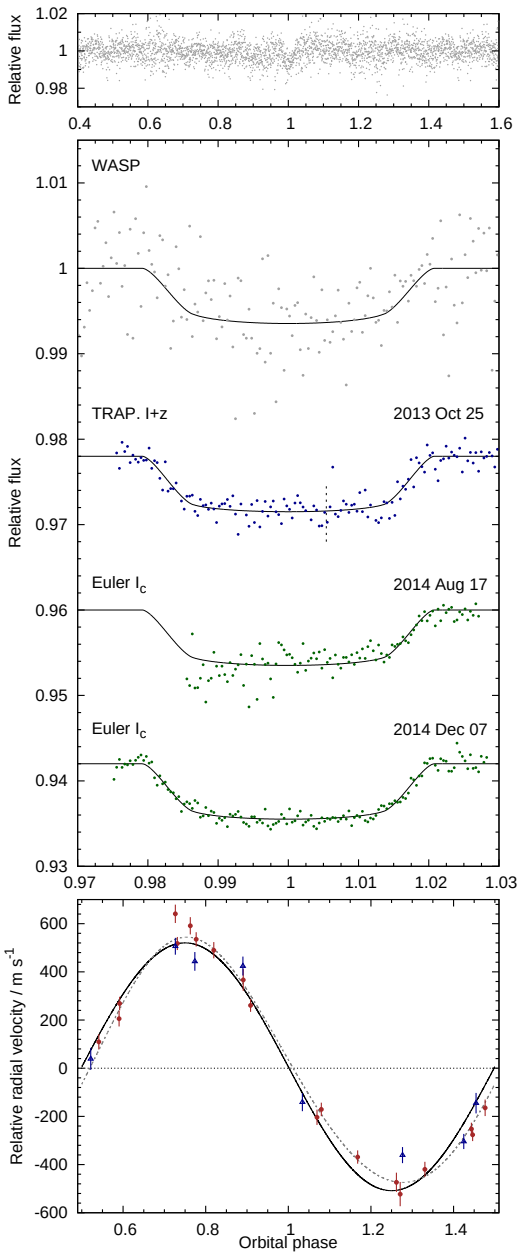

Figure 6.1: Discovery data for WASP-120 b. Top panel: Phase folded WASP photometry for WASP-120. Middle panel: WASP discovery photometry (grey), TRAPPIST (blue) and EulerCam (green) follow-up photometry with our transit model over-plotted. The meridian flip in the TRAPPIST data has been corrected for and marked with a vertical dashed line. All photometric data have been binned with a duration of 2 minutes for clarity. Bottom panel: CORALIE radial velocity data from before (red circles) and after (blue triangles) the upgrade, over-plotted with the circular (black-solid) and eccentric (grey-dashed) solutions.

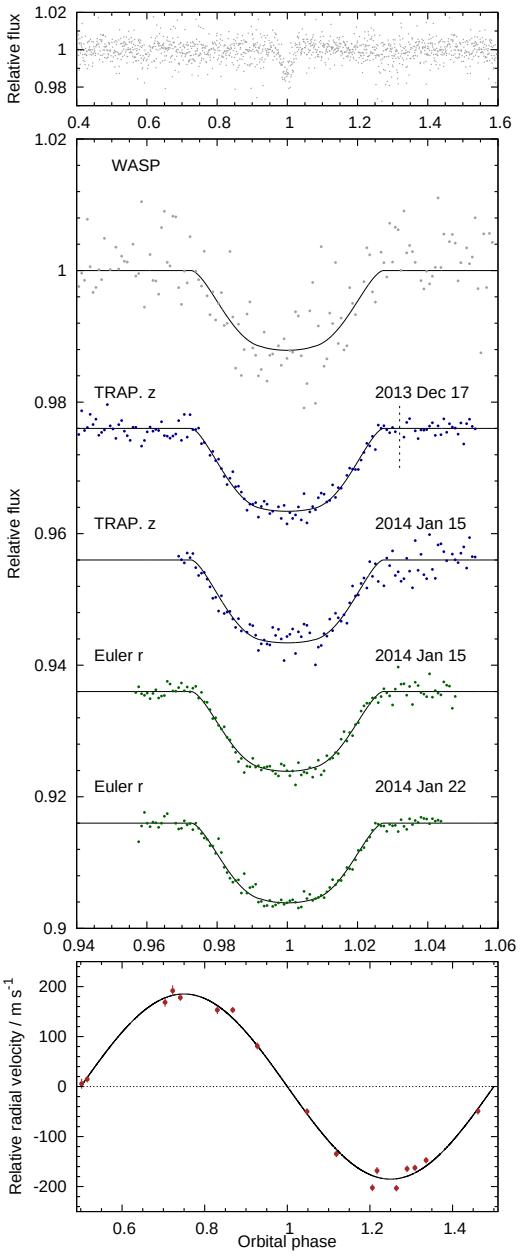

Figure 6.2: Discovery data for WASP-122 b. Top panel: Phase folded WASP photometry for WASP-122. Middle panel: WASP discovery photometry (grey), TRAPPIST (blue) and EulerCam (green) follow-up photometry with our transit model over-plotted. The meridian flip in the TRAPPIST data has been corrected for and marked with a vertical dashed line. All photometric data have been binned with a duration of 2 minutes for clarity. Bottom panel: CORALIE radial velocity data, over-plotted with our circular solution.

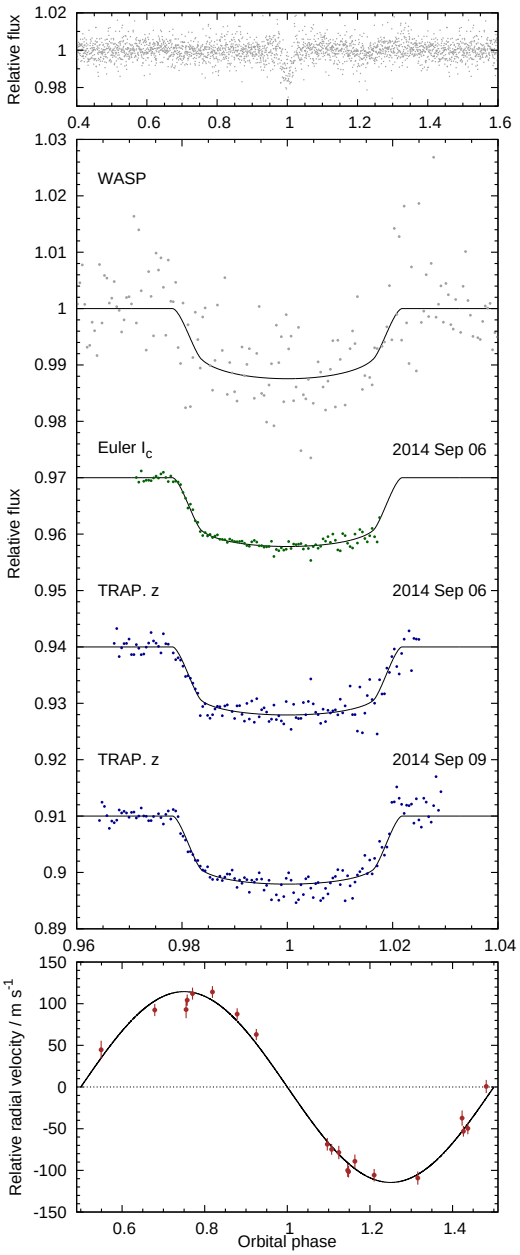

Figure 6.3: Discovery data for WASP-123 b. Caption as for Fig. 6.2.

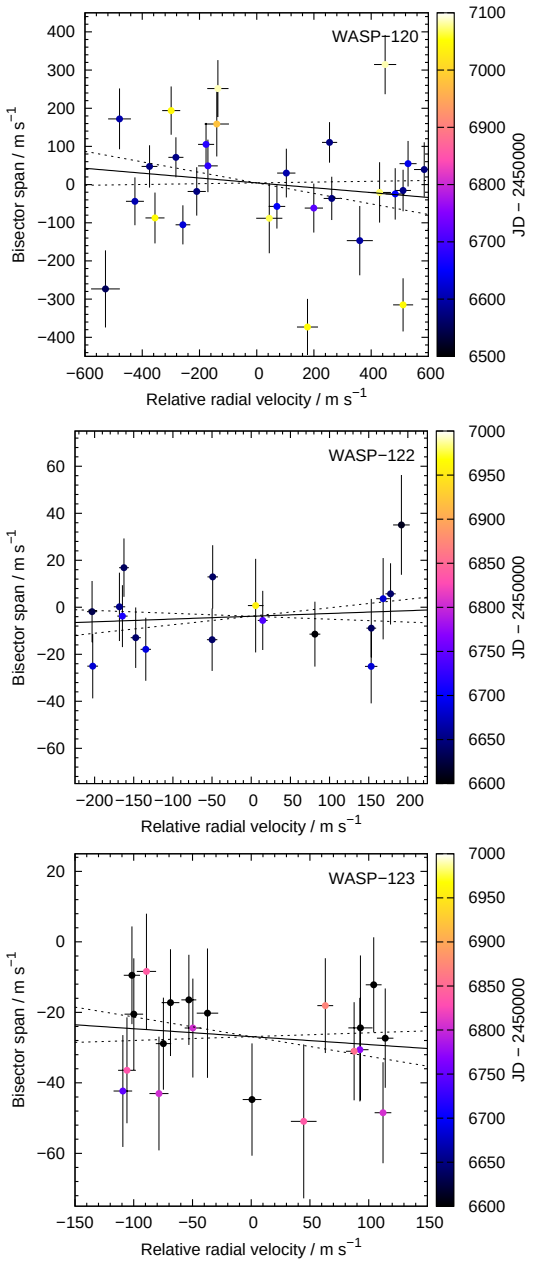

Figure 6.4: Bisector spans plotted against relative radial velocities for WASP-120 (top), WASP-122 (middle) and WASP-123 (bottom) showing no correlation. Solid lines are results of least-squares fits to the data, dashed lines are the 1σ uncertainties of the fits. Date of observation is denoted by point colour. The increased dispersion of points seen in more recent data for WASP-120 is attributed to an increase in stellar activity.

Table 6.1: Observations of WASP-120, WASP-122 and WASP-123

Date	Source	N.Obs. / Filter	Comment
WASP-120			
2006 Aug–2012 Jan	WASP-South	27 079	
2013 Sep–2015 Mar	CORALIE	29	
2013 Nov 12	TRAPPIST	I+z	Meridian flip
2014 Aug 17	EulerCam	I_c	
2014 Dec 07	EulerCam	I_c	
WASP-122			
2011 Oct–2012 Mar	WASP-South	4 834	
2013 Nov–2014 Oct	CORALIE	17	
2013 Dec 17	TRAPPIST	z	Meridian flip
2014 Jan 15	TRAPPIST	z	Slight cloud
2014 Jan 15	EulerCam	r	Slight cloud
2014 Jan 22	EulerCam	r	Slight cloud
WASP-123			
2006 May–2012 Jun	WASP-South	13 267	
2013 Sep–2014 Aug	CORALIE	20	
2014 Sep 06	EulerCam	I_c	
2014 Sep 06	TRAPPIST	z	
2014 Sep 09	TRAPPIST	z	

Table 6.2: Radial velocity data from CORALIE. Data available in this format at CDS. The data are provided to the full precision used in our calculations but times are only accurate to a few seconds at best.

HJD − 2 540 000	RV (km s^{-1})	Error (km s^{-1})	BS (km s^{-1})	Target Name
6552.902673	19.30305	0.05043	−0.27331	WASP-120
6572.735422	20.41666	0.03569	0.03952	WASP-120
6573.843533	19.62205	0.03173	−0.01785	WASP-120
...	...	...	...	...
...	...	...	...	...
6871.746191	16.99747	0.00673	−0.01808	WASP-123

observation. These occurred at BJD = 2456609.725 during the transit of WASP-120 on 2013 Nov 12 and at BJD = 2456644.758 during the transit of WASP-122 on 2013 Dec 17. We account for any offsets introduced by treating them as two separate datasets during our analysis. The photometric data are presented in Table 6.3. This follow up revealed a star within 2.2" of WASP-120 which is 4.35 ± 0.02 magnitudes fainter in the I band and 3.89 ± 0.02 magnitudes fainter in the z band. CORALIE's fibres are 2" in diameter and the RVs were obtained in good seeing, so the star is sufficiently distant that it did not contaminate the observations and thus could not cause a false positive.

Table 6.3: Follow-up photometry from TRAPPIST and EulerCam. Data available in this format at CDS. The data are provided to the full precision used in our calculations but times are only accurate to a few seconds at best.

HJD_{UTC} − 2 540 000	Norm. Flux	Error	ΔX Position	ΔY Position	Airmass	Target FWHM	Sky Bkg. (Counts)	Exp. Time (s)	Target Name	Instrument	Band
6887.720753	0.990347	0.002159	−1.91	−2.21	2.64	11.12	71.30	50.00	WASP-120	EulerCam	IC
6887.721534	0.996407	0.002145	0.25	−1.40	2.62	12.18	70.00	50.00	WASP-120	EulerCam	IC
6887.722324	0.994713	0.002114	0.06	−1.04	2.60	10.85	68.82	50.00	WASP-120	EulerCam	IC
...	...	...	...	...	...	...	...	...	...	...	...
...	...	...	...	...	...	...	...	...	...	...	...
6910.766640	0.992689	0.008096	−0.92	−0.64	2.91	4.08	293.86	13.00	WASP-123	TRAPPIST	z

Table 6.4: Limb-darkening parameters extrapolated using the $T_{\rm LD}$ resulting from each analysis.

Planet	Instrument	Instrument Band	Claret band	a_1	a_2	a_3	a_4
WASP-120	WASP	Broadband (400-700 nm)	Cousins R	0.136	1.286	−1.188	0.391
	TRAPPIST	I+z	Sloan z	0.221	0.827	−0.760	0.226
	EulerCam	Cousins I	Cousins I	0.200	0.951	−0.863	0.263
WASP-122	WASP	Broadband (400-700 nm)	Cousins R	0.717	−0.503	1.076	−0.515
	TRAPPIST	z	Sloan z	0.799	−0.743	1.095	−0.492
	EulerCam	Gunn R	Cousins R	0.717	−0.503	1.076	−0.515
WASP-123	WASP	Broadband (400-700 nm)	Cousins R	0.683	−0.405	0.957	−0.473
	TRAPPIST	z	Sloan z	0.766	−0.664	1.010	−0.462
	EulerCam	Cousins I	Cousins I	0.763	−0.639	1.059	−0.491

6.3 Analysis

6.3.1 Stellar Parameters

We determined the atmospheric parameters of each host star by analysing the co-added CORALIE spectra after correcting them for shifts due to the radial motion of the star using the measured RVs. Our spectral analysis followed procedures given in Doyle et al. (2013). For each star we obtained the effective temperature, $T_{\rm eff}$, using the Hα line, $\log g$ from the Na D and Mg b lines and iron abundances from the analysis of equivalent width measurements of several unblended Fe I lines. We found the projected rotation velocity, $V \sin i$, by fitting the profiles of the Fe I lines after convolving with the instrumental resolution ($R = 55\,000$) and a macroturbulent velocity adopted from the calibration of Doyle et al. (2014).

6.3.2 System Parameters

We used a Markov chain Monte Carlo (MCMC) code to determine the system parameters using the discovery and follow-up photometry with RVs as described by Collier Cameron et al. (2007) and Anderson et al. (2015b).

For each system we modelled our transit lightcurves using the formulation of

Mandel & Agol (2002) and accounted for limb-darkening using the four-parameter non-linear law of Claret (2000, Claret (2004). The photometric bands and limb-darkening coefficients used in the lightcurve models are detailed in Table 6.4.

We used BAGEMASS (Maxted, Serenelli & Southworth 2015) to compare ρ_*, determined from the transit lightcurves coupled with the spectroscopic values of [Fe/H] and $T_{\rm eff}$, to stellar models in order to estimate the mass of the star. BAGEMASS also gives an estimate of the age of the system.

To calculate the distance we use the apparent K_s band magnitude from Skrutskie et al. (2006), the radius of the star from Table 6.5 and the angular diameter of the star based on the calibration of K-band surface brightness – effective temperature relation from Kervella et al. (2004). We assume that interstellar reddening is negligible and that K= $K_s + 0.044$.

The free parameters in our MCMC analysis were T_0, P, $(R_P/R_*)^2$, T_{14}, b, K_1, γ, [Fe/H] and $T_{\rm LD}$. Here T_0 is the epoch of mid-transit, P, is the orbital period, $(R_P/R_*)^2$ is the planet-to-star area ratio, T_{14} is the total transit duration, b is the impact parameter of the planet's path across the stellar disc, K_1 is the reflex velocity semi-amplitude, γ is the systemic velocity, [Fe/H] is the stellar metallicity and $T_{\rm LD}$ is the limb-darkening temperature. $T_{\rm LD}$ and [Fe/H] were constrained by the spectroscopic values of $T_{\rm eff}$ and [Fe/H]. $T_{\rm LD}$ was used by the MCMC to interpolate limb-darkening coefficients at each step from the Claret limb-darkening tables for the appropriate photometric band of each lightcurve. At each step of our MCMC these values were perturbed by a small random value and the χ^2 of the model based on the new values was calculated. If this lead to a lower χ^2 the step was accepted while a larger value would be accepted with a probability proportional to $\exp(-\Delta\chi^2/2)$. Our final values were calculated from the medians of the posterior distributions with uncertainties corresponding to the 1σ confidence intervals. When we allow the MCMC to explore eccentric solutions we fit $\sqrt{e}\cos\omega$ and $\sqrt{e}\sin\omega$ to ensure a uniform probability distribution. Our results for each system are in the lower part of Table 6.5 and corner plots of the jump parameter posterior distributions of each analysis in Figures 6.5, 6.6 and 6.7.

We checked for trends in the derived transit depths with respect to the colour of

the observational band for each star by running each lightcurve through our MCMC separately. The depths for WASP-122 and WASP-123 agree to within 1σ of the depth derived from the combined analysis. The depths from this analysis of the two complete lightcurves of WASP-120 show a slight difference of $(1.2 \pm 0.4) \times 10^{-3}$ which could be accounted for by a low level of inherent stellar variability in either the host star or faint, nearby companion.

6.3.3 Gyrochronological Ages

Where possible, we used the gyrochronology calibrations of Barnes (2007), Mamajek & Hillenbrand (2008) and Meibom, Mathieu & Stassun (2009) to estimate the lower limits of the stellar ages. Each calibration is a function of the star's rotational period and colour with the form:

$$\log \tau = \left[\log P_{\rm rot} - \log a - b \log((\mathrm{B}-\mathrm{V}) - c)\right] / n \tag{6.1}$$

Where, τ is the age, $P_{\rm rot}$ is the stellar rotational period, $(\mathrm{B}-\mathrm{V})$ is the colour and a, b, c and n are constants dependant on the calibration. As the discovery lightcurves do not show significant rotational modulation that could be used to suggest a rotational period. Instead we use the spectral $V \sin i_*$ and the stellar radius given by our MCMC. As we have no constraint on i_* the stellar rotational velocity estimated from the $V \sin i_*$ is a lower limit. Thus, the period calculated using the $V \sin i_*$ represents an upper limit:

$$P_{\rm rot} \leq \frac{2\pi R_*}{V \sin i_*} \tag{6.2}$$

As a result, the ages calculated in this way give maximum age estimates.

6.4 WASP-120

WASP-120 b is a 4.85-$M_{\rm Jup}$, 1.73-$R_{\rm Jup}$ planet orbiting a moderately bright ($V = 11.0$) F5 star. The effective temperature of WASP-120 places it in the lithium gap (Böhm-

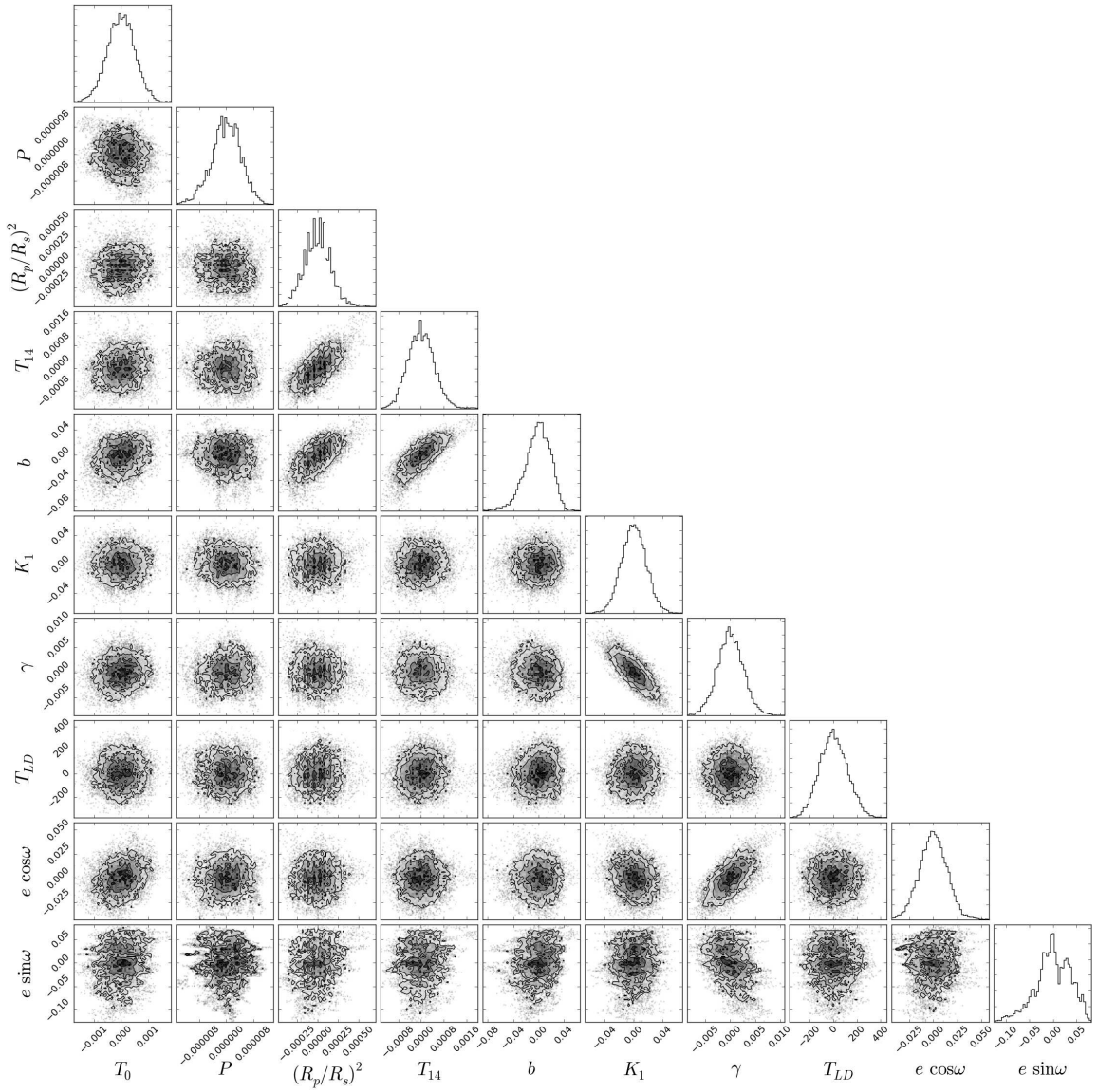

Figure 6.5: Plots showing the relationships of various jump parameters T_0, P, $(R_P/R_*)^2$, T_{14}, b, K_1, γ, [Fe/H], $T_{\rm LD}$, $\sqrt{e}\cos\omega$ and $\sqrt{e}\sin\omega$ from the analysis of WASP-120. All distributions have had the mean value from Table 6.5 subtracted. Plots were prepared with a modifed version of trangle.py by Foreman-Mackey et al. (2014)

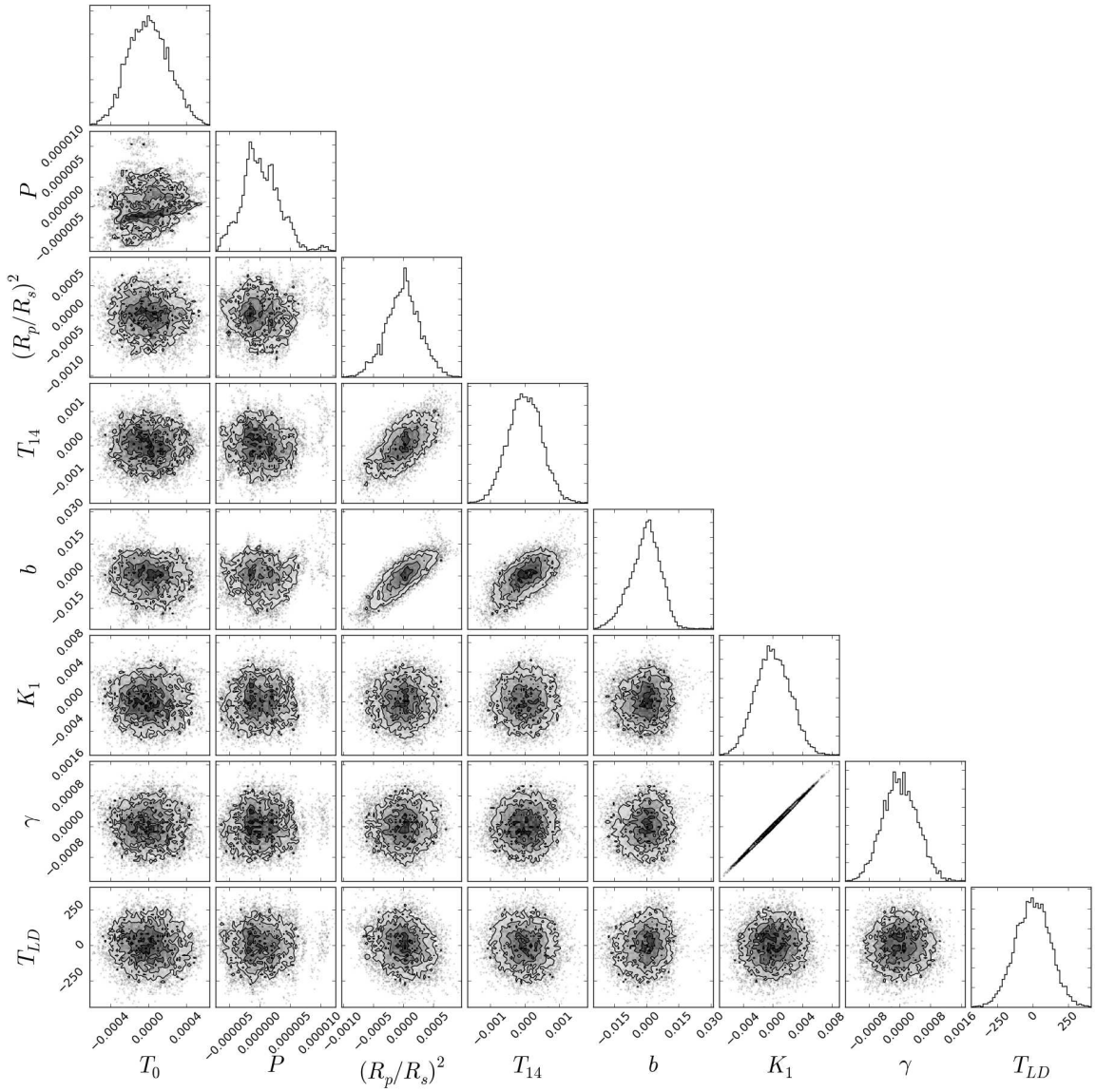

Figure 6.6: Caption as for Fig. 6.5 for WASP-122. As we enforced a circular orbit we did not fit $\sqrt{e}\cos\omega$ and $\sqrt{e}\sin\omega$.

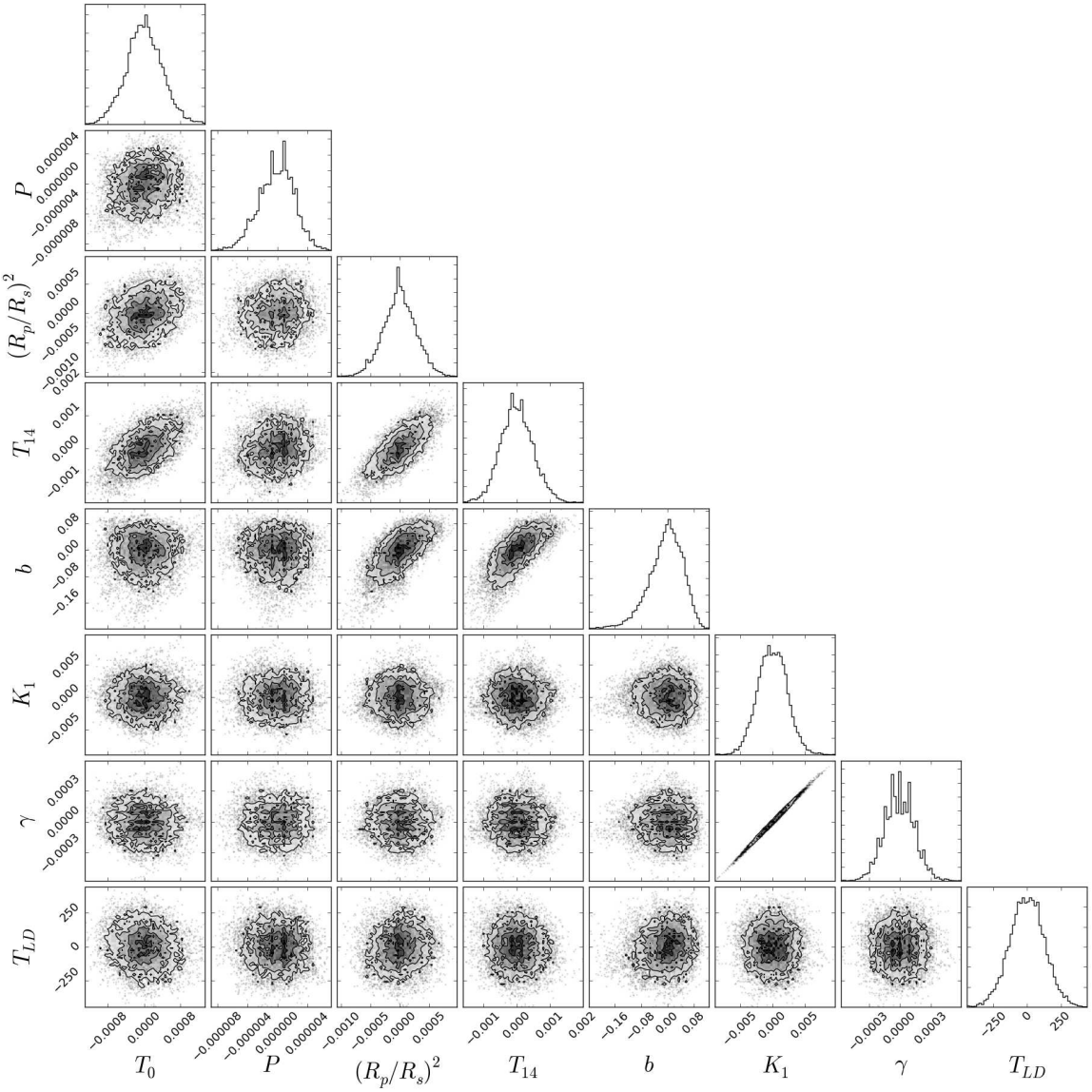

Figure 6.7: Caption as for Fig. 6.6 for WASP-123.

Vitense 2004), so we cannot estimate the age of this star based on the lithium abundance. Using the gyrochronology calibration of Barnes (2007) we estimate an age of 0.7 ± 0.6 Gyr. For comparison, the calibration of Mamajek & Hillenbrand (2008) gives 1.0 ± 1.8 Gyr. We cannot apply the calibration of Meibom, Mathieu & Stassun (2009) as the star's colour results in a term requiring the logarithm of a negative value. Using BAGEMASS we find an age of 2.6 ± 0.5 Gyr which is consistent with that of the Mamajek & Hillenbrand calibration.

The FWHM of the lines in the spectra and the bisector spans show more scatter in the later data, after the CORALIE upgrade (Fig. 6.9), suggesting that the star may have become more active, and therefore have variable activity like the Sun. It is unlikely that the increased scatter is caused by the change to CORALIE since datasets on other stars don't show an increased scatter (e.g. recent RV data taken of WASP-47; Neveu-VanMalle et al. 2016).

Due to the upgrade to CORALIE we partitioned the data into two sets. We added jitter of 5.1 ± 0.2 $\mathrm{m\,s^{-1}}$ to the older data and 6.3 ± 0.8 $\mathrm{m\,s^{-1}}$ to the newer data. These values were adopted such that both datasets gave reduced χ^2 values of one compared to a circular-orbit solution, and are in keeping with jitter determined for similar stars by Wright (2005). The uncertainties were estimated using a jackknife re-sampling. The difference between the jitter values of 0.8 ± 0.8 is consistent with zero, thus the jitter values are consistent to 1σ.

Our resulting orbital solution had an eccentricity of $0.057^{+0.022}_{-0.018}$. This is significantly non-zero at 3.3σ, while a Lucy-Sweeney test (Lucy & Sweeney 1971) gives a probability of only 0.1% that the orbit is circular. We note, though, that this result is somewhat dependent on the jitter values used. Fitting with no jitter increased the eccentricity to 0.068 ± 0.014. This led to a higher apparent significance (4.9σ) though the Lucy-Sweeney test no longer excluded the circular solution since neither solution is a good fit to the data. We thus adopt the value of eccentricity with jitter added but regard this as needing confirmation.

More massive planets, such as WASP-120 b at 5.0-M_{Jup}, often have eccentric orbits (Fig 6.11), though it is unclear if the correlation is due to a real phenomenon

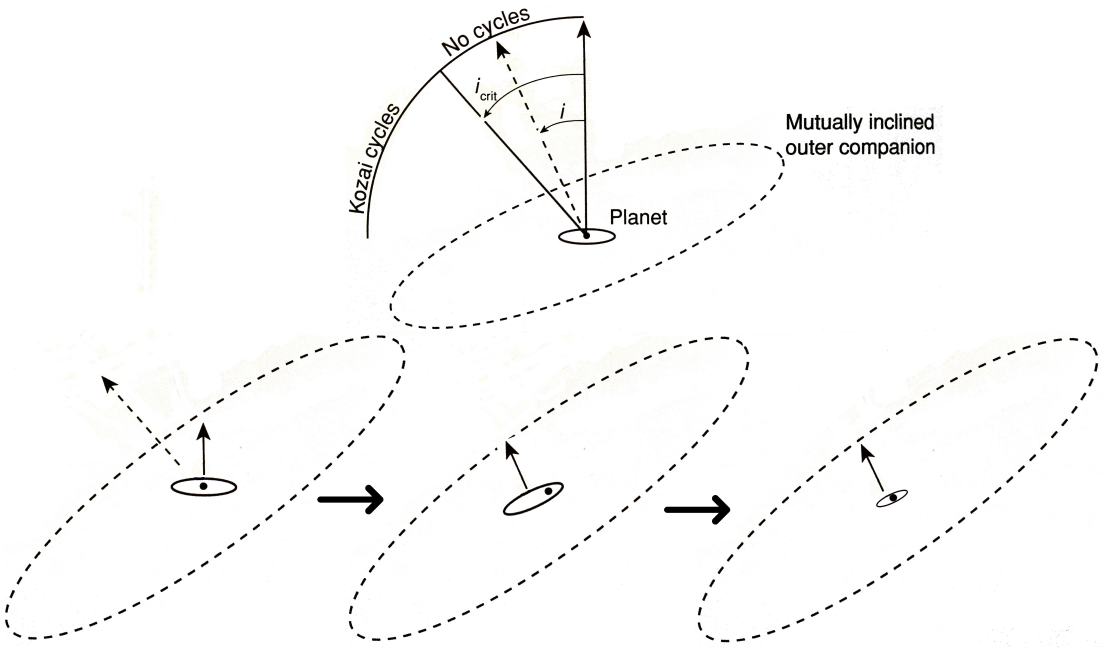

Figure 6.8: Illustration of migration via the Kozai-Lidov mechanism modified from (Armitage 2013) figure 7.6. Top: Configuration required for Kozai-Lidov cycles to be induced. Bottom-left: Initial orientation; Bottom-Middle: Planet orbit inclination has been changed and its eccentricity increased. Bottom-Right: Orbit after tidal circularisation.

or observation bias as the eccentricities of more massive planets are easier to detect from RVs. A conclusive determination of this system's eccentricity would come from observation of an occultation which we expect to be delayed by 2.6 ± 1.1 hours if our eccentricity value is accurate. Based on the equilibrium temperature of the planet, we estimate occultation depths in the *Spitzer* 3.6 μm and 4.5 μm bands of approximately 780 and 960 ppm, respectively. Recent observations with *Spitzer* (Zhao et al. 2014; Deming et al. 2015) show detecting such an occultation is easily achievable.

The faint star close to WASP-120 may provide evidence in support of the planet having undergone high-eccentricity migration due to Kozai-Lidov cycles. The Kozai-Lidov mechanism can function in the case where there is a comparatively tight inner binary, e.g. an exoplanet system, orbited by a third component. The third compo-

nent can perturb the inner binary in such a way as to induce cyclical evolution of its inclination and eccentricity. This can occur as long as the third component is sufficiently massive, another stellar body for instance, and its orbit is inclined to the orbit of the inner binary beyond a critical value. The perturbations act to decrease the mutual inclination while increasing the eccentricity of the inner binary and vice versa. This can lead to a hot-Jupiter system if the orbit becomes sufficiently eccentric and is circularised via tidal interaction with the host star. This is illustrated in Figure 6.8.

According to the models of Dotter et al. (2008), the companion's colour is consistent with a 0.6 $M_{\odot}$, K9 star at the same distance as WASP-120. Assuming this to be the case, the on sky separation gives a minimum separation of 950 AU. Using the equations of Fabrycky & Tremaine (2007), a star of this mass could induce Kozai-Lindov cycles if the planet's original orbital distance was 14.5 AU or greater. As the periodogram of the RVs for WASP-120 show no significant peaks beyond that of the planet (Fig. 6.10) we checked for the presence of an additional, long period, object in the system by fitting a linear trend to the residuals of the RVs. The result was an RV drift, $\dot{\gamma}$, of $(84 \pm 73)\ \mathrm{m\,s^{-1}\,yr^{-1}}$ which is consistent with zero at $\sim 1.2\sigma$. Following Montet et al. (2014), for a planet on a circular orbit:

$$\dot{\gamma} = (6.57 \mathrm{m\,s^{-1}\,yr^{-1}}) \left(\frac{M_2}{M_{\mathrm{Jup}}}\right) \left(\frac{a_2}{5\mathrm{AU}}\right)^{-2} \sin i_2 \tag{6.3}$$

Therefore, if there is an additional object in the system it has a mass, M_2, semi-major axis a_2, and inclination, i_2, such that, $M_2 \sin i_2 / a_2^2 \lesssim 0.51 M_{\mathrm{Jup}}\ \mathrm{AU}^{-2}$.

Notable examples of massive planets with confidently detected eccentricities are HAT-P-16 b (Buchhave et al. 2010), HAT-P-21 b (Bakos et al. 2011), WASP-14 b (Joshi et al. 2009) and WASP-89 b (Hellier et al. 2015). All of these are in sub 7-day orbits with masses $> 4M_{\mathrm{Jup}}$. Also notable are HAT-P-20 b (Bakos et al. 2011), which has the smallest eccentricity of the group and Kepler-14 b with the longest orbital period at 6.79-days (Buchhave et al. 2011). Like WASP-120, 3 of these 6 systems are known to have other stars nearby; HAT-P-16, WASP14 and Kepler-14 (Wöllert et al. 2015; Wöllert & Brandner 2015; Ngo et al. 2015; Buchhave et al. 2011). However, this

sample is too small to draw conclusions about a link between orbital eccentricity and the presence of a stellar-mass neighbour.

It is thought that stars with effective temperatures cooler than 6200 K have convective envelopes which enhance orbit circularisation/re-alignment Winn et al. (2010a). This could erase any correlation between the type of orbit a planet is in and the presence of a further companion.

In a study on the prevalence of multiple stars in planetary systems Ngo et al. (2015) found that, of their sample of hot host stars ($T_{\rm eff} > 6200K$) with evidence of misaligned or eccentric planet orbits $59\% \pm 17\%$ had companions while $83\% \pm 14\%$ of their well-aligned/circular orbit sample had companions. When Ngo et al. (2015) considered just the spin-orbit alignment of these systems, $73\% \pm 15\%$ of misaligned systems had companions as opposed to $53\% \pm 14\%$ of well aligned systems. They concluded that there is no evidence for a link between multiplicity and orbital eccentricity/misalignment, though so far the sample is just 18 hot stars, fewer when just those systems with measured spin-orbit alignments are used.

The typical time-scale of orbital circularisation is expected to be shorter than that of tidal realignment meaning that observations of spin-orbit misalignment may provide a better record of migration pathway than eccentricity. Therefore, increasing the number of hot-host star systems with measured spin-orbit alignment that have been evaluated for stellar multiplicity could change the current picture.

6.5 WASP-122

WASP-122 b is a $1.28 M_{\rm Jup}$, $1.74 R_{\rm Jup}$ planet orbiting a moderately bright (V = 11.0), metal rich ([Fe/H] = $+0.32 \pm 0.09$), G4 star. WASP-122 is depleted in lithium ($\log A(Li) < 1.0$) and so must be several Gyr old (Sestito & Randich 2005). Using the star's colour and rotational period from its $V \sin i$, we calculate a gyrochronological ages of 2.3 ± 1.4 Gyr (Barnes 2007), 2.8 ± 1.4 (Mamajek & Hillenbrand 2008) and 2.9 ± 4.8 (Meibom, Mathieu & Stassun 2009). Using BAGEMASS we find two possible

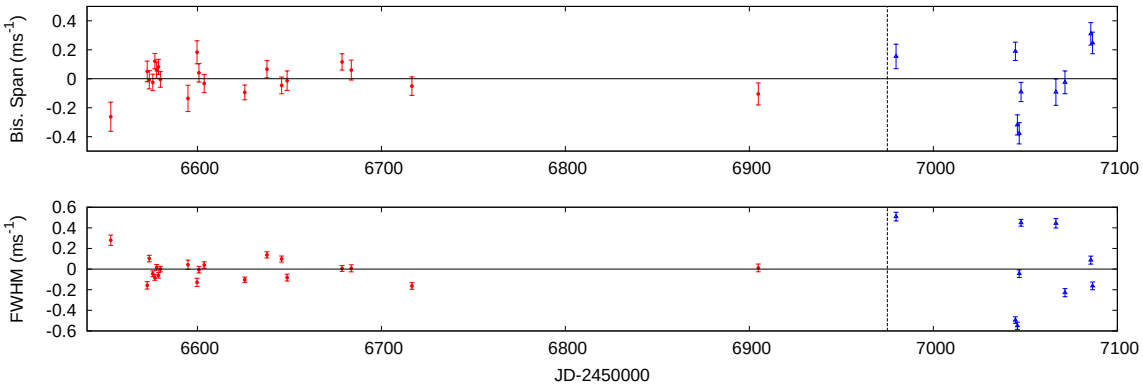

Figure 6.9: Full width at half-maximum (FWHM) and bisector spans of spectra as a function of time for WASP-120. The increase in scatter in more recent data is taken as an indication the star may be entering a phase of increased activity. Red circles are data taken before the CORALIE upgrade and blue triangles are those taken after, the black dotted lines denote the date CORALIE was back on sky after the upgrade. The data have all had the mean of their distribution subtracted before plotting.

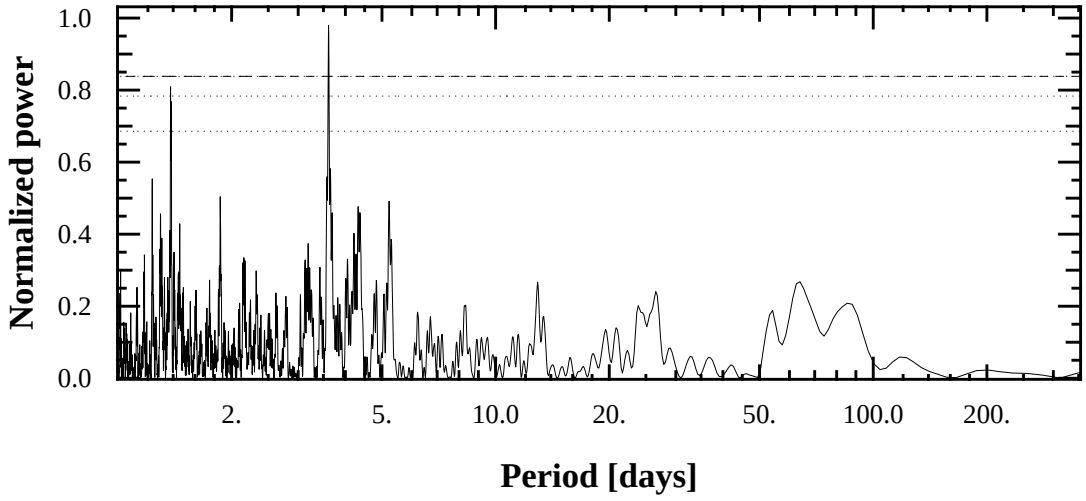

Figure 6.10: Periodogram for the RV data of the WASP-120 system. The only significant peak is that corresponding to the planetary period.

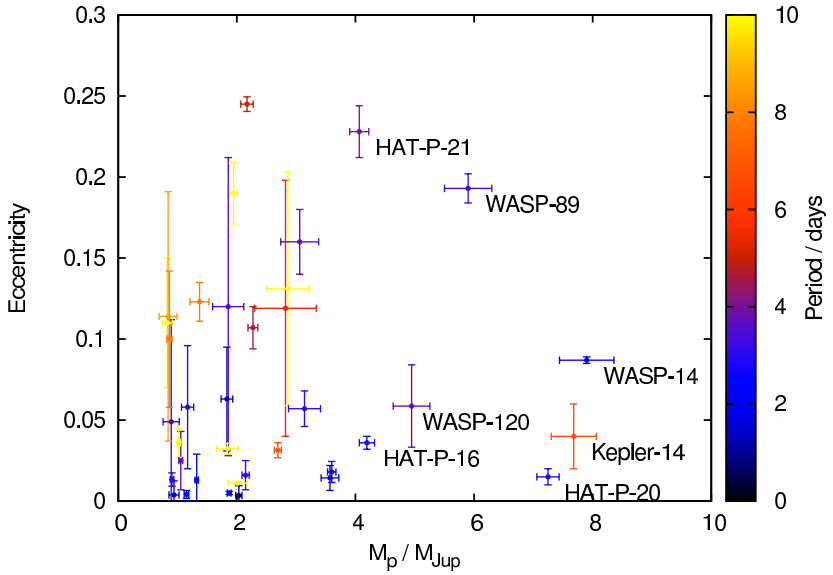

Figure 6.11: Masses, eccentricities and periods of transiting planets with non-zero eccentricities quoted in literature and masses $> 0.5 M_{\rm Jup}$ mass. The most convincing eccentricities are those associated with more massive planets. Notable examples and WASP-120 b are labelled. Data from TEPCat (Southworth 2011a).

solutions. Approximately 75% of the Markov chain output by BAGEMASS favour a mass of $1.24 \pm 0.04\ M_{\odot}$ and an age of 5.11 ± 0.80 Gyr. The other 25% of the output prefer a solution giving a mass of $1.10 \pm 0.03\ M_{\odot}$ and an age of 8.67 ± 1.05 Gyr. The favoured, younger, higher-mass solution is a better match to, though still older than, the gyrochronological ages.

WASP-122 b presents a good target for atmospheric characterisation via transmission spectroscopy. Assuming the atmosphere is isothermal and adequately described as an ideal gas we can calculate the atmospheric scale height, H, using:

$$H = \frac{kT_{\rm eq}}{g\mu} \tag{6.4}$$

Here, k is Boltzmann's constant, $T_{\rm eq}$ is the planetary equilibrium temperature, g is the planetary surface gravity and μ is the mean molecular mass of the atmosphere. We can use H to predict the transit depth variation due the addition of one atmospheric

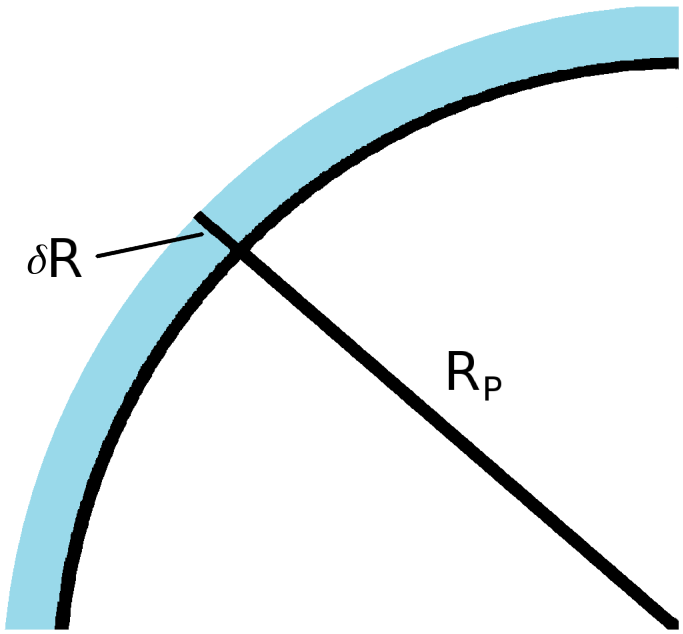

Figure 6.12: Cartoon of the effect of a planet's atmosphere on the overall planet radius.

scale height to the planetary radius. We can calculate the effect the addition of this scale height of atmosphere has by considering an annulus around the planet with a thickness of δr, illustrated in Figure 6.12. The transit depth with this addition, ΔF_+, is:

$$\Delta F_+ = \frac{(R_p + \delta r)^2}{R_*^2} \simeq \frac{R_p^2}{R_*^2} + \frac{2R_p \delta r}{R_*^2} \tag{6.5}$$

The resulting part of the transit depth that can be attributed to one scale height of atmosphere, ΔF_{atm}, is:

$$\Delta F_{atm} \simeq \frac{2R_p \delta r}{R_*^2} = \frac{2R_p H}{R_*^2} \tag{6.6}$$

In the case of WASP-122 b this is 142 ppm. The same calculation for the well-studied HD209458 b yields a variation of $\approx$ 200 ppm. Deming et al. (2013) found evidence for water absorption on this scale in HD209458 b. While WASP-122 is dim by comparison to HD209458, constraints have been put on the atmospheric compositions

of planets with similarly bright hosts. For example, studies of WASP-12 (V = 11.6,) show evidence of aerosols and a lack of TiO (Sing et al. 2013) as well as placing constraints on the C/O ratio of the planet (Kreidberg et al. 2015) which has been suggested may be an indicator of formation environment. We predict occultation depths in 3.6 μm and 4.5 μm *Spitzer* bands of 2100 and 2500 ppm respectively. In the K-band we predict a depth of 1000 ppm. Similar K-band depths have been detected, for example that of WASP-10b (Cruz et al. 2015), making ground-based follow up possible. Such observations of WASP-122 b stand to shed light on our understanding of atmospheric albedo and opacity sources as well as its formation history.

6.6 WASP-123

WASP-123 b is a 0.90-$M_{\rm Jup}$, 1.32-$R_{\rm Jup}$ planet orbiting a moderately bright (V = 11.1), G5 star with a super-solar metal abundance ([Fe/H] = $+0.18 \pm 0.08$). WASP-123 is depleted in lithium ($\log A(Li) < 0.5$) suggesting an age of several Gyr. This star falls into an area of parameter space for which gyrochronology is poorly calibrated (Jeffries 2014). The Barnes calibration gives an age greater than the present age of the universe and Mamajek and Meibom calibrations are not applicable as the star's colour results in the calibrations requiring the logarithm of a negative value. The age we derive using BAGEMASS, 6.9 ± 1.4 Gyr, supports an advanced age. Planets of similar mass and radius are not uncommon and are frequently found in orbits $\sim$ 3-days around such host stars. This makes WASP-123 a typical example of a hot-Jupiter system. However, even these can prove surprising (e.g. WASP-47; Becker et al. 2015; Neveu-VanMalle et al. 2016) and/or contribute as vital controls to other studies.

Table 6.5: Stellar and planetary parameters parameters determined from spectra and MCMC analysis. Spectral parameters have formal uncertainties while parameters found via MCMC are the median values of the posterior distributions with an uncertainty corresponding to the 1σ confidence interval.

Spectroscopic Parameter	WASP-120	WASP-122	WASP-123
Tycho-2 ID	8068-01208-1	7638-00981-1	7427-00581-1
USNO-B ID	0441-0033568	0475-0113097	0571-1147509
RA (J2000)	04:10:27.85	07:13:12.34	19:17:55.04
Dec (J2000)	−45:53:53.5	−42:24:35.1	−32:51:35.8
V Magnitude	11.0	11.0	11.1
Tycho (B−V) colour	0.523 ± 0.083	0.78 ± 0.11	0.48 ± 0.17
Spectral Type	F5	G4	G5
Distance (pc)	437 ± 21	266 ± 10	214 ± 11
BAGEMASS Age (Gyr)	2.6 ± 0.5	5.11 ± 0.80	6.9 ± 1.4
Stellar Effective Temperature, $T_{\rm eff}$ (K)	6450 ± 120	5720 ± 130	5740 ± 130
Stellar Surface Gravity, $\log g_*$	4.3 ± 0.1	4.3 ± 0.1	4.3 ± 0.1
Stellar Metallicity, [Fe/H]	-0.05 ± 0.07	0.32 ± 0.09	0.18 ± 0.08
Projected Rot. Vel., $V \sin i$ (km s^{-1})	15.1 ± 1.2	3.3 ± 0.8	1.0 ± 0.7
Stellar Lithium Abundance, $\log A$(Li)	< 1.2	< 1.0	< 0.5
Micro turbulence (km s^{-1})	1.5 ± 0.1	0.9 ± 0.1	1.0 ± 0.1
Macro turbulence (km s^{-1})	6.0 ± 0.8	3.4 ± 0.5	3.4 ± 0.5
MCMC Parameter	**WASP-120**	**WASP-122**	**WASP-123**
Period, P (d)	3.6112706 ± 0.0000043	$1.7100566^{+0.0000032}_{-0.0000026}$	2.9776412 ± 0.0000023
Transit Epoch, T_0	6779.43556 ± 0.00051	6665.22401 ± 0.00021	6845.17082 ± 0.00039
Transit Duration, T_{14} (d)	0.1483 ± 0.0016	0.09117 ± 0.00082	0.1289 ± 0.0014
Scaled Semi-major Axis, a/R_*	5.90 ± 0.33	4.248 ± 0.072	7.13 ± 0.25
Transit Depth, $(R_p/R_*)^2$	0.00655 ± 0.00016	0.01386 ± 0.00029	0.01110 ± 0.00027
Impact Parameter, b	0.78 ± 0.02	0.8622 ± 0.0071	0.530 ± 0.049
Orbital Inclination, i (°)	82.54 ± 0.78	78.3 ± 0.3	85.74 ± 0.55
Eccentricity, e	$0.057^{+0.022}_{-0.018}$	0 (adopted;< 0.08 at 2σ)	0 (adopted;< 0.12 at 2σ)
Argument of Periastron, ω (°)	-27^{+48}_{-28}	–	–
Systemic Velocity, γ (kms^{-1})	19.836 ± 0.013	34.5934 ± 0.0017	16.9344 ± 0.0017
Semi-amplitude, K_1 (ms^{-1})	509 ± 17	185.1 ± 2.3	114.2 ± 2.2
Semi-major Axis, a (AU)	0.0514 ± 0.0007	0.03005 ± 0.00031	0.04263 ± 0.00074
Stellar Mass, M_* ($M_\odot$)	1.393 ± 0.057	1.239 ± 0.039	1.166 ± 0.061
Stellar Radius, R_* ($R_\odot$)	1.87 ± 0.11	1.52 ± 0.03	1.285 ± 0.051
Stellar Density, ρ_* ($\rho_\odot$)	$0.212^{+0.041}_{-0.031}$	0.351 ± 0.018	0.548 ± 0.059
Stellar Surface Gravity, $\log(g_*)$ (cgs)	4.035 ± 0.049	4.166 ± 0.016	4.286 ± 0.032
Limb-Darkening Temperature, $T_{\rm LD}$ (K)	6440 ± 120	5750 ± 120	5740 ± 130
Planet Mass, M_p ($M_{\rm Jup}$)	4.85 ± 0.21	1.284 ± 0.032	0.899 ± 0.036
Planet Radius, R_p ($R_{\rm Jup}$)	1.473 ± 0.096	1.743 ± 0.047	1.318 ± 0.065
Planet Density, ρ_p ($\rho_{\rm Jup}$)	$1.51^{+0.33}_{-0.26}$	0.243 ± 0.019	0.393 ± 0.056
Planet Surface Gravity, $\log(g_p)$ (cgs)	3.707 ± 0.056	2.985 ± 0.022	3.07 ± 0.04
Planet Equilibrium Temperature, $T_{\rm eq}$ (K)	1880 ± 70	1970 ± 50	1520 ± 50

7 Signal injection to assess the potential recovery fraction of 85-mm data

7.1 Introduction

The upgraded WASP-South survey currently has no confirmed planets orbiting our brighter sample of stars. Is this because they are rare and troublesome to find? Or, is the data quality using the 85-mm lenses too poor to detect them? In this chapter I seek to put aside the latter concern and to answer the question of if it is worth using the 85-mm lenses to acquire a 4^{th} season of data. I do this by injecting artificial transit signals into real data.

Signal injection has often been used to estimate the detection efficiency of transiting planet surveys. The idea behind the method is to take real data, that does not contain the kind of signal to being searched for, and add such a signal. The signals that are injected into the data are known exactly and so it is possible to make an accurate estimate of the fraction of these signals that are recovered. Since the noise in the data is real noise how well the injected signals can be identified in that same noise can be investigated along with, potentially, what systematic effects the noise might introduce. In this way different methods of data analysis can also be compared. As part of this process it is important to consider to what kind of real signals the injected signals are analogous. To this end I will look at the appropriateness of assumptions and simplifications made later in the chapter.

The WASP project has a history of using signal injection to test the effectiveness of the detrending algorithms we use and the detectability of signals in our data. Collier Cameron et al. (2006) used injected signals to "optimize and quantify the recovery rate and false-alarm probability as functions of stellar magnitude and transit depth". They also tested plausibility checks used to eliminate non-planetary sources of periodic signals (e.g. variable stars) and spurious detections caused by red noise features or data gaps mimicking transits. When Smith et al. (2009) found no additional transiting

objects in the WASP systems they searched, they used signal injection to place limits on their ability to find additional planets in longer orbits. They concluded that, using 3 seasons of WASP data, they had a $> 50\%$ chance of detecting a Saturn analogue in an orbit of up to 10 days. They also said they had a "sporting" chance ($\sim 20\%$) to detect a Saturn analogue in a 20 day orbit. To date, the longest period planet published by the WASP survey is WASP-117 b at 10-days ($1.02R_{\rm Jup}$, $0.27M_{\rm Jup}$, Lendl et al. 2014) and the smallest is WASP-59 b with an orbital period of 7.92-days and a Saturn-like radius ($0.78R_{\rm Jup}$, $0.86M_{\rm Jup}$, Hébrard et al. 2013). Christiansen et al. (2013) and Christiansen et al. (2015) used signal injection with data from the *Kepler* satellite to check the recoverability of single transit events and the overall detection efficiency. This gives us an idea about how complete we can expect any given survey to be and thus the areas of parameter space where it is likely to miss any planets.

7.2 Method

7.2.1 Signal Injection

I selected stars from the WASP archive at latitudes south of the equator with V magnitudes of $9^{\rm th}$ and brighter that had data collected with the 85-mm lenses. I excluded stars that are in the overlap region with the northern WASP installation to eliminate the possibility of our injected signals being detected due to data from 200-mm lenses. I also excluded stars with known eclipsing stellar or planetary companions and stars identified as candidate transiting exoplanets systems. This left 275 stars with light curves suitable for analysis.

After discussion with David Anderson and Ben Clark, I chose to inject transits with one of five fixed depths. I chose not to randomise the depth as to do so would require more repeats on a larger sample size of stars to draw reliable conclusions. The transit depths I chose were; 2%, 1%, 0.5%, 0.2% and 0.1%. They range from the signal that would be expected from a bloated gas giant in a centrally transiting orbit

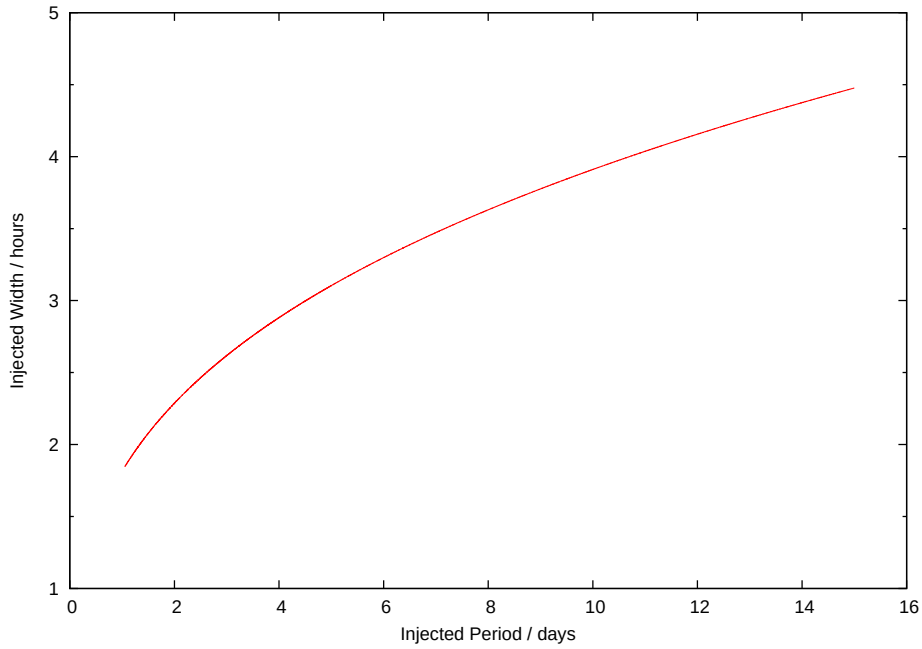

Figure 7.1: Assumed transit width as a function of orbital period for the injected transit signals.

of a Sun-like star to that of a super-Earth around an M-dwarf. To inject the transit I decreased the flux recorded in the archive lightcurve by the corresponding percentage, neglecting transit shape. The resulting transits were therefore box shaped. So that the duration of each injected transit was not completely unphysical I scaled it to be consistent with that of Jupiter on a Keplerian orbit, with the injected period, around the Sun. The end result of this can be found in Fig. 7.1.

For each object I injected transits with one of our chosen transit depths with an independent random ephemeris. I generated random periods using a uniform probability from two broad period bins; $1.05 - 5$ days and $5 - 10$ days. Two period bins were used to ensure that there would be a sufficiently high number of long (> 5 days) and short (< 5 days) periods to be able to draw reliable conclusions. To allow each signal to begin at a random phase in the injected 'orbit', I drew the epoch from a period of 15 days beginning at a JD of 2456000.

I ran the signal injection five times on each star per injected transit depth for both broad period bins resulting in 13750 different ephemerides; 2750 for each depth. In order to generate data for the extra seasons I duplicated the season of data available and added multiples of the lunar period to preserve effects due to the moon and prevent noise stacking easily on aliases.

7.2.2 Signal Recovery

To search the data I used a box-least-squares algorithm (Collier Cameron et al. 2006) to look for periods between 1.05 and 10 days. This closely mimics the method used by the WASP survey to search for transit signals previously described in the chapter on discovery and follow-up methods. This method identifies a maximum of 5 of the strongest signals based on minimising the χ^2 of a simple box shaped transit model. It is worthwhile to note that the box shape of our injected transit will more readily match with the box-shaped model used for transit recovery. While this may increase the detectability of injected transits with respect to genuine signals it will still allow us to investigate the effect of extra seasons as any increase in detectability will only be due to the additional data.

7.2.3 Recovery Analysis

I reasoned that an absolute measure of accuracy would be more useful than a relative one. Checking for period and epoch matches to within a certain percentage means that the longer period signals would have an artificially higher tolerance. Fig. 7.2 details my reasoning behind the values of the limits graphically. As genuine signals are sometimes found on aliases of their true period I checked if any of the recorded peaks corresponded to the injected period, P_i, or the $P_i/2$ or $2P_i$ aliases. To ensure the epoch matched the injected epoch I checked that the difference between them was near an integer number of recovered periods.

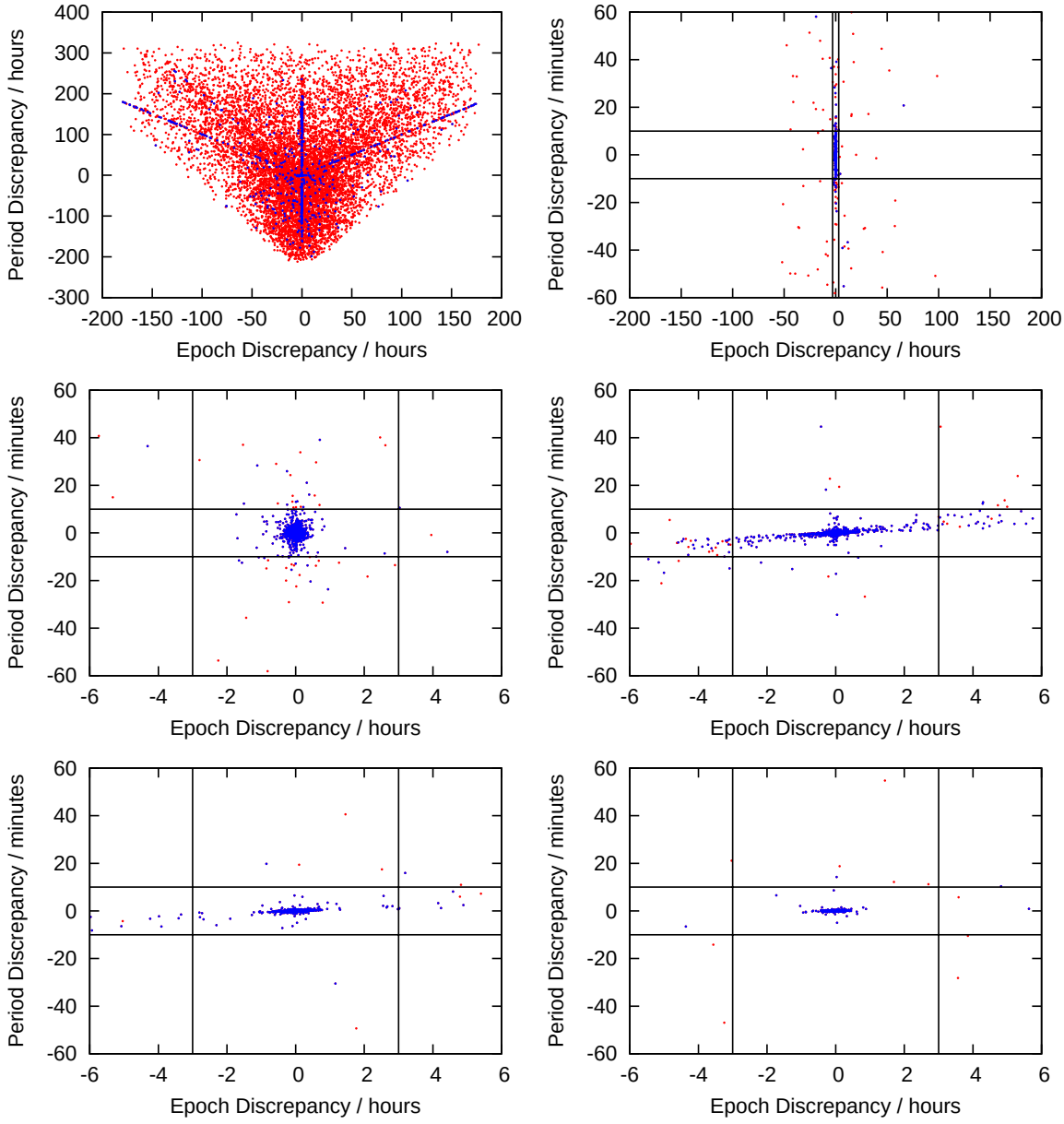

Figure 7.2: Plots of absolute difference between injected and recovered values of period and epoch. Red points are considered 'un-recovered' while blue points are 'recovered'. Top-left: Output over whole parameter space. Recovered points cluster into 3 groups. The group around the origin are recovered on the correct period and a matching epoch. The group below are recovered on the $2P_i$ alias and above are recovered on the $P_i/2$ alias. The next 3 panels show the same data at different zoom levels. The final 4 panels are all at the same zoom level. The first shows the distribution with one season of data, the next two, then three and finally four.

The overall uncertainty on an ephemeris depends on the uncertainties on the epoch, which contributes once, and the period, which contributes more with subsequent transits, so I made the tolerance on the period difference more strict. Fig. 7.2 shows that with a range of ±60 minutes most of the data is centred strongly around the origin in the period-epoch difference plot. Data is sparse at the limits of the epoch difference range, indeed most falls within ±3 hours of the origin. With further consideration of the core of the distribution in Fig. 7.2, I regarded a peak to have correctly recovered the injected transit if the absolute difference between its epoch and a matching epoch was under 3 hours and the absolute difference between the recovered period and one of the aliases of the injected period was less than 10 minutes. It is possible to relax these limits to encompass more of the central distribution, but, extra seasons of data tighten up the distribution considerably making relaxing the limits less meaningful. Relaxing the limits also serves little purpose as it includes few extra points and runs a higher risk of not excluding spurious points.

In the first panel of Fig. 7.2 there are many points on the diagonal lines that contain signals found on the $P_i/2$ alias that are not recorded as recovered. To check that this apparent lack of recovery was not due to the limits imposed being too strict I isolated the points in these lines and checked how well their recovered periods match the injected period. The results of this can be seen in Fig. 7.3. The recovered points appear on the lines of $P_i/P_r = 0.5$, 1 and 2. Other aliases are tentatively detected as there are also lines at 1.5, just above 1.3 and just below 1.7. However, most of the points in the horizontal lines of Fig. 7.2. are there by coincidence.

7.3 Results

7.3.1 Overall Recovery Fraction

We can see from Figs. 7.4 and 7.5 that, as with all transit searches, short period signals are picked up most readily. We also see that a second season has the greatest effect

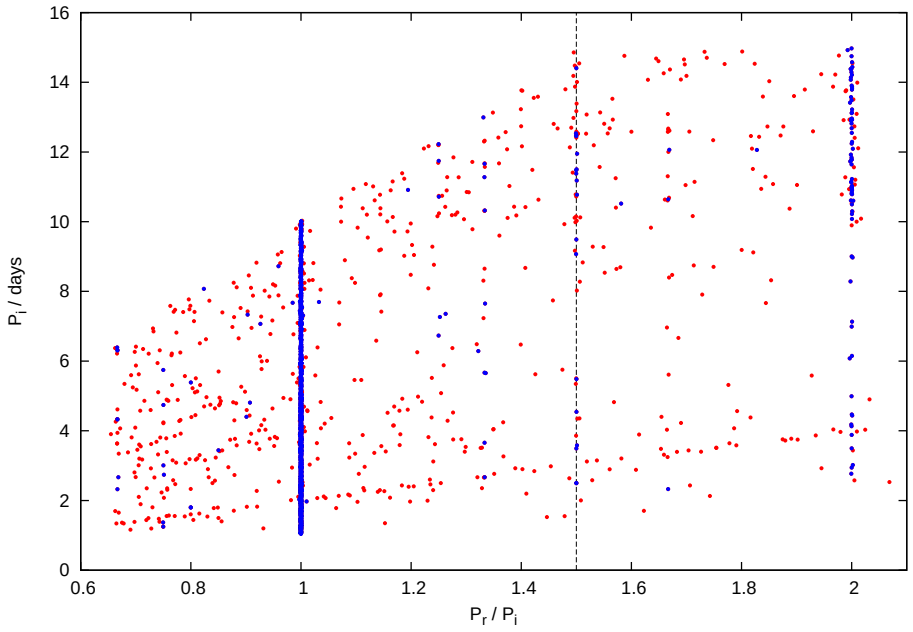

Figure 7.3: Ratio of period injected to recovered plotted w.r.t period injected. Blue points are all recovered periods and lie on the 0.5, 1 and 2 P_i aliases recovered from the 1^{st} search peak. Blue points not on these aliases are points recovered from other peaks and coincidentally close to the horizontal alias lines. The red points are the points isolated from the diagonal alias lines in Fig. 7.2. Few red points occupy aliases of the injected period. Some occupy aliases of $4/3P_i$ and $5/3P_i$ but, again, these contribute little and are not commonly checked. The dotted line shows the $3/2P_i$ alias. This alias was not chosen as an alias to search as it adds few extra detections.

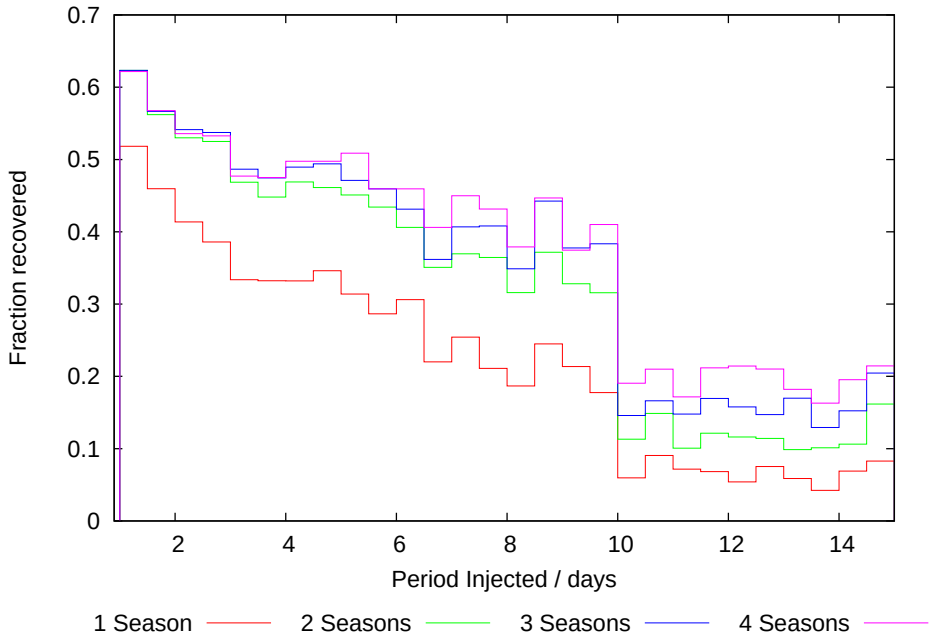

Figure 7.4: Recovery fraction as a function of injected period. The different line colours denote the number of seasons of data used. Overall efficiency is highest for the shortest periods. The drop in detections for periods < 10 days. is not in keeping with the general trend seen for shorter periods. This is an artefact of the search method.

on recovery fraction. Over the period range 1 to 10 days I recover 36.8% more signals with two seasons than with one season alone. This effect is more significant for longer period signals. The addition of a third season gives an overall increase in detections of signals < 10 days of 5.0%. Again, this is more significant at longer periods. There an increase of 10.2% if we consider periods between 5 and 10 days. A fourth season shows an increase of just 1.5% overall for periods < 10 days. For periods between 5 and 10 days there is a 5.8% increase. This suggests there is little to be gained in adding a fourth season to the data already acquired by WASP-South.

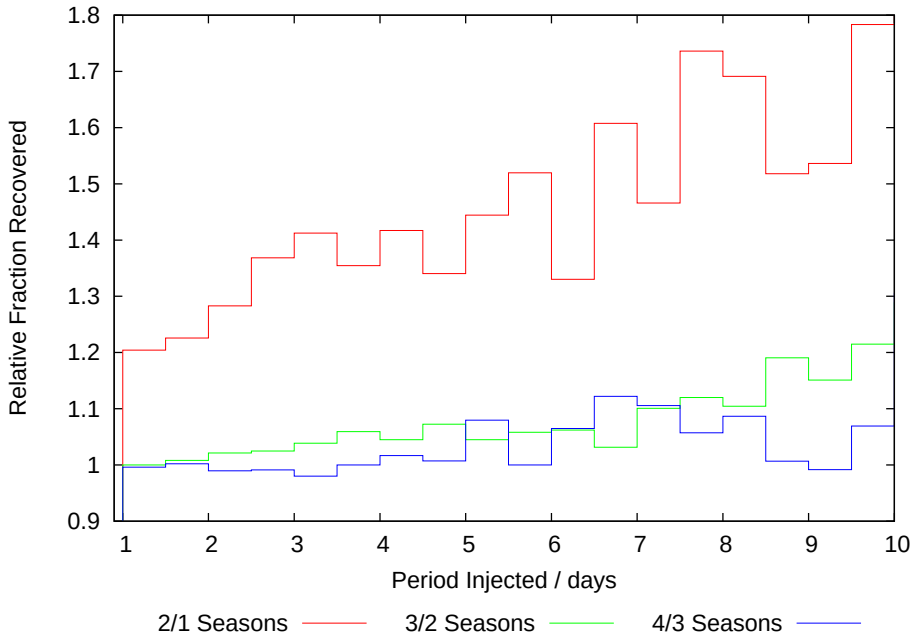

Figure 7.5: Ratio of the recovery fractions as a function of injected period from consecutive 'seasons' up to periods of 10 days. Most improvement is seen from the addition of a second season of data.

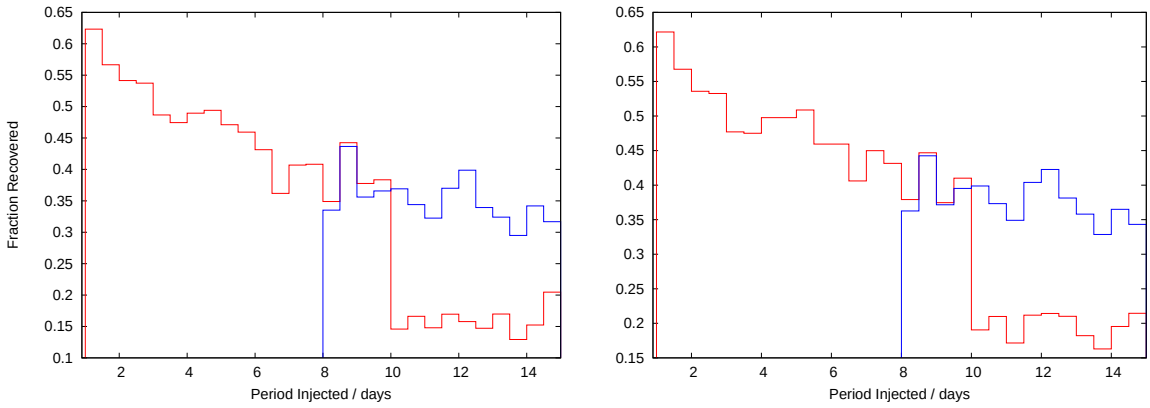

Figure 7.6: Recovery fraction as a function of injected period for 3 seasons (left) and 4 seasons (right) of data. Red lines are the same results as show in Fig. 7.4. Blue lines are the result of re-running the search with a period limit of 15 days rather than 10 for objects with injected periods longer than 8 days. The recovery fractions match well in the overlap region showing that the decrease after 10 days in the original search is due to inefficient detection of signals using aliases alone.

7.3.1.1 Periods > 10 Days

It is clear from Fig. 7.4 that something odd is occurring regarding detecting periods longer than 10 days. To investigate if this is due to the limits put on the search algorithm I re-ran the search with a new upper limit of 15 day signals. To limit the time this would take while ensuring comparability I only ran this second search for objects with 3 and 4 'seasons' of data and injected periods of longer than 8 days.

The results of this investigation are shown in Fig. 7.6. They allow me to conclude that the lack of sensitivity to signals with periods > 10 days is an artefact of having to detect such signals by their aliases alone. If I allow the finding routine to locate them on the injected period our ability to recover them follows the same general trend seen with signals of < 10 days.

Taking this into account, the overall increase in detections from three to four seasons of data for periods < 15 days is 3.0%. However, a fourth season actually shows a decrease in the ability to detect signals with periods < 2.5 days.

7.3.2 Depth Dependent Recovery Fraction

Due to the limitations I have noted about recovering signals with periods longer than 10 days I treat the results for < 10 days and > 10 days separately. The results are shown in Fig. 7.7 where the different coloured lines denote one of the five depths I injected. I do not display the results for depths of 0.1% and P < 10 days, except in the recovery fraction graph, too few were recovered to draw conclusions. The same is true for depths of 0.2% and 0.1.% with P > 10 days.

For signals with periods less than 10 days the most noticeable improvement in recovery fraction is seen when a second season of data is added. This is accompanied by a significant decrease in the scatter of the detected periods, ΔP_{sc}. However there is an increase in the scatter of the epochs, ΔE_{sc} for all depths except 0.2%. This increase is likely due to the increase in signals detected as the standard deviation, used to calculate the scatter, is not normalised for the number of detections.

The addition of a third season again leads to an increase in recovery fraction, though less significant than the first. It also refines the parameters of the recovered signals. The values of ΔP_{sc} for all depths are less than 1.5 minutes and for ΔE_{sc} are less than 30 minutes, except in the case of signals with depths of 0.2%.

A fourth season of data continues these trends; ΔP_{sc} for signals with depths $\geq 0.5\%$ improve to under 30 seconds and ΔE_{sc} to ~ 12 minutes for signals with depths of 0.5% and ~ 6 minutes for depths $\geq 1.0\%$. These precisions are far in excess of those needed to discover planets. The fourth season of data does slightly decrease the fraction of 0.2% depth signals detected. These results also show, for P < 10 days, aliases add very few extra detections.

For signals with injected periods greater than 10 days I show results from both our signal searches. Similar general behaviour can be seen. Extra seasons of data increase the recovery fraction and decrease the ΔP_{sc}. However, when I limit the recovery of signals to just their aliases the ΔE_{sc} stays at a value of between 40 and 60 minutes and so does not appear in Fig. 7.7. Searching for signals up to 15 days dramatically improves the recovery fractions for periods greater than 10-days. Four seasons of data

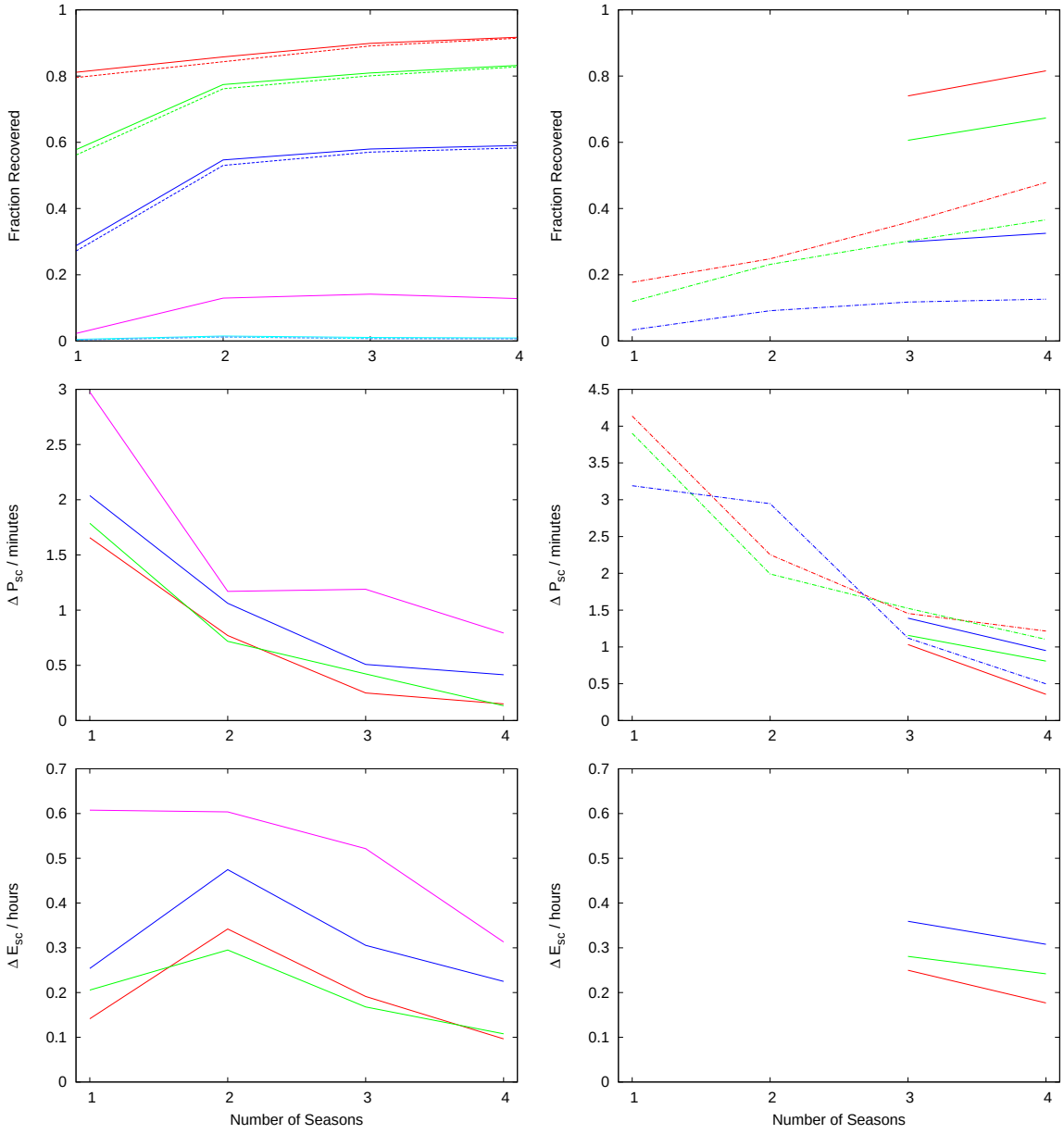

Figure 7.7: Graphs of recovery fraction (top), period discrepancy scatter, ΔP_{sc}, (middle) and epoch discrepancy scatter, ΔE_{sc} (bottom) as a function of number of seasons of data for injected periods < 10 days (left) and > 10 days (right). For periods < 10 days, dotted lines denote the recovery fraction neglecting recoveries using period aliases. For periods > 10 days dotted lines denote results from the initial search with the limit of 10 days while solid lines denote the results of the search with a 15 day limit. Line colours denote the different transit depths injected: red is 2.0%, green is 1.0%, blue is 0.5%, magenta is 0.2% and teal is 0.1%. The results for 0.2% and 0.1% are not displayed where detections are negligible.

for these long periods are similar in their recovery fraction to one season for the shorter periods. It also results in $\Delta P_{sc} < 1$ minute and $\Delta E_{sc} < 30$ minutes. Both are more than sufficient to accurately identify signals.

7.4 Discussion

Here I will look in more depth at some of the deviations from real data that this method has. The transit models I inject are not affected by limb-darkening or partial covering of the stellar disk by the planet during ingress and egress. Transit durations are calculated in a highly simplified manner. The potential effects of correlated noise and blending from other stellar sources are also considered.

7.4.1 Transit Model

In Fig. 7.8 I show lightcurves computed using the models of Mandel & Agol (2002) with the small planet approximation and limb-darkening parameters consistent with a G0-type star. I compare them to models without limb-darkening which are more similar in form to the injected transits. The models use a planet-to-star radius ratio, $p = 0.1$, and three different impact parameters.

7.4.1.1 Shape

The ingress, egress and maximum depth of a transit lightcurve depends on the limb-darkening of an individual star in the range of the photometric band being observed. This is individual to the colour, type and composition of each star. When the effects of limb-darking are included the maximum transit depth of the more centrally crossing transits exceed the depth of the injected transits. This effect decreases for larger impact parameters. Meanwhile, the ingress and egress slopes are less pronounced than when limb-darkening is neglected and than the box-like injected transits. However,

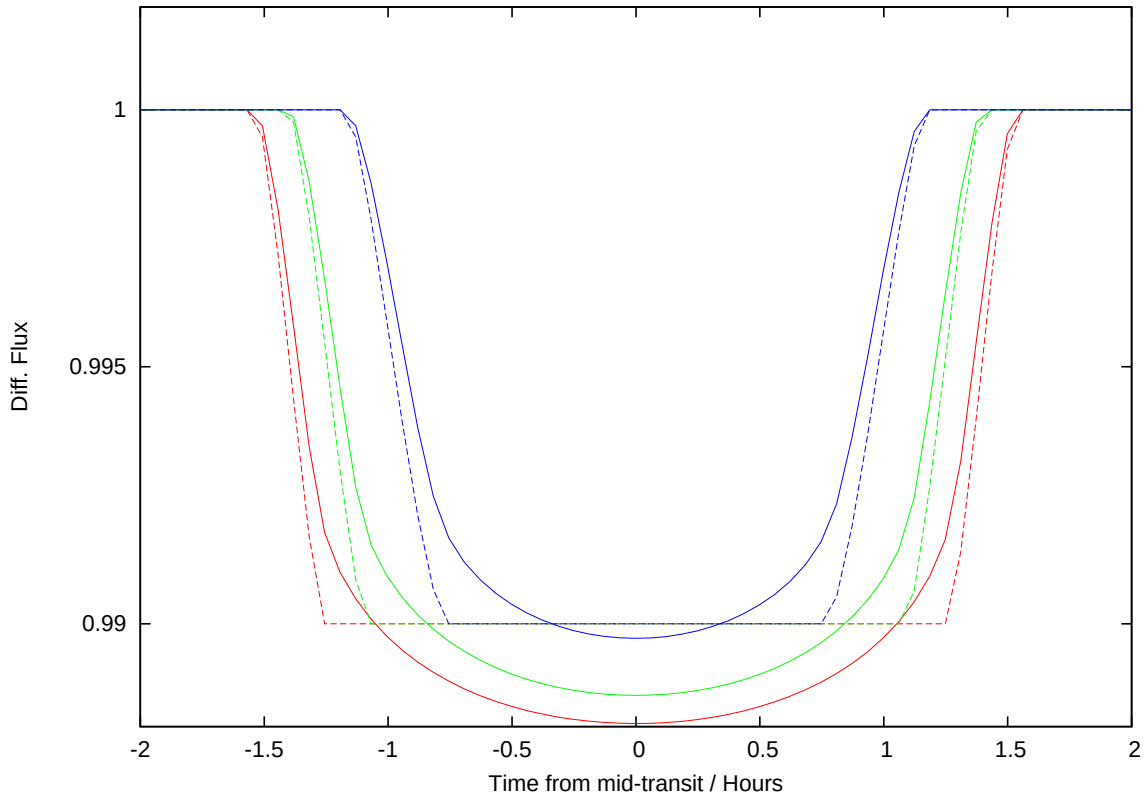

Figure 7.8: Mandel & Agol (2002) transit models for a system with $p = 0.1$. Solid curves use limb-darkening parameters consistent with a G0 star while dashed lines use no limb-darkening. The red line corresponds to a centrally crossing transit,$b = 0$. The green line corresponds to $b = 0.45$ while the blue line corresponds to $b = 0.71$.

the photometric precision of WASP discovery photometry is relatively low, thus not simulating the ingress and egress shape is likely to have little impact. Indeed, the transit search method neglects these. The depth modulation may be pronounced enough to have an effect on the precise recovery fractions but the impact of this is mitigated by my use of several transit depths.

7.4.1.2 Duration

Ignoring limb-darkening, the system parameters affecting the duration of a transit in a circular orbit can be found in equation 7.1 (c.f. Equ. 3, Seager & Mallén-Ornelas 2003) and equation 7.2, Kepler's Third Law:

$$t_T = \frac{P}{\pi} \arcsin\left(\frac{R_*}{a}\left[\frac{(1+\frac{R_p}{R_*})^2 - (\frac{a}{R_*}\cos i)}{1-\cos^2 i}\right]^{1/2}\right) \tag{7.1}$$

$$P^2 = \frac{4\pi^2 a^3}{G(M_* + M_p)} \tag{7.2}$$

The system semi-major axis, a, planet and star radii (R_p and R_*) and masses (M_p and M_*) all contribute along with the inclination of the system to our line of sight, i. There are other factors that can contribute which cause the duration to vary; the presence of other bodies orbiting the star or the the planet for example. I neglect these due to the complexity they would add and the evidence to suggest most close in giant planet systems have a solitary planet.

The only factor I take into account for the duration is the period of the orbit. The search method used scales the duration of transits it searches for in the same way. I do not expect this to lead to an artificial increase in the recoverability of the signals I inject because, rather than applying a model with precisely the same period, the search method uses a grid of durations around the scaled estimate.

Fig. 7.9 shows that it is likely that concerns of over-recovery due to duration similarity are likely unfounded. While there is good agreement, there is scatter around the best fitting relation. There is also an offset from a 1:1 relation. The recovered

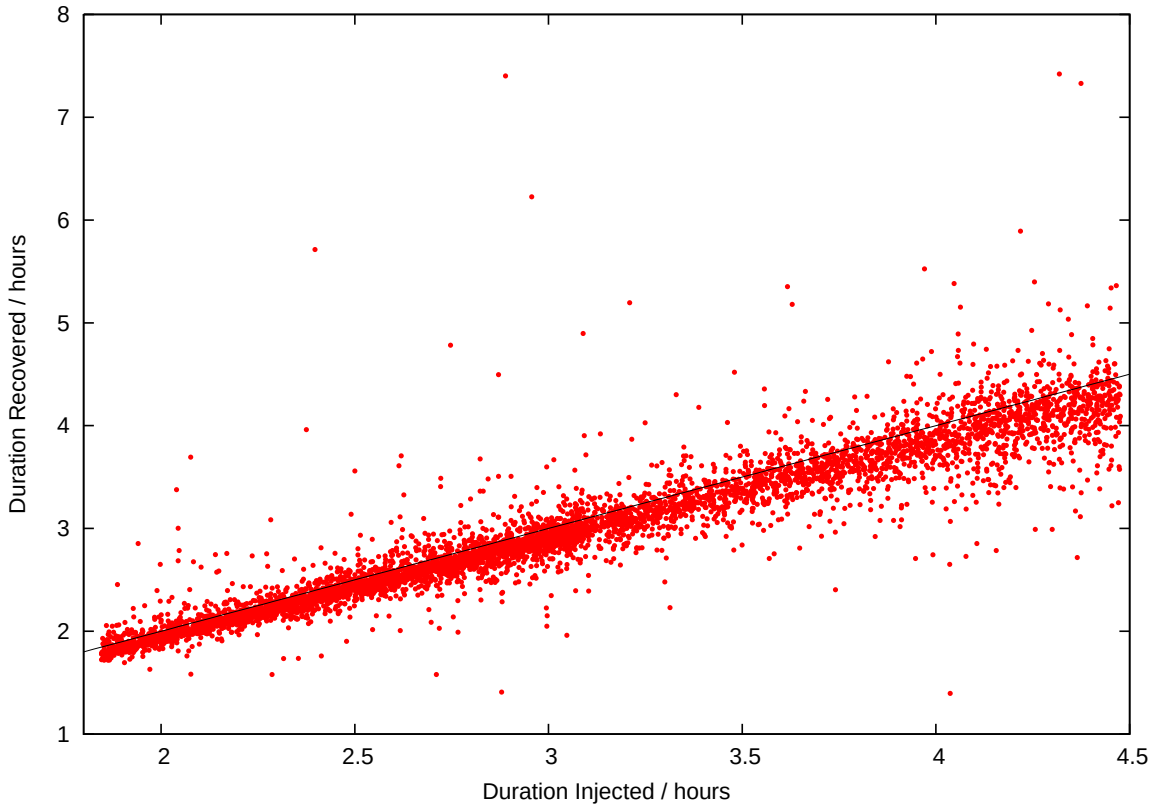

Figure 7.9: Relationship between injected transit duration and recovered transit duration. Red points are results from correctly recovered signals. The black line shows a 1:1 relationship. Most of the recovered durations are below this line.

durations appear systematically shorter than the injected ones. This is an artefact of the recovery procedure. In their description of the transit search algorithm Collier Cameron et al. (2006) make a grid of possible transit durations based on an estimate using the period under consideration, Kepler's third law and the assumption the stellar mass is $0.9M_{\odot}$. The only difference between this and our duration scaling is our use of a solar mass star. Given the use of a main sequence star with a planet mass companion, the transit duration scales as $(M_*/M_{\odot})^{2/3}$ so a less massive star results in a shorter transit. This explains why all the recovered durations are shorter than those I injected. The scatter is due to the recovered duration being derived from a best fit.

A greater loss to this investigation may be the modulation of the transit duration seen between the different impact parameters, $b = \frac{a}{R_*}\cos i$. The examples in Fig. 7.8 show that differing impact parameters change the transit duration on the order of hours. This loss of time during transit has not been probed and would likely have a detrimental effect on the detection efficiency at longer periods or smaller depths. In retrospect, this could have been easily approximated by allowing time, of the order of about an hour, to be randomly added to or subtracted from the injected duration with a uniform probability.

7.4.2 Correlated Noise

Correlated noise can be one of the main causes of low discovery rates for planet transit surveys (Pont, Zucker & Queloz 2006). My signal injection method using real data does account for correlated but noise, but if the correlated noise that results from duplicating one season of data to create extra seasons behaves differently to how genuine multiple seasons are affected then it could undermine this method of making additional seasons. I investigated the behaviour of correlated noise by looking at WASP 200-mm data for known planets that had been transit searched after combining multiple seasons of data. I queried the WASP archive for all the signal peaks for all objects that are flagged as planets. I cross matched the positions of these objects with known planets with data from TEPcat (Southworth 2011a) to identify them and find the correctly

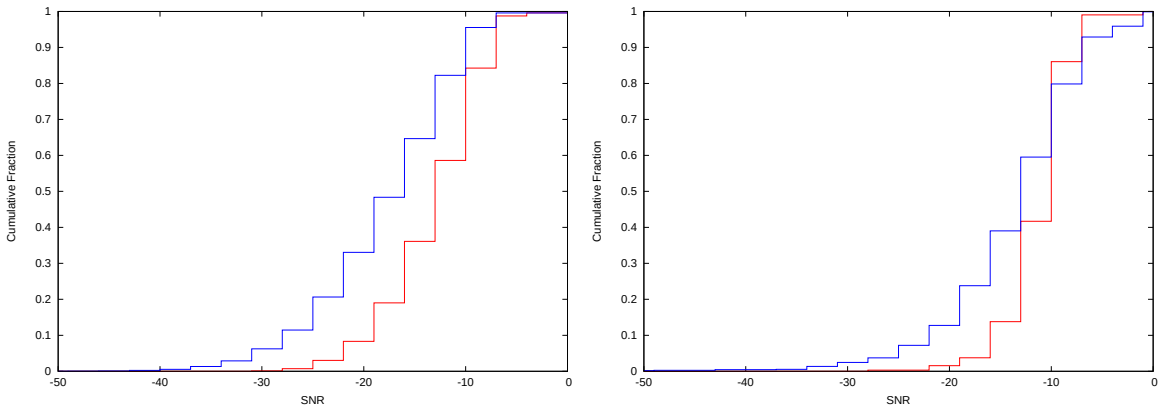

Figure 7.10: Cumulative distributions of signal-to-noise ratios for transits detected on accurate periods. Signals found in one season of data are shown in red while multiple seasons are blue. Results from the signal injection are on the left and results from the WASP archive are on the right

recovered periods amongst the signal peaks. I separated the peaks with correct periods that were identified using a single season of data from those identified using multiple seasons. Those peaks identified using a single season of data from one camera have individual camera IDs. Those with camera IDs of 100, 200 or 300 are found using data from multiple seasons, multiple cameras or both. In addition, to try an eliminate peaks found using data from multiple cameras but only one season, I required that the period of observation[1] exceeded 95 days. This estimate was based on the median and then median absolute deviation of the number of nights observed for each field in the 2006 to 2011 observing seasons of WASP-South, 77 ± 17 nights.

Fig. 7.10 shows the cumulative distributions of signal-to-noise ratios from data containing real planetary signals from one and multiple seasons to that of the data with injected transits. The peaks of the distributions for the real signals are more negative than those of the simulated data and the tail of the multiple season distribution is less pronounced. However, the behaviour is similar enough that I conclude the effect of correlated noise on signals detected in multiple seasons of real data is the same as that

[1]Defined as period $\times$ number of transits in the data.

for our simulated seasons and so does not undermine our method.

7.4.3 Blending

The transit depth depends on the contribution of third light in the aperture as:

$$\Delta F_{\mathrm{True}} = \Delta F_{\mathrm{Obs}} \left(\frac{F_{\mathrm{T}} + F_3}{F_{\mathrm{T}}} \right) \tag{7.3}$$

where ΔF_{True} is the true transit depth, ΔF_{Obs} is the observed depth, F_{T} is the flux contribution of the target star and F_3 is the flux contribution from other sources in the aperture. This investigation has assumed the effect that blending has on our targets will be minimal. To test this assumption I extracted two catalogues; one each using the same sky area covered by a single 200-mm and 85-mm lens but with a dimmer magnitude limit to those used in the reduction pipeline. I cross-matched the positions of the stars in these deeper-than-normal catalogues with the match distance set to the reduction aperture size; 48" for the 200-mm field and 132" for the 85-mm field. From the resulting matches I calculated the fraction of the total flux in the reduction aperture from the main target for each star brighter than USNO-B R2 magnitude of 13. This assumes that the R2 magnitudes are accurate and that significant contributions of third light only occur if blended stars are mostly inside the reduction aperture.

Fig. 7.11 shows the fraction of stars between 5^{th} and 13^{th} that should contribute 90% and 50% of the light in their reduction apertures for the 200-mm and 85-mm field. It is clear that a greater number of stars are blended in the new data. However the effect of this is not so significant. Between 9^{th} and 13^{th}, the effective magnitude range of the old set up, 91.4% of the stars in our sample field contributed 90% or more of the light in their apertures. This rises to 96.7% of the stars in the sample if we consider those that contribute 50% or greater. Comparing this to the results for stars brighter than 9^{th} for the field using the new setup; 90% of the stars contribute 90% or more of the light in their apertures, while 93.5% contribute 50% or more. As such, we can expect a similar fraction of targets to be affected by blending to a similar degree. However, in the case of the 85-mm lenses we may well benefit from the 200-mm data

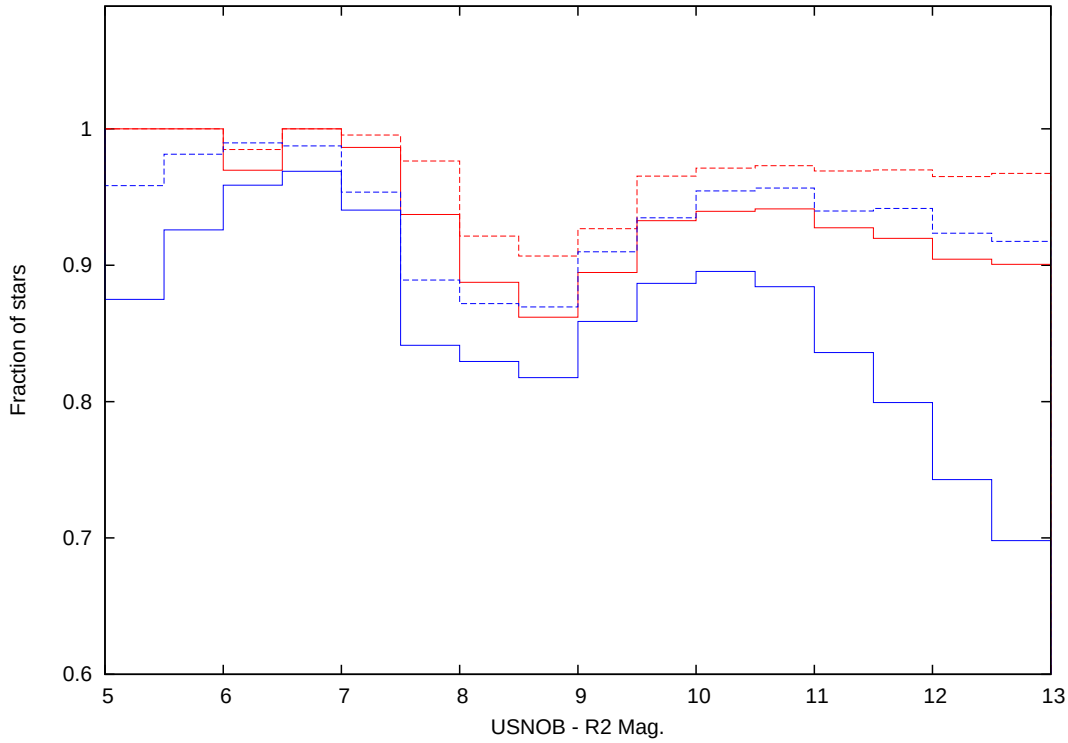

Figure 7.11: The fraction of stars contributing a given fraction of the light in a WASP reduction aperture. The solid (dashed) lines correspond to a primary target contribution of 90% (50%). Red lines are the results for a typical field of 200-mm data, blue are those for a typical 85-mm data.

on the blending objects. As the 200-mm data has a better resolution we may be able to rule out some false positives by identifying them as eclipsing binaries or other variable stars using it.

7.4.4 False Positives

It is important to consider how many of these signals would, in reality, be flagged for human attention. So far the recovery rate has been calculated by checking for a match with the injected signal. Clearly, this benefit does not exist for real signals. Hunt1star returns the ephemeris information for the 5 most significant peaks of the periodogram it

constructs for *every* lightcurve. This raises the question, can false positives be identified without prior knowledge of the correct period. If not then each of the detections made in this analysis would be treated as a real candidate. Some could be ruled out with a visual inspection of the lightcurve though others would be selected for further follow-up observations like those in Section 2.5. The visual inspection alone would be time consuming and so have a negative impact on the ultimate recovery rate.

By taking into account if these peaks would pass the rejection criteria adopted by Collier Cameron et al. (2006), and detailed in Section 2.4.1, I can determine if they would ever be considered a possible candidate and thus the potential impact they would have on the determined recovery rates. I applied the criteria to all of the recovered peaks for each injected signal. To pass this check each lightcurve must have at least one signal peak which: has more than two transits, has gaps no larger than 2.5 times the transit duration, has a signal-to-red-noise ratio of smaller than -5 and an anti-transit ratio greater than 1.5. Each lightcurve then falls into one of four categories: a true positive - it has at least one peak recovered on a matching ephemeris by the previous analysis and passes the selection criteria; a true negative - it has no peaks matching the inject ephemeris and fails the selection criteria; a false positive - it has no peaks matching the inject ephemeris but has at least one that passes the selection criteria; or a false negative - it has at least one peak recovered on a matching ephemeris but none of the peaks pass the selection criteria. The results of this investigation are detailed in table 7.1

Table 7.1: Table showing the results of applying the rejection criteria. Results are given to the nearest whole number.

Seasons of data	1	2	3	4
% True positives:	22	33	35	36
% False positives:	12	18	17	14
% True negatives:	60	44	43	43
% False negatives:	5	5	6	6

Once applied, the rejection criteria lead us to conclude that, over the four seasons $67 \pm 2\%$ of the positive detections are True Positives. Thus we would expect for every 3 objects sent for further follow-up that 2 of them are planets. In reality this figure is closer to one planet in every 12 objects sent for follow-up. This higher false positive rate includes the contribution of astrophysical sources of false positives such as shallow or blended eclipsing binaries that the rejection criteria cannot eliminate. As the blending fraction is similar for data collected using 200-mm and 85-mm lenses in the magnitude range of interest there is no reason to expect a significant increase in the ultimate number of false positives. The False Negative rate is also of interest. Of the peaks that do show signals recovered with correct ephemerides $15 \pm 2\%$ are not sufficiently significant to be considered as candidates. This has the effect of lowering the recovery rates from section 7.3.

7.5 Conclusion

Having investigated various effects that could undermine the results of the signal injection I conclude that the data acquired with the upgraded WASP-South instrument is suitable for detecting planets transiting bright stars, as intended. There is no reason to expect that the shape of the transit injected significantly increased the detectability of our signals. The profile of the red-noise in the signals detected with the artificial extra seasons behaves in a similar way to the red-noise in real planet signals detected with multiple seasons of data. And, while the on sky radius of the reduction apertures has increased by a factor of 2.75, I do not expect that blending will have a more significant impact than it did with the 200-mm lenses.

These results show that we can expect to recover between 50% and 85% of real signals with periods shorter than 10 days and depths $> 0.5\%$ in cases of centrally crossing transits with the 3 years of data. Due to the random orientation of planet orbits, these recovery rates represent the maximum that can be expected from WASP-South data. As these planets will be Jupiter-like in size we can expect their bulk

properties to be similar to known examples. Their real value will be the ease with which they can be investigated further. Their host stars will have visual magnitudes of 9 or greater and studies will benefit from telescope facilities available in the southern hemisphere. Taking into account the False Negative rate drops these figures by around 15% to between 42% and 72%.

By way of comparison with the old instrument, Smith et al. (2009) found that they had a $> 50\%$ chance to detect, using 3 seasons of 200-mm data, a Saturn analogue with a period of ≤ 10 days and a $\sim 20\%$ chance if it has a period of ~ 20 days. I find that, using 3 seasons of 85-mm data, there is $\sim 60\%$ chance to detect a sub-Saturn ($0.82\ R_{Sat}$) with a period of ≤ 10 days and $\sim 20\%$ chance if it has a period between 10 and 15 days.

In addition, we are capable of detecting signals as small as 0.2% with periods < 10 days. These would be interesting as they represent examples of Neptune sized objects orbiting early K-type stars and smaller. Three seasons of data will allow us to find more than 50% of the systems with signal depths greater than 1% in orbits longer than 10 days. As a practical demonstration of these capabilities I include Fig 7.12, WASP-South data collected with the 85-mm lenses of an eclipsing binary system. The primary eclipse has a depth of 0.37% and the visible secondary eclipse is shallower.

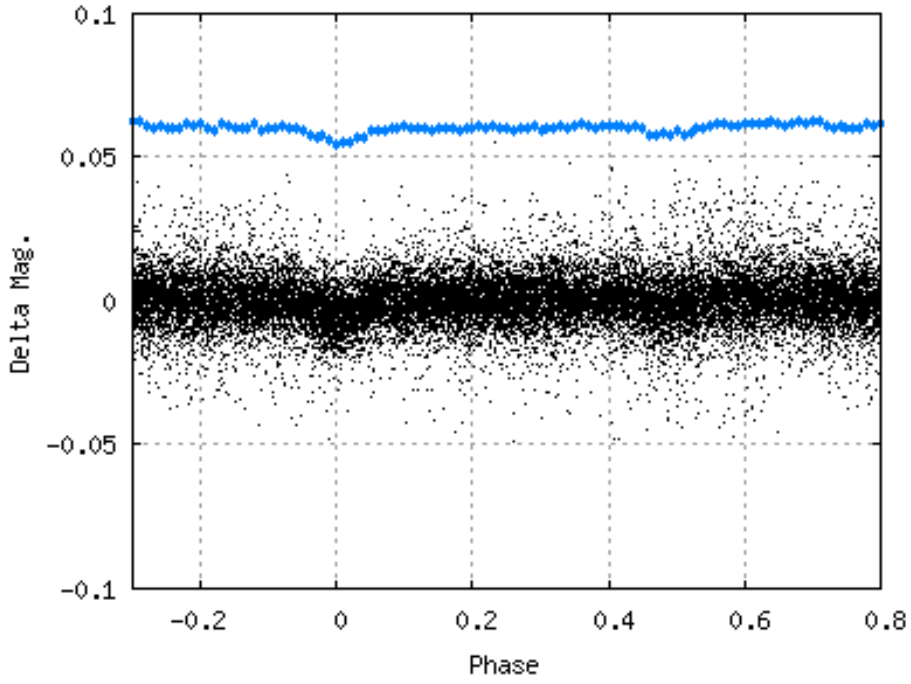

Figure 7.12: Phase folded lightcurve of the eclipsing binary identified as 1SWASPJ230002.76-462931.7. The primary eclipse at phase 0 has a depth of 0.37% with a shallower seconday eclipse visible at a phase of 0.5.

8 Conclusions

8.1 Introduction

Just over twenty years ago we did not know for certain if there were any planets other than those in our solar system. The discovery of 51 Peg b was a great surprise of which the discovery team said; "[the] very small distance between the companion and 51 Peg is certainly not predicted by current models of giant planet formation" (Mayor & Queloz 1995). Discovering close-in, giant planets like this was the motivation behind many wide-field transit surveys, of which WASP (Pollacco et al. 2006) has arguably become the most successful ground-based example.

This success, the dearth of planets known to transit bright stars in the southern hemisphere and the wealth of information from only two such targets in the north were the motivations behind modifying the WASP-South instrument. Over the course of this thesis I have detailed the modifications to the instrument and the software used to analyse the data. I have shown that the data *can* be used to detect planets orbiting bright stars. These planets will orbit stars that are around 2 magnitudes brighter than the survey's previous limiting magnitude using 200-mm lenses. I have shown that hot-Jupiters with transit depths between 0.5% and 2% and periods of less than 10 days can be recovered with an efficiency of between 42% and 72%, though it is not impossible to detect signals as small as 0.2%. Planets with periods between 10 and 15 days can be detected with an efficiency of around 50% if their transit depths are 1% or greater. Despite the reduction in the spatial resolution of the data due to the lens change, we can expect the effect of blending on our main targets to remain similar.

I have contributed to the follow-up of several newly discovered and previously known planets. Using new and archival data, I have updated and refined parameters for 7 previously known WASP planets. By doing this I have resolved discrepancies in previous studies of the spin-orbit alignment of WASP-31, show that WASP-42 may be an important probe of planet migration theory and show that seemingly "typical"

systems may warrant re-observing. As for the newly discovered systems: WASP-120 b is a system with a star showing variable activity and a possibly eccentric planet orbit, WASP-122 b offers a good opportunity for atmospheric study, and WASP-123 b, which orbits an old star ($\sim$ 7 Gyr) looks initially unremarkable as hot-Jupiters go, though this has been said erroneously before.

In this chapter I will build on the information we can gain from the planets WASP-South can find and look forward to the kinds of investigation that planets orbiting bright stars will permit in the near future. I will consider some of the instruments available now for use in such investigation. I will look at the next generation of transit surveys and the kinds of planets they aim to discover. I will also look at the next generation of instruments with which we can study planets in ever more depth.

8.2 Great Expectations

8.2.1 Hot Jupiters

As shown in the previous chapter, WASP-South remains most sensitive to hot Jupiter planets in short period orbits. Most systems with well defined parameters already fall into this category simply because the signals they produce - both transit and radial velocity (RV) - are much larger than those of less massive or longer-period planets. In addition, there are still many open questions about close-in, giant exoplanets particularly regarding their mass-radius relation, formation and migration.

In recent years many groups have begun to simulate the atmospheres of exoplanets taking into account their irradiation, tidal forces, magnetic fields and potential compositions (analytical model including Ohmic heating, Ginzburg & Sari 2016; CLOUDY, Ferland et al. 1998; Turner et al. 2016a; THOR, Grosheintz et al. 2015; HELIOS, Malik et al. 2015; Tau-REx, Waldmann et al. 2015; Exo-transit, Kempton et al. 2015; etc..) in an effort to answer outstanding questions like the very large radii of some hot Jupiters. Solar system planets and environments make good checks for

models as high quality data has been gathered however they provide poor constraints for more extreme, close-in planets. High quality observations of exoplanet atmospheres are needed to constrain and refine these models. The models themselves can be used to predict winds, chemical abundances and equilibria. If they are developed far enough, simulations of what a life bearing world might look like will be possible. This will be important to be able to tell the difference between, for example, biotic and aboitic oxygen production.

Transits of inflated, short period, hot exoplanets are a good place to start. During a transit we can use transmission spectroscopy (or spectrophotometry) to measure the wavelength dependence of the transit depth. The magnitude of the effect depends on the proportion of light that passes through the atmosphere and how strongly it is absorbed. The proportion of light that passes though the atmosphere depends on the relative radii of the planet and star as well as the scale hight of the atmosphere. In turn the scale height, depends on the planet density, temperature and mean molecular mass of the atmosphere. Meanwhile, the strength of the absorption depends on the abundance of the opacity sources at the observed wavelengths.

A big challenge to the study of exoplanet atmospheres is the availability of targets with spectral features that are not masked by clouds/hazes. These absorb or scatter light of all wavelengths and suppress the wavelength dependence of the planet's apparent radius. The extent and nature of clouds and hazes in hot Jupiter atmospheres and how this relates to the planet's other properties is an open question and currently an active area for research. Fig. 8.1 shows the predicted transit depth variation expected for one atmospheric scale height for all planets with measured radii, masses and V magnitudes in the exoplanet.eu database. The planets found by WASP-South will begin to populate the left-hand side of this plot.

The HD 209458 and HD 189733 systems have been observed repeatedly, mainly due to the brightness of their host stars, resulting in many discoveries. Results for other transiting planets have been less decisive. Simultaneous observations in several photometric bands have been performed on several planets. WASP-15 b, WASP-19 b, WASP-23 b, WASP-67 b, WASP-80 b, and Qatar-2 b (Mancini et al. 2013; Mancini et al.

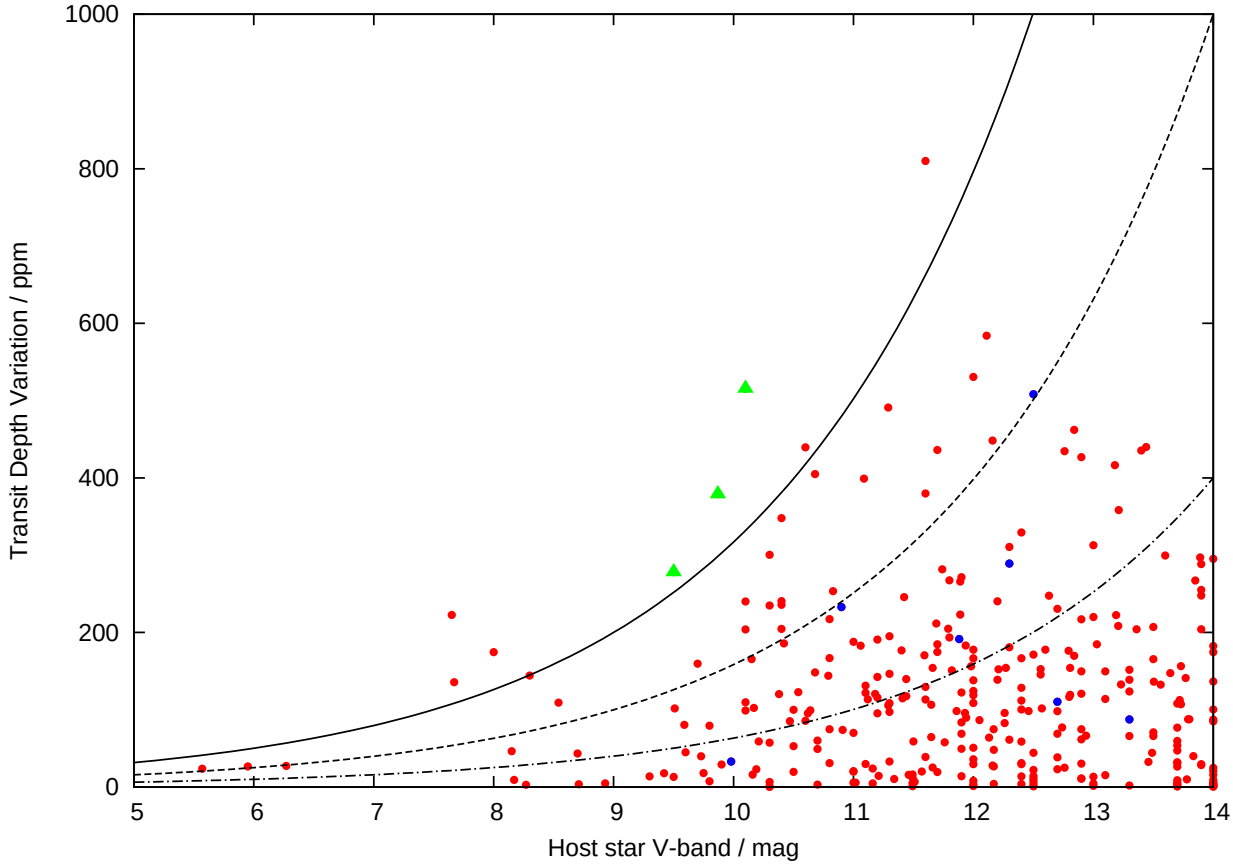

Figure 8.1: Predicted transit depth variation of known transiting planets. The blue points show a sample of planets that have been investigated using spectrophotometry; WASP-15 b, WASP-19 b, WASP-23 b, WASP-67 b, WASP-80 b, Qatar-2 b and HAT-P-14 b. Few of these are expected to exhibit exceptional depth variations and only HAT-P-14 b orbits a star brighter than V= 11. The green triangles indicate more suitable targets with larger predicted depth variations and brighter host-stars; WASP-69,WASP-76 and WASP-94. The solid line represents a curve of constant signal-to-noise ratio (SNR) for an instrument capable of detecting a depth difference of 200-ppm in a target with a V=9 host star. The dotted line is constant SNR twice that of the first and the dot-dashed line is four times that of the first. The brighter WASP-South survey will add targets to the upper-left area of the plot. Data taken from exoplanet.eu 07/2016.

2014b; Mancini et al. 2014a; Mancini et al. 2014c; Nikolov et al. 2013; Southworth et al. 2013) have been investigated using the GROND 7-band imager on the MPI

2.2-m telescope at la Silla, Chile. WASP-80 b and HAT-P-14 b have been observed using MITSuME on the 0.5-m telescope and MuSCAT on the 1.88-m telescope at the Okayama Astrophysical Observatory (OAO) by Fukui et al. (2014) and Fukui et al. (2016). These planets are highlighted in Fig. 8.1. None are exceptional candidates for atmospheric investigation with current equipment as they orbit relatively dim stars with small predicted transit depth variations. Some systems that may be more favourable are WASP-69, WASP-76 and WASP-94 as they orbit brighter stars and have larger predicted signals.

The two studies of WASP-80 b show some interesting results. Fig. 8.2 is a modified version of Fig. 8 from Fukui et al. (2014). In it we see a comparison between the results using the MITSuME instrument on the Okayama Astronomical Observatory 0.5-m telescope with the results using GROND from Mancini et al. (2014b). Despite the size disparity between the telescopes, the uncertainties on the derived planet-to-star radius ratios are similar at longer optical wavelengths. The optical observations of Fukui et al. (2014) from 2013-Sep-22 lack data after egress. Less data out of transit makes it more difficult to establish a baseline stellar brightness against which to determine the transit depth. As a result, the observations of 2013-Sep-22 have a larger uncertainty than those from 2013-Aug-13. It is possible that performing a joint analysis of both lightcurves from each optical band could improve the overall uncertainties. However, the lightcurves are separated by nearly a year. This separation gives plenty of time for the atmospheric conditions of WASP-80 b to have changed making the validity of combining the data questionable. The difference in precision between the GROND and MITSuME data is most pronounced in the g-band suggesting this is where use of a larger telescope is more favourable.

8.2.2 Warm Jupiters

The likelihood of WASP-South finding planets with periods longer than 10 days is not particularly high. Our 3 seasons of data allow the detection of transits with depths of 1% or deeper with periods longer than 10 days with an efficiency of just over 50%. This

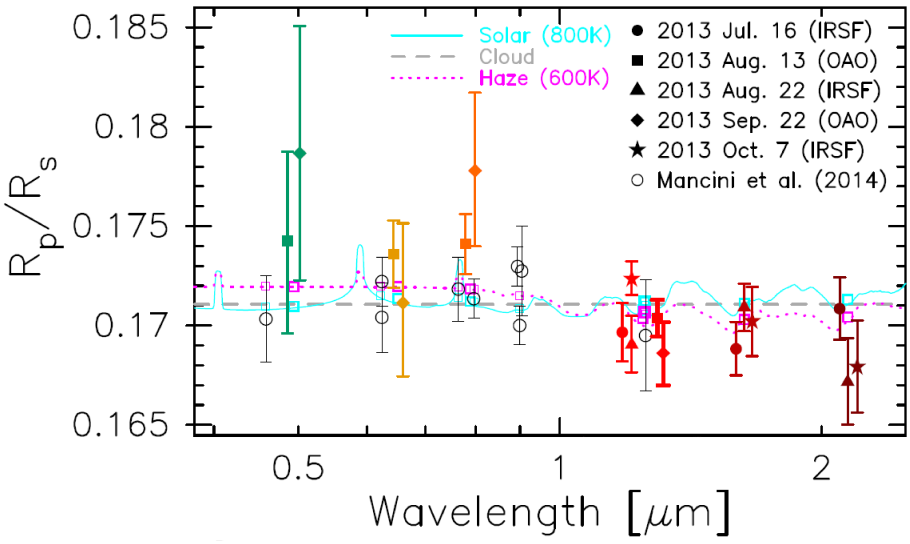

Figure 8.2: Modified version of figure 8 from Fukui et al. (2014) showing their derived transit depths of the WASP-80 system. Coloured points are those gathered for the paper, black, open circles are from a study by Mancini et al. (2014b) using GROND. The green, yellow and orange points were observed using MITSuME. Of these, the square points are a full transit and the diamonds are an observation missing the ingress and some data before it. This missing data leads to a larger uncertainty on the transit depth. The uncertainties on the points corresponding to the full transit are easily comparable to those from GROND except at the shortest wavelength of observation.

being said, the WASP survey does boast two such planets discovered using southern data, both with transit depths of close to 1%; WASP-117 b (P = 10-days; Lendl et al. 2014) and WASP-130 b (P = 11.6-days Hellier et al. 2016, Sub.). Planets like these are of interest as the tidal forces between them and their host stars are weaker than hot Jupiters, thus extending the time scale for tidal circularisation of the orbit and realignment with the host star spin. This makes them important systems for the study of planetary migration.

While orbital alignment can be measured for planets of all sizes it is of particular interest for giant planets as they are thought to form beyond the ice line. However, there have been recent suggestions for in-situ formation mechanisms for close-in giant planets together with evidence of a fully formed planet orbiting a very young star (5−10

Myr, K2-33; David et al. 2016). Boley, Granados Contreras & Gladman (2016) suggest that, if a critical mass of material has formed a rocky core before circumstellar gas has dissipated during the star's formation then it can capture enough gas to become a giant planet. Indeed, K2-33 still "has a tenuous dust disk" which lends credence to the idea. They do note that there are problems with this scenario, namely the observed distribution of spin-orbit inclinations and the presence of other companions at large separations which favour some kind of scattering scenario. Batygin, Bodenheimer & Laughlin (2015) put forward a similar scenario requiring a $10 - 20$ Earth-mass core which then accretes gas. A testable consequence of their scenario is the presence of additional, low-mass planets with orbital periods shorter than 100 days. They suggest dynamical interactions will likely cause these planets not to transit, thus they should be searched for using RVs. Formation location, internal or external to the ice line, is likely to leave chemical markers in the atmospheres of exoplanets. Madhusudhan (2012) and Madhusudhan, Amin & Kennedy (2014) suggested that carbon-to-oxygen ratio could give clues as to formation environments and even migration pathways. Thus, any systems like these discovered will be favourable targets to test these theories.

8.2.3 Smaller Objects

Finding an object analogous to Neptune is highly unlikely with the WASP-South instrument but our study showed that with 3 years of data it is not impossible. The previous chapter gives a recovery rate of approximately 10% for such objects using 3 years of data. Objects like this, particularly orbiting a bright star would be intensely studied due to the lack of favourable targets in this area of parameter space. GJ 1214 b (Charbonneau et al. 2009) and GJ 3470 b (Bonfils et al. 2012) are two such objects and have been studied intensely and repeatedly for signs of atmospheric spectral features. In the case of GJ 1214 b this is despite the host star being quite faint (V= 14.7).

Nascimbeni et al. (2015) combined new observations of GJ 1214 from the Large Binocular Telescope with archival observations and compared them to the atmospheric models of Howe & Burrows (2012). They ruled out the tentative detection of a Rayleigh

scattering slope by de Mooij et al. (2012) and Fraine et al. (2013) and find in favour of a cloudy atmosphere which hides any spectral features. Likewise, the most recent study of GJ 3470 b by Dragomir et al. (2015) includes data from previous atmospheric studies. While they conclude that the best fitting atmospheric models do have clouds masking infrared spectral features (see Fig. 8.3), the presence of hazes lead to a strong Rayleigh scattering feature. From this feature and planetary parameters from Biddle et al. (2014) they calculate a mean molecular weight consistent with a hydrogen-helium dominated atmosphere, as did Nascimbeni et al. (2013). This result shows that a cloudy atmosphere does not always completely rule out further compositional analysis.

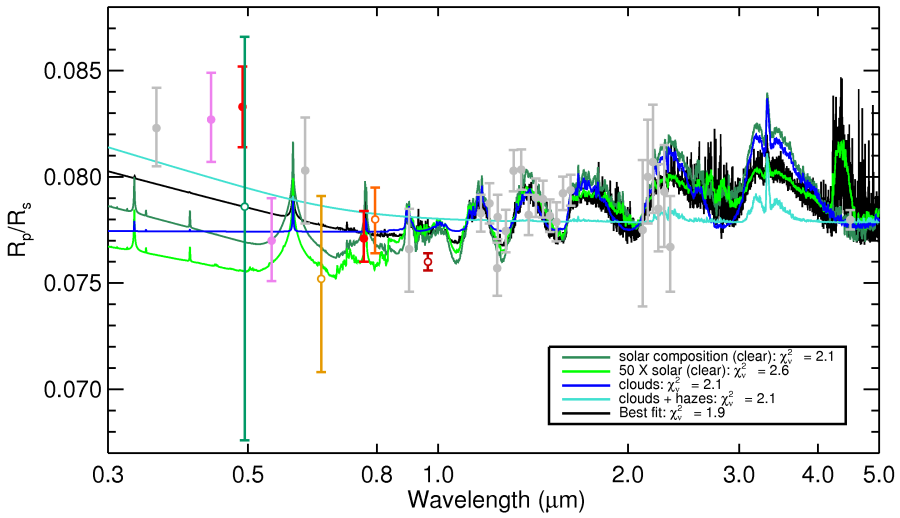

Figure 8.3: Modified version of Figure 4 from Dragomir et al. (2015). showing atmospheric models fit to new and archival data for GJ 3470. Solid coloured points are new observations from the paper. Hollow, coloured points are observations from Fukui et al. (2013). The results from Fukui et al. (2013) favour a model less affected by clouds than the re-analysis by Dragomir et al. (2015).

8.2.4 Current Instruments

A relatively "low cost" way to investigate atmospheres is with multi-colour spectrophotometry - making observations of transits in multiple bands, preferably simultaneously. Simultaneous observations ensure that any lightcurve features due to external factors like stellar activity or potentially transient planetary cloud are common. The impact of transient events on the data quality may vary, e.g. star spots, which have a different contrast to the stellar surface at different wavelengths. However, simultaneous observation avoids the added complication of the magnitude of the effect varying in time.

Observations like these will not allow us to precisely distinguish between atmospheric models in much the same way that two-colour observations from "warm-*Spitzer*" are less useful for breaking the degeneracies than previous four-colour observations (Madhusudhan 2012) or observations supplemented in some other way such as the Hubble Space Telescope's Wide-Field Camera 3 (Mahtani et al. 2013). Spectrophotometric observations can allow us to determine if there is colour dependence to the transit depth and over what spectral range it extends. This would demonstrate if the atmosphere was clear or cloudy during the period of observation. On Earth we see variations in atmospheric clarity on time scales ranging between hours and weeks while larger weather phenomena, e.g. el Niño, can last for years. The giant planets also show great variety: Uranus appears quite featureless, Saturn's cloud patterns are fairly uniform while Neptune has occasional cloud features. Jupiter's cloud patterns show the most obvious variation, though even their time scales vary. For example, Jupiter's Great Red Spot has persisted for between 170 and 300 years (see Morrison & Owen 2003 and other similar texts). Thus, we cannot say for certain how clouds on exoplanets will behave over time or if an atmosphere once found to be cloudy (or clear) will remain so.

Planets from WASP-South will, of course, have the best visibility from southern latitudes. I include here some details of current telescopes and instruments that can be used to perform spectrophotometry. In theory any facility capable of multicolour

photometry is a potential resource to this kind of investigation. In practice facilities with larger telescopes and instruments capable of simultaneous observations in multiple bands are preferable. However, the brightness of the host stars of systems WASP-South will find will make them valuable targets for even small facilities.

I have already mentioned GROND on the MPG 2.2-m telescope. This 7 colour instrument has been used to observe several planets, both in transit and secondary eclipse.

The PISCO instrument on the 6.5-m Clay telescope is a 4-colour imager similar in design to GROND. This stands to be an excellent instrument as the telescope has a larger collecting area than the MPG 2.2-m to which the GROND instrument is installed. Thus this will increase precision for brighter stars and extend the range of viable targets to dimmer stars.

Smaller facilities such as the new ROS2 instrument on the 0.6-m REM telescope and the PROMPT array of 6 0.4-m telescopes are also potentially viable. ROS2 is a 4 colour imager similar to PISCO and GROND. Each of the PROMPT array's 6 telescopes can image the same object in a different band. While these are 0.6-m, and 0.4-m respectively, the WASP project do regularly use follow-up from TRAPPIST which is a similar size. Fukui et al. (2013, 2014) have performed multicolour observations of GJ3470 b and WASP-80 b using the 0.5-m MITSuME telescope. Fig. 8.2 shows their results for WASP-80 b while their results for GJ 3470 b can be found as part of Fig. 8.3. The results for WASP-80 are particularly useful as we see the capabilities of the small MITSuME facility compared with those available to GROND. The real strength of the larger facility is increased precision at shorter wavelengths.

8.3 Next Generations

8.3.1 Detection

8.3.1.1 Next Generation Transit Survey

Building on the success of WASP, the Next Generation Transit Survey (NGTS; Wheatley et al. 2014) has begun operations at Paranal, Chile. NGTS is comprised of an array of 12 independent telescopes, each capable of observing 13^{th} mag star to better than 0.1% precision. We show an example lightcurve obtained by an NGTS prototype camera in Fig. 8.4. The goal is to discover more examples of Neptune and super-Earth type planets by targeting stars smaller than the Sun; K and M dwarfs. By surveying select regions of the southern sky NGTS will discover examples of these kinds of planets orbiting brighter stars. The host star's inherent brightness and the larger comparative cross-section of the planet's atmosphere in transit will facilitate further atmospheric study of the kind performed on GJ 3470 b.

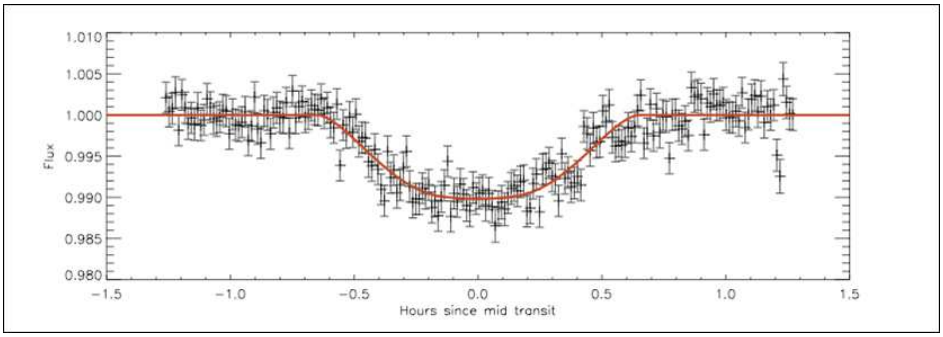

Figure 8.4: Example lightcurve of a transit of GJ436 taken using a prototype NGTS telescope. The data quality is easily equal to follow-up lightcurves regularly used in planet discovery papers. Sourced from http://www.ngtransits.org/prototype.shtml on 15/07/2016.

8.3.1.2 Transiting Exoplanet Survey Satelite

All going well, the Transiting Exoplanet Survey Satellite (TESS: Ricker et al. 2015) will complete the mission for which WASP was started. The primary goal of TESS is to perform a transit survey of the whole sky excepting the area 6˚above and below the ecliptic and small areas between its pointings. It will do this using 4 cameras oriented so as to image from 6˚ above (or below) the ecliptic to the pole of one hemisphere. Over the course of a year it will step though 13 pointings which provide varying degrees of overlap with the previous fields. Towards the ecliptic there will be no overlap with increasing overlap towards the pole, which will be monitored continuously for just under a year. Each camera will have a field of view (FOV) of 24×24 degrees for a combined FOV of 2300 degrees^2 as there will be no overlap in camera FOV.

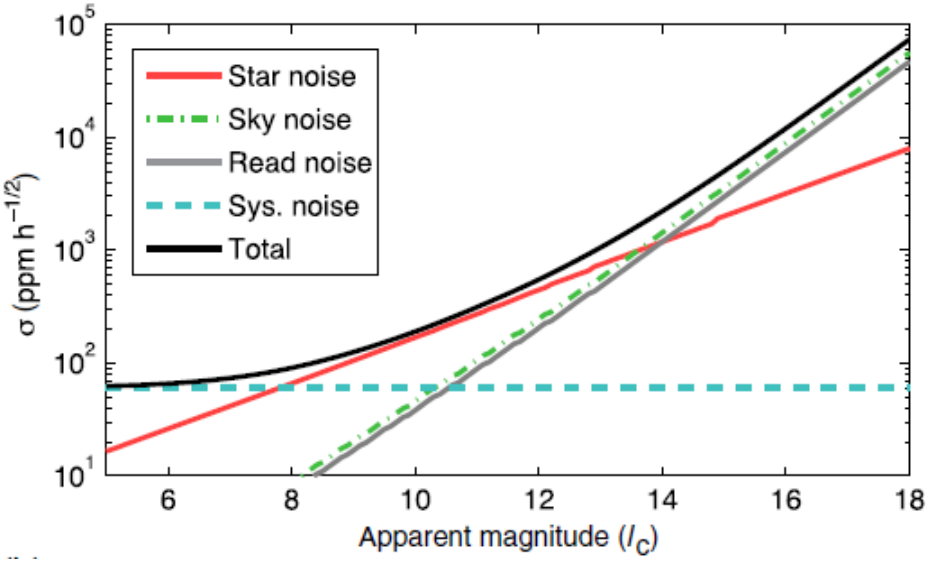

Figure 8.5: Expected precision of TESS instrument from Ricker et al. (2015)

The expected photometric precision of TESS is illustrated in Fig. 8.5. It is easily capable of detecting Jupiter size planets orbiting sun-like stars down to I-band magnitudes of 13. Combined with a minimum observational window of 27 days, this precision will allow the confident detection of every Jupiter sized planet with an orbital

period under 9 days. TESS is also expected to detect thousands of sub-Neptune planets, hundreds of super-Earths and even a handful of Earth sized bodies. As it is surveying nearly the whole sky, examples of these kinds of planets can be expected orbiting all kinds of stars. While *Kepler* has found thousands of planets, many orbit dim stars limiting their usefulness to further study. Many TESS planets will have bright host stars and the longest period planets found will, by design, be in the continuous viewing zone of the James Webb Space Telescope.

8.3.1.3 Planetary Transits and Oscillations

The *Pla*netary Transits and Oscillations (PLATO:Rauer et al. 2014) mission is another space based, wide field transit survey set for launch by the European Space Agency (ESA) by 2024. PLATO will be comprised of 34 individual refracting telescopes with a FOV of 1100 degrees^2 which overlap to give an overall FOV of 2232 degrees^2. The overlap in camera FOV is to provide increased photometric precision in areas covered by multiple cameras while giving a very large overall footprint. The expected photometric precision is illustrated in Fig. 8.6. Around brighter stars and in areas with more overlapping cameras PLATO is expected to reach precisions of the order 0.001% or better. This unprecedented precision will allow the detection of extremely small objects. For example, an object the size of Ganymede passing in-front of the Sun will cause a transit with a depth of 0.0014% (14 ppm). Thus we can expect the direct detection of large, co-transiting exo-moons via photometry if the host star is very bright. For comparison, the transit of the Earth in front of the Sun would have a depth of 0.0084% (84 ppm).

It is planned for PLATO to observe two fields for a period of 2 years each and then cover several other fields for a number of months each. These two long "stare" phases will allow for the detection of planets in much longer orbits than TESS. This will increase the likelihood of detections of planets in the habitable zones of stars more like the Sun; G and K-dwarfs as opposed to smaller, cooler M-dwarfs.

One of the factors affecting the precision of planetary parameters is the precision

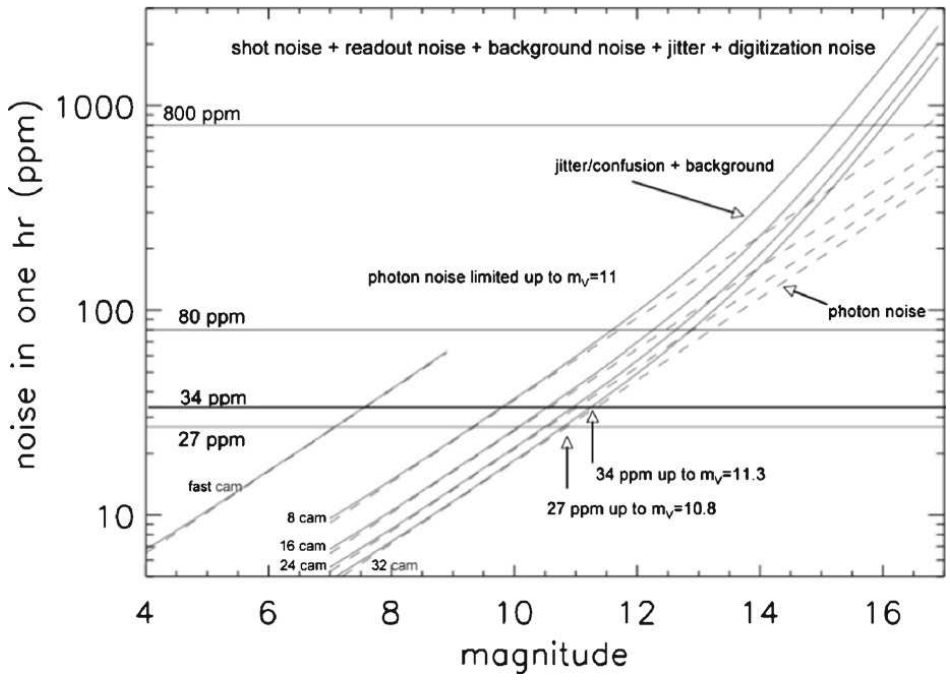

Figure 8.6: Expected precision of PLATO instrument from Rauer et al. (2014)

to which stellar parameters are known. By observing stellar oscillations it is possible to derive masses, radii and ages via astroseismology. PLATO is designed to be able to measure stellar oscillations of solar-like stars in order to derive host star masses and radii to high precision. This is expected to allow planetary parameters to be determined with a precision of $\approx 10\%$ for masses and $\approx 2\%$ for radii. Observations of stellar oscillations will also help determine stellar ages to $\approx 10\%$.

8.3.2 Characterisation

As well as new discovery missions, there are multiple tools under construction and planned to further detailed observation of transiting planets. These start with the CHaracterising ExOplanet Satellite (CHEOPS: Fortier et al. 2014), planned for late 2017, coinciding with the launch of TESS. The James Webb Space Telescope (JWST) is planned to follow in 2018 and a smaller mission, TWINKLE (Savini et al. 2016)

aims to be ready before 2019. The European Extremely Large Telescope (E-ELT) is expected to see first light in 2024 around the same time PLATO is due for launch.

8.3.2.1 CHEOPS

CHEOPS is a 0.3-m telescope that will occupy a low Earth orbit. Its science goal is to characterise exoplanets in the super-Earth to Neptune mass range by determining their radii to a precision of $\sim 10\%$. It will also search for additional transiting planets similar to those in the WASP-47 system (Becker et al. 2015) using a detector with a wavelength range between 0.4 and 1.1-μm. Transit timing and duration variations (TTVs and TDVs) can also be used to search for additional non-transiting objects or exo-moons (Simon et al. 2015). Simon et al. (2015) used the calculations of Barnes & O'Brien (2002) to calculate the stability of various sizes of exo-moon orbiting various classes of planets. For example, they show that a Ganymede sized exo-moon could be stable in orbit of a "super-Neptune" with an orbital period over 25-days; a Neptune with an orbital period of just over 30-days; and a super-Earth with an orbital period of around 40-days[1].

8.3.2.2 JWST

JWST is a 6.5-m telescope that will occupy the Earth-Sun L2 point. It will host a range of instruments designed for observations in the near to mid infra-red which are summarised in Table 8.1. Greene et al. (2016) performed a study with simulated emission and transmission spectra for a generic hot Jupiter, warm Neptune, warm sub-Neptune and cool super-Earth and applied expected JWST instrument responses. They make a number of interesting conclusions which they present in more detail than this summary. They note that their conclusions are dependent on what the true systematic noise of JWST turns out to be or how binning/ co-adding data will improve observations. Obtaining spectra over JWST's entire range of 1-11μm will take at least 4 transit or

[1]These calculations were made assuming a solar mass star and a lone moon-planet pair

Table 8.1: A summary of information about the instruments included on JWST.

Instrument	Description
MIRI	*Mid Infrared Instrument* - Provides: low resolution spectra (R$\sim$ 100) for $\lambda = 5 - 10\mu$m; Medium resolution spectra (R$\sim$ 3000) for $\lambda = 5 - 28.3\mu$m; Coronagraphic imaging at 10.65, 11.4, 15.5 and 23μm
NIRCam	*Near Infrared Camera* - Main imaging camera, $\lambda = 0.6 - 5\mu$m
NIRISS	*Near Infrared Imager and Slitless Spectrograph* - Provides; wide-field grism spectroscopy (R$\sim$ 150) for $\lambda = 1 - 2.5\mu$m; single object grism spectroscopy (R$\sim$ 700) for $\lambda = 0.6 - 3\mu$m; Aperture-masking interferometry for $\lambda = 3.8 - 4.8\mu$m; Broadband imaging between $\lambda = 1.0 - 5.0\mu$m with a $2.2' \times 2.2'$ field of view.
NIRSpec	*Near Infrared Spectrograph* - Multi-object spectrograph able to observe over 100 objects in a field of view of $3' \times 3'$.

secondary eclipse events for planets with bright hosts. Emission spectra are expected to provide better constraints on molecular mixing ratios than transmission spectra in the case of cloudy atmospheres for hot Jupiters and warm Neptunes, assuming clouds do not also significantly impact emission. Their cool, super-Earth emission spectrum had insufficient signal-to-noise (from a single secondary eclipse) to retrieve information from due to the planet-to-star contrast ratio. However, the hot Jupiter and warm Neptune-like planets' spectra do allow for the retrieval of metallicity information via transmission spectra if their atmospheres are clear. Emission spectra also allow the measurement of Carbon-to-Oxygen ratios for hot Jupiters and warm Neptunes, though transmission spectra work better for 'warm' planets. These open up the investigation of planet-to-star metallicity differences and the use of C/O ratio to investigating if the planets formed interior or exterior to their system's water-ice line.

JWST will be launched in the early days of NGTS and the very early days of TESS. As a result, many of the first targets observed will be those known now. Stevenson et al. (2016) identified several criteria that make for preferred targets: a high ecliptic latitude, making them closer to JWST's continuous viewing zone; short orbital periods, this has several benefits including favourable insolation and the ability

to observe multiple transits in a short space of time; well constrained ephemerides and planet masses, needed to plan observations well and interpret observed spectra respectively; a bright, preferably quiet, host star; and a transmission spectrum with large features. These last two criteria have already been discussed regarding Fig. 8.1. Of the 12 planets they identify, 7 are WASP planets.

8.3.2.3 Twinkle

Twinkle is designed to be a low cost space mission to obtain optical to infra-red spectra of transiting exoplanets (Savini et al. 2016)[2]. It will have a 0.45-m aperture and use three spectrographs; one optical for observations in the range $0.4 - 1.0\mu$m and two IR to make up the range $1.3 - 4.5\mu$m. The IR channels will have a resolving power of 300 at wavelengths shorter than 2.4μm and 70 at longer wavelengths. This large spectral range will allow Twinkle to look for signatures of H_2O, CO, CH_4, H_2S, other hydrocarbons and "amino acid precursors" NH_3 and HCN. It is expected to have a photometric stability of 100 ppm which opens up a large number of planets in Fig. 8.1 to investigation.

8.3.2.4 E-ELT

The E-ELT is to be a 39-m telescope, giving it huge light gathering power. Two instruments the High Resolution Spectrograph (HIRES; Zerbi et al. 2014) and the Mid-infrared ELT Imager and Spectrograph (METIS; Brandl et al. 2014) are expected to be instrumental in planetary investigation. Both will have modes allowing a resolving power of 100 000. A summary of the kinds of characterisation that can be performed with these instruments can be found in Snellen (2013). They focus on the ability of these high resolution spectrographs to pick out lines caused by molecules as has been done with HD 209458 b (Snellen et al. 2010). These allow compositional analysis to be

[2]Information in this section is also taken from the Twinkle website http://www.twinkle-spacemission.co.uk/. Retrieved 07/2016.

performed throughout a planet's orbit and so enable molecular signals to be mapped as a function of planet longitude, thus showing if there is positional dependencies on the state of atmospheric chemistry. Reflected light can also be observed at optical wavelengths allowing constraints to be placed on the planet albedo and energy-budget. Line broadening of these features will allow direct investigation of rotation and global winds.

Another interesting line of enquiry is possible with the Exo-planet Imaging Camera and Spectrograph (EPICS; Kasper et al. 2010). The imager is intended to achieve contrast ratios of 10^{8-9} at separations of a few tenths of an arc second. This should allow the direct detection of cold Jupiters, Neptunes and super-Earths, planets distant from their host-stars (Salter et al. 2014). This offers an alternative to using long baseline RV observations to look for non-transiting or long-period companions to hot Jupiter systems to build a more full picture of what these system architectures look like.

8.4 Final Word

Since its inception, WASP-South has been responsible for the discovery of over 120 planets and has contributed to the discovery of 30 others. With the upgrades to WASP-South and its pipeline we now know that it is capable of achieving the goal the modifications were intended for; finding planets transiting stars with magnitudes V$<$ 9. This next generation of planets from WASP-South will be studied for years to come with all kinds of equipment. The question remains then, where are they? In part this is due to delays in searching processed data for planets. We know that planets orbiting bright stars are out there (HD209458 b, HD189733 b, KELT-11 b). We know that they can be found in WASP-South data. It is just a matter of time and liberal application of the "ultimate planet finding tool", see Fig. 8.7.

Figure 8.7: Photo of the "ultimate planet finding tool". Taken in the Swiss telescope, La Silla.

Publications

Refereed

- **WASP-120b, WASP-122b and WASP-123b: Three newly discovered planets from the WASP-South survey**
  Turner, O. D., Anderson, D. R., Collier Cameron, A., Delrez, L., Gillon, M., Hellier, C., Jehin, E., Lendl, M., Maxted, P. F. L., Pepe, F., Pollacco, D., Queloz, D., Sgransan, D., Smalley, B., Smith, A. M. S., Triaud, A. H. M. J., Udry, S., West, R. G.
  Publications of the Astronomical Society of the Pacific (2016) 128, 964

- **Absolute parameters for AI Phoenicis using WASP photometry**
  Kirkby-Kent, J. A., Maxted, P. F. L., Serenelli, A. M., **Turner, O. D.**, Evans, D. F., Anderson, D. R., Hellier, C., West, R. G.
  Astronomy & Astrophysics (2016) 591, 124
  Modifications to the WASP reduction pipeline.

- **Hot Jupiters with relatives: discovery of additional planets in orbit around WASP-41 and WASP-47**
  Neveu-VanMalle, M., Queloz, D., Anderson, D. R., Brown, D. J. A., Collier Cameron, A., Delrez, L., Daz, R. F., Gillon, M., Hellier, C., Jehin, E., Lister, T., Pepe, F., Rojo, P., Sgransan, D., Triaud, A. H. M. J., **Turner, O. D.**, Udry, S.
  Astronomy & Astrophysics (2016) 586, 93
  Observed and reduced Danish R-band lightcurve of WASP-41.

- **Three WASP-South Transiting Exoplanets: WASP-74b, WASP-83b, and WASP-89b**
  Hellier, Coel, Anderson, D. R., Collier Cameron, A., Delrez, L., Gillon, M.,

Jehin, E., Lendl, M., Maxted, P. F. L., Pepe, F., Pollacco, D., Queloz, D., Sgransan, D., Smalley, B., Smith, A. M. S., Southworth, J., Triaud, A. H. M. J., **Turner, O. D.**, Udry, S., West, R. G.

Astronomical Journal (2015) 150, 18

Observed and reduced Liverpool Telescope/RISE V+R lightcurve of WASP-74.

- **The Well-aligned Orbit of Wasp-84b: Evidence for Disk Migration of a Hot Jupiter**

  Anderson, D. R., Triaud, A. H. M. J., **Turner, O. D.**, Brown, D. J. A., Clark, B. J. M., Smalley, B., Collier Cameron, A., Doyle, A. P., Gillon, M., Hellier, C., Lovis, C., Maxted, P. F. L., Pollacco, D., Queloz, D., Smith, A. M. S.

  Astrophysical Journal (2015) 800, 9

  Observed and reduced new Liverpool Telescope/RISE V+R lightcurve of WASP-84.

- **Three newly discovered sub-Jupiter-mass planets: WASP-69b and WASP-84b transit active K dwarfs and WASP-70Ab transits the evolved primary of a G4+K3 binary**

  Anderson, D. R., Collier Cameron, A., Delrez, L., Doyle, A. P., Faedi, F., Fumel, A., Gillon, M., Gmez Maqueo Chew, Y., Hellier, C., Jehin, E., Lendl, M., Maxted, P. F. L., Pepe, F., Pollacco, D., Queloz, D., Sgransan, D., Skillen, I., Smalley, B., Smith, A. M. S., Southworth, J., Triaud, A. H. M. J., **Turner, O. D.**, Udry, S., West, R. G.

  Monthly Notices of the Royal Astronomical Society (2014) 445, 1114

  Reduced 2 Liverpool Telescope/RISE V+R lightcurves of WASP-84.

- **WASP-104b and WASP-106b: two transiting hot Jupiters in 1.75-day and 9.3-day orbits**

  Smith, A. M. S., Anderson, D. R., Armstrong, D. J., Barros, S. C. C., Bonomo, A. S., Bouchy, F., Brown, D. J. A., Collier Cameron, A., Delrez, L., Faedi, F., Gillon, M., Gmez Maqueo Chew, Y., Hbrard, G., Jehin, E., Lendl, M., Louden,

T. M., Maxted, P. F. L., Montagnier, G., Neveu-VanMalle, M., Osborn, H. P., Pepe, F., Pollacco, D., Queloz, D., Rostron, J. W., Segransan, D., Smalley, B., Triaud, A. H. M. J., **Turner, O. D.**, Udry, S., Walker, S. R., West, R. G., Wheatley, P. J.

Astronomy & Astrophysics (2014) 570, 64

Observed and reduced Liverpool Telescope/RISE V+R lightcurve of WASP-106.

In proceedings

- **Planets Transiting Bright Stars with WASP-South**

  Turner, O. D., Anderson, D. R., Maxted, P. L. F., Hellier, C.

  Twenty years of giant exoplanets - Proceedings of the Haute Provence Observatory Colloquium, 5-9 October 2015

Bibliography

Adams E. R., Seager S., Elkins-Tanton L., 2008, ApJ, 673, 1160

Agol E., Steffen J., Sari R., Clarkson W., 2005, MNRAS, 359, 567

Albrecht S., Winn J. N., Johnson J. A., Howard A. W., Marcy G. W., Butler R. P., Arriagada P., Crane J. D., Shectman S. A., Thompson I. B., Hirano T., Bakos G., Hartman J. D., 2012, ApJ, 757, 18

Alsubai K. A., Parley N. R., Bramich D. M., Horne K., Collier Cameron A., West R. G., Sorensen P. M., Pollacco D., Smith J. C., Fors O., 2013, ACA, 63, 465

Andersen J., Andersen M. I., Klougart J., Knudsen P., Larsen H. H., Michaelsen N., Nielsen R. F., Nørregaard P., Olsen E., Rasmussen P. K., Seifert K. E., Jønch-Sørensen H., 1995, The Messenger, 79, 12

Anderson D. R., 2013, PhD thesis, Keele University

Anderson D. R., Collier Cameron A., Hellier C., Lendl M., Lister T. A., Maxted P. F. L., Queloz D., Smalley B., Smith A. M. S., Triaud A. H. M. J., West R. G., Brown D. J. A., Gillon M., Pepe F., Pollacco D., Ségransan D., Street R. A., Udry S., 2011, A&A, 531, A60

Anderson D. R., Collier Cameron A., Gillon M., Hellier C., Jehin E., Lendl M., Maxted P. F. L., Queloz D., Smalley B., Smith A. M. S., Triaud A. H. M. J., West R. G., Pepe F., Pollacco D., Ségransan D., Todd I., Udry S., 2012, MNRAS, 422, 1988

Anderson D. R., Brown D. J. A., Collier Cameron A., Delrez L., Fumel A., Gillon M., Hellier C., Jehin E., Lendl M., Maxted P. F. L., Neveu-VanMalle M., Pepe F., Pollacco D., Queloz D., Rojo P., Segransan D., Serenelli A. M., Smalley B., Smith A. M. S., Southworth J., Triaud A. H. M. J., Turner O. D., Udry S., West R. G., 2014, ArXiv e-prints

Anderson D. R., Collier Cameron A., Hellier C., Lendl M., Lister T. A., Maxted P. F. L., Queloz D., Smalley B., Smith A. M. S., Triaud A. H. M. J., Brown D. J. A., Gillon M., Neveu-VanMalle M., Pepe F., Pollacco D., Ségransan D., Udry S., West R. G., Wheatley P. J., 2015a, A&A, 575, A61

Anderson D. R., Collier Cameron A., Hellier C., Lendl M., Lister T. A., Maxted P. F. L., Queloz D., Smalley B., Smith A. M. S., Triaud A. H. M. J., Brown D. J. A., Gillon M., Neveu-VanMalle M., Pepe F., Pollacco D., Ségransan D., Udry S., West R. G., Wheatley P. J., 2015b, A&A, 575, A61

Anderson D. R., Triaud A. H. M. J., Turner O. D., Brown D. J. A., Clark B. J. M., Smalley B., Collier Cameron A., Doyle A. P., Gillon M., Hellier C., Lovis C., Maxted P. F. L., Pollacco D., Queloz D., Smith A. M. S., 2015c, ApJL, 800, L9

Armitage P. J., 2013, Astrophysics of Planet Formation

Bakos G., Noyes R. W., Kovács G., Stanek K. Z., Sasselov D. D., Domsa I., 2004, PASP, 116, 266

Bakos G., Afonso C., Henning T., Jordán A., Holman M., Noyes R. W., Sackett P. D., Sasselov D., Kovács G., Csubry Z., Pál A., 2009, IAU Symposium, 253, 354

Bakos G. Á., Hartman J., Torres G., Latham D. W., Kovács G., Noyes R. W., Fischer D. A., Johnson J. A., Marcy G. W., Howard A. W., Kipping D., Esquerdo G. A., Shporer A., Béky B., Buchhave L. A., Perumpilly G., Everett M., Sasselov D. D., Stefanik R. P., Lázár J., Papp I., Sári P., 2011, ApJ, 742, 116

Bakos G. Á., Csubry Z., Penev K., Bayliss D., Jordán A., Afonso C., Hartman J. D., Henning T., Kovács G., Noyes R. W., Béky B., Suc V., Csák B., Rabus M., Lázár J., Papp I., Sári P., Conroy P., Zhou G., Sackett P. D., Schmidt B., Mancini L., Sasselov D. D., Ueltzhoeffer K., 2013, PASP, 125, 154

Barnard E. E., 1916, AJ, 29, 181

Barnes J. W., O'Brien D. P., 2002, ApJ, 575, 1087

Barnes S. A., 2007, ApJ, 669, 1167

Batygin K., Bodenheimer P. H., Laughlin G. P., 2015, ArXiv e-prints

Beauge C., Ferraz-Mello S., Michtchenko T. A., 2008, Extrasolar Planets, Wiley-VCH

Becker J. C., Vanderburg A., Adams F. C., Rappaport S. A., Schwengeler H. M., 2015, ApJL, 812, L18

Berdyugina S. V., Berdyugin A. V., Fluri D. M., Piirola V., 2011, ApJL, 728, L6

Bessell M. S., 1979, pasp, 91, 589

Biddle L. I., Pearson K. A., Crossfield I. J. M., Fulton B. J., Ciceri S., Eastman J., Barman T., Mann A. W., Henry G. W., Howard A. W., Williamson M. H., Sinukoff E., Dragomir D., Vican L., Mancini L., Southworth J., Greenberg A., Turner J. D., Thompson R., Taylor B. W., Levine S. E., Webber M. W., 2014, MNRAS, 443, 1810

Böhm-Vitense E., 2004, AJ, 128, 2435

Boley A. C., Granados Contreras A. P., Gladman B., 2016, ApJL, 817, L17

Bonfanti A., Ortolani S., Piotto G., Nascimbeni V., 2015, A&A, 575, A18

Bonfils X., Gillon M., Udry S., Armstrong D., Bouchy F., Delfosse X., Forveille T., Fumel A., Jehin E., Lendl M., Lovis C., Mayor M., McCormac J., Neves V., Pepe F., Perrier C., Pollaco D., Queloz D., Santos N. C., 2012, A&A, 546, A27

Bouchy F., Udry S., Mayor M., Moutou C., Pont F., Iribarne N., da Silva R., Ilovaisky S., Queloz D., Santos N. C., Ségransan D., Zucker S., 2005, A&A, 444, L15

Brahm R., Jordán A., Bakos G. Á., Penev K., Espinoza N., Rabus M., Hartman J. D., Bayliss D., Ciceri S., Zhou G., Mancini L., Tan T. G., de Val-Borro M., Bhatti

W., Csubry Z., Bento J., Henning T., Schmidt B., Rojas F., Suc V., Lázár J., Papp I., Sári P., 2016, AJ, 151, 89

Brandl B. R., Feldt M., Glasse A., Guedel M., Heikamp S., Kenworthy M., Lenzen R., Meyer M. R., Molster F., Paalvast S., Pantin E. J., Quanz S. P., Schmalzl E., Stuik R., Venema L., Waelkens C., 2014, Proc.SPIE, 9147, 914721

Brogi M., de Kok R. J., Albrecht S., Snellen I. A. G., Birkby J. L., Schwarz H., 2016, ApJ, 817, 106

Brown D. J. A., Cameron A. C., Anderson D. R., Enoch B., Hellier C., Maxted P. F. L., Miller G. R. M., Pollacco D., Queloz D., Simpson E., Smalley B., Triaud A. H. M. J., Boisse I., Bouchy F., Gillon M., Hébrard G., 2012a, MNRAS, 423, 1503

Brown D. J. A., Collier Cameron A., Díaz R. F., Doyle A. P., Gillon M., Lendl M., Smalley B., Triaud A. H. M. J., Anderson D. R., Enoch B., Hellier C., Maxted P. F. L., Miller G. R. M., Pollacco D., Queloz D., Boisse I., Hébrard G., 2012b, ApJ, 760, 139

Buchhave L. A., Bakos G. Á., Hartman J. D., Torres G., Kovács G., Latham D. W., Noyes R. W., Esquerdo G. A., Everett M., Howard A. W., Marcy G. W., Fischer D. A., Johnson J. A., Andersen J., Fűrész G., Perumpilly G., Sasselov D. D., Stefanik R. P., Béky B., Lázár J., Papp I., Sári P., 2010, ApJ, 720, 1118

Buchhave L. A., Latham D. W., Carter J. A., Désert J.-M., Torres G., Adams E. R., Bryson S. T., Charbonneau D. B., Ciardi D. R., Kulesa C., Dupree A. K., Fischer D. A., Fressin F., Gautier, III T. N., Gilliland R. L., Howell S. B., Isaacson H., Jenkins J. M., Marcy G. W., McCarthy D. W., Rowe J. F., Batalha N. M., Borucki W. J., Brown T. M., Caldwell D. A., Christiansen J. L., Cochran W. D., Deming D., Dunham E. W., Everett M., Ford E. B., Fortney J. J., Geary J. C., Girouard F. R., Haas M. R., Holman M. J., Horch E., Klaus T. C., Knutson H. A., Koch

D. G., Kolodziejczak J., Lissauer J. J., Machalek P., Mullally F., Still M. D., Quinn S. N., Seager S., Thompson S. E., Van Cleve J., 2011, ApJs, 197, 3

Budaj J., 2011, AJ, 141, 59

Burke C. J., Gaudi B. S., DePoy D. L., Pogge R. W., 2006, AJ, 132, 210

Burrows A., Budaj J., Hubeny I., 2008, ApJ, 678, 1436

Burton J. R., Watson C. A., Littlefair S. P., Dhillon V. S., Gibson N. P., Marsh T. R., Pollacco D., 2012, ApJs, 201, 36

Carter J. A., Winn J. N., 2009, ApJ, 704, 51

Charbonneau D., 2003, Astronomical Society of the Pacific Conference Series, 294, 449

Charbonneau D., Brown T. M., Latham D. W., Mayor M., 2000, ApJL, 529, L45

Charbonneau D., Brown T. M., Noyes R. W., Gilliland R. L., 2002, ApJ, 568, 377

Charbonneau D., Allen L. E., Megeath S. T., Torres G., Alonso R., Brown T. M., Gilliland R. L., Latham D. W., Mandushev G., O'Donovan F. T., Sozzetti A., 2005, ApJ, 626, 523

Charbonneau D., Knutson H. A., Barman T., Allen L. E., Mayor M., Megeath S. T., Queloz D., Udry S., 2008, ApJ, 686, 1341

Charbonneau D., Berta Z. K., Irwin J., Burke C. J., Nutzman P., Buchhave L. A., Lovis C., Bonfils X., Latham D. W., Udry S., Murray-Clay R. A., Holman M. J., Falco E. E., Winn J. N., Queloz D., Pepe F., Mayor M., Delfosse X., Forveille T., 2009, Nature, 462, 891

Chen G., van Boekel R., Wang H., Nikolov N., Fortney J. J., Seemann U., Wang W., Mancini L., Henning T., 2014, A&A, 563, A40

Christiansen J. L., Clarke B. D., Burke C. J., Jenkins J. M., Barclay T. S., Ford E. B., Haas M. R., Sabale A., Seader S., Claiborne Smith J., Tenenbaum P., Twicken J. D., Kamal Uddin A., Thompson S. E., 2013, ApJS, 207, 35

Christiansen J. L., Clarke B. D., Burke C. J., Seader S., Jenkins J. M., Twicken J. D., Catanzarite J. D., Smith J. C., Batalha N. M., Haas M. R., Thompson S. E., Campbell J. R., Sabale A., Kamal Uddin A., 2015, ApJ, 810, 95

Ciceri S., Mancini L., Southworth J., Lendl M., Tregloan-Reed J., Brahm R., Chen G., D'Ago G., Dominik M., Figuera Jaimes R., Galianni P., Harpsøe K., Hinse T. C., Jørgensen U. G., Juncher D., Korhonen H., Liebig C., Rabus M., Bonomo A. S., Bott K., Henning T., Jordán A., Sozzetti A., Alsubai K. A., Andersen J. M., Bajek D., Bozza V., Bramich D. M., Browne P., Calchi Novati S., Damerdji Y., Diehl C., Elyiv A., Giannini E., Gu S.-H., Hundertmark M., Kains N., Penny M., Popovas A., Rahvar S., Scarpetta G., Schmidt R. W., Skottfelt J., Snodgrass C., Surdej J., Vilela C., Wang X.-B., Wertz O., 2016, MNRAS, 456, 990

Claret A., 2000, A&A, 363, 1081

Claret A., 2004, A&A, 428, 1001

Collier Cameron A., Pollacco D., Street R. A., Lister T. A., West R. G., Wilson D. M., Pont F., Christian D. J., Clarkson W. I., Enoch B., Evans A., Fitzsimmons A., Haswell C. A., Hellier C., Hodgkin S. T., Horne K., Irwin J., Kane S. R., Keenan F. P., Norton A. J., Parley N. R., Osborne J., Ryans R., Skillen I., Wheatley P. J., 2006, MNRAS, 373, 799

Collier Cameron A., Wilson D. M., West R. G., Hebb L., Wang X.-B., Aigrain S., Bouchy F., Christian D. J., Clarkson W. I., Enoch B., Esposito M., Guenther E., Haswell C. A., Hébrard G., Hellier C., Horne K., Irwin J., Kane S. R., Loeillet B., Lister T. A., Maxted P., Mayor M., Moutou C., Parley N., Pollacco D., Pont F., Queloz D., Ryans R., Skillen I., Street R. A., Udry S., Wheatley P. J., 2007, MNRAS, 380, 1230

Collier Cameron A., Guenther E., Smalley B., McDonald I., Hebb L., Andersen J., Augusteijn T., Barros S. C. C., Brown D. J. A., Cochran W. D., Endl M., Fossey S. J., Hartmann M., Maxted P. F. L., Pollacco D., Skillen I., Telting J., Waldmann I. P., West R. G., 2010, MNRAS, 407, 507

Cowan N. B., Agol E., 2011, ApJ, 729, 54

Cowan N. B., Agol E., Charbonneau D., 2007, MNRAS, 379, 641

Cruz P., Barrado D., Lillo-Box J., Diaz M., Birkby J., López-Morales M., Hodgkin S., Fortney J. J., 2015, A&A, 574, A103

David T. J., Hillenbrand L. A., Petigura E. A., Carpenter J. M., Crossfield I. J. M., Hinkley S., Ciardi D. R., Howard A. W., Isaacson H. T., Cody A. M., Schlieder J. E., Beichman C. A., Barenfeld S. A., 2016, Nature, 534, 658

de Mooij E. J. W., Brogi M., de Kok R. J., Koppenhoefer J., Nefs S. V., Snellen I. A. G., Greiner J., Hanse J., Heinsbroek R. C., Lee C. H., van der Werf P. P., 2012, A&A, 538, A46

de Wit J., Seager S., 2013, Science, 342, 1473

Deming D., Wilkins A., McCullough P., Burrows A., Fortney J. J., Agol E., Dobbs-Dixon I., Madhusudhan N., Crouzet N., Desert J.-M., Gilliland R. L., Haynes K., Knutson H. A., Line M., Magic Z., Mandell A. M., Ranjan S., Charbonneau D., Clampin M., Seager S., Showman A. P., 2013, ApJ, 774, 95

Deming D., Knutson H., Kammer J., Fulton B. J., Ingalls J., Carey S., Burrows A., Fortney J. J., Todorov K., Agol E., Cowan N., Desert J.-M., Fraine J., Langton J., Morley C., Showman A. P., 2015, ApJ, 805, 132

Désert J.-M., Vidal-Madjar A., Lecavelier Des Etangs A., Sing D., Ehrenreich D., Hébrard G., Ferlet R., 2008, AAP, 492, 585

Dotter A., Chaboyer B., Jevremović D., Kostov V., Baron E., Ferguson J. W., 2008, ApJS, 178, 89

Doyle A. P., Smalley B., Maxted P. F. L., Anderson D. R., Cameron A. C., Gillon M., Hellier C., Pollacco D., Queloz D., Triaud A. H. M. J., West R. G., 2013, MNRAS, 428, 3164

Doyle A. P., Davies G. R., Smalley B., Chaplin W. J., Elsworth Y., 2014, MNRAS, 444, 3592

Dragomir D., Kane S. R., Pilyavsky G., Mahadevan S., Ciardi D. R., Gazak J. Z., Gelino D. M., Payne A., Rabus M., Ramirez S. V., von Braun K., Wright J. T., Wyatt P., 2011, AJ, 142, 115

Dragomir D., Benneke B., Pearson K. A., Crossfield I. J. M., Eastman J., Barman T., Biddle L. I., 2015, ApJ, 814, 102

Enoch B., Collier Cameron A., Parley N. R., Hebb L., 2010, A&A, 516, A33

Fabrycky D., Tremaine S., 2007, ApJ, 669, 1298

Ferland G. J., Korista K. T., Verner D. A., Ferguson J. W., Kingdon J. B., Verner E. M., 1998, PASP, 110, 761

Fernandez J. M., Holman M. J., Winn J. N., Torres G., Shporer A., Mazeh T., Esquerdo G. A., Everett M. E., 2009, AJ, 137, 4911

Ford E. B., 2005, AJ, 129, 1706

Ford E. B., 2006, ApJ, 642, 505

Foreman-Mackey D., Price-Whelan A., Geoffrey R., Smith E., Smith M., Barbary K., Hogg D. W., J. Brewer B. J., 2014, triangle.py v0.1.1, Online: http://dx.doi.org/10.5281/zenodo.11020

Fortier A., Beck T., Benz W., Broeg C., Cessa V., Ehrenreich D., Thomas N., 2014, Proc.SPIE, 9143, 91432J

Fortney J. J., Baraffe I., Militzer B., Exoplanets, chapter 17, p. 397, University of Arizona Press, 2011

Fortney J. J., Lodders K., Marley M. S., Freedman R. S., 2008, ApJ, 678, 1419

Fraine J. D., Deming D., Gillon M., Jehin E., Demory B.-O., Benneke B., Seager S., Lewis N. K., Knutson H., Désert J.-M., 2013, ApJ, 765, 127

Freedman R. A., Geller R. M., Kaufmann W. J., 2011, Universe, W.H. Freeman

Fukui A., Narita N., Kurosaki K., Ikoma M., Yanagisawa K., Kuroda D., Shimizu Y., Takahashi Y. H., Ohnuki H., Onitsuka M., Hirano T., Suenaga T., Kawauchi K., Nagayama S., Ohta K., Yoshida M., Kawai N., Izumiura H., 2013, ApJ, 770, 95

Fukui A., Kawashima Y., Ikoma M., Narita N., Onitsuka M., Ita Y., Onozato H., Nishiyama S., Baba H., Ryu T., Hirano T., Hori Y., Kurosaki K., Kawauchi K., Takahashi Y. H., Nagayama T., Tamura M., Kawai N., Kuroda D., Nagayama S., Ohta K., Shimizu Y., Yanagisawa K., Yoshida M., Izumiura H., 2014, ApJ, 790, 108

Fukui A., Narita N., Kawashima Y., Kusakabe N., Onitsuka M., Ryu T., Ikoma M., Yanagisawa K., Izumiura H., 2016, ApJ, 819, 27

Gaudi B. S., Winn J. N., 2007, ApJ, 655, 550

Gazak J. Z., Johnson J. A., Tonry J., Dragomir D., Eastman J., Mann A. W., Agol E., 2012, Ad Ast, 2012, 697967

Gelman A., Carlin J. B., Stern H. S., Rubin D. B., 2003, Bayesian data analysis, Chapman& Hall

Gianni G., Mazzitelli I., Natali G., 1975, A&A, 44, 277

Gibson N. P., Aigrain S., Roberts S., Evans T. M., Osborne M., Pont F., 2012, MNRAS, 419, 2683

Gillon M., Smalley B., Hebb L., Anderson D. R., Triaud A. H. M. J., Hellier C., Maxted P. F. L., Queloz D., Wilson D. M., 2009, A&A, 496, 259

Gillon M., Lanotte A. A., Barman T., Miller N., Demory B.-O., Deleuil M., Montalbán J., Bouchy F., Collier Cameron A., Deeg H. J., Fortney J. J., Fridlund M., Harrington J., Magain P., Moutou C., Queloz D., Rauer H., Rouan D., Schneider J., 2010, A&A, 511, A3

Gillon M., Doyle A. P., Lendl M., Maxted P. F. L., Triaud A. H. M. J., Anderson D. R., Barros S. C. C., Bento J., Collier-Cameron A., Enoch B., Faedi F., Hellier C., Jehin E., Magain P., Montalbán J., Pepe F., Pollacco D., Queloz D., Smalley B., Segransan D., Smith A. M. S., Southworth J., Udry S., West R. G., Wheatley P. J., 2011a, A&A, 533, A88

Gillon M., Jehin E., Magain P., Chantry V., Hutsemékers D., Manfroid J., Queloz D., Udry S., 2011b, European Physical Journal Web of Conferences, 11, 6002

Gillon M., Triaud A. H. M. J., Fortney J. J., Demory B.-O., Jehin E., Lendl M., Magain P., Kabath P., Queloz D., Alonso R., Anderson D. R., Collier Cameron A., Fumel A., Hebb L., Hellier C., Lanotte A., Maxted P. F. L., Mowlavi N., Smalley B., 2012, A&A, 542, A4

Gillon M., Anderson D. R., Collier-Cameron A., Delrez L., Hellier C., Jehin E., Lendl M., Maxted P. F. L., Pepe F., Pollacco D., Queloz D., Ségransan D., Smith A. M. S., Smalley B., Southworth J., Triaud A. H. M. J., Udry S., Van Grootel V., West R. G., 2014, A&A, 562, L3

Ginzburg S., Sari R., 2016, ApJ, 819, 116

Gould A., Morgan C. W., 2003, ApJ, 585, 1056

Greene T. P., Line M. R., Montero C., Fortney J. J., Lustig-Yaeger J., Luther K., 2016, ApJ, 817, 17

Greiner J., Bornemann W., Clemens C., Deuter M., Hasinger G., Honsberg M., Huber H., Huber S., Krauss M., Krühler T., Küpcü Yoldaş A., Mayer-Hasselwander H., Mican B., Primak N., Schrey F., Steiner I., Szokoly G., Thöne C. C., Yoldaş A., Klose S., Laux U., Winkler J., 2008, PASP, 120, 405

Grosheintz L., Mendonça J., Käppeli R., Lukas Grimm S., Mishra S., Heng K., 2015, AAS/Division for Extreme Solar Systems Abstracts, 3, 111.09

Hall D. S., Genet R. M., 1988, Photoelectric photometry of variable stars. A practical guide for the smaller observatory, Willmann-Bell, Inc.

Hébrard G., Collier Cameron A., Brown D. J. A., Díaz R. F., Faedi F., Smalley B., Anderson D. R., Armstrong D., Barros S. C. C., Bento J., Bouchy F., Doyle A. P., Enoch B., Gómez Maqueo Chew Y., Hébrard É. M., Hellier C., Lendl M., Lister T. A., Maxted P. F. L., McCormac J., Moutou C., Pollacco D., Queloz D., Santerne A., Skillen I., Southworth J., Tregloan-Reed J., Triaud A. H. M. J., Udry S., Vanhuysse M., Watson C. A., West R. G., Wheatley P. J., 2013, A&A, 549, A134

Hecht S., 1924, J Gen Physiol, 7, 235

Hellier C., Anderson D. R., Collier Cameron A., Gillon M., Hebb L., Maxted P. F. L., Queloz D., Smalley B., Triaud A. H. M. J., West R. G., Wilson D. M., Bentley S. J., Enoch B., Horne K., Irwin J., Lister T. A., Mayor M., Parley N., Pepe F., Pollacco D. L., Segransan D., Udry S., Wheatley P. J., 2009, Nature, 460, 1098

Hellier C., Anderson D. R., Collier Cameron A., Gillon M., Jehin E., Lendl M., Maxted P. F. L., Pepe F., Pollacco D., Queloz D., Ségransan D., Smalley B., Smith A. M. S., Southworth J., Triaud A. H. M. J., Udry S., West R. G., 2011, A&A, 535, L7

Hellier C., Anderson D. R., Collier Cameron A., Doyle A. P., Fumel A., Gillon M., Jehin E., Lendl M., Maxted P. F. L., Pepe F., Pollacco D., Queloz D., Ségransan D., Smalley B., Smith A. M. S., Southworth J., Triaud A. H. M. J., Udry S., West R. G., 2012, MNRAS, 426, 739

Hellier C., Anderson D. R., Collier Cameron A., Delrez L., Gillon M., Jehin E., Lendl M., Maxted P. F. L., Pepe F., Pollacco D., Queloz D., Ségransan D., Smalley B., Smith A. M. S., Southworth J., Triaud A. H. M. J., Turner O. D., Udry S., West R. G., 2015, AJ, 150, 18

Hellier C., Anderson D. R., Collier Cameron A., Delrez L., Gillon M., Jehin E., Lendl M., Maxted P. F. L., Neveu-VanMalle M., Pepe F., Pollacco D., Queloz D., Segransan D., Smalley B., Southworth J., Triaud A. H. M. J., Udry S., Wagg T., West R. G., 2016, ArXiv e-prints:1604.04195

Henry G. W., Marcy G. W., Butler R. P., Vogt S. S., 2000, ApJL, 529, L41

Hirano T., Suto Y., Winn J. N., Taruya A., Narita N., Albrecht S., Sato B., 2011, ApJ, 742, 69

Hoeijmakers H. J., de Kok R. J., Snellen I. A. G., Brogi M., Birkby J. L., Schwarz H., 2015, A&A, 575, A20

Høg E., Fabricius C., Makarov V. V., Urban S., Corbin T., Wycoff G., Bastian U., Schwekendiek P., Wicenec A., 2000, A&A, 355, L27

Horne K., 2003, Astronomical Society of the Pacific Conference Series, 294, 361

Howard A. W., Sanchis-Ojeda R., Marcy G. W., Johnson J. A., Winn J. N., Isaacson H., Fischer D. A., Fulton B. J., Sinukoff E., Fortney J. J., 2013, Nature, 503, 381

Howarth I. D., Murray J., Mills D., Berry D. S., 2004, Starlink User Note, 50

Howe A. R., Burrows A. S., 2012, ApJ, 756, 176

Howell S. B., 1989, PASP, 101, 616

Hoyer S., Pallé E., Dragomir D., Murgas F., 2016, AJ, 151, 137

Husnoo N., Pont F., Hébrard G., Simpson E., Mazeh T., Bouchy F., Moutou C., Arnold L., Boisse I., Díaz R. F., Eggenberger A., Shporer A., 2011, MNRAS, 413, 2500

Jeffries R. D., 2014, EAS Publications Series, 65, 289

Jiang I.-G., Lai C.-Y., Savushkin A., Mkrtichian D., Antonyuk K., Griv E., Hsieh H.-F., Yeh L.-C., 2016, AJ, 151, 17

Joshi Y. C., Pollacco D., Collier Cameron A., Skillen I., Simpson E., Steele I., Street R. A., Stempels H. C., Christian D. J., Hebb L., Bouchy F., Gibson N. P., Hébrard G., Keenan F. P., Loeillet B., Meaburn J., Moutou C., Smalley B., Todd I., West R. G., Anderson D. R., Bentley S., Enoch B., Haswell C. A., Hellier C., Horne K., Irwin J., Lister T. A., McDonald I., Maxted P., Mayor M., Norton A. J., Parley N., Perrier C., Pont F., Queloz D., Ryans R., Smith A. M. S., Udry S., Wheatley P. J., Wilson D. M., 2009, MNRAS, 392, 1532

Kasper M., Beuzit J.-L., Verinaud C., Gratton R. G., Kerber F., Yaitskova N., Boccaletti A., Thatte N., Schmid H. M., Keller C., Baudoz P., Abe L., Aller-Carpentier E., Antichi J., Bonavita M., Dohlen K., Fedrigo E., Hanenburg H., Hubin N., Jager R., Korkiakoski V., Martinez P., Mesa D., Preis O., Rabou P., Roelfsema R., Salter G., Tecza M., Venema L., 2010, Proc.SPIE, 7735, 77352E

Kempton E., Lupu R. E., Slough P., Owusu-Asare A., Cale B., 2015, American Astronomical Society Meeting Abstracts, 225, 257.17

Kervella P., Thévenin F., Di Folco E., Ségransan D., 2004, A&A, 426, 297

Kippenhahn R., Weigert A., Weiss A., 2012, *Astronomy and Astrophysics Library*, Stellar Structure and Evolution, Springer Berlin Heidelberg

Kipping D. M., Bakos G. Á., Buchhave L., Nesvorný D., Schmitt A., 2012, ApJ, 750, 115

Knutson H. A., Charbonneau D., Allen L. E., Fortney J. J., Agol E., Cowan N. B., Showman A. P., Cooper C. S., Megeath S. T., 2007, Nat, 447, 183

Knutson H. A., Charbonneau D., Allen L. E., Burrows A., Megeath S. T., 2008, ApJ, 673, 526

Knutson H. A., Howard A. W., Isaacson H., 2010, ApJ, 720, 1569

Kovács G., Zucker S., Mazeh T., 2002, A&A, 391, 369

Kreidberg L., Line M. R., Bean J. L., Stevenson K. B., Désert J.-M., Madhusudhan N., Fortney J. J., Barstow J. K., Henry G. W., Williamson M. H., Showman A. P., 2015, ApJ, 814, 66

Kristian J., Blouke M., 1982, Scientific American, 247, 66

Lee J.-M., Heng K., Irwin P. G. J., 2013, ApJ, 778, 97

Lendl M., Anderson D. R., Collier-Cameron A., Doyle A. P., Gillon M., Hellier C., Jehin E., Lister T. A., Maxted P. F. L., Pepe F., Pollacco D., Queloz D., Smalley B., Ségransan D., Smith A. M. S., Triaud A. H. M. J., Udry S., West R. G., Wheatley P. J., 2012, A&A, 544, A72

Lendl M., Gillon M., Queloz D., Alonso R., Fumel A., Jehin E., Naef D., 2013, A&A, 552, A2

Lendl M., Triaud A. H. M. J., Anderson D. R., Collier Cameron A., Delrez L., Doyle A. P., Gillon M., Hellier C., Jehin E., Maxted P. F. L., Neveu-VanMalle M., Pepe F., Pollacco D., Queloz D., Ségransan D., Smalley B., Smith A. M. S., Udry S., Van Grootel V., West R. G., 2014, A&A, 568, A81

Linsky J. L., Yang H., France K., Froning C. S., Green J. C., Stocke J. T., Osterman S. N., 2010, ApJ, 717, 1291

Lucy L. B., Sweeney M. A., 1971, AJ, 76, 544

Maciejewski G., Dimitrov D., Mancini L., Southworth J., Ciceri S., D'Ago G., Bruni I., Raetz S., Nowak G., Ohlert J., Puchalski D., Saral G., Derman E., Petrucci R., Jofre E., Seeliger M., Henning T., 2016, AcA, 66, 55

Madhusudhan N., Seager S., 2010, ApJ, 725, 261

Madhusudhan N., 2012, ApJ, 758, 36

Madhusudhan N., Amin M. A., Kennedy G. M., 2014, ApJL, 794, L12

Mahtani D. P., Maxted P. F. L., Anderson D. R., Smith A. M. S., Smalley B., Tregloan-Reed J., Southworth J., Madhusudhan N., Collier Cameron A., Gillon M., Harrington J., Hellier C., Pollacco D., Queloz D., Triaud A. H. M. J., West R. G., 2013, MNRAS, 432, 693

Malik M., Grosheintz L., Lukas Grimm S., Mendonça J., Kitzmann D., Heng K., 2015, AAS/Division for Extreme Solar Systems Abstracts, 3, 111.05

Mamajek E. E., Hillenbrand L. A., 2008, ApJ, 687, 1264

Mancini L., Ciceri S., Chen G., Tregloan-Reed J., Fortney J. J., Southworth J., Tan T. G., Burgdorf M., Calchi Novati S., Dominik M., Fang X.-S., Finet F., Gerner T., Hardis S., Hinse T. C., Jørgensen U. G., Liebig C., Nikolov N., Ricci D., Schäfer S., Schönebeck F., Skottfelt J., Wertz O., Alsubai K. A., Bozza V., Browne P., Dodds P., Gu S.-H., Harpsøe K., Henning T., Hundertmark M., Jessen-Hansen J., Kains N., Kerins E., Kjeldsen H., Lund M. N., Lundkvist M., Madhusudhan N., Mathiasen M., Penny M. T., Prof S., Rahvar S., Sahu K., Scarpetta G., Snodgrass C., Surdej J., 2013, MNRAS, 436, 2

Mancini L., Southworth J., Ciceri S., Calchi Novati S., Dominik M., Henning T., Jørgensen U. G., Korhonen H., Nikolov N., Alsubai K. A., Bozza V., Bramich D. M., D'Ago G., Figuera Jaimes R., Galianni P., Gu S.-H., Harpsøe K., Hinse

T. C., Hundertmark M., Juncher D., Kains N., Popovas A., Rabus M., Rahvar S., Skottfelt J., Snodgrass C., Street R., Surdej J., Tsapras Y., Vilela C., Wang X.-B., Wertz O., 2014a, A&A, 568, A127

Mancini L., Southworth J., Ciceri S., Dominik M., Henning T., Jørgensen U. G., Lanza A. F., Rabus M., Snodgrass C., Vilela C., Alsubai K. A., Bozza V., Bramich D. M., Calchi Novati S., D'Ago G., Figuera Jaimes R., Galianni P., Gu S.-H., Harpsøe K., Hinse T., Hundertmark M., Juncher D., Kains N., Korhonen H., Popovas A., Rahvar S., Skottfelt J., Street R., Surdej J., Tsapras Y., Wang X.-B., Wertz O., 2014b, A&A, 562, A126

Mancini L., Southworth J., Ciceri S., Tregloan-Reed J., Crossfield I., Nikolov N., Bruni I., Zambelli R., Henning T., 2014c, MNRAS, 443, 2391

Mancini L., Kemmer J., Southworth J., Bott K., Mollière P., Ciceri S., Chen G., Henning T., 2016, MNRAS, 459, 1393

Mandel K., Agol E., 2002, ApJL, 580, L171

Maxted P. F. L., Anderson D. R., Collier Cameron A., Hellier C., Queloz D., Smalley B., Street R. A., Triaud A. H. M. J., West R. G., Gillon M., Lister T. A., Pepe F., Pollacco D., Ségransan D., Smith A. M. S., Udry S., 2011, PASP, 123, 547

Maxted P. F. L., Serenelli A. M., Southworth J., 2015, A&A, 575, A36

Mayor M., Queloz D., 1995, Nature, 378, 355

McLaughlin D. B., 1924, ApJ, 60, 22

Meibom S., Mathieu R. D., Stassun K. G., 2009, ApJ, 695, 679

Mink D. J., 1997, Astronomical Society of the Pacific Conference Series, 125, 249

Monet D. G., Levine S. E., Canzian B., Ables H. D., Bird A. R., Dahn C. C., Guetter H. H., Harris H. C., Henden A. A., Leggett S. K., Levison H. F., Luginbuhl C. B.,

Martini J., Monet A. K. B., Munn J. A., Pier J. R., Rhodes A. R., Riepe B., Sell S., Stone R. C., Vrba F. J., Walker R. L., Westerhout G., Brucato R. J., Reid I. N., Schoening W., Hartley M., Read M. A., Tritton S. B., 2003, AJ, 125, 984

Montet B. T., Crepp J. R., Johnson J. A., Howard A. W., Marcy G. W., 2014, ApJ, 781, 28

Morrison D., Owen T., 2003, The Planetary System, Addison Wesley

Mortier A., Santos N. C., Sousa S. G., Fernandes J. M., Adibekyan V. Z., Delgado Mena E., Montalto M., Israelian G., 2013, A&A, 558, A106

Murgas F., Pallé E., Zapatero Osorio M. R., Nortmann L., Hoyer S., Cabrera-Lavers A., 2014, A&A, 563, A41

Nascimbeni V., Piotto G., Pagano I., Scandariato G., Sani E., Fumana M., 2013, A&A, 559, A32

Nascimbeni V., Mallonn M., Scandariato G., Pagano I., Piotto G., Micela G., Messina S., Leto G., Strassmeier K. G., Bisogni S., Speziali R., 2015, A&A, 579, A113

Naylor T., 1998, MNRAS, 296, 339

Neveu-VanMalle M., Queloz D., Anderson D. R., Brown D. J. A., Collier Cameron A., Delrez L., Díaz R. F., Gillon M., Hellier C., Jehin E., Lister T., Pepe F., Rojo P., Ségransan D., Triaud A. H. M. J., Turner O. D., Udry S., 2016, A&A, 586, A93

Ngo H., Knutson H. A., Hinkley S., Crepp J. R., Bechter E. B., Batygin K., Howard A. W., Johnson J. A., Morton T. D., Muirhead P. S., 2015, ApJ, 800, 138

Nikolov N., Chen G., Fortney J. J., Mancini L., Southworth J., van Boekel R., Henning T., 2013, A&A, 553, A26

Oberst T. E., Rodriguez J. E., Colón K. D., Angerhausen D., Bieryla A., Ngo H., Stevens D. J., Stassun K. G., Gaudi B. S., Pepper J., Penev K., Mawet D., Latham

D. W., Heintz T. M., Osei B. W., Collins K. A., Kielkopf J. F., Visgaitis T., Reed P. A., Escamilla A., Yazdi S., McLeod K. K., Lunsford L. T., Spencer M., Joner M. D., Gregorio J., Gaillard C., Matt K., Dumont M. T., Stephens D. C., Cohen D. H., Jensen E. L. N., Calchi Novati S., Bozza V., Labadie-Bartz J., Siverd R. J., Lund M. B., Beatty T. G., Eastman J. D., Penny M. T., Manner M., Zambelli R., Fulton B. J., DePoy D. L., Marshall J. L., Pogge R. W., Gould A., Trueblood M., Trueblood P., 2016, ArXiv e-prints

Ohta Y., Taruya A., Suto Y., 2005, ApJ, 622, 1118

Pepper J., Pogge R. W., DePoy D. L., Marshall J. L., Stanek K. Z., Stutz A. M., Poindexter S., Siverd R., O'Brien T. P., Trueblood M., Trueblood P., 2007, PASP, 119, 923

Pepper J., Kuhn R. B., Siverd R., James D., Stassun K., 2012, PASP, 124, 230

Pepper J., Rodriguez J. E., Collins K. A., Johnson J. A., Fulton B. J., Howard A. W., Beatty T., Stassun K. G., Isaacson H., Colón K. d., Lund M. B., Kuhn R. B., Siverd R. J., Gaudi B. S., Tan T. G., Curtis I., Stockdale C., Mawet D., Bottom M., James D., Zhou G., Bayliss D., Cargile P., Bieryla A., Penev K., Latham D. W., Labadie-Bartz J., Kielkopf J., Eastman J. D., Oberst T. E., Jensen E. L. N., Nelson P., Sliski D. H., Wittenmyer R. A., McCrady N., Wright J. T., Relles H. M., 2016, ArXiv e-prints: 1607.01755

Pollacco D. L., Skillen I., Collier Cameron A., Christian D. J., Hellier C., Irwin J., Lister T. A., Street R. A., West R. G., Anderson D. R., Clarkson W. I., Deeg H., Enoch B., Evans A., Fitzsimmons A., Haswell C. A., Hodgkin S., Horne K., Kane S. R., Keenan F. P., Maxted P. F. L., Norton A. J., Osborne J., Parley N. R., Ryans R. S. I., Smalley B., Wheatley P. J., Wilson D. M., 2006, PASP, 118, 1407

Pont F., Zucker S., Queloz D., 2006, MNRAS, 373, 231

Queloz D., Eggenberger A., Mayor M., Perrier C., Beuzit J. L., Naef D., Sivan J. P., Udry S., 2000, A+A, 359, L13

Queloz D., Henry G. W., Sivan J. P., Baliunas S. L., Beuzit J. L., Donahue R. A., Mayor M., Naef D., Perrier C., Udry S., 2001, A&A, 379, 279

Rauer H., Catala C., Aerts C., Appourchaux T., Benz W., Brandeker A., Christensen-Dalsgaard J., Deleuil M., Gizon L., Goupil M.-J., Güdel M., Janot-Pacheco E., Mas-Hesse M., Pagano I., Piotto G., Pollacco D., Santos Ċ., Smith A., Suárez J.-C., Szabó R., Udry S., Adibekyan V., Alibert Y., Almenara J.-M., Amaro-Seoane P., Eiff M. A.-v., Asplund M., Antonello E., Barnes S., Baudin F., Belkacem K., Bergemann M., Bihain G., Birch A. C., Bonfils X., Boisse I., Bonomo A. S., Borsa F., Brandão I. M., Brocato E., Brun S., Burleigh M., Burston R., Cabrera J., Cassisi S., Chaplin W., Charpinet S., Chiappini C., Church R. P., Csizmadia S., Cunha M., Damasso M., Davies M. B., Deeg H. J., Díaz R. F., Dreizler S., Dreyer C., Eggenberger P., Ehrenreich D., Eigmüller P., Erikson A., Farmer R., Feltzing S., de Oliveira Fialho F., Figueira P., Forveille T., Fridlund M., García R. A., Giommi P., Giuffrida G., Godolt M., Gomes da Silva J., Granzer T., Grenfell J. L., Grotsch-Noels A., Günther E., Haswell C. A., Hatzes A. P., Hébrard G., Hekker S., Helled R., Heng K., Jenkins J. M., Johansen A., Khodachenko M. L., Kislyakova K. G., Kley W., Kolb U., Krivova N., Kupka F., Lammer H., Lanza A. F., Lebreton Y., Magrin D., Marcos-Arenal P., Marrese P. M., Marques J. P., Martins J., Mathis S., Mathur S., Messina S., Miglio A., Montalban J., Montalto M., Monteiro M. J. P. F. G., Moradi H., Moravveji E., Mordasini C., Morel T., Mortier A., Nascimbeni V., Nelson R. P., Nielsen M. B., Noack L., Norton A. J., Ofir A., Oshagh M., Ouazzani R.-M., Pápics P., Parro V. C., Petit P., Plez B., Poretti E., Quirrenbach A., Ragazzoni R., Raimondo G., Rainer M., Reese D. R., Redmer R., Reffert S., Rojas-Ayala B., Roxburgh I. W., Salmon S., Santerne A., Schneider J., Schou J., Schuh S., Schunker H., Silva-Valio A., Silvotti R., Skillen I., Snellen I., Sohl F., Sousa S. G., Sozzetti A., Stello D., Strassmeier K. G., Švanda M., Szabó G. M., Tkachenko A., Valencia D., Van Grootel V., Vauclair S. D., Ventura P., Wagner F. W., Walton N. A., Weingrill J., Werner S. C., Wheatley P. J., Zwintz K., 2014, Exp. Astron., 38, 249

Redfield S., Endl M., Cochran W. D., Koesterke L., 2008, ApJL, 673, L87

Reif K., Bagschik K., de Boer K. S., Schmoll J., Mueller P., Poschmann H., Klink G., Kohley R., Heber U., Mebold U., 1999, SPIE, 3649, 109

Ricci D., Ramón-Fox F. G., Ayala-Loera C., Michel R., Navarro-Meza S., Fox-Machado L., Reyes-Ruiz M., Sevilla S. B., Curiel S., 2015, PASP, 127, 143

Ricker G. R., Winn J. N., Vanderspek R., Latham D. W., Bakos G. Á., Bean J. L., Berta-Thompson Z. K., Brown T. M., Buchhave L., Butler N. R., Butler R. P., Chaplin W. J., Charbonneau D., Christensen-Dalsgaard J., Clampin M., Deming D., Doty J., De Lee N., Dressing C., Dunham E. W., Endl M., Fressin F., Ge J., Henning T., Holman M. J., Howard A. W., Ida S., Jenkins J. M., Jernigan G., Johnson J. A., Kaltenegger L., Kawai N., Kjeldsen H., Laughlin G., Levine A. M., Lin D., Lissauer J. J., MacQueen P., Marcy G., McCullough P. R., Morton T. D., Narita N., Paegert M., Palle E., Pepe F., Pepper J., Quirrenbach A., Rinehart S. A., Sasselov D., Sato B., Seager S., Sozzetti A., Stassun K. G., Sullivan P., Szentgyorgyi A., Torres G., Udry S., Villasenor J., 2015, JATIS, 1(1), 014003

Rossiter R. A., 1924, ApJ, 60, 15

Sada P. V., Deming D., Jennings D. E., Jackson B. K., Hamilton C. M., Fraine J., Peterson S. W., Haase F., Bays K., Lunsford A., O'Gorman E., 2012, PASP, 124, 212

Salter G. S., Thatte N. A., Tecza M., Clarke F., Kasper M. E., 2014, IAU Symposium, 293, 442

Santos N. C., Mayor M., Naef D., Pepe F., Queloz D., Udry S., Burnet M., Clausen J. V., Helt B. E., Olsen E. H., Pritchard J. D., 2002, A&A, 392, 215

Savini G., Ade P., Arena C., Barnes K., Bezawada N., Brooke T., Bryson I., Crook M., Curry P., Eccleston P., Friend J., Hipwood L., Jason S., Griffin M. J., Johnston G., Knowles P., Leese M., MacLeod A., Mason J., Papageorgiou A., Pascale E.,

Patel M., Prasad S., Saad A., Sarkar S., Saunders C., Shaughnessy B., Smith A., Sudiwala R., Wright G. S., Taylor W., Tennyson J., Tessenyi M., Tosh I., Vora A., Wells M., Williams J., Winter B., Zingales T., 2016, Proc.SPIE, 9904

Seager S., Deming D., 2010, Annual Review of Astronomy and Astrophysics, 48(1), 631

Seager S., Mallén-Ornelas G., 2003, ApJ, 585, 1038

Sestito P., Randich S., 2005, A&A, 442, 615

Shahbaz T., Naylor T., Charles P. A., 1994, MNRAS, 268, 756

Simon A. E., Szabó G. M., Kiss L. L., Fortier A., Benz W., 2015, PASP, 127, 1084

Simpson E. K., Faedi F., Barros S. C. C., Brown D. J. A., Collier Cameron A., Hebb L., Pollacco D., Smalley B., Todd I., Butters O. W., Hébrard G., McCormac J., Miller G. R. M., Santerne A., Street R. A., Skillen I., Triaud A. H. M. J., Anderson D. R., Bento J., Boisse I., Bouchy F., Enoch B., Haswell C. A., Hellier C., Holmes S., Horne K., Keenan F. P., Lister T. A., Maxted P. F. L., Moulds V., Moutou C., Norton A. J., Parley N., Pepe F., Queloz D., Segransan D., Smith A. M. S., Stempels H. C., Udry S., Watson C. A., West R. G., Wheatley P. J., 2011a, AJ, 141, 8

Simpson E. K., Pollacco D., Cameron A. C., Hébrard G., Anderson D. R., Barros S. C. C., Boisse I., Bouchy F., Faedi F., Gillon M., Hebb L., Keenan F. P., Miller G. R. M., Moutou C., Queloz D., Skillen I., Sorensen P., Stempels H. C., Triaud A., Watson C. A., Wilson P. A., 2011b, MNRAS, 414, 3023

Sing D. K., Lecavelier A., Désert J.-M., Vidal-Madjar A., Ballester G., 2008, Proceedings of the International Astronomical Union, 4, 532

Sing D. K., Désert J.-M., Fortney J. J., Lecavelier Des Etangs A., Ballester G. E., Cepa J., Ehrenreich D., López-Morales M., Pont F., Shabram M., Vidal-Madjar A., 2011, A+A, 527, A73

Sing D. K., Huitson C. M., Lopez-Morales M., Pont F., Désert J.-M., Ehrenreich D., Wilson P. A., Ballester G. E., Fortney J. J., Lecavelier des Etangs A., Vidal-Madjar A., 2012, MNRAS, 426, 1663

Sing D. K., Lecavelier des Etangs A., Fortney J. J., Burrows A. S., Pont F., Wakeford H. R., Ballester G. E., Nikolov N., Henry G. W., Aigrain S., Deming D., Evans T. M., Gibson N. P., Huitson C. M., Knutson H., Showman A. P., Vidal-Madjar A., Wilson P. A., Williamson M. H., Zahnle K., 2013, MNRAS, 436, 2956

Sing D. K., Wakeford H. R., Showman A. P., Nikolov N., Fortney J. J., Burrows A. S., Ballester G. E., Deming D., Aigrain S., Désert J.-M., Gibson N. P., Henry G. W., Knutson H., Lecavelier des Etangs A., Pont F., Vidal-Madjar A., Williamson M. W., Wilson P. A., 2015, MNRAS, 446, 2428

Skrutskie M. F., Cutri R. M., Stiening R., Weinberg M. D., Schneider S., Carpenter J. M., Beichman C., Capps R., Chester T., Elias J., Huchra J., Liebert J., Lonsdale C., Monet D. G., Price S., Seitzer P., Jarrett T., Kirkpatrick J. D., Gizis J. E., Howard E., Evans T., Fowler J., Fullmer L., Hurt R., Light R., Kopan E. L., Marsh K. A., McCallon H. L., Tam R., Van Dyk S., Wheelock S., 2006, AJ, 131, 1163

Smalley B., 2014, IAU Symposium, 301, 39

Smith A. M. S., Hebb L., Collier Cameron A., Anderson D. R., Lister T. A., Hellier C., Pollacco D., Queloz D., Skillen I., West R. G., 2009, MNRAS, 398, 1827

Smith A. M. S., Anderson D. R., Collier Cameron A., Gillon M., Hellier C., Lendl M., Maxted P. F. L., Queloz D., Smalley B., Triaud A. H. M. J., West R. G., Barros S. C. C., Jehin E., Pepe F., Pollacco D., Segransan D., Southworth J., Street R. A., Udry S., 2012a, AJ, 143, 81

Smith A. M. S., Anderson D. R., Madhusudhan N., Southworth J., Collier Cameron A., Blecic J., Harrington J., Hellier C., Maxted P. F. L., Pollacco D., Queloz D., Smalley B., Triaud A. H. M. J., Wheatley P. J., 2012b, A&A, 545, A93

Snellen I., 2013, European Physical Journal Web of Conferences, 47, 11001

Snellen I. A. G., de Kok R. J., de Mooij E. J. W., Albrecht S., 2010, Nature, 465, 1049

Snellen I. A. G., de Kok R. J., le Poole R., Brogi M., Birkby J., 2013, ApJ, 764, 182

Southworth J., 2009, MNRAS, 394, 272

Southworth J., 2011a, MNRAS, 417, 2166

Southworth J., 2011b, MNRAS, 417, 2166

Southworth J., Hinse T. C., Dominik M., Fang X.-S., Harpsøe K., Jørgensen U. G., Kerins E., Liebig C., Mancini L., Skottfelt J., Anderson D. R., Smalley B., Tregloan-Reed J., Wertz O., Alsubai K. A., Bozza V., Calchi Novati S., Dreizler S., Gu S.-H., Hundertmark M., Jessen-Hansen J., Kains N., Kjeldsen H., Lund M. N., Lundkvist M., Mathiasen M., Penny M. T., Rahvar S., Ricci D., Scarpetta G., Snodgrass C., Surdej J., 2012, MNRAS, 426, 1338

Southworth J., Mancini L., Browne P., Burgdorf M., Calchi Novati S., Dominik M., Gerner T., Hinse T. C., Jørgensen U. G., Kains N., Ricci D., Schäfer S., Schönebeck F., Tregloan-Reed J., Alsubai K. A., Bozza V., Chen G., Dodds P., Dreizler S., Fang X.-S., Finet F., Gu S.-H., Hardis S., Harpsøe K., Henning T., Hundertmark M., Jessen-Hansen J., Kerins E., Kjeldsen H., Liebig C., Lund M. N., Lundkvist M., Mathiasen M., Nikolov N., Penny M. T., Proft S., Rahvar S., Sahu K., Scarpetta G., Skottfelt J., Snodgrass C., Surdej J., Wertz O., 2013, MNRAS, 434, 1300

Southworth J., Hinse T. C., Burgdorf M., Calchi Novati S., Dominik M., Galianni P., Gerner T., Giannini E., Gu S.-H., Hundertmark M., Jørgensen U. G., Juncher D., Kerins E., Mancini L., Rabus M., Ricci D., Schäfer S., Skottfelt J., Tregloan-Reed J., Wang X.-B., Wertz O., Alsubai K. A., Andersen J. M., Bozza V., Bramich D. M., Browne P., Ciceri S., D'Ago G., Damerdji Y., Diehl C., Dodds P., Elyiv A., Fang X.-S., Finet F., Figuera Jaimes R., Hardis S., Harpsøe K., Jessen-Hansen

J., Kains N., Kjeldsen H., Korhonen H., Liebig C., Lund M. N., Lundkvist M., Mathiasen M., Penny M. T., Popovas A., Prof. S., Rahvar S., Sahu K., Scarpetta G., Schmidt R. W., Schönebeck F., Snodgrass C., Street R. A., Surdej J., Tsapras Y., Vilela C., 2014, MNRAS, 444, 776

Southworth J., Mancini L., Tregloan-Reed J., Calchi Novati S., Ciceri S., D'Ago G., Delrez L., Dominik M., Evans D. F., Gillon M., Jehin E., Jørgensen U. G., Haugbølle T., Lendl M., Arena C., Barbieri L., Barbieri M., Corfini G., Lopresti C., Marchini A., Marino G., Alsubai K. A., Bozza V., Bramich D. M., Jaimes R. F., Hinse T. C., Henning T., Hundertmark M., Juncher D., Korhonen H., Popovas A., Rabus M., Rahvar S., Schmidt R. W., Skottfelt J., Snodgrass C., Starkey D., Surdej J., Wertz O., 2015, MNRAS, 454, 3094

Southworth J., Tregloan-Reed J., Andersen M. I., Calchi Novati S., Ciceri S., Colque J. P., D'Ago G., Dominik M., Evans D. F., Gu S.-H., Herrera-Cordova A., Hinse T. C., Jørgensen U. G., Juncher D., Kuffmeier M., Mancini L., Peixinho N., Popovas A., Rabus M., Skottfelt J., Tronsgaard R., Unda-Sanzana E., Wang X.-B., Wertz O., Alsubai K. A., Andersen J. M., Bozza V., Bramich D. M., Burgdorf M., Damerdji Y., Diehl C., Elyiv A., Figuera Jaimes R., Haugbølle T., Hundertmark M., Kains N., Kerins E., Korhonen H., Liebig C., Mathiasen M., Penny M. T., Rahvar S., Scarpetta G., Schmidt R. W., Snodgrass C., Starkey D., Surdej J., Vilela C., Essen C. v., Wang Y., 2016, MNRAS, 457, 4205

Steele I. A., Bates S. D., Gibson N., Keenan F., Meaburn J., Mottram C. J., Pollacco D., Todd I., 2008, SPIE, 7014, 70146J

Sterken C., Manfroid J., 1992, Astronomical Photometry, A Guide, Kluwer Academic Publishers

Stevenson K. B., Désert J.-M., Line M. R., Bean J. L., Fortney J. J., Showman A. P., Kataria T., Kreidberg L., McCullough P. R., Henry G. W., Charbonneau D., Burrows A., Seager S., Madhusudhan N., Williamson M. H., Homeier D., 2014, Science, 346, 838

Stevenson K. B., Lewis N. K., Bean J. L., Beichman C., Fraine J., Kilpatrick B. M., Krick J. E., Lothringer J. D., Mandell A. M., Valenti J. A., Agol E., Angerhausen D., Barstow J. K., Birkmann S. M., Burrows A., Charbonneau D., Cowan N. B., Crouzet N., Cubillos P. E., Curry S. M., Dalba P. A., de Wit J., Deming D., Désert J.-M., Doyon R., Dragomir D., Ehrenreich D., Fortney J. J., García Muñoz A., Gibson N. P., Gizis J. E., Greene T. P., Harrington J., Heng K., Kataria T., Kempton E. M.-R., Knutson H., Kreidberg L., Lafrenière D., Lagage P.-O., Line M. R., Lopez-Morales M., Madhusudhan N., Morley C. V., Rocchetto M., Schlawin E., Shkolnik E. L., Shporer A., Sing D. K., Todorov K. O., Tucker G. S., Wakeford H. R., 2016, PASP, 128(9), 094401

Street R. A., Simpson E., Barros S. C. C., Pollacco D., Joshi Y., Todd I., Collier Cameron A., Enoch B., Parley N., Stempels E., Hebb L., Triaud A. H. M. J., Queloz D., Segransan D., Pepe F., Udry S., Lister T. A., Depagne É., West R. G., Norton A. J., Smalley B., Hellier C., Anderson D. R., Maxted P. F. L., Bentley S. J., Skillen I., Gillon M., Wheatley P., Bento J., Cathaway-Kjontvedt P., Christian D. J., 2010, ApJ, 720, 337

Swain M. R., Tinetti G., Vasisht G., Deroo P., Griffith C., Bouwman J., Chen P., Yung Y., Burrows A., Brown L. R., Matthews J., Rowe J. F., Kuschnig R., Angerhausen D., 2009, ApJ, 704, 1616

Tamuz O., Mazeh T., Zucker S., 2005, MNRAS, 356, 1466

Tegmark M., Strauss M. A., Blanton M. R., Abazajian K., Dodelson S., Sandvik H., Wang X., Weinberg D. H., Zehavi I., Bahcall N. A., Hoyle F., Schlegel D., Scoccimarro R., Vogeley M. S., Berlind A., Budavari T., Connolly A., Eisenstein D. J., Finkbeiner D., Frieman J. A., Gunn J. E., Hui L., Jain B., Johnston D., Kent S., Lin H., Nakajima R., Nichol R. C., Ostriker J. P., Pope A., Scranton R., Seljak U., Sheth R. K., Stebbins A., Szalay A. S., Szapudi I., Xu Y., Annis J., Brinkmann J., Burles S., Castander F. J., Csabai I., Loveday J., Doi M., Fukugita M., Gillespie B., Hennessy G., Hogg D. W., Ivezić Ž., Knapp G. R., Lamb D. Q.,

Lee B. C., Lupton R. H., McKay T. A., Kunszt P., Munn J. A., O'Connell L., Peoples J., Pier J. R., Richmond M., Rockosi C., Schneider D. P., Stoughton C., Tucker D. L., vanden Berk D. E., Yanny B., York D. G., 2004, Phys. Rev. D, 69(10), 103501

Torres G., Andersen J., Giménez A., 2010, A&A Rv., 18, 67

Triaud A. H. M. J., 2011, AAP, 534, L6

Turner J. D., Christie D., Arras P., Johnson R. E., Schmidt C., 2016a, MNRAS, 458, 3880

Turner J. D., Pearson K. A., Biddle L. I., Smart B. M., Zellem R. T., Teske J. K., Hardegree-Ullman K. K., Griffith C. C., Leiter R. M., Cates I. T., Nieberding M. N., Smith C.-T. W., Thompson R. M., Hofmann R., Berube M. P., Nguyen C. H., Small L. C., Guvenen B. C., Richardson L., McGraw A., Raphael B., Crawford B. E., Robertson A. N., Tombleson R., Carleton T. M., Towner A. P. M., Walker-LaFollette A. M., Hume J. R., Watson Z. T., Jones C. K., Lichtenberger M. J., Hoglund S. R., Cook K. L., Crossen C. A., Jorgensen C. R., Romine J. M., Thompson A. R., Villegas C. F., Wilson A. A., Sanford B., Taylor J. M., Henz T. N., 2016b, MNRAS, 459, 789

Turner O. D., Anderson D. R., Collier Cameron A., Delrez L., Evans D. F., Gillon M., Hellier C., Jehin E., Lendl M., Maxted P. F. L., Pepe F., Pollacco D., Queloz D., Ségransan D., Smalley B., Smith A. M. S., Triaud A. H. M. J., Udry S., West R. G., 2016c, PASP, 128(6), 064401

Vidal-Madjar A., Huitson C. M., Bourrier V., Désert J.-M., Ballester G., Lecavelier des Etangs A., Sing D. K., Ehrenreich D., Ferlet R., Hébrard G., McConnell J. C., 2013, A&A, 560, A54

Waldmann I. P., Tinetti G., Rocchetto M., Barton E. J., Yurchenko S. N., Tennyson J., 2015, ApJ, 802, 107

Wheatley P. J., Pollacco D. L., Queloz D., Rauer H., Watson C. A., West R. G., Chazelas B., Louden T. M., Bannister N., Bento J., Burleigh M., Cabrera J., Eigmüller P., Erikson A., Genolet L., Goad M., Grange A., Jordán A., Lawrie K., McCormac J., Neveu M., Walker S., 2014, IAU Symposium, 299, 311

Widenhorn R., Blouke M. M., Weber A., Rest A., Bodegom E., 2002, Proc. SPIE, 4669, 193

Williams P. K. G., Charbonneau D., Cooper C. S., Showman A. P., Fortney J. J., 2006, ApJ, 649, 1020

Wilson D. M., 2007, PhD thesis, University of Keele

Winn J. N., Fabrycky D., Albrecht S., Johnson J. A., 2010a, ApJL, 718, L145

Winn J. N., Johnson J. A., Howard A. W., Marcy G. W., Isaacson H., Shporer A., Bakos G. Á., Hartman J. D., Albrecht S., 2010b, ApJL, 723, L223

Wöllert M., Brandner W., 2015, A&A, 579, A129

Wöllert M., Brandner W., Bergfors C., Henning T., 2015, A&A, 575, A23

Wood P. L., Maxted P. F. L., Smalley B., Iro N., 2011, MNRAS, 412, 2376

Wright J. T., 2005, PASP, 117, 657

Wu Y., Lithwick Y., 2013, ApJ, 772, 74

Zerbi F. M., Bouchy F., Fynbo J., Maiolino R., Piskunov N., Rebolo Lopez R., Santos N., Strassmeier K., Udry S., Vanzi L., Riva M., Basden A., Boisse I., Bonfils X., Buscher D., Cabral A., Dimarcantonio P., Di Varano I., Henry D., Monteiro M., Morris T., Murray G., Oliva E., Parry I., Pepe F., Quirrenbach A., Rasilla J. L., Rees P., Stempels E., Valenziano L., Wells M., Wildi F., Origlia L., Allende Prieto C., Chiavassa A., Cristiani S., Figueira P., Gustafsson B., Hatzes A., Haehnelt M., Heng K., Israelian G., Kochukhov O., Lovis C., Marconi A., Martins C. J. A. P.,

Noterdaeme P., Petitjean P., Puzia T., Queloz D., Reiners A., Zoccali M., 2014, Proc.SPIE, 9147, 914723

Zhao M., O'Rourke J. G., Wright J. T., Knutson H. A., Burrows A., Fortney J., Ngo H., Fulton B. J., Baranec C., Riddle R., Law N. M., Muirhead P. S., Hinkley S., Showman A. P., Curtis J., Burruss R., 2014, ApJ, 796, 115